Voltammetry of Electrochemically Heterogeneous Surfaces

A thesis submitted for degree of Doctor of Philosophy in Physical and Theoretical Chemistry

by

Kristopher R. Ward

St John's College,
University of Oxford

October 2013

Abstract

In this thesis, mathematical modelling is used to theoretically investigate the electrochemical behaviour of surfaces which can be broadly classified as being 'electrochemically heterogeneous'. Simulated voltammetry is used in the exploration of a number of specific systems as listed below.

- The cyclic voltammetry of electrodes composed of two different electroactive materials that differ in terms of their electrochemical rate constants towards any given redox couple. The effect of the distribution of the two materials was investigated and the occurrence of split peak cyclic voltammetry where two peaks are observed in the forward sweep, was studied. The technique was specifically applied to the modelling of highly-ordered pyrolytic graphite (HOPG).

- The steady-state voltammetry of a conducting spherical particle resting on an insulating supporting surface. An algebraic expression that completely describes the voltammetric waveform in the limit of irreversible kinetics was developed.

- The cyclic voltammetry of the EC′ (catalytic) mechanism at a regularly distributed array of hemispherical particles on an insulating supporting surface. Particular attention was paid to the 'split-wave' phenomenon, where two peaks are observed in the forward scan of a cyclic voltammogram and the conditions under which these peaks are resolvable were elucidated.

- The linear sweep voltammetry of micro- and nano-particle modified electrodes and other electrodes of *partially covered and non-planar* geometry. It was demonstrated that the apparent electrochemical rate constant of the reaction

and thus the peak position of the voltammetry is dependent only on the relative electroactive surface area of the particles on the surface and not upon their shape or distribution. This has wide reaching implications as it can be used to explain some instances of a purported nano-catalytic effect without appeal to altered properties at the nanoscale.

- The linear sweep voltammetry of the interior of a partially electroactive cylindrical pore. Four limiting cases were observed and fully characterised.

- The linear sweep voltammetry of porous surfaces. It was established that if the pores are less than a certain threshold depth, then a porous surface will also display an apparent catalytic effect that is dependent on the relative electroactive surface area (including the area in the interior of the pores).

Acknowledgements

First, I would like to thank Prof. Richard Compton for his help and guidance in his roles as my undergraduate tutor, Master's supervisor and inevitably, D. Phil. supervisor over the course of the last seven years. Special thanks also go to Schlumberger, particularly Drs. Nathan S. Lawrence and R. Seth Hartshorne for providing the funding that made this research possible.

My heartfelt thanks go to every member of the Compton group for making the last four years so much fun. In particular, I wish to thank Dr Edmund J. F. Dickinson for his patient instruction during my Master's project, and Dr Eduardo Laborda for his boundless competence and unparalleled work ethic. Honourable mentions also go to Dr Debbie S. Silvester-Dean, Linhongjia Xiong, Dr Christopher Batchelor-McAuley, Christopher C. M. Neumann, Matthew Gara, Edward O. Barnes, Sven Ernst, Ying Wang, and Patricia Lee, for their efforts in collaborative work.

Most importantly, I would like to thank both my parents and Grace for their continuing love and support.

Finally, I wish to thank the humble electron, without which, none of this would be possible.

Contents

Glossary of Symbols

Roman symbols

A	electrode area / m^2
c^*	concentration / mol dm^{-3}
c_s	concentration of species s / mol dm^{-3}
C_s	dimensionless concentration of species s
d	centre-to-centre distance / m
d_s	dimensionless diffusion coefficient
D_s	diffusion coefficient / m^2 s^{-1}
E	potential / V
E_f^0	formal potential of redox couple / V
F	Faraday constant / C mol^{-1}
i	spatial step index
I	current / A
j	spatial step index
j_s	flux of species s / mol m^{-2} s^{-1}
J	dimensionless current
k	temporal step index
k^0	Butler–Volmer rate constant / m s^{-1}

k_2	second order homogeneous rate constant / m^3 mol^{-1} s^{-1}
l	microband length / m
N	number of unit cells in array
r	radial coordinate in polar coordinate system / m
$\mathcal{R}$	gas constant / J mol^{-1} K^{-1}
t	time / s
T	dimensionless time
$\mathcal{T}$	temperature / K
V	volume / m^3
x	spatial coordinate / m
y	spatial coordinate / m
z	spatial coordinate / m

Greek symbols

α	transfer coefficient
α_i	Thomas algorithm coefficient
β_i	Thomas algorithm coefficient
γ_i	Thomas algorithm coefficient
γ	space expansion coefficient
δ_i	Thomas algorithm coefficient
ν	scan rate / V s^{-1}
ϕ	angle
σ	dimensionless scan rate
θ	dimensionless potential
Θ	surface coverage
Γ	error
Ψ	surface area ratio
ω	angle

Table of Dimensionless Coordinates

Dimensionless Coordinates

C_s	c_s/c^*_{A}	concentration
d_s	D_s/D^*_{A}	diffusion coefficient
X	x/ϵ	normal coordinate (1D)
R	r/ϵ	radial coordinate (2D)
Z	z/ϵ	axial coordinate (2D)
T	$D_{\mathrm{A}}t/\epsilon^2$	time
θ	$F(E-E^0_f)/\mathcal{RT}$	potential
σ	$\epsilon^2 F\nu/D_{\mathrm{A}}RT$	scan rate
J	$I\epsilon/FAD_{\mathrm{A}}c^*_{\mathrm{A}}$	current
K^0	$k^0\epsilon/D_{\mathrm{A}}$	rate constant
K_2	$k^0\epsilon^2 c^*/D_{\mathrm{A}}$	2^{nd} order rate constant

where ϵ is a characteristic length e.g., x_{e}, r_{e}.

Chapter 1

Fundamentals of Electrochemistry

This thesis is concerned with the voltammetry of electrochemically heterogeneous surfaces, that is, electrodes where the electroactivity is spatially variant. Accordingly, this chapter introduces the fundamental concepts that are necessary in order to understand and interpret voltammetry in general and highlights some specific features of the voltammetry of arrays of microelectrodes, which are one particular type of heterogeneous surface.

1.1 Electrochemical Equilibria

Consider two chemical species, A and B, in solution which may interconvert by the addition or removal of an electron:

$$\mathrm{A} + \mathrm{e}^- \rightleftharpoons \mathrm{B} \tag{1.1}$$

In a neutral solution there is no source (or sink) of electrons, so the reaction may only proceed by the introduction of an electrode to the solution.

In a metal, electron energy levels exist in a continuum and are filled to an energy maximum known as the Fermi level,[1] whereas those associated with the solution phase species, A and B, are discrete. If the energy of the LUMO (lowest unoccupied molecular orbital) of A is lower than that of the Fermi level, then it is energetically favourable for an electron to transfer from the metal to the LUMO of A, transforming it into B, and lowering the Fermi level (reduction). Likewise, if the energy of the

HOMO (highest occupied molecular orbital) of species B is higher than that of the Fermi level, the reverse process, oxidation, is favourable.

When an electrode is immersed in the solution (and connected to an external circuit), both of these processes will take place until a situation is reached where the Fermi level lies in between the energy levels of the two ions such that the rates of the forward and reverse reactions are the same and a dynamic equilibrium is attained. In reaching equilibrium, there is typically a net transfer of electrons in one direction or the other, resulting in a charge separation between the electrode and the solution, establishing a potential difference. After equilibrium is reached, there is no further net transfer of electrons.

Measurements of potential difference are typically carried out with a voltmeter which measures the potential between two test leads. Direct measurement of the difference in potential between the metal, ϕ_{M}, and the solution, ϕ_{S}, is therefore not possible without the addition of a second electrode to the solution. The second electrode is usually a standard reference electrode which has a constant composition and therefore the potential difference across its interface with the solution is invariant. The potential difference at the first (working) electrode may therefore be measured *relative* to that at the reference electrode. The measured potential, E, is:

$$E = (\phi_{\mathrm{M}} - \phi_{\mathrm{S}})_{\mathrm{working}} - (\phi_{\mathrm{M}} - \phi_{\mathrm{S}})_{\mathrm{reference}} \tag{1.2}$$

The potential established at the electrode under equilibrium conditions is given by the Nernst equation:

$$E = E_f^0 + \frac{RT}{F} \ln \frac{c_{\mathrm{A}}}{c_{\mathrm{B}}} \tag{1.3}$$

where c_{A} and c_{B} are the concentrations (at the electrode surface) of A and B respectively, and E_f^0 is the formal potential of the A/B couple. Note that in establishing equilibrium, only a tiny amount of net current is passed such that the concentrations of A and B are essentially unchanged.

1.2 Dynamic Electrochemistry

If instead of allowing a spontaneous equilibrium to be established, a potentiostat is used to apply a potential to the working electrode (relative to some reference electrode), a current is induced to flow. The application of a negative potential raises the energy of the Fermi level, causing electrons to flow from the metal to the solution, promoting the reduction of A versus the oxidation of B. The measured current, I, is given by

$$I = FAj_{0,\mathrm{A}} \tag{1.4}$$

where A is the electrode area and $j_{0,\mathrm{A}}$ is the net flux of species A at the electrode surface.

In addition to the applied potential, a number of other properties of the electrode/solution system can affect the measured current and hence flux, including the rate of transport of solution phase species between the electrode surface and bulk solution, the kinetics of the electron transfer process, and the nature and structure of the electrode surface. The aim of any voltammetric experiment is to study the current flow as a function of the applied potential. As the current is proportional to the rate of reaction, the current-potential relationship can be used to investigate one or more of these system properties.

1.2.1 Electrode Kinetics

For a reduction process such as that in Equation 1.1, the net flux at the electrode is

$$j = k_{\mathrm{red}}c_{\mathrm{A},0} - k_{\mathrm{ox}}c_{\mathrm{B},0} \tag{1.5}$$

where k_{red} and k_{ox} are the rate constants of the forward and reverse processes respectively and $c_{\mathrm{A},0}$ and $c_{\mathrm{B},0}$ are the surface concentrations of A and B respectively which are not necessarily equal to their bulk values. The measured current is therefore:

$$I = FA(k_{\mathrm{red}}c_{\mathrm{A},0} - k_{\mathrm{ox}}c_{\mathrm{B},0}) \tag{1.6}$$

The values of the rate constants, $k_{\text{red/ox}}$ are strongly influenced by the applied potential. The most widely adopted model that relates the rate constants to the potential is the Butler-Volmer model which is derived using transition state theory and posits that:

$$k_{\text{red}} = k^0 \exp\left(\frac{-\alpha F(E - E_f^0)}{RT}\right) \tag{1.7}$$

$$k_{\text{ox}} = k^0 \exp\left(\frac{(1-\alpha) F(E - E_f^0)}{RT}\right) \tag{1.8}$$

where k^0 is the standard electrochemical rate constant (cm s^{-1}), and α is the transfer coefficient, which is a measure of the symmetry of transition state of the reaction.[2] For a one electron transfer, $0 < \alpha < 1$, and it is often the case that $\alpha \approx \frac{1}{2}$. The values of k^0 and α are particular to a given redox couple-electrode system and are often determined empirically, though may be derived using Marcus theory[3] which is based on a microscopic consideration of the electron transfer process.

1.2.2 Mass Transport

In an electrochemical experiment, three separate process can act to move solution-phase species from one region to another, and thereby alter the local concentration: diffusion, migration and convection. The latter two can often be ignored if care is taken with experimental design, as described below, and this work focuses exclusively on experiments where mass transport is solely due to diffusion.

In a typical experiment, reduction of species A at the electrode surface results in a concentration gradient as the concentration of A is near the electrode is reduced relative to its value in bulk solution. This leads to diffusion of A from the bulk solution to the electrode surface as quantified by Fick's second law:

$$\frac{\partial c}{\partial t} = D\nabla^2 c \tag{1.9}$$

where D is the diffusion coefficient (particular to each species) and ∇^2 is the Laplace operator which is the sum of second partial derivatives of the concentration with respect to each spatial coordinate. In three dimensional Cartesian coordinates, (x,

y, z), this is

$$\frac{\partial c}{\partial t} = D\left(\frac{\partial^2 c}{\partial x^2} + \frac{\partial^2 c}{\partial y^2} + \frac{\partial^2 c}{\partial z^2}\right) \tag{1.10}$$

Such a concentration gradient can also result in a gradient of electrical potential, which causes transport of any charged species by migration. In most experimental situations this represents and unwelcome complication and makes analysis of the results considerably more challenging. Typically then, a large excess of some "supporting electrolyte",[4] which is electrochemically inert under the range of potentials studied, is added to the solution. The addition of these added ionic species acts to restrict the potential drop to a very small distance from the electrode surface such that the effect of migration can be considered to make only a negligible contribution to mass transport of electroactive species.

Apart from diffusion and migration, transport by convection can also take place due to different internal and external forces. Natural convection due to gradients of density can occur when the electrode reaction provokes a significant local change in the solution composition or due to thermal variations. These effects are minimised experimentally through the use of low concentrations of analyte and thermostated cells. Forced convection results from the use of non-static electrodes, such as rotating disc electrodes, and from non-static solutions, as used in e.g., channel electrodes. Forced convection induced in either of these ways is experimentally useful but is not considered by any of the work in this thesis.

1.2.3 Homogeneous Reactions

It is often the case that an electron transfer at the electrode produces a chemically unstable species that undergoes further reaction in solution. In the simplest case, the product of the reduction, B, undergoes a solution-phase reaction (such as electron transfer to/from some other species that is present in excess, or a rearrangement reaction); producing some third species, P. This is called the EC mechanism[2] where E is an electrochemical reaction step and C is a chemical reaction step:

$$\mathrm{A} + \mathrm{e}^- \rightleftharpoons \mathrm{B} \tag{1.11}$$

$$B \rightarrow P \tag{1.12}$$

In the event that P = A, the reaction mechanism is called EC′ (catalytic). Under the second order EC′ mechanism, B reacts with some other solution phase species, X, producing some product species, Y, as well as regenerating A:

$$A + e^- \rightleftharpoons B \tag{1.13}$$

$$B + X \rightarrow A + Y \tag{1.14}$$

Note that with this mechanism, the reaction cycles, constantly regenerating A when X is consumed, as long as there is sufficient X in the solution.

Many different homogeneous reaction mechanisms are possible, and complex sequences of heterogeneous and homogeneous steps are often observed experimentally. The classification of such processes always need to be carefully considered when analysing experimentally derived data, particular for novel systems.

1.2.4 Cyclic Voltammetry

The primary experimental techniques considered are this thesis are linear sweep voltammetry (LSV) and cyclic voltammetry (CV). In a typical LSV experiment, the potential is swept at a constant rate from some starting value where A is electrochemically stable, to some more negative value where reduction to B is favoured. The resulting current response is recorded and is subsequently analysed, yielding previously unknown details about the experimental system. CV extends this technique by reversing the direction of the potential sweep, and returning to the starting potential. A detailed mathematical model of this technique is developed in Chapter 2.

1.3 Diffusional modes

Voltammetry experiments often involve the use of macroelectrodes, i.e., electrodes that are large in comparison to the thickness of the diffusion layer, δ, where:

$$\delta \sim \sqrt{Dt} \tag{1.15}$$

In this case, the diffusion field is always perpendicular to the plane of the electrode surface. For smaller electrodes, the diffusional mode changes from linear to convergent[5] due to the increasing importance of diffusion to the edges of the electrode as they become smaller. If one of the dimensions of an electrode is on the order of 10 microns or less, it is known as a microelectrode. For such electrodes, at a sufficiently slow voltage sweep rate, a steady-state is eventually achieved where the current is unchanging with increasing potential as a consequence of convergent diffusion.

1.3.1 Microelectrode Arrays

One of the types of heterogeneous surfaces considered in this work is an array of microdisc electrodes. Here the diffusional and voltammetric behaviour of a microdisc array as it varies with the surface coverage (or equivalently with the disc-to-disc separation) and disc size is considered. It is observed that there are four limiting cases of behaviour; this classification applies generally to all partially active electrodes and was originally based on observations of partially blocked electrode systems.[6,7]

The category that any given experiment/simulation will fall into depends largely upon the distance that the electroactive species diffuse on the time scale (t) of the experiment ($\sim \sqrt{Dt}$) relative to the average separation between neighbouring discs, as well as upon the average disc radius. The time scale may be controlled in, for example, cyclic voltammetry, through the scan rate (high scan rate leads to short experimental time and low scan rate leads to a long experimental time); or in potential step chronoamperometry, by the duration of the potential pulse applied.

The diffusional behaviour observed in each case is illustrated schematically in Figure 1.1, accompanied by an example of the simulated linear sweep voltammetry that can be expected under each regime. The example voltammograms are simulated based on a system with a surface coverage $\Theta = 0.01$, disc radius $r_e = 1$ μm and diffusion coefficient $D_A = 10^{-5}$ cm^2 s^{-1}, and vary only in terms of the voltammetric scan rate, ν.

Case 1 behaviour, depicted in Figure 1.1(a), describes diffusion that is perpendicular to the surface of the electroactive site. This behaviour is observed when the size of the discs is large compared with $\sqrt{Dt}$. This can correspond to either a large (macroscale) disc, or to an experiment conducted over an extremely short time scale, such as a cyclic voltammetry with a very fast scan rate; the faster the scan rate, the smaller the discs can be while still observing case 1 behaviour. In the limit of fully reversible kinetics, the voltammetric response reflects linear diffusion to the electroactive area such that the peak current, I_p, is given by the Randles–Ševčík equation:

$$I_\mathrm{p} = -0.446\,\mathrm{F}A_\mathrm{ea}c^*\sqrt{\frac{\mathrm{F}D\nu}{\mathcal{R}T}} \tag{1.16}$$

where $A_\mathrm{ea} = N\pi r_\mathrm{e}^2$ is the total *electroactive* surface area of the microdisc array.

Case 2 behaviour, depicted in Figure 1.1(b), is observed when the size of the discs is small compared with $\sqrt{Dt}$. Under this category, each disc behaves as a microelectrode and diffusion to it is convergent rather than linear. In both cases 1 and 2, neighbouring discs are sufficiently far apart that they are effectively diffusionally independent on the experimental time scale. The voltammetric response in case 2 is therefore that of a single isolated microdisc electrode, scaled by the number of discs in the array; steady-state voltammetry is therefore observed for such arrays (assuming the scan rate is not too high). It should be emphasised again that diffusional independence in this case depends not on the absolute size of the inter-disc separation, d, but upon the ratio of this distance to the distance that electroactive species can diffuse on the time scale of the experiment ($\sim \sqrt{Dt}$); specifically, diffusional independence is achieved in cases 1 and 2 if $d > \sqrt{Dt}$. Consequently, the concept of diffusional independence can only apply to an electrode array for a finite amount of time

Case 3 behaviour, depicted in Figure 1.1(c), is also observed when the size of the discs is small but when the inter-disc separation is less than that in case 2 (again relative to $\sqrt{Dt}$). In this category, diffusion to each individual disc is still convergent, but the diffusion fields of neighbouring discs begin to overlap somewhat, a situation that is sometimes referred to as shielding. The current density is therefore

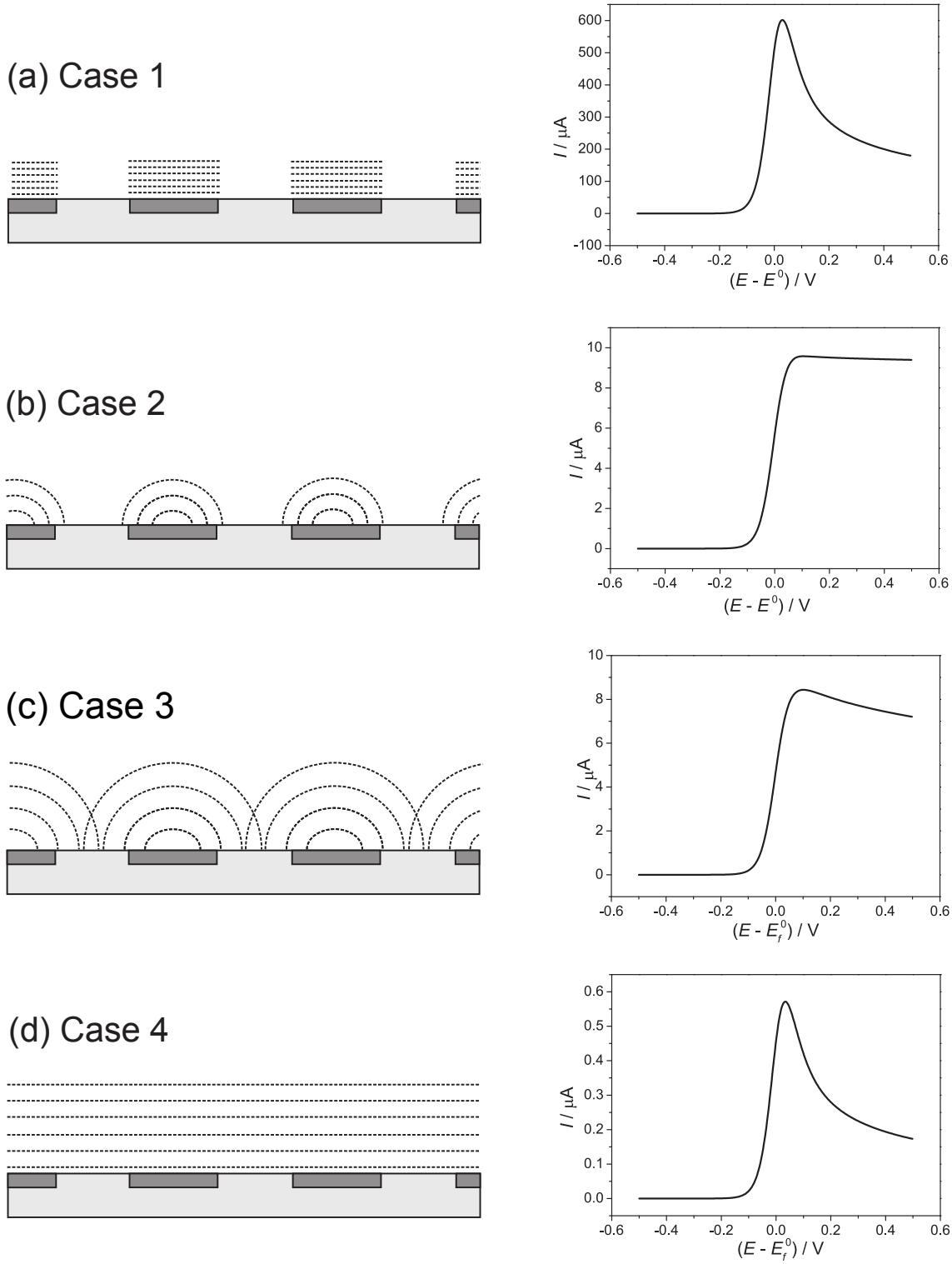

Figure 1.1: *The four limiting cases of diffusional behaviour to an array of microdisc electrodes.*

lower than in case 2 where each disc is effectively independent. The voltammetric response is intermediate in character between the sigmoidal, steady-state voltamme-

try observed for case 2 and the peaked voltammetry observed in case 1 (and case 4). When designing microelectrode arrays for use as, e.g., certain types of sensors, it is often desirable to maintain diffusional independence and thus avoid case 3 (shielding) behaviour in order to achieve a linear signal enhancement without additionally complicating the response.[8]

Case 4 behaviour, depicted in Figure 1.1(d), represents the extreme limit of case 3, where the spacing between adjacent discs is very small, such that there is very strong overlap of neighbouring diffusion fields and $d < \sqrt{Dt}$. In this case, diffusion is linear to the entire surface and the voltammetric response shows a well-defined peak. Perhaps surprisingly, in this limit, the peak current is given by the Randles–Ševčík equation where A is the total geometric area of the electrode system (active and inert); it is the same as it would be were the entire surface electroactive! Note that the occurrence of these four cases is time-dependent; given a long enough experimental time-scale, every array of discs (regardless of the size of the individual discs) will transition in behaviour from case 1 to case 4.

This classification scheme may be extended to a fifth case.[9] In case 5, the experimental time scale is very long (very slow scan rate) so that diffusion to the entire substrate is convergent, giving sigmoidal voltammetry. This behaviour is most readily observed experimentally when the supporting substrate itself is of microscale and the electroactive particles are of sub-micron size.

Although the voltammetric peak current in case 4 doesn't vary with the surface coverage of electroactive material, Θ, it is seen to affect the apparent electrochemical rate constant, k_{app}. It has been shown[6,10] that so long as the diffusional behaviour is strictly in the case 4 limit,

$$k^0_{\text{app}} = k^0\Theta \tag{1.17}$$

such that a lower surface coverage results in slower apparent kinetics. In the limit of fully reversible electrode kinetics, this has no influence on the observed voltammetry; however, this does not hold for the irreversible limit. In the latter case, the peak potential, E_{p}, is given by:[2]

$$E_{\mathrm{p}} = E_{\mathrm{f}}^{0} - \frac{RT}{\alpha F}\left[0.780 - \ln(\Theta k^{0}) + \ln\left(\sqrt{\frac{\alpha F D \nu}{RT}}\right)\right] \tag{1.18}$$

Bibliography

[1] R. G. Compton, G. H. W. Sanders and Editors., *Electrode Potentials.*, Oxford University Press, Oxford, 1996.

[2] A. J. Bard and L. R. Faulkner, *Electrochemical Methods: Fundamentals and Applications.*, John Wiley & Sons, New York, 2nd edn., 2001.

[3] R. A. Marcus and N. Sutin, *Biochim. Biophys. Acta*, 1985, **811**, 265–322.

[4] F. G. Cottrell, *Z. Physik. Chem.*, 1903, **42**, 385–431.

[5] K. Aoki, *Electroanal.*, 1993, **5**, 627–39.

[6] T. J. Davies, C. E. Banks and R. G. Compton, *J. Solid State Electrochem.*, 2005, **9**, 797–808.

[7] R. G. Compton and C. E. Banks, *Understanding Voltammetry*, ICP, London, 2nd edn., 2010.

[8] D. Menshykau and R. G. Compton, *J. Phys. Chem. C*, 2009, **113**, 15602–15620.

[9] I. Streeter, N. Fietkau, J. Del. Campo, R. Mas, F. X. Munoz and R. G. Compton, *J. Phys. Chem. C*, 2007, **111**, 12058–12066.

[10] C. Amatore, J. M. Savéant and D. Tessier, *J. Electroanal. Chem.*, 1983, **147**, 39–51.

Chapter 2

Mathematical Model of Cyclic Voltammetry

In a controlled-potential electrochemical experiment, a potential waveform, E, is applied to an experimental system and a current response, I, is recorded. The experimental system consists of a set of physical components (the electrodes and potentiostat, a number of chemical species in solution, beakers, etc.) which each posses a number of quantifiable characteristics; and a set of processes that act on those components (heterogeneous electron transfer, homogeneous chemical reaction, mass transport effects, etc.). In mathematical terms, the system may therefore by thought of as a function which operates on E and produces I as a result.

The goal of an electroanalytical experiment is to analyse the current response and use it and the applied potential waveform in order to infer the value/s of one or more of the system's parameters, or the existence/nature of some process that acts upon it, using previously developed theory. In the simple case, some or most of the system parameters are either known ahead of time or directly controlled, and some other parameter may be directly extracted by comparison of the current response to some known equation, such as the determination of concentration and diffusion coefficient in potential step chronoamperometry. In other cases, such as the determination of a homogeneous chemical reaction mechanism, or the analysis of a novel electrode geometry, such an approach may not be possible.

Mathematical modelling enables the prediction of the current response of an

arbitrary experimental system, so long as the initial state of the system is specified (perhaps subject to some simplifying assumptions). When one encounters a novel experimental system with, e.g., an unknown parameter in the simple case, or e.g., an unknown reaction mechanism, one can work backwards by comparing modelled and empirical results to infer the initial state of the novel system. In this chapter, a detailed mathematical model of a cyclic voltammetry experiment is developed. Much of material in this and the following chapter is adapted from a textbook co-written by the author which is currently awaiting publication by Imperial College Press[1]

2.1 Cyclic Voltammetry

Throughout this chapter, a simple one-electron reduction mechanism with no follow-up chemistry is assumed, however details of other reaction schemes are included in later chapters where appropriate. A general reduction process at the electrode is represented as:

$$\mathrm{A} + \mathrm{e}^- \rightleftharpoons \mathrm{B} \tag{2.1}$$

In a typical cyclic voltammetry experiment, the potential is swept linearly with time from some starting potential, E_i, where species A is stable, to some other, more negative potential, E_v, at which electron transfer between species A and the electrode is rapid, and species B is formed. The potential is then swept back to E_i causing electron transfer in the opposite direction and the reformation of A. This potential waveform is shown in Figure 2.1.

Throughout this process the current, I (proportional to the rate of electron transfer), is recorded; plotting the current against the potential gives a characteristic peaked cyclic voltammogram of a macroelectrode as shown in Figure 2.2.

The scan rate, ν, in V s^{-1}, is the constant rate at which the voltage sweeps from the initial potential, E_i, to the vertex potential, E_v, and back again. Figure 2.1 demonstrates that the scan rate is the rate of change of potential defined as:

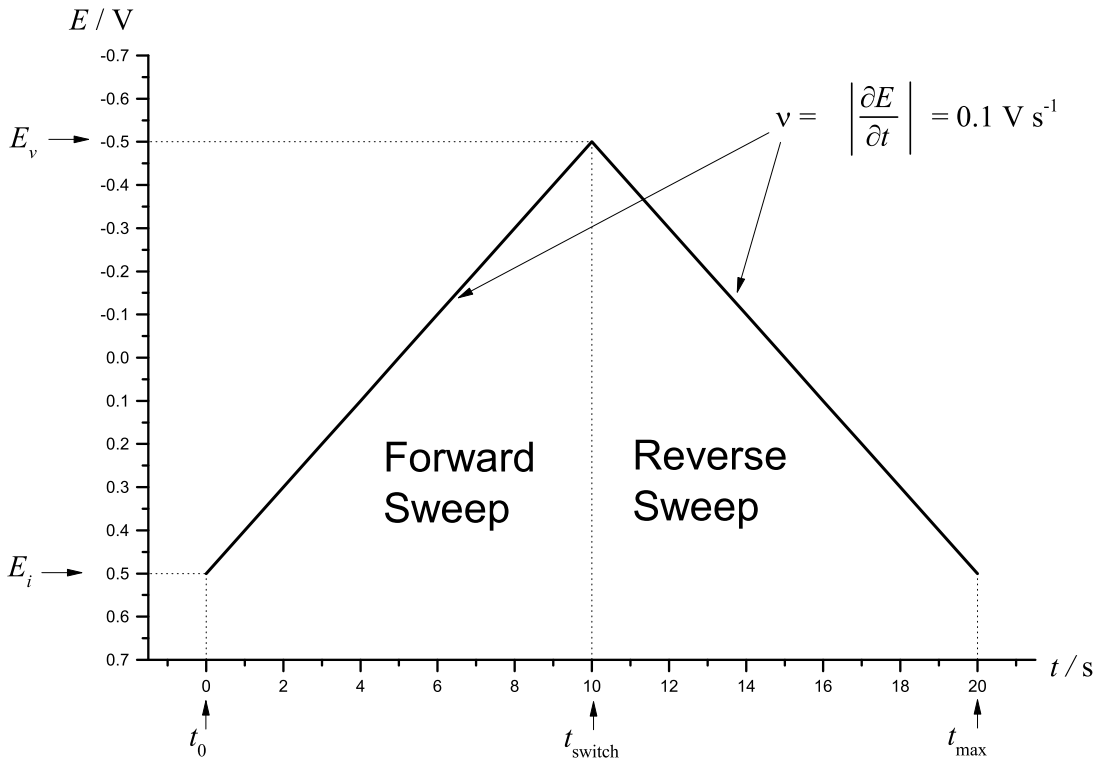

Figure 2.1: *The waveform of the potential applied during a typical cyclic voltammetry experiment. In this case the initial potential, E_i, is 0.5 V, the vertex potential, E_v, is -0.5 V, and the scan rate, ν, is 0.1 V s^{-1}*

$$\nu = \left| \frac{\partial E}{\partial t} \right| \tag{2.2}$$

At any time, t (s), on the forward sweep, the potential, E (V), is given by:

$$E = E_i - \nu t \tag{2.3}$$

At time $t = t_{\text{switch}}$, the potential reaches E_v and the potential sweep reverses direction. For $t > t_{\text{switch}}$:

$$E = E_v + \nu(t - t_{\text{switch}}) \tag{2.4}$$

2.2 Electrode Kinetics

Assuming the kinetics of the electron transfer are fast relative to the rate of mass transport, Nernstian equilibrium is attained at the electrode surface throughout the

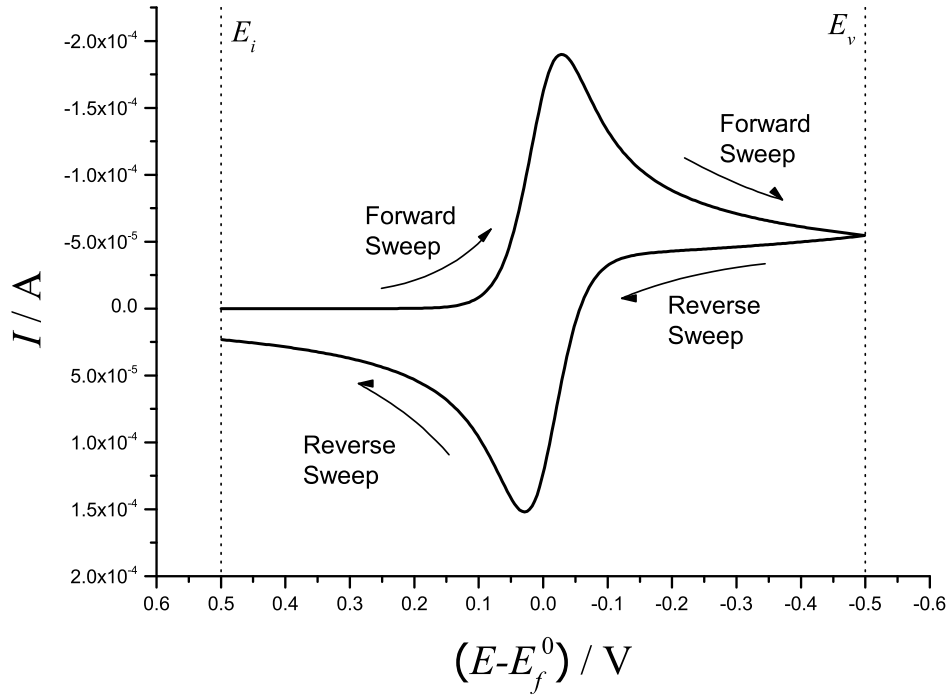

Figure 2.2: *A typical cyclic voltammogram produced by the application of the potential waveform in Figure 2.1.*

potential scan, and the Nernst equation therefore relates the surface concentrations of species A and B to the applied potential at the electrode, E:

$$E = E_f^0 + \frac{\mathcal{RT}}{\mathrm{F}} \ln\left(\frac{c_{\mathrm{A},0}}{c_{\mathrm{B},0}}\right) \tag{2.5}$$

where E_f^0 is the formal potential of the reaction, $\mathcal{R}$ is the gas constant, $\mathcal{T}$ is the temperature (often 298 K), F is the Faraday constant, and $c_{\mathrm{A},0}$ and $c_{\mathrm{B},0}$ are the concentrations at (next to) the electrode surface of A and B respectively.

In the case of finite kinetics, the surface concentrations may be related to the surface flux through the Butler-Volmer equation:

$$j_{\mathrm{A},0} = k^0 \left[\exp\left(\frac{(-\alpha)F(E-E_f^0)}{RT}\right) c_{\mathrm{A},0} - \exp\left(\frac{(1-\alpha)F(E-E_f^0)}{RT}\right) c_{\mathrm{B},0}\right] \tag{2.6}$$

where $j_{\mathrm{A},0}$ is the flux of species A at the electrode surface, k^0 is the electrochemical rate constant, and α is the transfer coefficient.

2.3 Diffusion

In a typical CV experiment, the concentration of the chemical species A is initially uniform and equal to its bulk value while that of species B is 0. When a relatively negative potential is applied, A is converted into B at the electrode, thus in the vicinity of the electrode, the concentration of A decreases and that of B increases. Consequently, fresh A diffuses toward the electrode from the bulk solution, and B diffuses away from the electrode. This process is illustrated schematically in Figure 2.3.

Fick's second law[2–4] predicts how the diffusion causes the concentration field to change with time

$$\frac{\partial c}{\partial t} = D\nabla^2 c \tag{2.7}$$

in a three-dimensional Cartesian coordinate system this is:

$$\frac{\partial c}{\partial t} = D\left(\frac{\partial^2 c}{\partial x^2} + \frac{\partial^2 c}{\partial y^2} + \frac{\partial^2 c}{\partial z^2}\right) \tag{2.8}$$

where the diffusion coefficient, D, is assumed to be direction-independent and c is the concentration of the species which is a function of the time, t, and spatial coordinates, x, y, and z. Simple electrochemical modelling consists of solving this partial differential equation (PDE) subject to certain boundary conditions, thereby determining the full time-evolution of the system.

Modelling a three-dimensional PDE is often difficult, especially when using numerical methods where it is extremely time consuming. As many of the systems commonly encountered in electrochemical experiments contain a high degree of symmetry, some simplifications may be employed to reduce the dimensionality of the problem rendering it more tractable. If a macroelectrode is considered then only diffusion perpendicular to the plane of the electrode surface need be considered. This is because there will be negligible diffusion parallel to the surface as shown in Figure 2.4 (a), i.e. every (y, z) plane will be homogeneous. The problem is thus reduced to one spatial dimension, x, the distance normal to the surface of the electrode. Fick's second law in this space is given by:

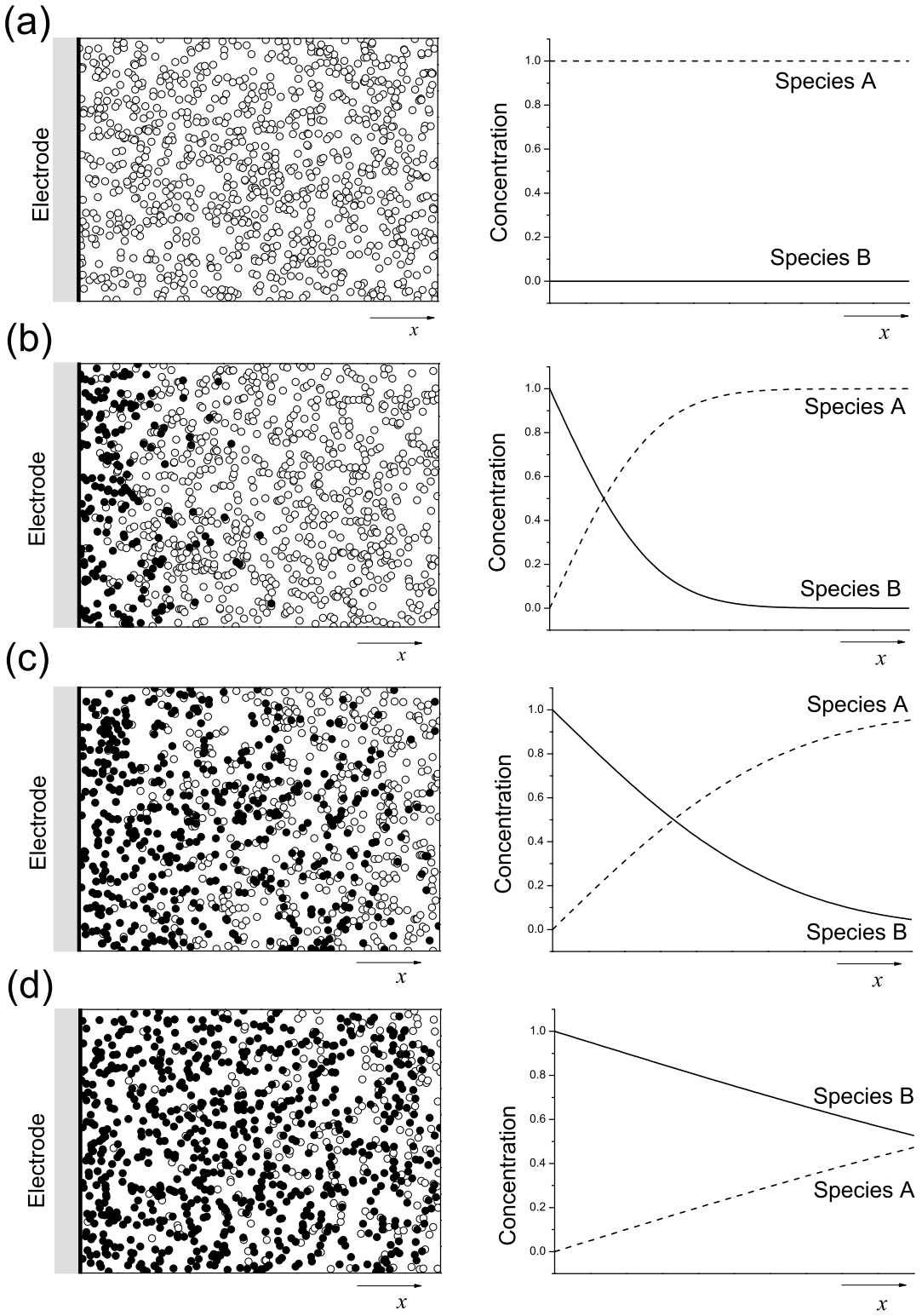

Figure 2.3: *Schematic showing the distribution of particles (a) 0, (b) 1, (c) 5, and (d) 50 arbitrary time units after a potential pulse is applied to the electrode. White dots are the starting species, A, and black dots are the reduced species, B. Concentration profiles over the same space are also shown.*

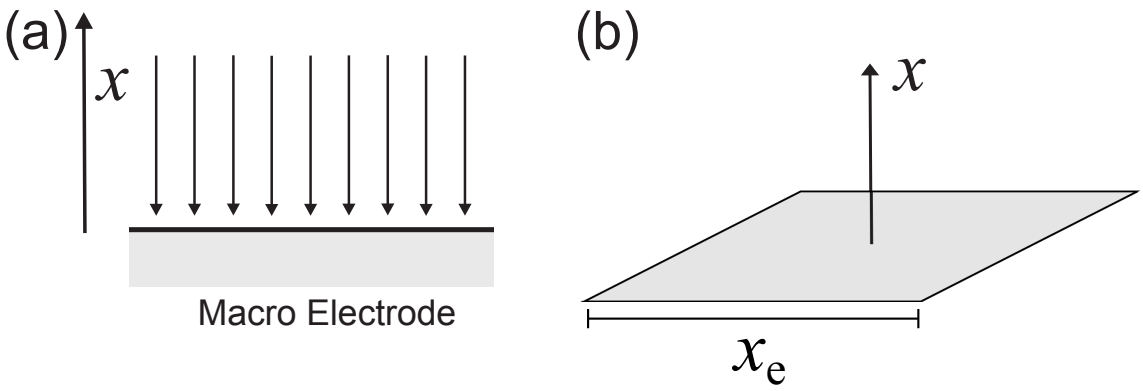

Figure 2.4: *(a) The diffusion field at a planar macroelectrode; (b) a one-dimensional square macroelectrode with normal coordinate x and side length x_e.*

$$\frac{\partial c}{\partial t} = D\frac{\partial^2 c}{\partial x^2} \tag{2.9}$$

A number of other electrode systems may also be faithfully represented in a one-dimensional coordinate system. A cylindrical or hemicylindrical 'wire' electrode can be modelled with a single radial coordinate, r, assuming that it is of macro-scale length, as every value of r corresponds to a cylindrical shell of isoconcentration. Fick's second law in a 1-dimensional cylindrical coordinate system is:

$$\frac{\partial c}{\partial t} = D\left(\frac{\partial^2 c}{\partial r^2} + \frac{1}{r}\frac{\partial c}{\partial r}\right) \tag{2.10}$$

A spherical electrode is likewise considered, however Fick's second law in a 1D spherical coordinate system is given by:

$$\frac{\partial c}{\partial t} = D\left(\frac{\partial^2 c}{\partial r^2} + \frac{2}{r}\frac{\partial c}{\partial r}\right) \tag{2.11}$$

In both cases, $r = r_e$ corresponds to the electrode surface. The former situation is usually achieved in practice by half embedding a conducting wire in an insulating surface, and the latter by a drop of mercury.[5]

2.3.1 Equal Diffusion Coefficients

Fick's first law states that the diffusive flux, j_i, through a plane normal to the x-axis at the point in space, i, is equal to the product of the diffusion coefficient and the

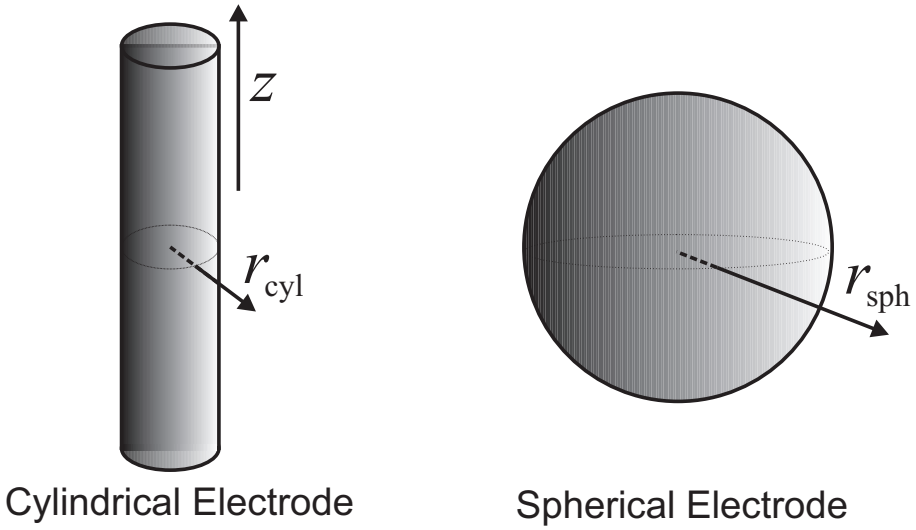

Figure 2.5: *The one-dimensional coordinate systems corresponding to cylindrical and spherical electrodes.*

concentration gradient at that point:

$$j_i = -D \left.\frac{\partial c}{\partial x}\right|_{x=i} \tag{2.12}$$

where the minus sign implies that the flux is down the local concentration gradient.

By conservation of mass, the amount of A lost at the electrode surface exactly equals the amount of B gained there, i.e. $-\Delta c_{\mathrm{A}} = \Delta c_{\mathrm{B}}$ and therefore the diffusive fluxes of the two species at the electrode surface are equal and opposite:

$$-D_{\mathrm{A}} \left(\frac{\partial c_{\mathrm{A}}}{\partial x}\right)_{\text{electrode}} = D_{\mathrm{B}} \left(\frac{\partial c_{\mathrm{B}}}{\partial x}\right)_{\text{electrode}} \tag{2.13}$$

If it is assumed that the diffusion coefficients of both species are equal, i.e. $D = D_{\mathrm{A}} = D_{\mathrm{B}}$, and no other mechanisms are in place to affect the concentrations of either species then it follows that:

$$-\left(\frac{\partial c_{\mathrm{A}}}{\partial x}\right)_{\text{electrode}} = \left(\frac{\partial c_{\mathrm{B}}}{\partial x}\right)_{\text{electrode}} \tag{2.14}$$

Therefore, a decrease in concentration of species A at some point in space is necessarily commensurate with an increase in the concentration of species B of the same magnitude so that:

$$\frac{\partial(c_{\mathrm{A}} + c_{\mathrm{B}})}{\partial x} = 0 \tag{2.15}$$

Therefore it is necessarily true that in every region of space:

$$c_{\mathrm{A}} = (c^*_{\mathrm{A}} + c^*_{\mathrm{B}}) - c_{\mathrm{B}} \tag{2.16}$$

where c^*_{A} and c^*_{B} are the initial concentrations of species A and B respectively. Consequently, when modelling a two species electrochemical system with equal diffusion coefficients, one need only consider the diffusional behaviour of species A, as the concentration profile of B may be inferred directly from that of A.

2.4 Boundary Conditions

Fick's second law (Equation 2.9) is an example of a parabolic second order partial differential equation. The equation describes a single property, concentration, which evolves in space and time. Solution of a problem of this type necessitates a complete description of the condition of the system at $t = 0$, the 'initial value'; as well as a set of spatial boundary conditions (two per spatial dimension, as the PDE is 2nd order).[6,7] The initial condition is that of uniform concentration, given by:

$$c_{\mathrm{A}}(x, t = 0) = c^*_{\mathrm{A}} \tag{2.17}$$

$$c_{\mathrm{B}}(x, t = 0) = 0 \tag{2.18}$$

The one-dimensional system is constrained to some finite region:

$$x_0 \leq x \leq x_{\max} \tag{2.19}$$

where x_0 and $x_{\max}$ are the lower and upper spatial boundaries respectively. A boundary condition is imposed on the concentration at each of these boundaries. The lower boundary is defined to be at $x = 0$, the electrode surface. The concentrations at the electrode surface vary with time, as a function of the potential, E, applied to the electrode. In general,

$$c(x = 0, t > 0) = f(E) \tag{2.20}$$

For a simple cyclic voltammetry experiment with Nernstian equilibrium at the electrode surface, this function is given by Equation 2.5, and for a system with finite electron transfer kinetics, by Equation 2.6.

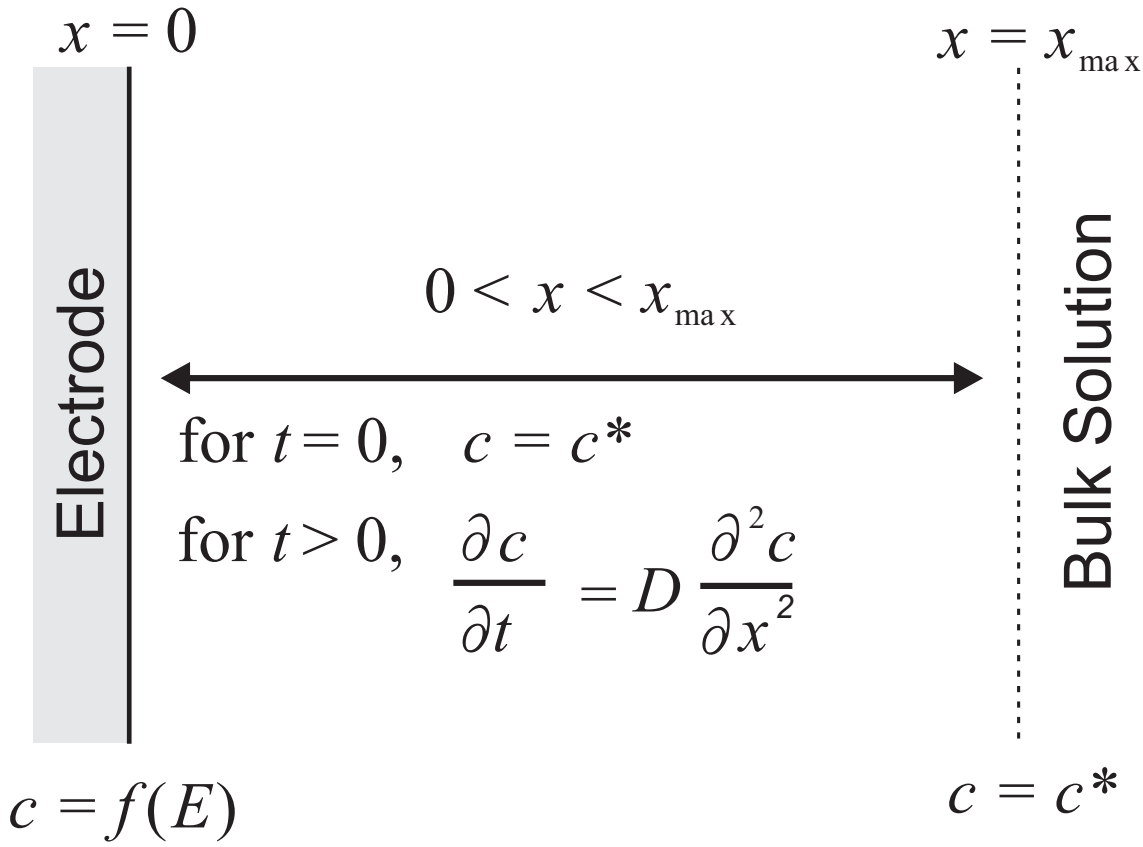

Figure 2.6: *The one-dimensional space and boundary conditions for a macroelectrode.*

The upper spatial boundary is defined as being infinitely far away from the electrode i.e., $x_{\max} = +\infty$, such that changes in concentration at the electrode cannot have any effect on the concentration at the boundary on the timescale of the experiment. In practice, it transpires that it is not necessary to place the boundary infinitely far away from the electrode in order to meet this condition. Einstein's work on Brownian motion[8] demonstrated that in one dimension, the root mean squared displacement of a particle from its starting position, is equal to:

$$\sqrt{\left\langle \overline{x^2} \right\rangle} = \sqrt{2Dt} \tag{2.21}$$

To be sure that no significant changes in concentration can propagate as far as the boundary, it is set to be at some distance greater than this. A boundary distance is established by running a series of simulations with increasing boundary distance, stopping when further increase in the distance has no effect on the results of the simulation. A commonly used value is:

$$x_{\max} = 6\sqrt{Dt_{\max}} \tag{2.22}$$

where $t_{\max}$ is the maximum time the experiment will run for. The concentration of each species at this distance does not change with time, and so is always equal to its bulk value:

$$c(x = x_{\max}, t > 0) = c^* \tag{2.23}$$

Figure 2.6 summarises the mathematical model of the system.

2.5 Current

The primary output of a voltammetry experiment is the voltammogram which is a plot of recorded current, I, against applied potential, E. At any point in time, the current for the reduction of species A is given by:

$$I = \mathrm{F}Aj_{0,\mathrm{A}} \tag{2.24}$$

where A is the area of the electrode and $j_{0,\mathrm{A}}$ is the net flux of electroactive material (species A) at the electrode surface which is proportional to the concentration gradient at that point by Fick's first law, Equation 2.12. In order to calculate the current, the model developed in the preceding sections is solved, and the value of $j_{0,\mathrm{A}}$ as a function of time is determined.

2.6 Dimensionless Coordinates

The particular solution of Fick's second law subject to the boundary conditions, changes for all values of bulk concentration, c^*, electrode size, x_e, and diffusion coefficient, D, and hence must be solved again when any one of these values change. The system variables (c, x, t, etc.) may be transformed into normalised (dimensionless) form by expressing each of them as multiples of some characteristic reference value with the same dimensionality.[9] This removes the dependence of the solution of Fick's second law on c^*, x_e, and D, making it much more general such that the equation needs only to be solved once; under this simple model, the resulting voltammogram can simply be scaled to apply to any set of values of c^*, x_e, and D.

For chemical species s, the dimensionless concentration, C_s, and dimensionless diffusion coefficient, d_s are defined as:

$$C_s = \frac{c_s}{c^*_A} \qquad d_s = \frac{D_s}{D_A} \tag{2.25}$$

If the diffusion coefficients are equal then $d_A = d_B = 1$. The dimensionless distance, X, is defined in terms of some characteristic length, e.g., the size of the electrode, x_e:

$$X = \frac{x}{x_e} \tag{2.26}$$

such that the dimensionless radius of the electrode is 1. Finally the dimensionless time, T, is defined in terms of both the size of the electrode and the diffusion coefficient of species A:

$$T = \frac{D_A t}{x_e^2} \tag{2.27}$$

Equation 2.9 and the boundary conditions may be transformed into this new dimensionless coordinate system using the following chain rules:

$$\frac{\partial y}{\partial x} = \frac{\partial u}{\partial x}\frac{\partial y}{\partial u} \tag{2.28}$$

$$\frac{\partial^2 y}{\partial x^2} = \frac{\partial}{\partial x}\left[\frac{\partial u}{\partial x}\frac{\partial y}{\partial u}\right] = \left[\frac{\partial u}{\partial x}\right]^2 \frac{\partial^2 y}{\partial u^2} + \left[\frac{\partial^2 u}{\partial x^2}\right]\frac{\partial y}{\partial u} \tag{2.29}$$

From the dimensionless transformations given above:

$$\frac{\partial c_s}{\partial t} = \frac{c_{\mathrm{A}}^* D_{\mathrm{A}}}{x_{\mathrm{e}}^2}\frac{\partial C_s}{\partial T} \tag{2.30}$$

$$D_s\frac{\partial^2 c_s}{\partial x^2} = d_s D_{\mathrm{A}}\frac{c_{\mathrm{A}}^*}{x_{\mathrm{e}}^2}\frac{\partial^2 C_s}{\partial X^2} \tag{2.31}$$

and so,

$$\frac{\partial C_s}{\partial T} = d_s\frac{\partial^2 C_s}{\partial X^2} \tag{2.32}$$

The dimensionless initial and outer boundary conditions are then:

$$\begin{aligned} c_s\left(x, t=0\right) = c_s^* \rightarrow &\begin{cases} C_{\mathrm{A}}\left(X, T=0\right) = 1 \\ C_{\mathrm{B}}\left(X, T=0\right) = 0 \end{cases} \\ c_s\left(x = x_{\max}, t\right) = c_s^* \rightarrow &\begin{cases} C_{\mathrm{A}}\left(X = X_{\max}, T\right) = 1 \\ C_{\mathrm{B}}\left(X = X_{\max}, T\right) = 0 \end{cases} \end{aligned} \tag{2.33}$$

where:

$$X_{\max} = 6\sqrt{T_{\max}} \tag{2.34}$$

The dimensionless potential, θ, is defined to be:

$$\theta = \frac{\mathrm{F}}{\mathcal{RT}}(E - E_f^0) \tag{2.35}$$

This allows for a dimensionless form of the Nernst equation (Equation 2.5),

$$e^{\theta} = \frac{C_{\mathrm{A},0}}{C_{\mathrm{B},0}} \tag{2.36}$$

and so the boundary conditions for concentration at the electrode surface are given by:

$$\begin{aligned} C_{\mathrm{A}}\left(X = 0, T\right) &= \frac{1}{1 + e^{-\theta}} \\ C_{\mathrm{B}}\left(X = 0, T\right) &= \frac{1}{1 + e^{\theta}} \end{aligned} \tag{2.37}$$

where for a cyclic voltammetry experiment, θ is a function of time. Figure 2.7 shows how the surface concentrations of species A and B vary with θ assuming Nernstian equilibrium. In a dimensionless form, the Butler–Volmer equation is written as:

$$\frac{\partial C}{\partial X} = K^0 \left[C_{\mathrm{A},0} e^{-\alpha\theta} - C_{\mathrm{B},0} e^{\theta - \alpha\theta} \right] \tag{2.38}$$

where the dimensionless electron transfer rate constant, K^0, is defined as

$$K^0 = \frac{k^0 x_{\mathrm{e}}}{D_{\mathrm{A}}} \tag{2.39}$$

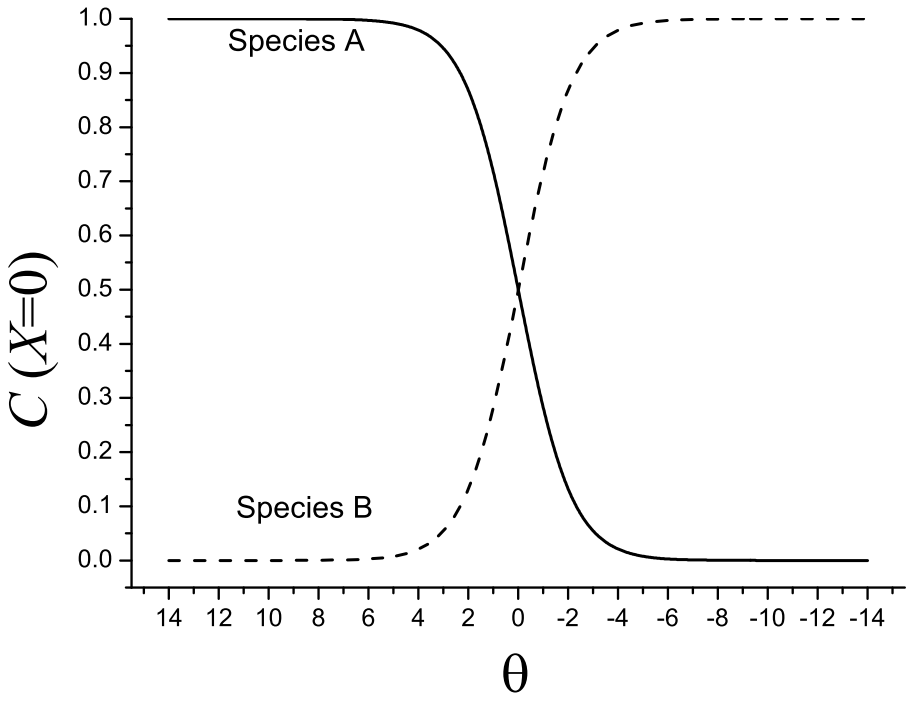

Figure 2.7: *Equilibrium surface concentrations of species A and B as a function of θ.*

The dimensionless scan rate, σ, is the rate of change of dimensionless potential with respect to dimensionless time:

$$\sigma = \frac{\partial \theta}{\partial T} \tag{2.40}$$

From Equation 2.28, this is related to the real scan rate by:

$$\sigma = \frac{x_{\mathrm{e}}^2}{D_{\mathrm{A}}} \frac{\mathrm{F}}{\mathcal{R}\mathcal{T}} \nu \tag{2.41}$$

The dimensionless flux at the electrode surface is defined as

$$J_{0,\mathrm{A}} = - \left. \frac{\partial C_{\mathrm{A}}}{\partial X} \right|_{X=0} \tag{2.42}$$

which is related to the real current by:

$$I = \frac{\mathrm{F} A D_{\mathrm{A}} c_{\mathrm{A}}^*}{x_{\mathrm{e}}} J_{0,\mathrm{A}} \tag{2.43}$$

2.7 Microdisc Electrodes

As the microdisc electrode is not uniformly accessible it cannot be simplified to a one-dimensional coordinate system. While the microdisc can be considered in terms of Cartesian coordinates (x, y, z), with the electrode surface in the (x, y) plane, the geometry lends itself best to treatment in terms of cylindrical polar coordinates (r, z, ϕ) as illustrated in Figure 2.8.

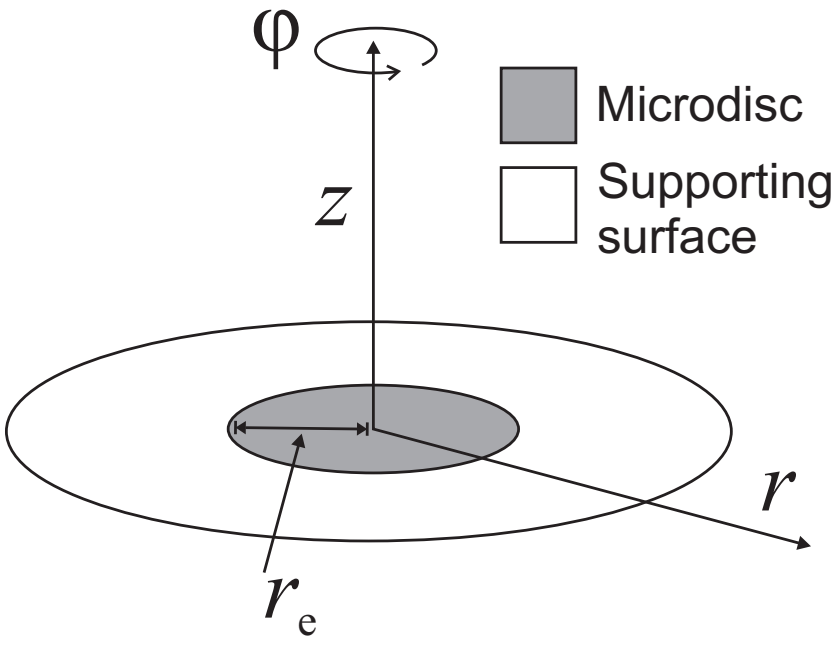

Figure 2.8: *The (r, z, ϕ) cylindrical polar coordinate system used to model a microdisc electrode. The disc radius is r_{e}.*

In this system, an axis passes through the centre of the disc perpendicular to the plane of its surface. r is the radial distance from the axis, z is the perpendicular distance from the surface, and ϕ is the angle around the axis. The origin is at the center of the disc. While the current at the electrode surface will vary with radial coordinate, r, there will be no variation with angle ϕ:

$$\frac{\partial c}{\partial \phi} = 0 \tag{2.44}$$

as the system is cylindrically symmetrical. The problem may therefore be reduced to two spatial dimensions, r and z, and only a single (r, z) plane needs to be considered as illustrated in Figure 2.9; integration across all ϕ achieves the full three-dimensional result.

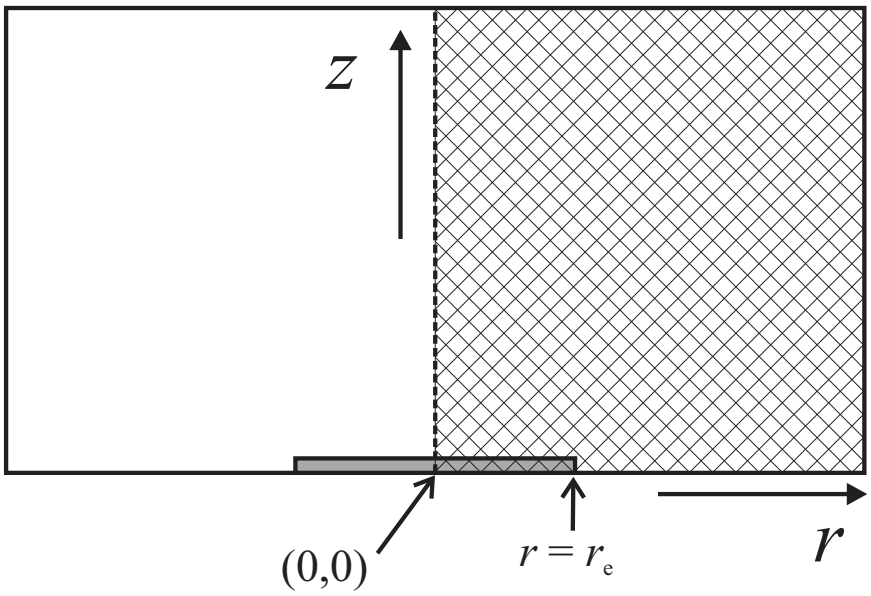

Figure 2.9: *The two-dimensional r, z 'slice' of the microdisc model. As the system has mirror symmetry in the line $z = 0$, only one half, indicated by cross-hatching, need be considered.*

In 3-dimensional cylindrical polar coordinates, (r, z, ϕ), Fick's second law is:

$$\frac{\partial c}{\partial t} = D\left(\frac{\partial^2 c}{\partial r^2} + \frac{1}{r}\frac{\partial c}{\partial r} + \frac{1}{r^2}\frac{\partial^2 c}{\partial \phi^2} + \frac{\partial^2 c}{\partial z^2}\right) \tag{2.45}$$

However, as the model microdisc system is cylindrically symmetrical,

$$\frac{\partial c}{\partial \phi} = \frac{\partial^2 c}{\partial \phi^2} = 0 \tag{2.46}$$

and so the equation is reduced to a two-dimensional form,

$$\frac{\partial c}{\partial t} = D\left(\frac{\partial^2 c}{\partial r^2} + \frac{1}{r}\frac{\partial c}{\partial r} + \frac{\partial^2 c}{\partial z^2}\right) \tag{2.47}$$

The normalisation scheme used for the microdisc model is almost identical to that used for the 1-dimensional system, except the spatial coordinates are now normalised against the microdisc radius, r_e:

$$R = \frac{r}{r_e} \tag{2.48}$$

$$Z = \frac{z}{r_e} \tag{2.49}$$

In these transformed coordinates, the radius of the microdisc is 1. The definitions of T and C are unchanged so that the dimensionless Fick's second law in this space is:

$$\frac{\partial C}{\partial T} = \frac{\partial^2 C}{\partial R^2} + \frac{1}{R}\frac{\partial C}{\partial R} + \frac{\partial^2 C}{\partial Z^2} \tag{2.50}$$

2.7.1 Boundary Conditions

The 2-dimensional space is a rectangular region of a flat plane, so four boundary lines, each with their own boundary conditions, are required. These boundary lines are $r = 0$, $z = 0$, $r = r_{max}$, and $z = z_{max}$.

It is assumed that the microdisc is embedded in a planar supporting surface that is infinite in extent and that the solution is also infinite in extent. Far away from the electroactive surface where the solution is unperturbed by the electrode reactions, the concentration of all species is always equal to their bulk value, c^*:

$$c(r = r_{max}, z) = c^* \tag{2.51}$$

$$c(r, z = z_{max}) = c^* \tag{2.52}$$

where the semi-infinite extent of the simulation space is given by:

$$r_{\max} = r_{\mathrm{e}} + 6\sqrt{Dt_{\max}} \tag{2.53}$$

$$z_{\max} = 6\sqrt{Dt_{\max}} \tag{2.54}$$

For the electrode plane ($z = 0$), two separate boundary conditions are required as the plane is composed of two different materials: the electroactive microdisc and the insulating supporting surface. As the microdisc surface is electroactive, a potential dependent boundary condition is applied; the Nernst equation or Butler-Volmer equation are used as appropriate.

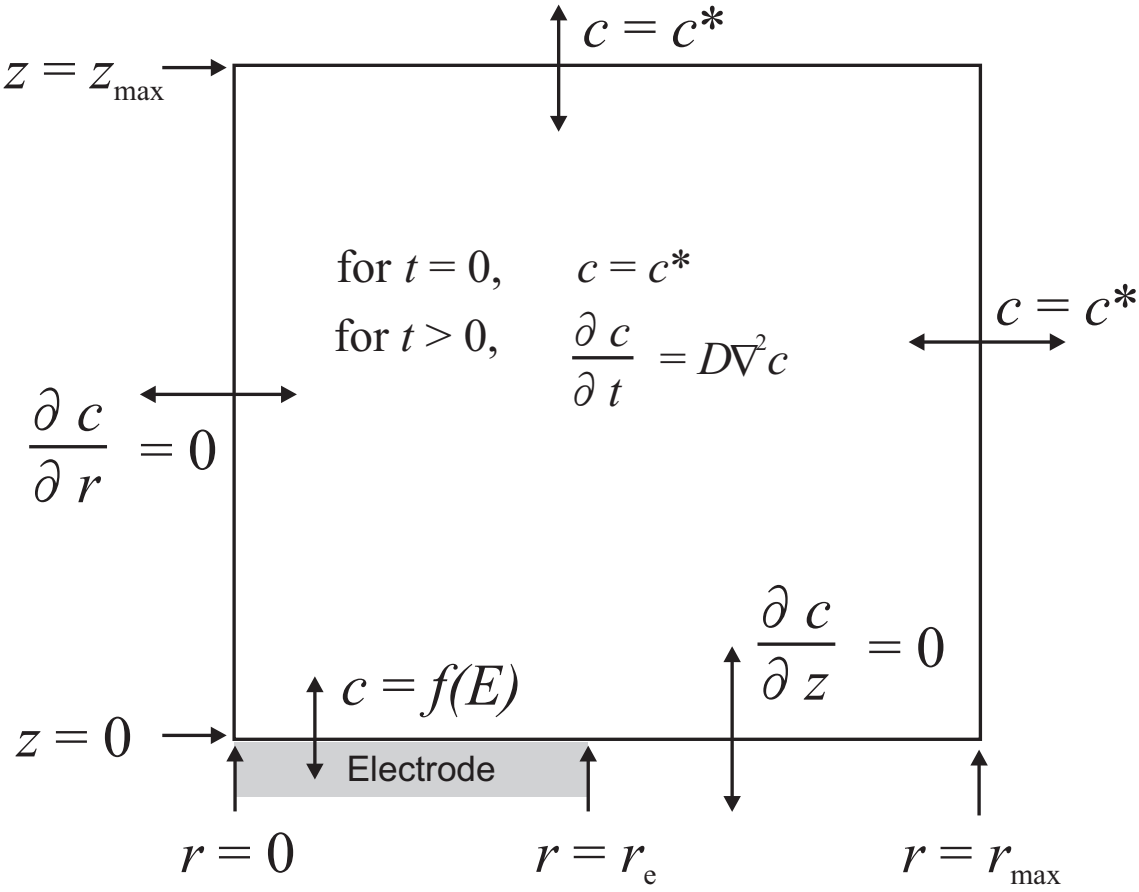

Figure 2.10: *The two-dimensional simulation space for a microdisc electrode*

$$c(r \leq r_{\mathrm{e}}, z = 0) = f(E) \tag{2.55}$$

The insulating supporting surface is a solid boundary so there can be no flux of solution-phase material across it. The boundary condition therefore specifies that the flux at the boundary, which is proportional to the first derivative of concentra-

tion, is zero:

$$\left.\frac{\partial c}{\partial z}\right|_{z=0} = 0 \qquad \text{for} \quad r > r_{\mathrm{e}} \tag{2.56}$$

The final spatial boundary is the cylindrical axis, $r = 0$; a line of mirror symmetry as illustrated in Figure 2.9. Consequently, for any given value of z, the concentration at the two points either side of the boundary is exactly equal, so the concentration gradient at the boundary must necessarily be 0. The boundary condition is therefore:

$$\left.\frac{\partial c}{\partial r}\right|_{r=0} = 0 \tag{2.57}$$

In addition, as with the 1-dimensional system, the concentration of each species is initially uniform and equal to its bulk value across all space:

$$c_s(r, z, t = 0) = c_s^* \tag{2.58}$$

The mathematical model of the microdisc system and its boundary conditions are summarised in Figure 2.10.

2.7.2 Current

For a microdisc electrode, the surface flux varies with radial coordinate r. The current is therefore calculated at every point across the radius of the disc (i.e., a line) and integrated across all angles, ϕ to give the total current for the whole electrode. The real current is therefore:

$$I = 2\pi F j_0' \tag{2.59}$$

where j_0' is the flux across the radius, which is calculated as:

$$j_0' = \int_0^{r_{\mathrm{e}}} j_0 r \partial r = -D \int_0^{r_{\mathrm{e}}} \frac{\partial c}{\partial z} r \, \partial r \tag{2.60}$$

where the factor of r arises from integration about angle ϕ. In terms of the dimensionless coordinate system, I is:

$$I = -2\pi F D c^* r_e \int_0^1 \frac{\partial C}{\partial Z} R \, \partial R \tag{2.61}$$

2.8 Arrays of Microdisc Electrodes

A large number of microdiscs may be embedded into a single surface and wired in parallel to form an array. It is assumed that electroactivity only occurs at the microdisc electrodes, not on the supporting surface.

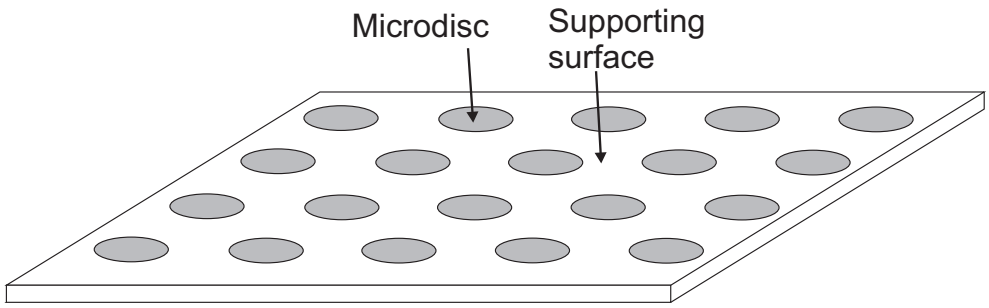

Figure 2.11: *A regularly distributed array of microdisc electrodes.*

If the discs are regularly distributed, it is reasonable to suppose that on average each disc sits in an identical diffusional environment, with differences in environment of the outer edges of the array making a negligible contribution to the whole (assuming a large number of discs). The surface may therefore be treated as though it is composed of a large number of identical unit cells, each centred around a single disc. These cells may be arranged in e.g., an hexagonal array[1] as shown in Figure 2.12. The centre-to-centre distance of two nearest neighbours, d, is the same as the height of the hexagon (distance between two parallel sides). As each unit cell behaves identically, it is only necessary to model one of them; the current response from the whole surface is simply the response of a single cell multiplied by the number of discs in the array.

Even though modelling a single unit cell is a much smaller problem than modelling the whole surface, it is still a 3-dimensional problem. The rotational symmetry of an isolated microdisc that is used to reduce that problem to 2 dimensions is not

[1]Here an hexagonal lattice is assumed, but this discussion applies equally to other regular distributions such as a square lattice.

present here, however a simplified solution is available through the use of the 'diffusion domain approximation'.

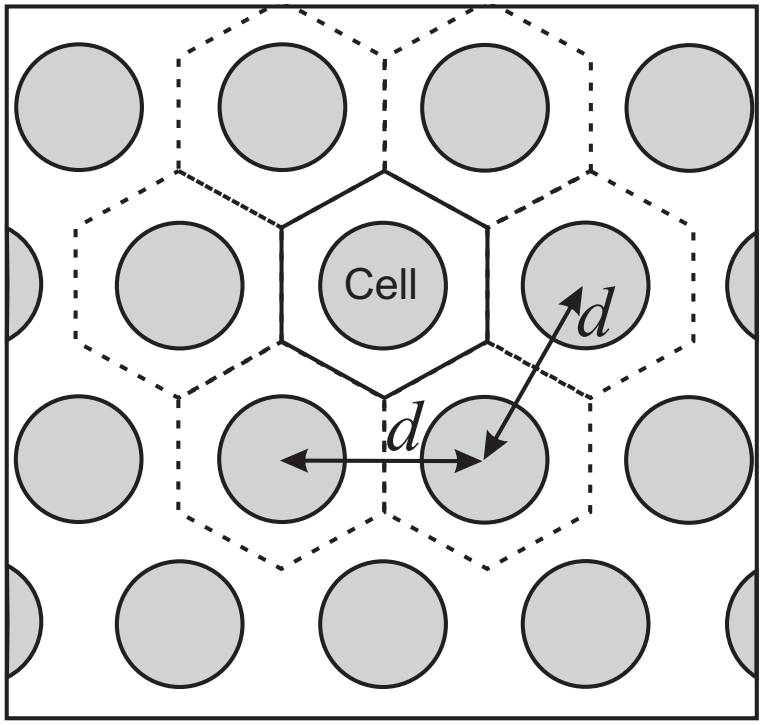

Figure 2.12: *A hexagonal array of microdisc electrodes with centre-to-centre separation, d.*

2.8.1 Diffusion Domain Approximation

Under the diffusion domain approximation,[10–13] the hexagonal unit cell is approximated as a cylindrical cell of the same base area as shown in Figure 2.13.
The area, A, of the hexagonal base is given by:

$$A = \frac{\sqrt{3}}{2}d^2 \tag{2.62}$$

The radius, r_d, of the circular base may therefore be calculated by equating the areas of the two shapes:

$$\pi r_\mathrm{d}^2 = \frac{\sqrt{3}}{2}d^2 \tag{2.63}$$

so:

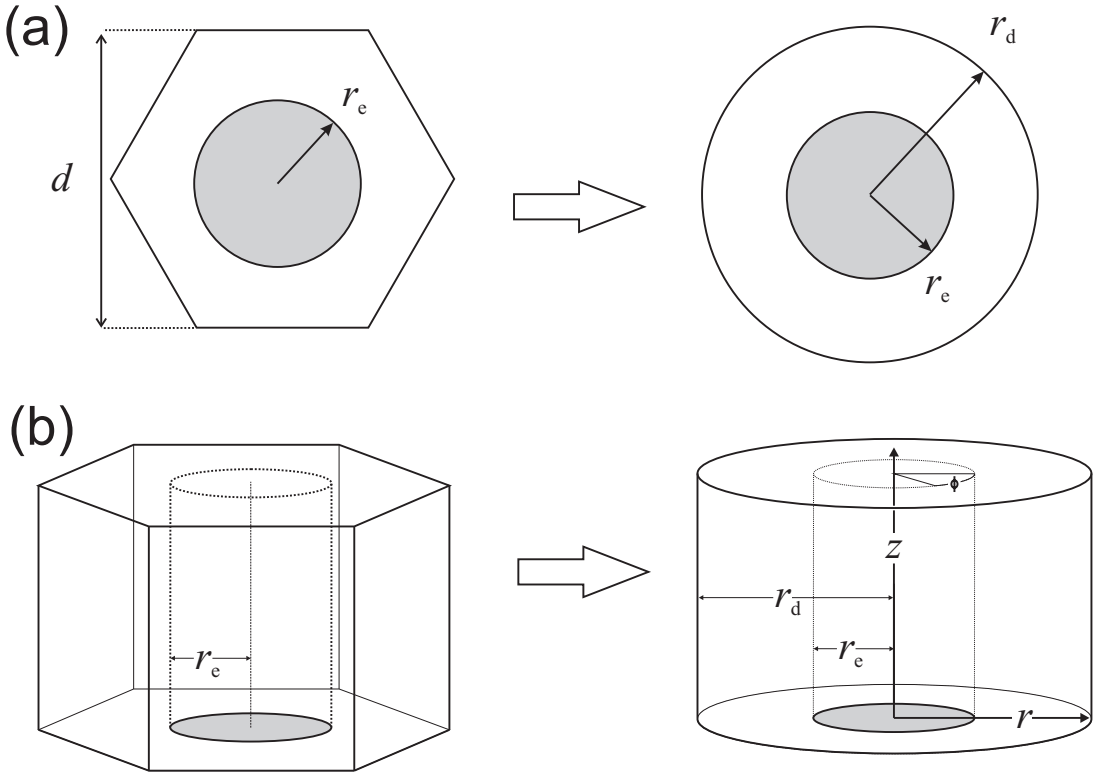

Figure 2.13: *Transformation of an hexagonal cell to a cylindrical cell of the same base area: (a) top-down view; (b) 3D unit cell view.*

$$r_{\mathrm{d}} \approx 0.525d \tag{2.64}$$

Previous studies have demonstrated that the results of simulations using the diffusion domain approximation show very good agreement with experiments.[14]

2.9 Conclusions

In this chapter, a mathematical model for cyclic voltammetry at a macroelectrode, a microelectrode, and an array of microelectrodes has been established. In the next chapter, techniques for solving this model, and thereby calculating the current response of an arbitrary system, will be discussed.

Bibliography

[1] R. G. Compton, E. Laborda and K. R. Ward, *Understanding Voltammetry: Simulation of Electrode Processes*, Imperial College Press, London, 2013.

[2] J. Crank, *The Mathematics of Diffusion*, Oxford University Press, Oxford, 1975.

[3] A. Fick, *Lond. Edinb. Dubl. Phil. Mag.*, 1855, **10**, 30–39.

[4] A. Fick, *Ann. Phys. (Berlin)*, 1855, **94**, 59–86.

[5] A. J. Bard and L. R. Faulkner, *Electrochemical Methods: Fundamentals and Applications.*, John Wiley & Sons, New York, 2nd edn., 2001.

[6] K. W. Morton and D. F. Mayers, *Numerical Solution of Partial Differential Equations: An Introduction*, Cambridge University Press, Cambridge, 2nd edn., 2005.

[7] G. D. Smith, *Numerical Solution of Partial Differential Equations: Finite Difference Methods*, Oxford University Press, Oxford, 3rd edn., 1985.

[8] A. Einstein, *Ann. Phys.*, 1905, **17**, 549–560.

[9] D. Britz, *Digital Simulation in Electrochemistry, Third edition.*, Springer, Heidelberg, Germany, 2005.

[10] C. Amatore, J. M. Savéant and D. Tessier, *J. Electroanal. Chem.*, 1983, **147**, 39–51.

[11] B. A. Brookes, T. J. Davies, A. C. Fisher, R. G. Evans, S. J. Wilkins, K. Yunus, J. D. Wadhawan and R. G. Compton, *J. Phys. Chem. B*, 2003, **107**, 1616–1627.

[12] T. J. Davies, B. A. Brookes, A. C. Fisher, K. Yunus, S. J. Wilkins, P. R. Greene, J. D. Wadhawan and R. G. Compton, *J. Phys. Chem. B*, 2003, **107**, 6431–6444.

[13] R. G. Compton and C. E. Banks, *Understanding Voltammetry*, ICP, London, 2nd edn., 2010.

[14] T. J. Davies, S. Ward-Jones, C. E. Banks, J. Del. Campo, R. Mas, F. X. Munoz and R. G. Compton, *J. Electroanal. Chem.*, 2005, **585**, 51–62.

Chapter 3

Numerical Solution of the CV Model

A number of analytical techniques exist that may be used for solving partial differential equations of the type encountered in electrochemical problems, including integral transform methods such as the Laplace transform, and the method of separation of variables. Unfortunately these techniques are not applicable in all cases and so it is often necessary to resort to the use of numerical methods to find a solution.

Numerical methods are a family of mathematical techniques for solving complicated problems approximately by the repetition of the elementary mathematical operations (+, -, $\times$, $\div$). In the past, numerical solution of a partial differential equation (PDE) was extremely time-consuming, requiring many man-hours of tedious calculation. However the utility of numerical methods has greatly increased since the advent of programmable computers. For the solution of the PDE model of cyclic voltammetry, the method of finite differences is usually the most widely used technique. In this chapter, this method is described in detail for application to the problem of cyclic voltammetry which was developed in the previous chapter.

3.1 Method of Finite Differences

Under a finite difference scheme, a continuous variable, x, is approximated as a series of discrete points x_1, x_2, ..., x_n. A continuous function of that variable, $f(x)$, can then be approximated by evaluating it at each discrete point, x_i, as illustrated in Figure 3.1. For simplicity, it is initially assumed that each point is separated by a constant distance, Δx, and that the value of the function varies linearly between adjacent points.

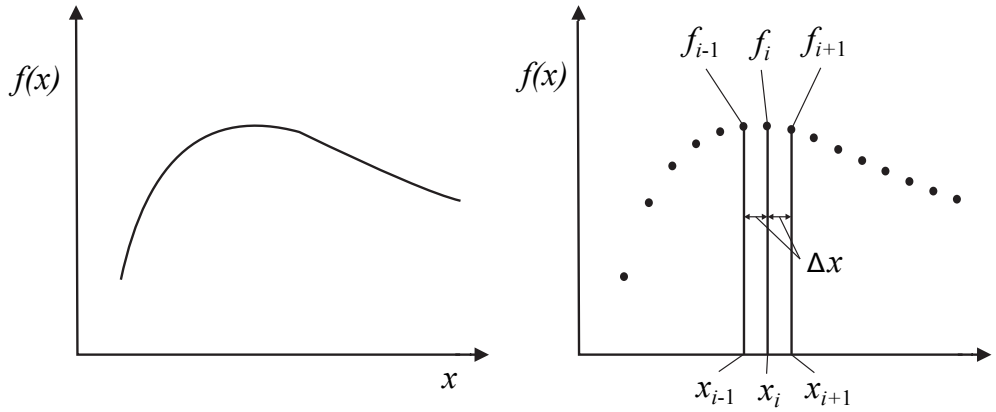

Figure 3.1: *(a) Continuously varying function $f(x)$; (b) discrete values of the function in a discretised space.*

It is often necessary to find discrete approximations of the first and second derivatives of $f(x)$. The mathematical definition of the first derivative is the ratio of the change in $f(x)$ to the change in x, i.e.:

$$\frac{df}{dx} = \lim_{\Delta x \to 0} \frac{f(x_{i+1}) - f(x_i)}{\Delta x} \tag{3.1}$$

From this definition, the first derivative may be approximated as:

$$\frac{df}{dx} \approx \frac{f_{i+1} - f_i}{\Delta x} \tag{3.2}$$

where for simplicity of notation, the concentration at point i, $f(x_i)$, is expressed as f_i. This is *forward difference approximation* of the first derivative. Alternatively the derivative may be approximated as:

$$\frac{df}{dx} \approx \frac{f_i - f_{i-1}}{\Delta x} \tag{3.3}$$

which is called the *backward difference approximation* and is equally valid.

In making these approximations, there is an implicit truncation error, Γ, defined as:

$$\Gamma = \frac{df}{dx} - \frac{f_{i+1} - f_i}{\Delta x} \tag{3.4}$$

The nature of this error can be explored by considering the Taylor series expansion of the concentration:

$$f_{i+1} = f_i + \Delta x \frac{df}{dx} + \frac{(\Delta x)^2}{2}\frac{d^2 f}{dx^2} + \frac{(\Delta x)^3}{6}\frac{d^3 f}{dx^3} + ... \tag{3.5}$$

For the forward difference scheme, the error, Γ_f is therefore equal to:

$$\Gamma_\mathrm{f} = -\frac{\Delta x}{2}\frac{d^2 f}{dx^2} - \frac{(\Delta x)^2}{6}\frac{d^3 f}{dx^3} - ... \tag{3.6}$$

and for the backward scheme:

$$\Gamma_\mathrm{b} = \frac{\Delta x}{2}\frac{d^2 f}{dx^2} - \frac{(\Delta x)^2}{6}\frac{d^3 f}{dx^3} - ... \tag{3.7}$$

Since in general, $\Delta x \ll 1$, it is necessarily true that $\Delta x > (\Delta x)^2 > (\Delta x)^3$, so in each of these series the first term (the term in Δx) is by far the largest source of error. Therefore for both the forward and backward differenced schemes, $\Gamma \propto \Delta x$. Consequently, the smaller Δx, the smaller the error.

An alternative differencing scheme may be arrived at by considering the average derivative given by the forward and backwards schemes; this is called the *central difference approximation*:

$$\frac{df}{dx} = \frac{f_{i+1} - f_{i-1}}{2\Delta x} + \Gamma_\mathrm{central} \tag{3.8}$$

The error is then the average of the errors of the forward and backward schemes. The terms in Δx in Equations (3.6) and (3.7) exactly cancel (as do all the terms in odd powers of Δx), leaving a total error:

$$\Gamma_\mathrm{central} = -\frac{(\Delta x)^2}{6}\frac{d^3 f}{dx^3} - \frac{(\Delta x)^4}{120}\frac{d^5 f}{dx^5} + ... \tag{3.9}$$

Again the leading term is the most significant, so for the central differencing scheme, $\Gamma \propto (\Delta x)^2$. This is a second order error, which is better than the first order error given by either the forward or backward schemes, and so the central scheme provides a more accurate approximation of the true value of the first derivative, and will thus be used throughout.

The second derivative of the concentration can be approximated by summing the Taylor series of the forward and backward schemes:[1]

$$\frac{d^2 f}{dx^2} = \frac{f_{i-1} - 2f_i + f_{i+1}}{(\Delta x)^2} \tag{3.10}$$

again with error, $\Gamma \propto (\Delta x)^2$.

Note that here the finite differences are formulated over 3 points; it is possible to use a greater number of points than this (resulting in a higher order error); however, assuming that Δx is small, the increase in accuracy is typically minimal.

3.1.1 Diffusion in 1 Dimension

By utilising the above, it is possible to arrive at a discrete formulation of Fick's second law. In a one-dimensional linear space, this is:

$$\frac{C_i^k - C_i^{k-1}}{\Delta T} = \frac{C_{i-1} - 2C_i + C_{i+1}}{(\Delta X)^2} \tag{3.11}$$

where k is the timestep, i is the space step and ΔT and ΔX are the time and space intervals respectively which are assumed to be constant. There exists a choice as to whether the concentrations on the right hand side of the equation are chosen to be at T^{k-1} or T^k. which are known as the explicit and implicit methods respectively. In the former case, Equation 3.11 may be rearranged to:

$$C_i^k = C_i^{k-1} + \lambda(C_{i-1}^{k-1} - 2C_i^{k-1} + C_{i+1}^{k-1}) \tag{3.12}$$

where $\lambda = \Delta T/(\Delta X)^2$.

This is a simple equation to solve, and each value of C_i^k can be solved for independently at every timestep because all of the terms appearing on the right hand

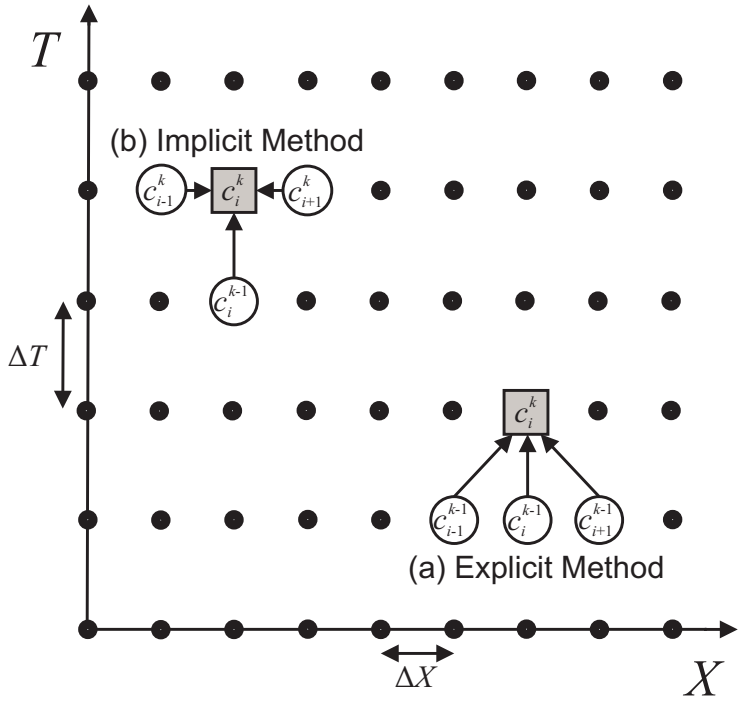

Figure 3.2: *Discrete simulation space-time grid showing concentration terms involved in the equation for C_i^k using the explicit and implicit methods. Grey squares show the term to be solved for and white circles show the terms that appear in the equation.*

side of the equation are fully known. This is illustrated in Figure 3.2 (a). While this method is very simple to implement computationally and was more popular before the advent of fast computers, it is only conditionally stable. Numerical stability is guaranteed[2,3] if $\lambda < 0.5$, but if this condition is not met, the solution will be unstable, diverging from the true solution, and the concentrations will oscillate wildly in both time and space. Consequently, to maintain accuracy, ΔT must decrease with decreasing ΔX, making it inefficient when one considers the small size of ΔX necessary to accurately represent a continuous function.[4] For this reason, the explicit method is of only limited general utility in electrochemistry though it does find use in some specific areas, particularly in the modelling of rotating disc electrodes.[5]

In the *backward implicit* method, Equation 3.11 may be rearranged to:

$$C_i^{k-1} = C_i^k - \lambda(C_{i-1}^k - 2C_i^k + C_{i+1}^k) \tag{3.13}$$

This equation contains a single known value, C_i^{k-1}, and three unknowns, C_{i-1}^k, C_i^k, and C_{i-1}^k and so unlike the explicit method cannot be solved in isolation for any

given point, i. At each timestep, k, the complete set of equations for concentration at every point must be solved simultaneously. While more complicated than the explicit scheme, the implicit scheme is not subject to the stability constraint imposed on the former, and is therefore unconditionally stable, which makes it much more computationally efficient.

3.1.2 Diffusion in 2 Dimensions

Discretisation of a 2-dimensional space transforms it into a 2-dimensional grid of discrete points. If the coordinates are labelled R and Z, then the space between adjacent points in the R direction will be ΔR and that in the Z direction will be ΔZ.

In the 2D cylindrical polar coordinate system used to model a microdisc electrode, the discretised form of Fick's second law is

$$\frac{C_{i,j}^{k} - C_{i,j}^{k-1}}{\Delta T} = \frac{C_{i-1,j} - 2C_{i,j} + C_{i+1,j}}{(\Delta R)^2} + \frac{C_{i,j-1} - 2C_{i,j} + C_{i,j-1}}{(\Delta Z)^2} + \frac{1}{i\Delta R}\frac{C_{i+1,j} - C_{i-1,j}}{2\Delta R} \tag{3.14}$$

Use of the fully implicit method is not numerically efficient in this case, for reasons explored in Section 3.2. Instead, an approach known as the alternating direction implicit method (ADI) is employed. Under the ADI method,[6–8] the explicit and implicit methods are combined. The timesteps, ΔT, are divided into two half-timesteps, $\Delta T/2$. For the first of these half-timesteps, $T_{k-\frac{1}{2}}$, the derivatives along the Z coordinate are discretised implicitly, while the derivatives along the R coordinate are discretised explicitly and therefore the equation to be solved for every point i, j is:

$$\begin{aligned}\lambda_Z C_{i,j-1}^{k-\frac{1}{2}} - (\lambda_Z + 2)C_{i,j}^{k-\frac{1}{2}} + \lambda_Z C_{i,j+1}^{k-\frac{1}{2}} = \\ - (\lambda_R - \lambda_R/2i)C_{i-1,j}^{k-1} + (\lambda_R + 2)C_{i,j}^{k-1} - (\lambda_R + \lambda_R/2i)C_{i+1,j}^{k-1}\end{aligned} \tag{3.15}$$

where $\lambda_Z = \Delta T/(\Delta Z)^2$ and $\lambda_R = \Delta T/(\Delta R)^2$. The terms on the right-hand side of this equation are known whereas those on the left-hand side are the unknowns to be solved for. For the second half-timestep, T_k, the derivatives along the R coordinate are discretised implicitly, while the derivatives along the Z coordinate are discretised

explicitly and therefore the equation to be solved for every point i, j is:

$$(\lambda_R - \lambda_R/2i)C^k_{i-1,j} - (\lambda_R + 2)C^k_{i,j} + (\lambda_R + \lambda_R/2i)C^k_{i+1,j} = \\ - \lambda_Z C^{k-\frac{1}{2}}_{i,j-1} + (\lambda_Z + 2)C^{k-\frac{1}{2}}_{i,j} - \lambda_Z C^{k-\frac{1}{2}}_{i,j+1} \quad (3.16)$$

where again the terms on the left-hand side are the unknowns to be solved for. In this way, at the end of each timestep, each coordinate has received an equal share of implicit and explicit discretisation. This method is found to minimise error and maintain ΔT stability.[9]

3.1.3 Boundary Conditions

In order to solve the discretised PDE, discretised initial and boundary conditions are also required. In most cases, the initial condition of each species is that of uniform concentration, equal to its bulk value:

$$C^{k=0}_{s,i,j} = C^*_s \quad \forall (i,j) \quad (3.17)$$

In the case of a one-dimensional system, there are 2 spatial boundary conditions: the electrode surface, and the semi-infinite, bulk concentration boundary. Typically, the electrode surface boundary condition is given by the Butler-Volmer model in discrete form:

$$\frac{C_{\mathrm{A},2} - C_{\mathrm{A},1}}{\Delta X} = K^0 \left[\exp(-\alpha\theta)C_{\mathrm{A},1} - \exp(\theta - \alpha\theta)C_{\mathrm{B},1}\right] \quad (3.18)$$

The bulk concentration boundary condition applies at the last spatial point, $i = n$:

$$C_s, n = C^*_s \quad (3.19)$$

For a two-dimensional system, the no flux boundaries at the axial symmetry boundary and the inert surface boundary are given respectively by:

$$\frac{C_{2,j} - C_{1,j}}{\Delta R} = 0 \quad \forall\, j \quad (3.20)$$

$$\frac{C_{i,2} - C_{i,1}}{\Delta Z} = 0 \quad \forall\, (R_i > 1) \quad (3.21)$$

If the simulation is an array of electrodes, then the unit cell boundary (at $i = n$) is given by a similar condition.

3.2 Solution of the Equation System

3.2.1 The Thomas Algorithm

The standard method of solving a set of simultaneous linear equations with a computer is to cast the set as a matrix equation of the form:

$$\mathbf{Ax} = \mathbf{b} \tag{3.22}$$

To find the set of solutions, $\mathbf{x}$, both sides of the equation are pre-multiplied by $\mathbf{A}^{-1}$, the inverse of $\mathbf{A}$:

$$\mathbf{x} = \mathbf{A}^{-1}\mathbf{b} \tag{3.23}$$

For a dense matrix $\mathbf{A}$, one with mostly non-zero values, the normal way to calculate $\mathbf{A}^{-1}\mathbf{b}$ is the general *Gaussian Elimination algorithm*.[4] This algorithm takes a number of mathematical operations that is proportional to n^3 where n is the number of unknowns.

For a one-dimensional system, the equation set has n equations so $\mathbf{A}$ will be an $n \times n$ matrix. As n may be arbitrarily large, the cost of calculating $\mathbf{A}^{-1}$ by Gaussian elimination may be very high; however, the equation set has a useful property that may be exploited to significantly ease the calculation. For each spatial point i, the equation is of the form:

$$\alpha_i C_{i-1}^k + \beta_i C_i^k + \gamma_i C_{i+1}^k = \delta_i \tag{3.24}$$

In the equation for C_i^k, the coefficients for the terms C_1^k to C_{i-2}^k and C_{i+2}^k to C_n^k are all 0; this makes $\mathbf{A}$ a *sparse matrix* where only the three central diagonals contain non-zero elements. The equation set may be written as:

$$\begin{pmatrix} 1 & 0 & 0 & 0 & 0 & 0 & 0 & 0 & 0 & 0 & \dots \\ \alpha & \beta & \gamma & 0 & 0 & 0 & 0 & 0 & 0 & 0 & \dots \\ 0 & \alpha & \beta & \gamma & 0 & 0 & 0 & 0 & 0 & 0 & \dots \\ & & \ddots & \ddots & \ddots & & & & & & \\ \dots & 0 & 0 & \alpha & \beta & \gamma & 0 & 0 & 0 & 0 & \dots \\ \dots & 0 & 0 & 0 & \alpha & \beta & \gamma & 0 & 0 & 0 & \dots \\ \dots & 0 & 0 & 0 & 0 & \alpha & \beta & \gamma & 0 & 0 & \dots \\ & & & & & & \ddots & \ddots & \ddots & & \\ \dots & 0 & 0 & 0 & 0 & 0 & 0 & \alpha & \beta & \gamma & 0 \\ \dots & 0 & 0 & 0 & 0 & 0 & 0 & 0 & \alpha & \beta & \gamma \\ \dots & 0 & 0 & 0 & 0 & 0 & 0 & 0 & 0 & 0 & 1 \end{pmatrix} \begin{pmatrix} C_1^k \\ C_2^k \\ C_3^k \\ \vdots \\ C_{44}^k \\ C_{45}^k \\ C_{46}^k \\ \vdots \\ C_{n-2}^k \\ C_{n-1}^k \\ C_n^k \end{pmatrix} = \begin{pmatrix} f(\theta) \\ C_2^{k-1} \\ C_3^{k-1} \\ \vdots \\ C_{44}^{k-1} \\ C_{45}^{k-1} \\ C_{46}^{k-1} \\ \vdots \\ C_{n-2}^{k-1} \\ C_{n-1}^{k-1} \\ 1 \end{pmatrix} \tag{3.25}$$

Equations of this type are called *tridiagonal matrix equations* and may be solved in a more efficient manner using the *Thomas algorithm*[4] which is a simplified version of Gaussian elimination.

Rather than directly calculating the product $\mathbf{A}^{-1}\mathbf{b}$, the solution uses a process called LU factorisation, to factor $\mathbf{A}$ as the product of two other matrices: a lower and an upper triangular matrix, so that $\mathbf{A} = \mathbf{LU}$:

$$\begin{pmatrix} \beta_1 & \gamma_1 & & & \\ \alpha_2 & \beta_2 & \gamma_2 & & \\ & \ddots & \ddots & \ddots & \\ & & \alpha_{n-1} & \beta_{n-1} & \gamma_{n-1} \\ & & & \alpha_n & \beta_n \end{pmatrix} = \begin{pmatrix} \beta_1' & & & & \\ \alpha_2 & \beta_2' & & & \\ & \ddots & \ddots & & \\ & & \alpha_{n-1} & \beta_{n-1}' & \\ & & & \alpha_n & \beta_n' \end{pmatrix} \begin{pmatrix} 1 & \gamma_1' & & & \\ & 1 & \gamma_2' & & \\ & & \ddots & \ddots & \\ & & & 1 & \gamma_{n-1}' \\ & & & & 1 \end{pmatrix} \tag{3.26}$$

where the β_i' and γ_i' are modified coefficients that have different values to the β_i

and γ_i coefficients respectively. This process results in the equation $\mathbf{LUx} = \mathbf{b}$. The algorithm then consists of two steps. First, both sides of the equation are pre-multiplied by $\mathbf{L}^{-1}$:

$$\mathbf{Ux} = \mathbf{L}^{-1}\mathbf{b} \tag{3.27}$$

and the product $\mathbf{d} = \mathbf{L}^{-1}\mathbf{b}$ is calculated. The equation $\mathbf{Ux} = \mathbf{d}$ may be written as:

$$\begin{pmatrix} 1 & \gamma_1' & & & \\ & 1 & \gamma_2' & & \\ & & \ddots & \ddots & \\ & & & 1 & \gamma_{n-1}' \\ & & & & 1 \end{pmatrix} \begin{pmatrix} C_1^k \\ C_2^k \\ \vdots \\ C_{n-1}^k \\ C_n^k \end{pmatrix} = \begin{pmatrix} \delta_1' \\ \delta_2' \\ \vdots \\ \delta_{n-1}' \\ \delta_n' \end{pmatrix} \tag{3.28}$$

where the vector $\mathbf{d}$ consists of the set of values δ_i', which are different to the set of values δ_i. To complete this first step, the values of the modified γ_i' and δ_i' are calculated. The γ_i' values in the $\mathbf{U}$ matrix may be calculated iteratively from:

$$\gamma_i' = \begin{cases} \gamma_i/\beta_i & \text{for } \; i = 1 \\ \\ \gamma_i/(\beta_i - \gamma_{i-1}'\alpha_i) & \text{for } \; i = 2, 3, ...n-1 \end{cases} \tag{3.29}$$

The vector $\mathbf{d}$ (the set of δ_i' values) could be calculated by first evaluating the lower diagonal matrix, $\mathbf{L}$, inversing it, then post-multiplying the result by $\mathbf{b}$. This would be computationally expensive by normal means, but fortunately, the δ_i' values may be calculated directly from:

$$\delta_i' = \begin{cases} \delta_i/\beta_i & \text{for } \; i = 1 \\ \\ (\delta_i - \delta_{i-1}'\alpha_i)/(\beta_i - \gamma_{i-1}'\alpha_i) & \text{for } \; i = 2, 3, ...n \end{cases} \tag{3.30}$$

This first step is called the *forward sweep*. In the second step of the algorithm, both sides of Equation 3.27 are pre-multiplied by $\mathbf{U}^{-1}$:

$$\mathbf{x} = \mathbf{U}^{-1}\mathbf{d} \tag{3.31}$$

Hence it is necessary to calculate the product $\mathbf{U}^{-1}\mathbf{d}$ in order to find the vector, $\mathbf{x}$, of unknown C_i^k values. These are calculated simply from

$$C_i^k = \begin{cases} \delta'_{n-1} & \text{for } \; i = n \\ \\ \delta'_i - \gamma'_i C_{i+1}^k & \text{for } \; i = n-1, n-2, ..., 1 \end{cases} \tag{3.32}$$

This second step is called *back substitution*.

In general, when implementing this algorithm, rather than storing several $n \times n$ matrices in the computers memory, the α_i, β_i, and γ_i are stored in three $1 \times n$ containers, saving a great deal of memory. For cyclic voltammetry, the α_i, β_i, and γ_i coefficients are invariant with time so the set of γ'_i coefficients need only to be calculated once at the start of a simulation and not at every timestep.

The Thomas algorithm may also be used in solution of the microdisc problem, since the 2-dimensional grid is divided into a series of rows/columns, each of which may be solved in isolation. It may also be used in the case of unequal diffusion coefficients, by careful ordering of the elements. For problems involving more than 2 chemical species, a generalised n-diagonal version of the algorithm may be utilised.

3.2.2 Solving Non-Linear Simultaneous Equations

In the case where the set of simultaneous equations generated by discretisation of the diffusion equation is non-linear, the above solution methodology is insufficient. Non-linear terms may arise, for example, because of second order homogeneous chemical reactions.

The iterative Newton-Raphson method[4,10] is a standard numerical procedure for finding successively better approximations to the roots of a real-valued function, or a set of such functions. It may therefore be used to (approximately) solve a system of coupled non-linear simultaneous equations. Each of the n equations is written in an homogeneous form:

$$f_i(x_1, x_2, ..., x_n) = 0 \tag{3.33}$$

If $\mathbf{x}$ is the vector containing the unknowns x_1 to x_n and $\mathbf{f}(\mathbf{x})$ is the vector containing the functions f_1 to f_n, then,

$$\mathbf{f}(\mathbf{x}) = 0 \tag{3.34}$$

The vector $\mathbf{u}$ contains the differences between $\mathbf{x}$ at consecutive iterations, such that

$$\mathbf{u} = \mathbf{x}_{z+1} - \mathbf{x}_z \tag{3.35}$$

In the one-dimensional Newton-Raphson method considering only a single function, the Taylor series of the function about some trial solution, x_0, is considered:

$$f(x) \approx f(x_0) + (x - x_0)f'(x_0) = 0 \tag{3.36}$$

The solution x is therefore derived from successive iterations of the form:

$$x_{z+1} = x_z - \frac{f(x_z)}{f'(x_z)} \tag{3.37}$$

For a function of multiple variables, a trial vector $\mathbf{x}_0$ may be altered similarly:

$$f(\mathbf{x}) \approx f(\mathbf{x}_0) + \sum_n (x_n - x_{n,0}) \frac{\partial f(\mathbf{x}_0)}{\partial x_n} \tag{3.38}$$

and hence,

$$\sum_n u_n \frac{\partial f(\mathbf{x}_0)}{\partial x_n} = -f(\mathbf{x}_0) \tag{3.39}$$

Where there are n simultaneous functions associated with the n variables, this may be extended, such that for each variable m:

$$\sum_n u_n \frac{\partial f_m(\mathbf{x}_0)}{\partial x_n} = -f_m(\mathbf{x}_0) \tag{3.40}$$

which may be expressed for the vectors $\mathbf{u}$ and $\mathbf{f}$ in the matrix form:

$$\mathbf{J}(\mathbf{x}_0)\mathbf{u} = -\mathbf{f}(\mathbf{x}_0) \tag{3.41}$$

Where **J** is the Jacobian matrix, being the $n \times n$ square matrix for which the element J_{mn} is defined:

$$J_{mn} = \frac{\partial f_m}{\partial x_n} \tag{3.42}$$

i.e. Equation (3.41) is a matrix equation of the form:

$$\begin{pmatrix} \frac{\partial f_0}{\partial x_0} & \frac{\partial f_0}{\partial x_1} & \frac{\partial f_0}{\partial x_2} & \cdots & \frac{\partial f_0}{\partial x_n} \\ \frac{\partial f_1}{\partial x_0} & \frac{\partial f_1}{\partial x_1} & \frac{\partial f_1}{\partial x_2} & \cdots & \frac{\partial f_1}{\partial x_n} \\ \vdots & \vdots & \vdots & \ddots & \vdots \\ \frac{\partial f_n}{\partial x_0} & \frac{\partial f_n}{\partial x_1} & \frac{\partial f_n}{\partial x_2} & \cdots & \frac{\partial f_n}{\partial x_n} \end{pmatrix} \begin{pmatrix} u_0 \\ u_1 \\ \vdots \\ u_n \end{pmatrix} = \begin{pmatrix} -f_0(\mathbf{x}_0) \\ -f_1(\mathbf{x}_0) \\ \vdots \\ -f_n(\mathbf{x}_0) \end{pmatrix} \tag{3.43}$$

This equation is solved iteratively and **x** is augmented by **u**, until all values u_0 to u_n are less than some characteristic parameter, ϵ, at which point **x** is taken as the correct set of concentrations at that time step. In general, the Newton-Raphson method requires the user to 'guess' some appropriate trial vector (set of concentrations). This is quite an issue in some applications, but fortunately when solving diffusion equations an excellent trial vector is provided, namely the set of concentrations from the previous timestep.

3.3 Current Calculation

The current is extracted at the end of each timestep, after solution by the Thomas algorithm. The dimensionless current J is equal to the dimensionless concentration gradient at the electrode surface. In the 1D model, this is

$$J = -\frac{C^k_{\mathrm{A},2} - C^k_{\mathrm{A},1}}{\Delta X} \tag{3.44}$$

This is a low order (2-point) approximation with error proportional to, h, but it is quite accurate as long as h is sufficiently small. As an alternative, an asymmetrical 3-point discretisation may be used:[1]

$$J = -\frac{-C^k_2 + 4C^k_1 - 3C^k_0}{2\Delta X} \tag{3.45}$$

which has error proportional to $(\Delta X)^2$. It has been established[11] that the use of

higher order expressions to calculate the flux does not necessarily lead to greater accuracy, since the limiting factor is the order of the finite difference approximations of the spatial derivatives used to represent Fick's second law. As a second order finite difference approximation has been used throughout, a second order current approximation is the most reasonable choice.

As the microdisc electrode is not uniformly accessible, the current cannot simply be found at one point and must instead be integrated over its surface. The dimensionless current, J_i, at some point, i, on the electrode surface is equal to the concentration gradient normal to the surface at that point:

$$J_i = -\left.\frac{\partial C}{\partial Z}\right|_{Z=0} = -\frac{C_{i,2} - C_{i,1}}{\Delta Z} \tag{3.46}$$

The total dimensionless current of the entire disc, J, is found by integrating $J_i R$ across the electrode surface:

$$J = \int_0^1 J_i R \, dR \tag{3.47}$$

The integral of a continuous function, $f(x)$ may be approximated numerically using the trapezium rule.[4] The function is divided into a series of discrete intervals (discretised) and evaluated at each point, x. The area under the curve of a single interval is approximated as being trapezoidal, and the area of all such trapezoids is summed to give the integral. In general for a function discretised into N points:

$$\int_a^b f(x)\, dx \approx \sum_{i=1}^{N} \frac{f(x_i) + f(x_{i-1})}{2}(x_i - x_{i-1}) \tag{3.48}$$

This process is illustrated in Figure 3.3. The accuracy depends on the interval size, Δx, the smaller this size, the more accurate the approximation.[4] The current response of a microdisc is therefore:

$$J \approx -\frac{\Delta R}{2\Delta Z} \sum_{i=2}^{n} [(C_{i,2} - C_{i,1})R_i + (C_{i-1,2} + C_{i-1,1})R_{i-1}] \tag{3.49}$$

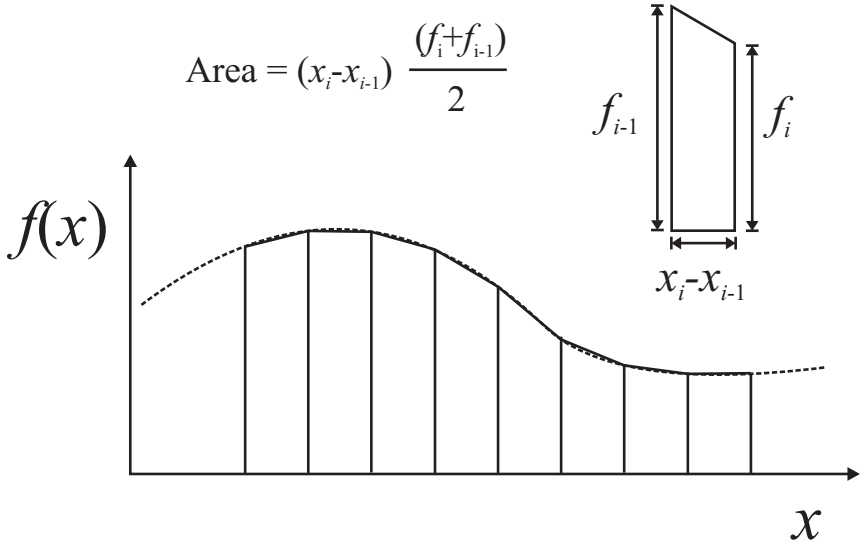

Figure 3.3: *The trapezium rule for numerical integration*

3.4 Simulation Efficiency

3.4.1 Expanding Grids

In order to ensure that the discrete simulation accurately approximates the continuous equations, it is necessary to employ a spatial grid that is dense relative to the steepness of the concentration gradient. This gradient is typically very steep at the surface of the electrode but becomes progressively shallower further away. Consequently, a dense spatial grid is necessary in the region of the electrode surface but is wasteful further away where a much less dense grid would be adequate. The solution is an expanding spatial grid that is dense near the electrode surface but grows progressively more sparse further away from it.

In one dimension, the intervals between adjacent space points are

$$\Delta X_1 = h \tag{3.50}$$

$$\Delta X_i = \gamma \Delta X_{i-1} \tag{3.51}$$

where $\Delta X_i = X_{i+1} - X_i$. Note that a convergence study is used to determine optimum values of h and γ. As ΔX is no longer constant, it is necessary to reformulate the finite differences over unequal intervals:

$$\frac{df}{dx} = \frac{f_{i+1} - f_{i-1}}{\Delta x_+ + \Delta x_-} \tag{3.52}$$

$$\frac{d^2 f}{dx^2} = \left(\frac{f_{i+1} - f_i}{\Delta x_+} - \frac{f_{i+1} - f_i}{\Delta x_+} \right) \frac{2}{\Delta x_+ + \Delta x_-} \tag{3.53}$$

where $\Delta x_+ = x_{i+1} - x_i$ and $\Delta x_- = x_i - x_{i-1}$.

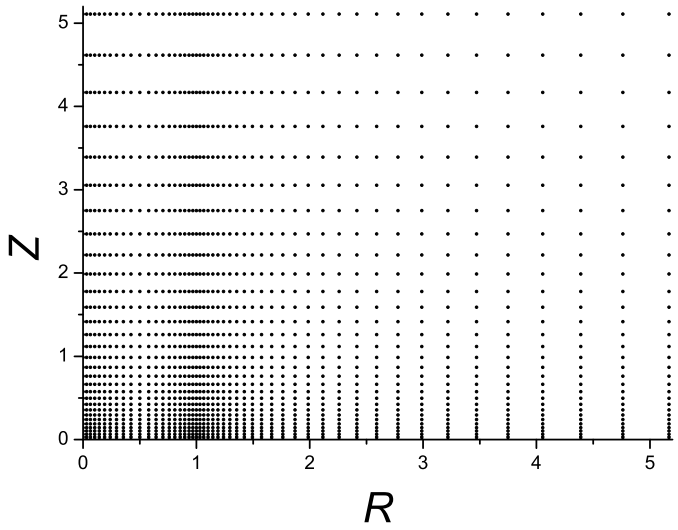

Figure 3.4: *An expanding spatial grid used for microdisc simulations*

In the two-dimensional microdisc system, the above scheme works well for grid spacing in the Z direction (perpendicular to the plane of the electrode surface), however in the R direction, the situation is complicated by the presence of additional finite boundaries: the $R = 0$ axis, and the singularity where the outer edge of the electrode meets the insulating surface, at $R = 1$. Consequently, a high grid density is necessitated in these regions as depicted in Figure 3.4

In potential step chronoamperometry, changes in concentration are rapid at short times and much slower at long times. This necessitates the use of an expanding *temporal* grid where the timesteps ΔT are initially very small but become increasingly larger with each timestep.

3.4.2 Concurrency

A machine with multiple processor cores is capable of executing multiple tasks simultaneously. This is only possible if the threads (sequences of tasks) are mutually independent of one another. In many cases however, this architectural feature can do nothing to increase the execution speed of a program. For the solution of the one-dimensional diffusion problem using the explicit method for example, calculations must proceed in a linear fashion, and there can be no division of labour as each calculation depends on those preceding it. However this is not the case when using the ADI method.

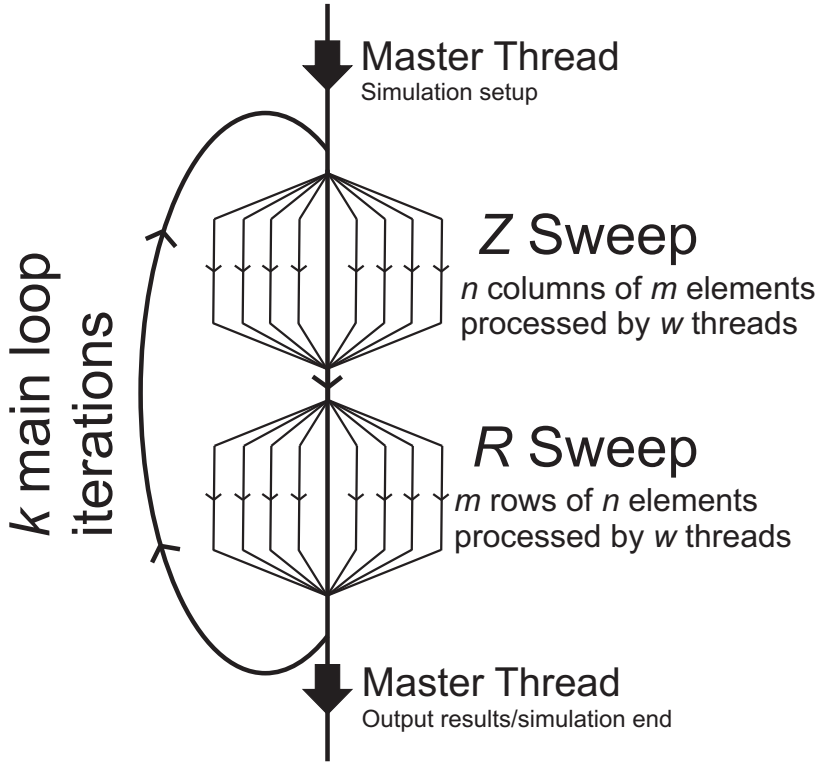

Figure 3.5: *Representation of the simulation in terms of threads.*

For ADI, within a given implicit sweep, each column or row may be evaluated completely independently as the results from one column/row in a given sweep do not in any way affect the results of another in the same sweep. Figure 3.5 illustrates the program flow using a multi-threaded approach. A single master thread handles simulation setup (creating data structures, generating the grid spacings, etc.). This thread then spawns a number of other worker threads which simultaneously process the columns/rows during a sweep. The number of rows/columns that can be eval-

uated simultaneously is equal to the number of available processor cores; when a thread has finished processing a given row/column, it starts on the next unprocessed one until the sweep is complete.

Note that there is a certain amount of computational overhead associated with creating and using multiple threads. As a consequence, doubling the number of available cores will not quite double the speed of the program, but will nevertheless lead to a large increase in speed. Each core added will increase the speed further up until the point where the number of cores is equal to the number of rows/columns in the sweep, beyond which adding additional cores will not result in any speed increase. A supercomputer may have an effectively unlimited number of cores so that all of the columns/rows in a sweep may be evaluated simultaneously, however the execution speed is still limited by the speed at which a single column can be evaluated.

3.5 Computational Details

The implementation of the numerical methods outlined in this and the following chapters was achieved through simulation programs written entirely by the author in C++[12] using Microsoft Visual Studio 2008/2010 as an integrated development environment. OpenMP,[13] an extension to the C++ language, was used to implement concurrency in all applicable programs. A general purpose simulation package was developed allowing for the simulation of an arbitrary sequence of electrochemical and chemical reaction steps. An object-oriented programming approach was utilised, allowing for considerable code reuse and therefore for the relatively simple implementation of arbitrary electrode geometries. Simulations were mostly performed on a Dell Precision T5500 computer with two quad-core hyper-threaded Intel Xeon E5520 processors (16 logical cores, 2.23 GHz).

Convergence studies were performed in order to find grid spacing parameters (h, γ, $\Delta\theta$) that ensured accurate simulation while minimising simulation runtime for each model system under study.

3.6 Conclusions

The method of finite differences has been applied to mathematical model of cyclic voltammetry that was developed in the previous chapter. In addition, numerical algorithms for the solution of the equations thus generated have been presented. Having fully established this solution method, the rest of this thesis focuses on the theoretical application of the model to a variety of novel electrode systems.

Bibliography

[1] D. Britz, *Digital Simulation in Electrochemistry, Third edition.*, Springer, Heidelberg, Germany, 2005.

[2] K. W. Morton and D. F. Mayers, *Numerical Solution of Partial Differential Equations: An Introduction*, Cambridge University Press, Cambridge, 2nd edn., 2005.

[3] G. D. Smith, *Numerical Solution of Partial Differential Equations: Finite Difference Methods*, Oxford University Press, Oxford, 3rd edn., 1985.

[4] W. H. Press, S. A. Teukolsky, W. T. Vetterling and B. P. Flannery, *Numerical Recipes*, Cambridge University Press, Cambridge, 3rd edn., 2007.

[5] R. G. Compton, M. E. Laing, D. Mason, R. J. Northing and P. R. Unwin, *Proc. R. Soc. Lond. A Math. Phys. Sci.*, 1988, **418**, 113–154.

[6] J. A. Alden and R. G. Compton, *J. Phys. Chem. B*, 1997, **101**, 8941–8954.

[7] J. Heinze, *J. Electroanal. Chem.*, 1981, **124**, 73–86.

[8] J. W. Peaceman and H. H. Rachford, *J. Soc. Ind. Appl. Math.*, 1955, **3**, 28–41.

[9] D. J. Gavaghan and J. S. Rollett, *J. Electroanal. Chem.*, 1990, **295**, 1–14.

[10] E. J. F. Dickinson, L. Freitag and R. G. Compton, *J. Phys. Chem. B*, 2010, **114**, 187197.

[11] D. J. Gavaghan, *J. Electroanal. Chem.*, 1997, **420**, 147–158.

[12] B. Stroustrup, *The C++ Programming Language*, Addison Wesley, 4th edn., 2013.

[13] L. Rohit Chandra, D. Dagum, D. Maydan, J. Kohr and R. M. McDonald, *Parallel Programming in OpenMP*, Morgan Kaufmann, 2000.

Chapter 4

Flat Heterogeneous Surfaces and Highly-Ordered Pyrolytic Graphite

In this chapter, the cyclic voltammetry at electrodes composed of two different electroactive materials which differ only in terms of their electrochemical rate constants is investigated. Of particular interest are cases where zones of one highly active material are distributed over a substrate of a second, much less active material.

The occurrence of split peak cyclic voltammetry where two peaks are observed in the forward sweep, is studied in terms of the diffusional effects present in the system. A number of surface geometries are compared: specifically the more active zones are modelled as long, thin bands, as steps in the surface, as discs, and as rings. Similar voltammetry for the band, step and ring models is seen but the disc geometry shows significant differences. Finally, the simulation technique is applied to the modelling of highly-ordered pyrolytic graphite (HOPG) surface and experimental conditions under which it may be possible to observe split peak voltammetry are predicted.

The work constituting this chapter has been published in *Physical Chemistry Chemical Physics*.[1]

4.1 Introduction

Electrodes composed of more than one material, each with differing electrochemical properties find widespread use within the field of electrochemistry. Arrays of microelectrodes distributed over an inert supporting substrate are commonly used in electroanalysis as they offer the same increased sensitivity of a single microelectrode (due to enhanced mass transport effects) coupled with the advantage of a much higher current output.[2,3] Available electrode geometries for such arrays include the microband and the microdisc which may both be easily fabricated by, for example screen-printing[4,5] and photolithography[6] respectively. Recent work has characterised the voltammetric behaviour of arrays of microdiscs[6,7] and of regularly and randomly distributed arrays of microbands.[8,9] Another class of electrochemically heterogeneous surfaces are partially blocked electrodes which are macro-electrodes covered with particles of some (usually) inert blocking material, and have been extensively studied both theoretically and experimentally.[10–12]

Spatial heterogeneity may also be seen in materials such as pyrolytic graphite that are uniform in composition but which possess more than one distinct crystallographic plane. Highly ordered pyrolytic graphite (HOPG) and its derivatives are popular electrode materials for use in electroanalysis. HOPG consists of planes of graphite with an interlayer spacing of 3.35 Å and possesses two electrochemically distinct surfaces: the basal plane which lies parallel to the graphite plane, and the edge plane which lies perpendicular to it.[13] Consequently, if an HOPG crystal is cleaved parallel to the graphite plane, the resulting electrode will be predominantly basal plane in character (a BPPG electrode) whereas if it is cut perpendicular to the plane, the resulting electrode will have mostly edge-plane character (an EPPG electrode). A BPPG electrode is not a perfect surface, rather it will contain a number of edge plane defects and the same is true for EPPG. A schematic of a graphitic surface is shown in Figure 4.1. A comprehensive review of HOPG and other carbon materials, their properties, and their applications as electrodes for use in electrochemistry has recently been presented by McCreery.[14]

It is widely, but not exclusively, thought that the edge plane surface displays an electrochemical rate constant (k^0_{edge}) that is many orders of magnitude faster

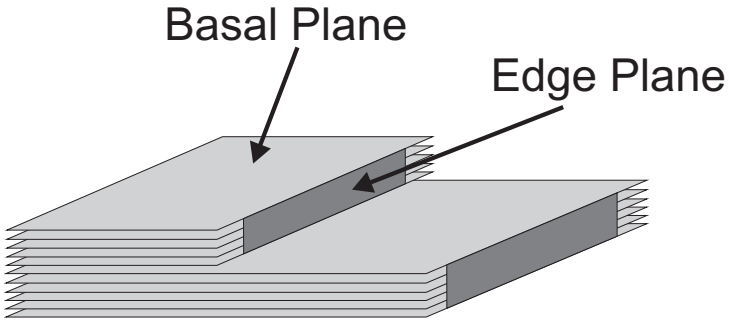

Figure 4.1: *Schematic of the surface of HOPG showing areas of differing electroactivity.*

than that of the basal plane (k^0_{basal}) for most redox couples; similarly, in studies of carbon nanotubes it is seen that the tube ends are far more reactive than the tube walls.[15,16] As a result of this difference in reactivity, EPPG electrodes will often display cyclic voltammetry that is reversible whereas BPPG electrodes will generally show irreversible voltammetry;[14] however it has not yet been established just how much greater k^0_{edge} is than k^0_{basal} for a typical redox couple.[17] The peak to peak separation (ΔE_{pp}) observed for HOPG voltammograms depends on the density of edge plane defects: the lower the amount of defects, the higher the observed ΔE_{pp} and hence the lower the effective rate constant. Analysis of voltammetry of high quality HOPG surfaces, i.e. those with the lowest defect densities, has yielded effective rate constants of 10^{-9} cm s^{-1} for certain redox couples.[18] It is still not unambiguously clear whether this value closely represents the rate constant k^0_{basal} or if the measured current response is due to the small number of edge plane defects. A study by Cline et al.[19] catalogued the electron transfer rates for 17 inorganic redox systems on basal plane HOPG and on glassy carbon (GC), demonstrating that transfers were at least 3-5 orders of magnitude faster on GC. This difference is attributed to the much lower density of electronic states of HOPG compared to GC.

Davies et al. have shown that selective coverage of the basal plane of a graphite electrode leads to no significant changes in the voltammetry,[20] suggesting that in most experimental situations the basal plane may be considered effectively inert. In a study by Edwards et al.[21] the diffusion of electroactive species above an HOPG surface was slowed considerably through the use of a thin layer of Nafion film.

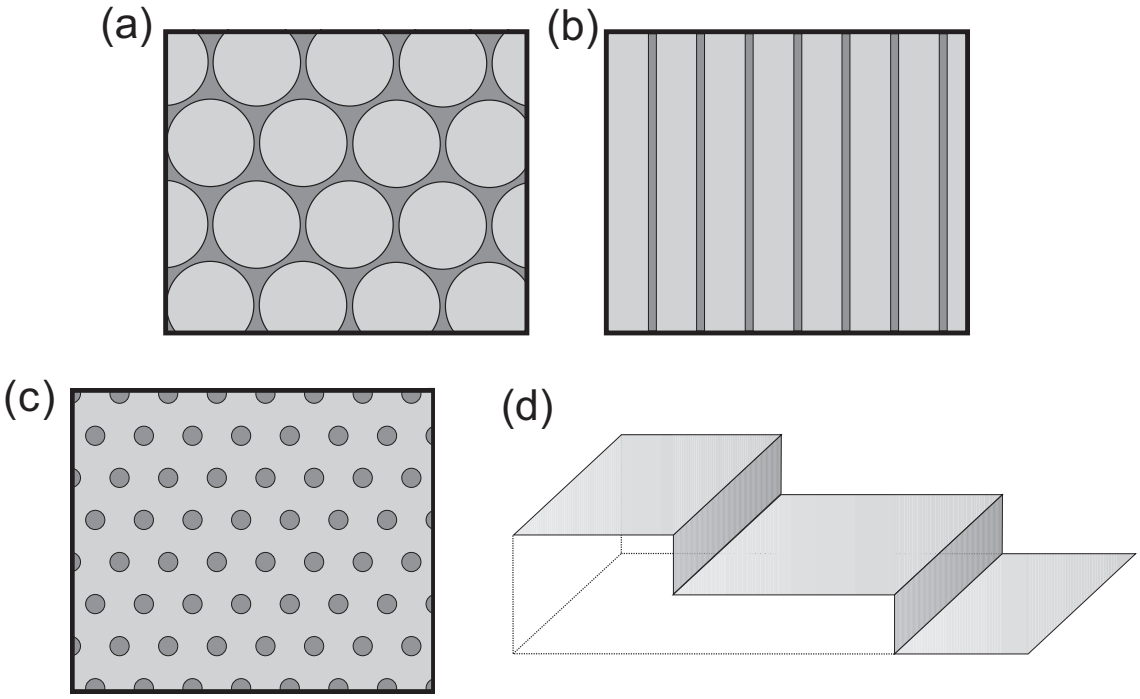

Figure 4.2: *Top-down schematic views of the surfaces of electrodes with (a) partially blocked electrode (ring), (b) band, (c) disc island geometries; and (d) a stepped surface. The darker shading indicates areas of greater electroactivity.*

It was demonstrated that it is possible to distinguish between different sites of electroactivity on the surface and therefore that electron transfer does occur at the basal plane.

In this chapter, the cyclic voltammetry of heterogeneous electrodes of a variety of geometries is simulated and analysed, building on previous theoretical work with partially blocked electrodes[10] and with heterogeneous surfaces.[22] Specifically the surface is modelled as an array of microbands, as an array of microdiscs, as a partially blocked electrode, and as series of steps corresponding to an HOPG-like material. In each case the surface is composed of one material overlaid with islands of a second material as shown schematically for a number of surface geometries in Figure 4.2. In each case, the island material is taken to exhibit significantly faster electrode kinetics than the supporting substrate material. Indicative voltammetric features are elucidated through exploration of the effect on voltammetry of variations in the size and surface coverage of the islands for each geometry. Particularly, the conditions under which two peaks arise in the forward sweep of a voltammogram, a previously reported phenomenon,[22] are examined, and thereby, the conditions under

which the kinetically slower surface can be considered to be inert are revealed. In addition, a comparative study of the surface geometries is undertaken. Further, experimentally derived values are used to simulate realistic HOPG systems in order to gain insight into the nature of the difference in the kinetics of its two planes.

4.2 Theoretical Model

A one-electron oxidation is considered throughout. It is assumed that at the start of each experiment, the concentration of reduced species A is uniform and equal to some bulk value, c_{A}^{*}, and that there is no oxidised species B present in the system. Additionally it is assumed that the diffusion coefficients, D, of the two chemical species are equal such that at every point in space, the concentrations of species A and B sum to c_{A}^{*} (See Section 2.3.1). Consequently, only the behaviour of species A need be considered as the concentration profile of species B can be inferred from that of A.

The electrode surface is modelled as a series of highly electroactive islands uniformly distributed over a macro-scale substrate made of a different electroactive material. As noted in the previous section, four different electrode geometries are considered in this study: microdisc array, microband array, partially blocked electrode, and stepped surface. In each case, the highly active islands are assumed to form a regular array, each with identical size and separation. The supporting substrate is large relative to the size of the islands, and there are a large number of islands. Consequently the electrode surface may be treated as though it is composed of a series of identical unit cells in each case.

As the electrode is composed of two different electroactive materials, each of which has different kinetic properties, the oxidation is described by two electron transfer processes:

$$\text{Island:} \qquad \mathrm{A} \overset{k^{0}_{\mathrm{isd}}}{\rightleftharpoons} \mathrm{B} + \mathrm{e}^{-} \tag{4.1}$$

$$\text{Substrate:} \qquad \mathrm{A} \overset{k^{0}_{\mathrm{sub}}}{\rightleftharpoons} \mathrm{B} + \mathrm{e}^{-} \tag{4.2}$$

where ‘isd’ and ‘sub’ refer to the islands and substrate respectively. The kinetics of

the electron transfer processes are not necessarily reversible, so the Butler–Volmer kinetic model is used to describe the flux, j_0, of species A at the electrode surface:

$$j_0 = k_i^0 \left[c_0 \exp\left((1-\alpha)\frac{F}{\mathcal{RT}}(E - E_f^0) \right) + (1 - c_0) \exp\left(-\alpha \frac{F}{\mathcal{RT}}(E - E_f^0) \right) \right] \quad (4.3)$$

where c_0 is the surface concentration of A and $k_i^0 = k_{\text{isd}}^0$ for the island and k_{sub}^0 for the substrate. Note that while it is possible for the value of α to differ between the two surfaces, here it is assumed to be constant.

The simulation procedure for the microdisc island model is very similar to that described in Section 2.8.1 for an array of microdisc electrodes. The surface is treated as a regular array of unit cells of radius r_{d}, each with a disc of radius r_{e} at its center such that $r_{\text{d}} > r_{\text{e}}$. The model is thus reduced to two dimensions through the use of the diffusion domain approximation (Section 2.8.1). A cylindrical polar coordinate system (r, z) is used and normalized according to the procedure given in Section 2.6. The only change from the microdisc array model is an altered boundary condition; where in that model the substrate surface was inactive imposing a no-flux boundary condition, here it is active imposing a potential dependent boundary condition.

In normalized units, the electrode surface ($Z = 0$) boundary conditions are given by: (i) for $0 \leq R \leq 1$,

$$\left.\frac{\partial C}{\partial Z}\right|_{Z=0} = K_{\text{isd}}^0 \left[\exp(\theta - \alpha\theta) C_0 - \exp(-\alpha\theta)(1 - C_0) \right] \quad (4.4)$$

and (ii) for $1 < R \leq R_{\text{d}}$

$$\left.\frac{\partial C_{\text{A}}}{\partial Z}\right|_{Z=0} = K_{\text{sub}}^0 \left[\exp(\theta - \alpha\theta) C_{\text{A},0} - \exp(-\alpha\theta) C_{\text{B},0} \right] \quad (4.5)$$

where $R_{\text{d}} = r_{\text{d}}/r_{\text{e}}$ is the normalized radius of the unit cell and the normalized rate constant is defined as:

$$K_i^0 = \frac{k_i^0 r_{\text{e}}}{D} \quad (4.6)$$

The simulation space for this model including the boundary conditions in normalized units is illustrated in Figure 4.3.

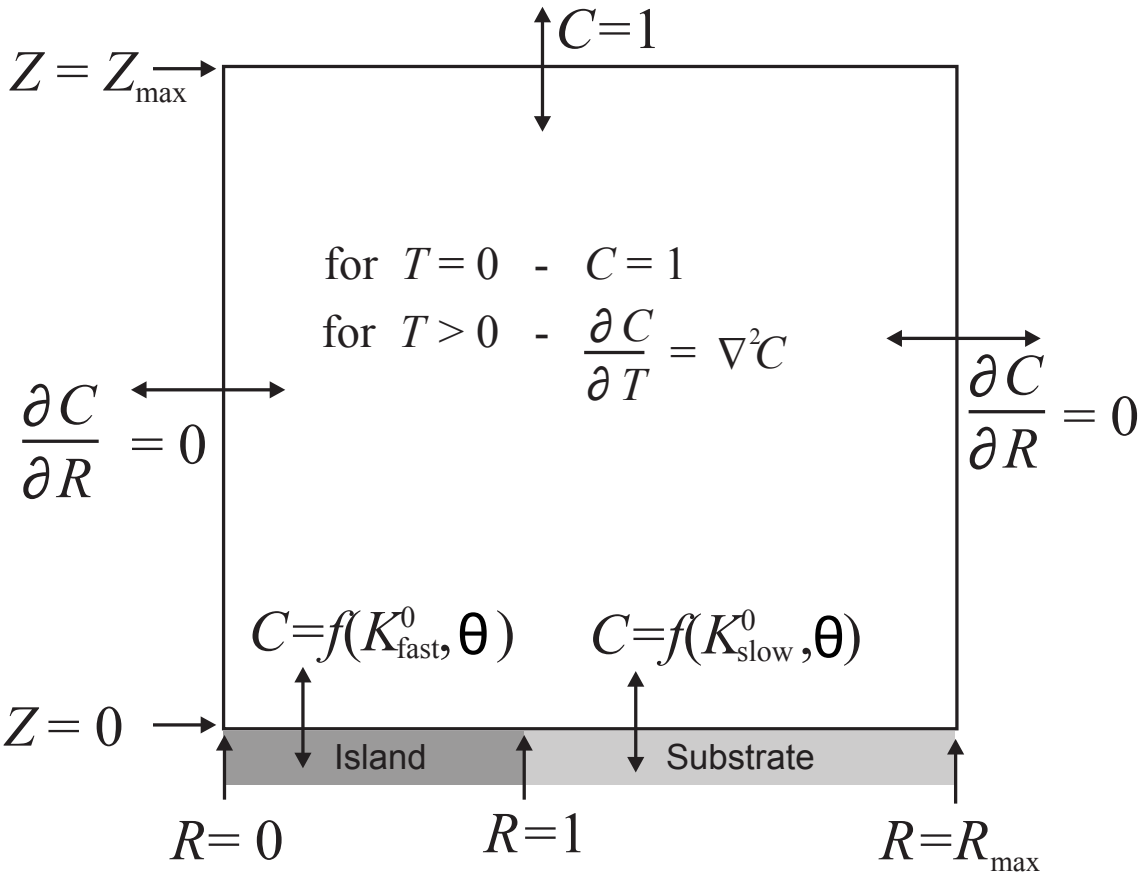

Figure 4.3: *The rectangular simulation space for an electrode with disc shaped islands.*

The partially blocked electrode model (Figure 4.2 (a)) may be thought of as the inverse of the disc model.[10–12,23] The simulation space is the same as that depicted in Figure 4.3, except that the electroactive boundary conditions are interchanged. The surface may therefore be viewed as a series of ring shaped highly active islands over a surface of less active supporting substrate.

It is often useful to consider the behaviour of the surface in terms of a parameter called the surface coverage, Θ, where

$$\Theta = \frac{\text{Area of island site}}{\text{Area of unit cell}} \tag{4.7}$$

For the disc model, this is:

$$\Theta_{\text{disc}} = \frac{r_{\text{e}}^2}{r_{\text{d}}^2} \tag{4.8}$$

and for the ring,

$$\Theta_{\text{ring}} = 1 - \frac{r_{\text{e}}^2}{r_{\text{d}}^2} \tag{4.9}$$

The number of unit cells that a surface is composed of may be calculated from:

$$N = \frac{\text{Total electrode area}}{\text{Area of one unit cell}} \tag{4.10}$$

4.2.1 Band and Step Models

In contrast to the disc and ring, the band electrode is most conveniently modelled in Cartesian coordinates. In this coordinate system, Fick's second law is

$$\frac{\partial c}{\partial t} = D\left(\frac{\partial^2 c}{\partial x^2} + \frac{\partial^2 c}{\partial y^2} + \frac{\partial^2 c}{\partial z^2}\right) \tag{4.11}$$

In the band array model, each band has identical width $= 2x_{\text{e}}$, length l, and centre-to-centre separation $= 2x_{\text{d}}$, and so like the disc, each individual band in the array is considered to behave identically. The band unit cell is shown in Figure 4.4. As the length of each band is of macro-scale, it is large compared to the thickness of the diffusion layer on the experimental timescale. It may therefore be approximated that the diffusional behaviour of the band (and thus its current response) does not vary across its major axis (the y coordinate). Consequently there can be no flux of material in the y-direction, i.e.,

$$\frac{\partial c}{\partial y} = \frac{\partial^2 c}{\partial y^2} = 0 \tag{4.12}$$

and the model may therefore be reduced to 2 spatial dimensions; a band may simply be modelled as an (x, z) plane. Further, as the band possesses a plane of mirror symmetry, the (y, z) plane, only one half of the 2 dimensional (x, z) plane need actually be considered.

The spatial coordinates are normalized against the half-width of the band, x_{e},

$$X = \frac{x}{x_{\text{e}}} \tag{4.13}$$

$$Z = \frac{z}{x_{\text{e}}} \tag{4.14}$$

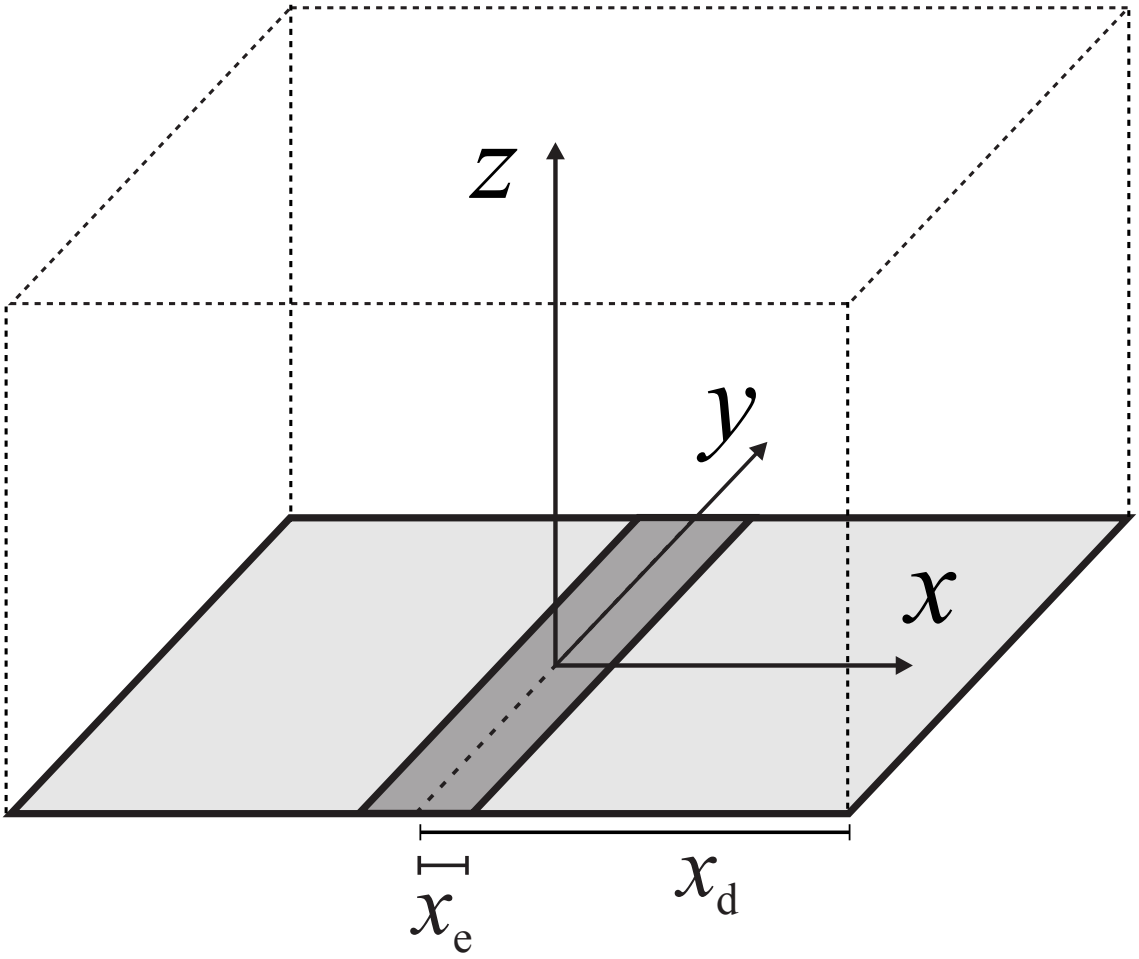

Figure 4.4: *The unit cell for the band array model with band half-width, x_e, and half-centre-to-centre distance, x_d.*

In normalized coordinates, Fick's second law is therefore

$$\frac{\partial C}{\partial T} = \frac{\partial^2 C}{\partial X^2} + \frac{\partial^2 C}{\partial Z^2} \tag{4.15}$$

The simulation space for a band is exactly the same as that for a disc, as illustrated in Figure 4.3, except that the form of $\nabla^2 C$ is as given by Equation 4.15. The current response at the electrode, I, is calculated by integrating the flux over the entire surface:

$$I = -2NFlx_e Dc^* \int_0^{X_d} \left.\frac{\partial C}{\partial Z}\right|_{Z=0} \partial X \tag{4.16}$$

where $X_d = x_d/x_e$ and N is the total number of unit cells on the surface. The integral may be evaluated numerically using the trapezium rule (see Section 3.3).

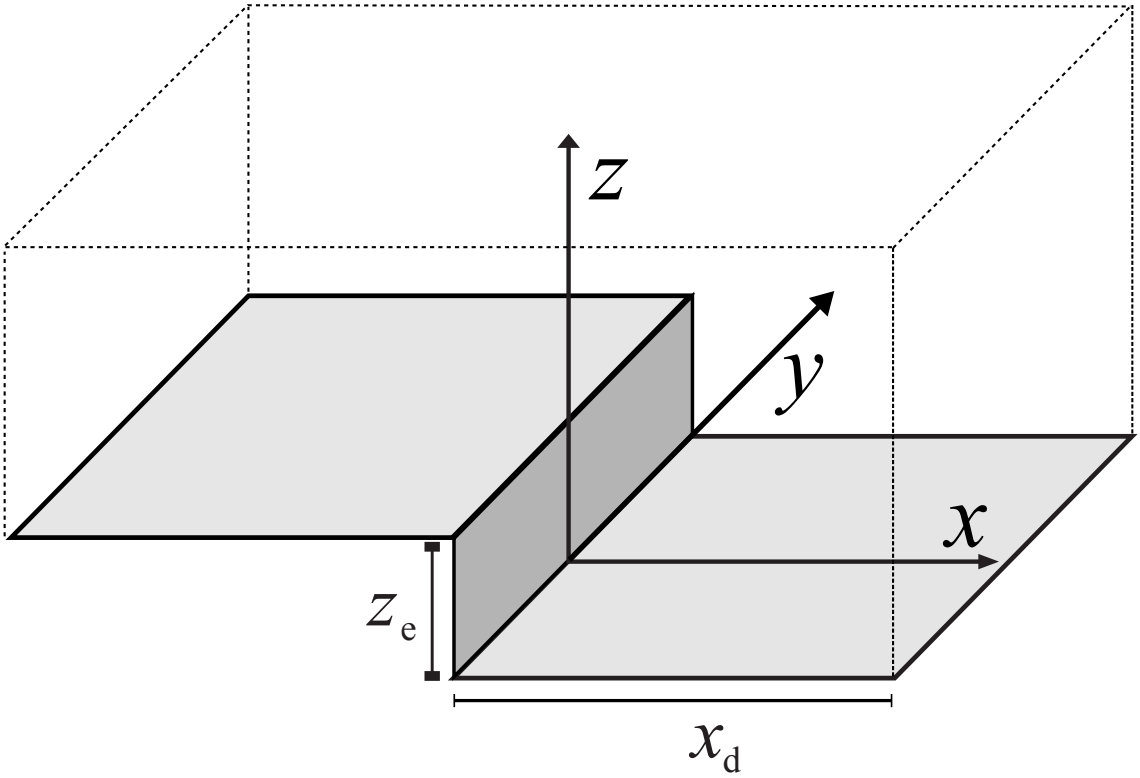

Figure 4.5: *The unit cell for the step array model with step half-height, z_e, and half-centre-to-centre distance, x_d.*

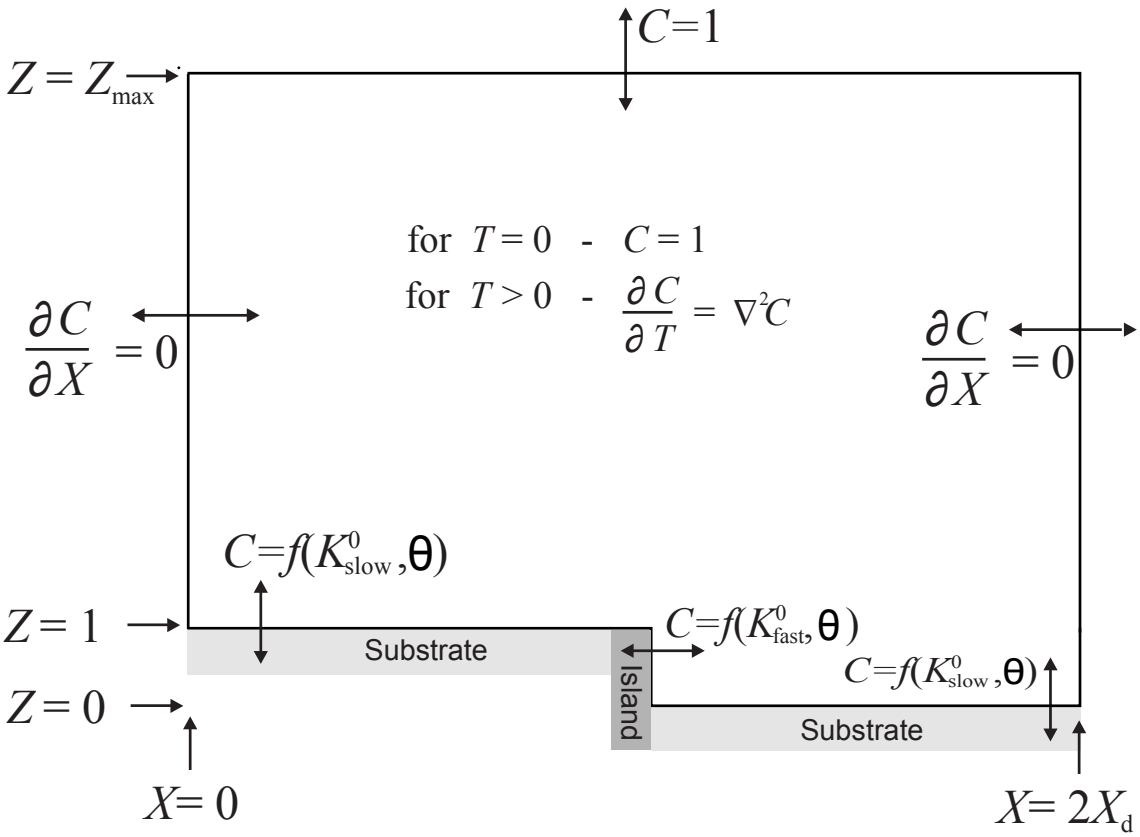

Figure 4.6: *The simulation space for an electrode with a stepped surface.*

The unit cell for the step model is illustrated in Figure 4.5. Like the band model, the step is most appropriately considered in terms of Cartesian coordinates. Each step has identical height = z_e, length, l, and horizontal step-to-step distance = $2x_d$. As is the case with the band, the length of the step is assumed to be greater than the scale of the diffusion layer and so only a two-dimensional (x, z) slice need be considered. In this case, the coordinates are normalized against the height of the step, z_e,

$$X = \frac{x}{z_e} \tag{4.17}$$

$$Z = \frac{z}{z_e} \tag{4.18}$$

The simulation space for the step model in normalized units is illustrated in Figure 4.6. The surface coverage for the band is calculated by:

$$\Theta_{band} = \frac{x_e}{x_d} \tag{4.19}$$

and for the step by:

$$\Theta_{step} = \frac{x_e}{x_e + x_d} \tag{4.20}$$

The current response for the step electrode is calculated by integrating the flux over both the horizontal and vertical electroactive surfaces:

$$I = -2NFlx_eDc^* \left(\int_0^{X_d} \left.\frac{\partial C}{\partial Z}\right|_{Z=1} \partial X + \int_0^{Z_e} \left.\frac{\partial C}{\partial X}\right|_{X=X_d} \partial Z + \int_{X_d}^{2X_d} \left.\frac{\partial C}{\partial Z}\right|_{0} \partial X \right) \tag{4.21}$$

where $X_d = x_d/z_e$.

In each case, the model may be solved numerically using the techniques developed in Chapter 3. As all of the models used in this particular study involve a two-dimensional space, the ADI method is used in each case. Note that while internally the simulations are performed in terms of dimensionless units, results in this chapter are presented in real units for ease of comprehension.

4.3 Results and Discussion

4.3.1 Split Peak Voltammetry

Under certain conditions, the cyclic voltammetry of one-electron transfer reactions on electrochemically heterogeneous electrodes is known to display two peaks on the forward potential sweep as reported by Davies et al.[6,7] for ensembles of microdiscs distributed over an electroactive surface.

If the islands are relatively large compared to the distance diffused parallel to the surface on the timescale of the experiment, then the voltammetry observed is equivalent to the weighted sum of the voltammetry of each band taken in isolation, as diffusion to each will be linear. Consequently, if the rate constants of the two materials are sufficiently different, a voltammogram with two peaks on the forward sweep will be observed, with the first peak corresponding to the faster islands. However for small, 'micro-scale' islands, this is not the case. If the rate constant of the islands is significantly faster than that of the substrate, rapid electron transfer at the former will result in depletion of material above the latter because of the convergent nature of diffusion to microelectrodes.

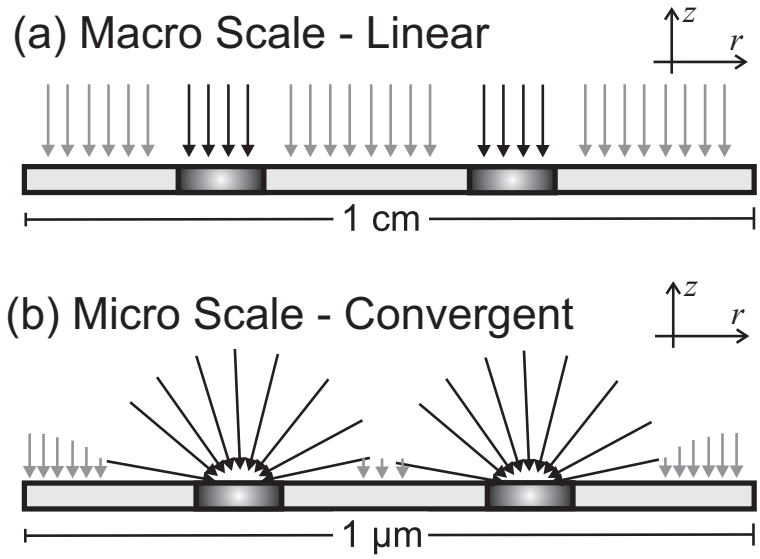

Figure 4.7: *Schematic difference between diffusion to macro- and micro-scale electrode systems. The darker area represents the island with the faster kinetics.*

Figure 4.7 illustrates schematically the difference between these two diffusion schemes. Figure 4.8 shows simulated voltammetry of microband arrays on an active

surface with fixed surface coverage of 10% but with varying band widths of 0.1, 1, and 10 μm. The simulations assume a fast rate constant of 10 cm s^{-1} for the band such that electron transfer is diffusion limited, and a relatively slow rate constant of 10^{-6} cm s^{-1} for the substrate. It can be seen that as the width of the band is increased, the diffusion scheme switches from being largely convergent to largely linear which is reflected by the transition from 1 to 2 peaks in the voltammetry, with a concomitant decrease in peak current.

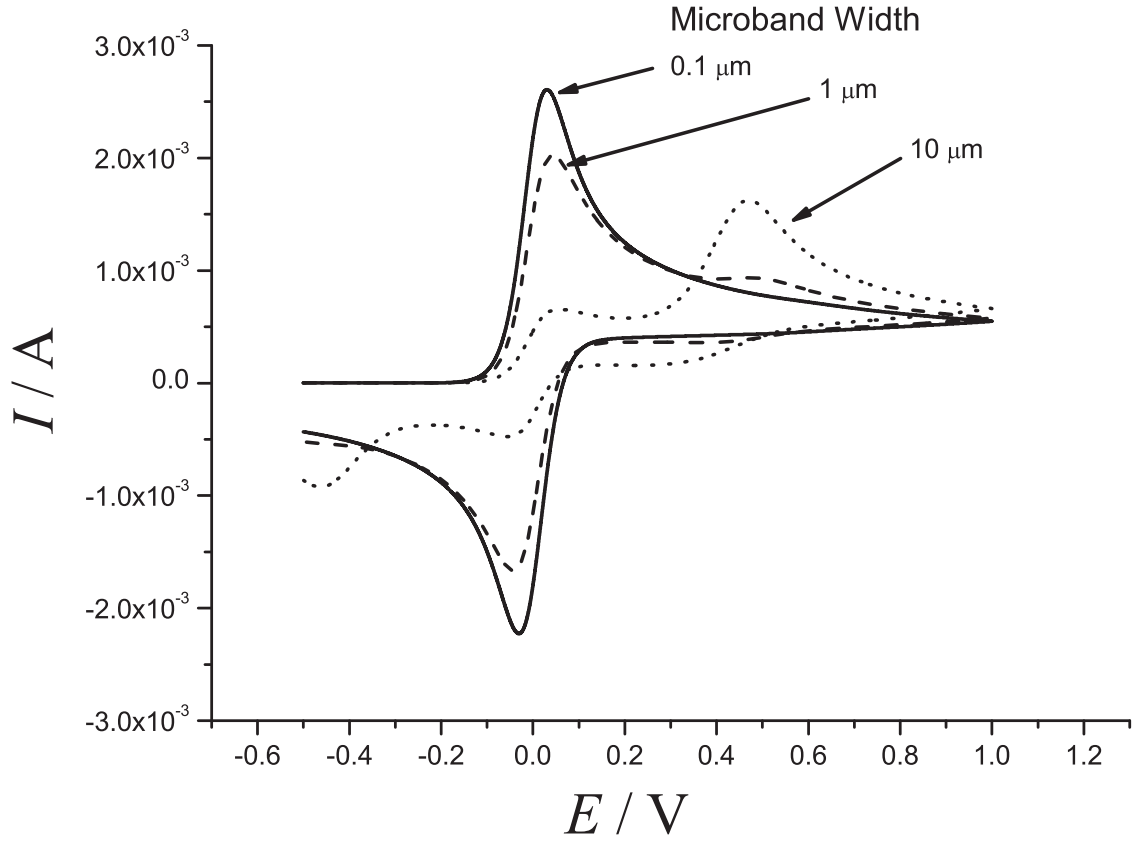

Figure 4.8: *Voltammetry of a one-electron transfer at an electrochemically heterogeneous electrode consisting of an array of microbands ($k^0 = 10$ cm s^{-1}) distributed over a substrate material ($k^0 = 10^{-6}$ cm s^{-1}) of area 1 mm^2 and a surface coverage of the bands of 10% at a scan rate of 0.1 V s^{-1}. The diffusion coefficient of all species is 10^{-5} cm^2 s^{-1} with an initial concentration of 10 mM. The voltammetry transitions from 1 peak to 2 peaks as the width of the band (labelled) is increased.*

As the band width is decreased at a fixed surface coverage, as in Figure 4.8, depletion above the kinetically slower substrate surface proceeds to a greater extent so the substrate has less of an influence on the diffusion of species 'A' and hence less of an influence on the observed voltammetry. The extent of the depleted layer

in terms of displacement from the island, parallel to the surface, is given by Einstein's equation[24] for the root mean square displacement of diffusing particles in one dimension, $\sqrt{<\overline{x}^2>}$:

$$\sqrt{<\overline{x}^2>} = \sqrt{2Dt} \tag{4.22}$$

where t is the time and D the diffusion coefficient of the diffusing species.

4.3.2 Simulated Microband Voltammetry

A large number of cyclic voltammetry simulations of systems with a band geometry were performed by varying the band width, r_{band} ($= 2r_{\text{e}}$), from 10^{-7} m to 10^{-2} m; the rate constant of the substrate, k_{sub}, from 10^{-7} cm s^{-1} to 10 cm s^{-1}; and the surface coverage, Θ, over the values 0.01, 0.1 and 0.5. The rate constant of the band, k_{isd} ($= k_{\text{isd}}$), was kept at a very 'fast' value of 10 cm s^{-1} (such that electron transfer at the band is diffusion limited), the scan rate was 0.1 V s^{-1}, the initial concentration of species 'A' was 10 mM and the diffusion coefficients of both species were 10^{-5} cm^2 s^{-1} throughout.

Figure 4.9 shows the range of values of k_{sub} and r_{band} for $\Theta = 0.01$, 0.1, and 0.5 for which two peaks are numerically resolvable, i.e. there are two distinct maxima in the voltammetry data where the gradient $\mathrm{d}i/\mathrm{d}E$ changes from a positive to a negative value. Note that this region does not include cases where a shoulder appears but where there is no actual peak with a defined maximum. The appearance of these diagrams is explained in the following discussion.

Effect of Domain Width

The following discussion makes use of the 4 diffusional mode classes detailed in Section 1.3. If t_{peak} is the time taken to sweep the potential from its initial value to the point where the current reaches a maximum (the first peak), it can be concluded from Equation (4.22) that if:

$$\sqrt{2Dt_{\text{peak}}} \gg r_{\text{sep}} \qquad \text{where} \quad r_{\text{sep}} = \frac{1}{2}\left(r_{\text{d}} - r_{\text{e}}\right) \tag{4.23}$$

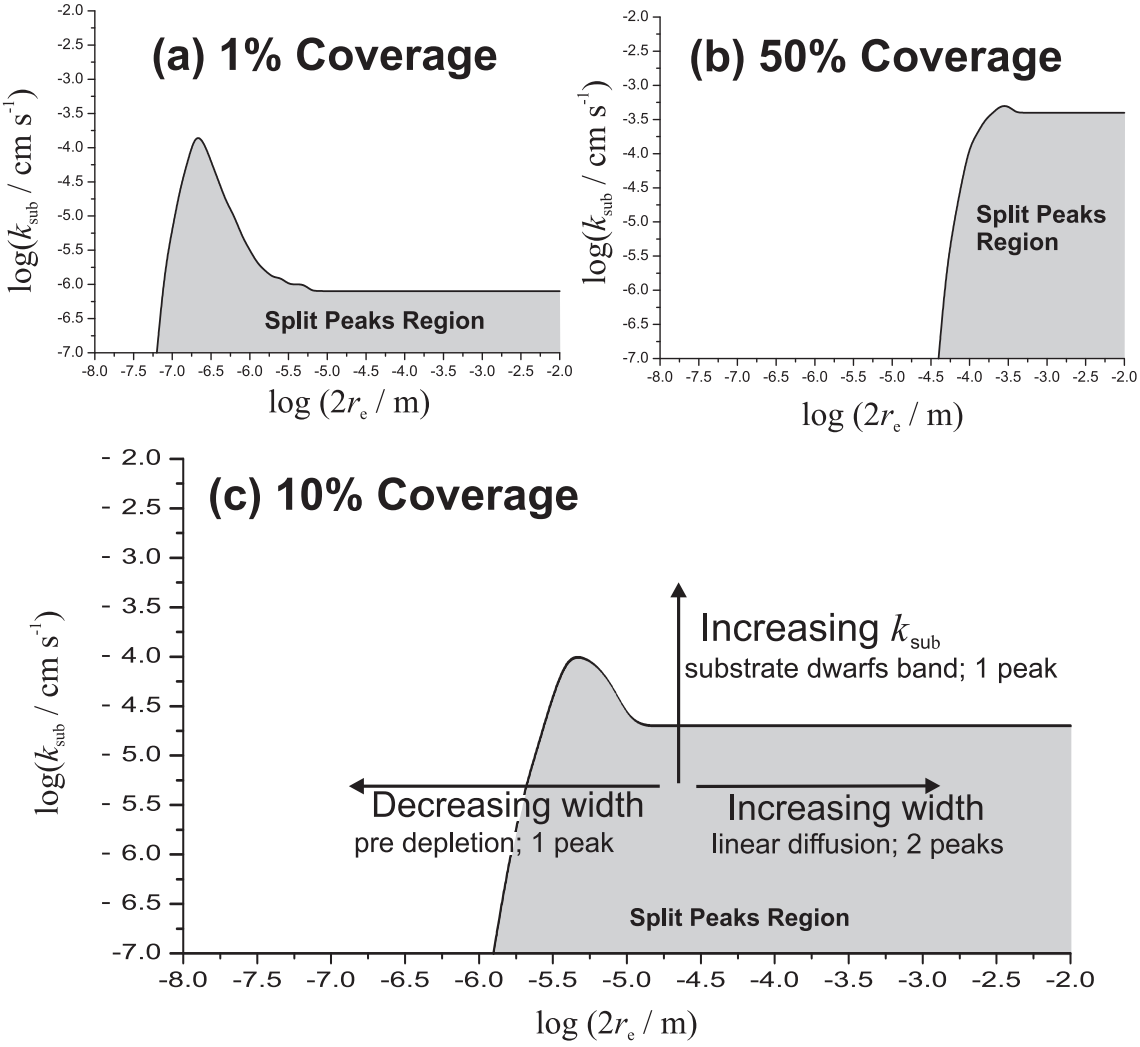

Figure 4.9: *Schematics showing the region of the 'Band Width'-'Substrate rate constant' space for which there are two peaks in the forward sweep of a cyclic voltammogram at band surface coverages of (a) 1%, (b) 50%, and (c) 10%. Scan rate* $= 0.1$ *V* s^{-1}*; diffusion coefficient* $= 10^{-5}$ *cm*^{2} *s*$^{-1}$*; island rate constant* $k_{\mathrm{isd}} = 10$ *cm* s^{-1}*.*

i.e. the inter-band separation is small compared to the spatial extent of diffusion parallel to the surface, then the voltammogram will only ever have one peak. This is indicated in Figure 4.9 (c). In this case, the voltammetric response is the same as the case where the substrate is inert, as demonstrated by the comparison in Figure 4.10 which shows an example of voltammetry for a band array with $r_{\mathrm{band}} = 0.1$ μm and $\Theta = 0.1$ where there is no difference between the active substrate and inert substrate cases. The same figure also shows the individual current responses of each component (band and substrate) from the active case. It is interesting to note that in the active case, although the overall voltammogram is the same as the inert case,

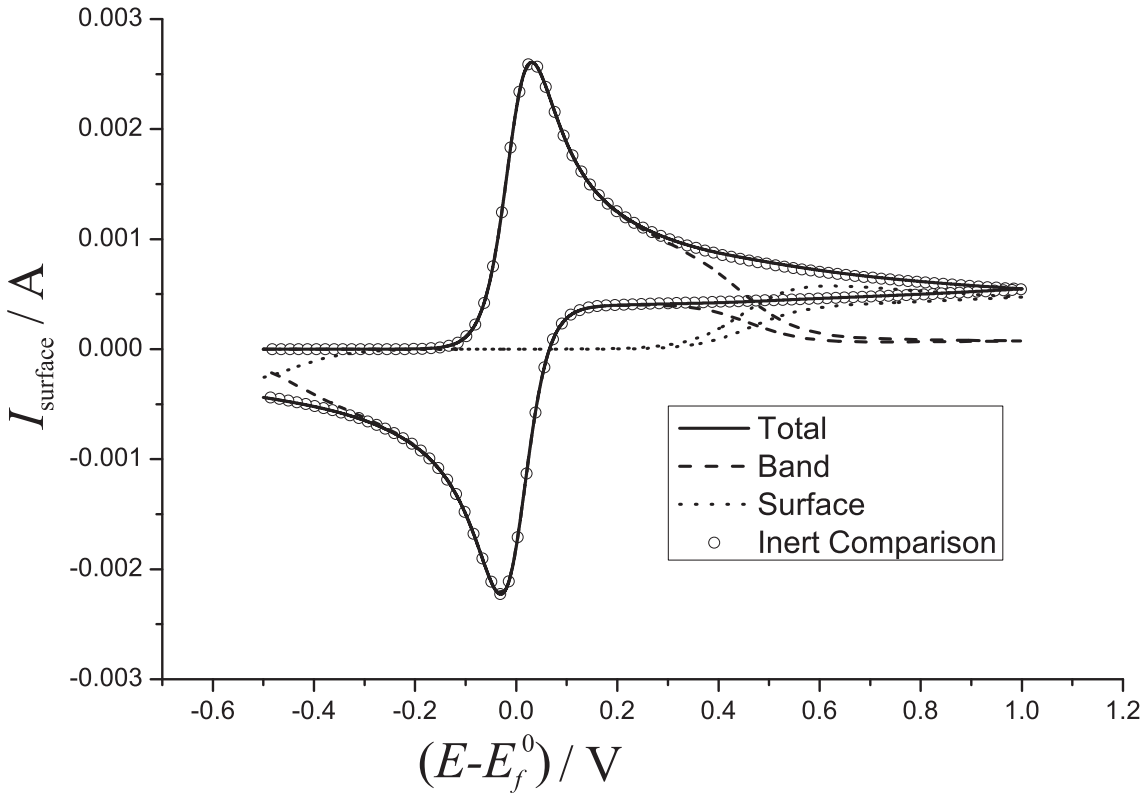

Figure 4.10: *Comparison of two systems with $\nu = 0.1$ $V\ s^{-1}$, $r_{\text{band}} = 0.1$ μm and $\Theta = 0.1$ where the substrate surface is active ($k_{\text{sub}} = 10^{-6}$ $cm\ s^{-1}$) and inert ($k_{\text{sub}} = 0$) respectively; the voltammetry of the active system resolved into individual components is also shown.*

there is still a significant amount of current passed at the substrate surface. This does not affect the shape of the overall voltammogram because by the time the substrate becomes active, diffusion to the whole surface has become linear (case 4 diffusion) and the current passed at each surface component is proportional to its surface area.

In the limit of large domain width (and consequently large band width), i.e.,

$$\sqrt{2Dt_{\text{peak}}} \ll r_{\text{sep}} \tag{4.24}$$

the voltammetry will always be a superposition of the voltammetry of the band and substrate each taken in isolation, since diffusion to each will be linear (case 1 diffusion) throughout, as indicated in Section 4.3.1. If the two rate constants are similar, the component peaks will occur at a similar potential and will therefore merge as shown in Figure 4.11 (a), leaving only one peak visible in the voltammetry.

However, a double peak voltammogram will always be observed if:

$$k^0_{band} \gg k^0_{sub} \tag{4.25}$$

as indicated in Figure 4.9 (c). Figure 4.11 (b) shows a split peak voltammogram ($\Theta = 0.5$, $r_{\text{band}} = 10^{-3}$) including a comparison with a voltammogram formed by performing a macroelectrode simulation of both the band and the substrate components in isolation and summing the results; it can be seen that the voltammograms are almost identical. Note that Figures 4.11 (a) and (b) differ only in terms of rate constant, k_{sub}.

The plots in Figure 4.9 contain a feature that has not yet been accounted for: they each have their own 'apex' (as distinct from a peak in a cyclic voltammogram) at a particular value of band width (log(band width) = -6.6 for 1% coverage; -5.3 for 10% coverage; and -3.6 for 50%), which is much more pronounced at a lower surface coverage.

As discussed, at low band width only one peak is seen in the CV since the island current contribution dominates because the separation between adjacent bands is lower and so the entire substrate surface is in range of the pre-depletion 'field'. At higher band width, the separation is greater and so the substrate is able to make a more significant contribution to the CV as neighbouring depletion fields do not overlap by the time the substrate is active. Therefore for a high band width and high surface coverage (e.g. 50% - Figure 4.9 (b)) two peaks will be seen as both surfaces contribute significantly to the CV (assuming the two rate constants are sufficiently different that the peaks are separable). However for a high band width and low surface coverage (e.g. 1% - Figure 4.9 (a)), the substrate contribution dwarfs that of the bands, even at very low k_{sub}. This explains why the plateau at larger band width is at a lower value of k_{sub} the lower the surface coverage is.

Taking the example of 1% coverage, if the band width is increased at a constant value of k_{sub} for example, $\log(k_{\text{sub}}) = -4.5$ there is a transition from a region where there is only 1 peak in the CV (island dominates), through the 2 peak region that forms the apex, and finally to the region in which the substrate dominates (again only 1 peak). In the region of the apex, the CV therefore switches from being dominated by the island contribution to being dominated by the substrate

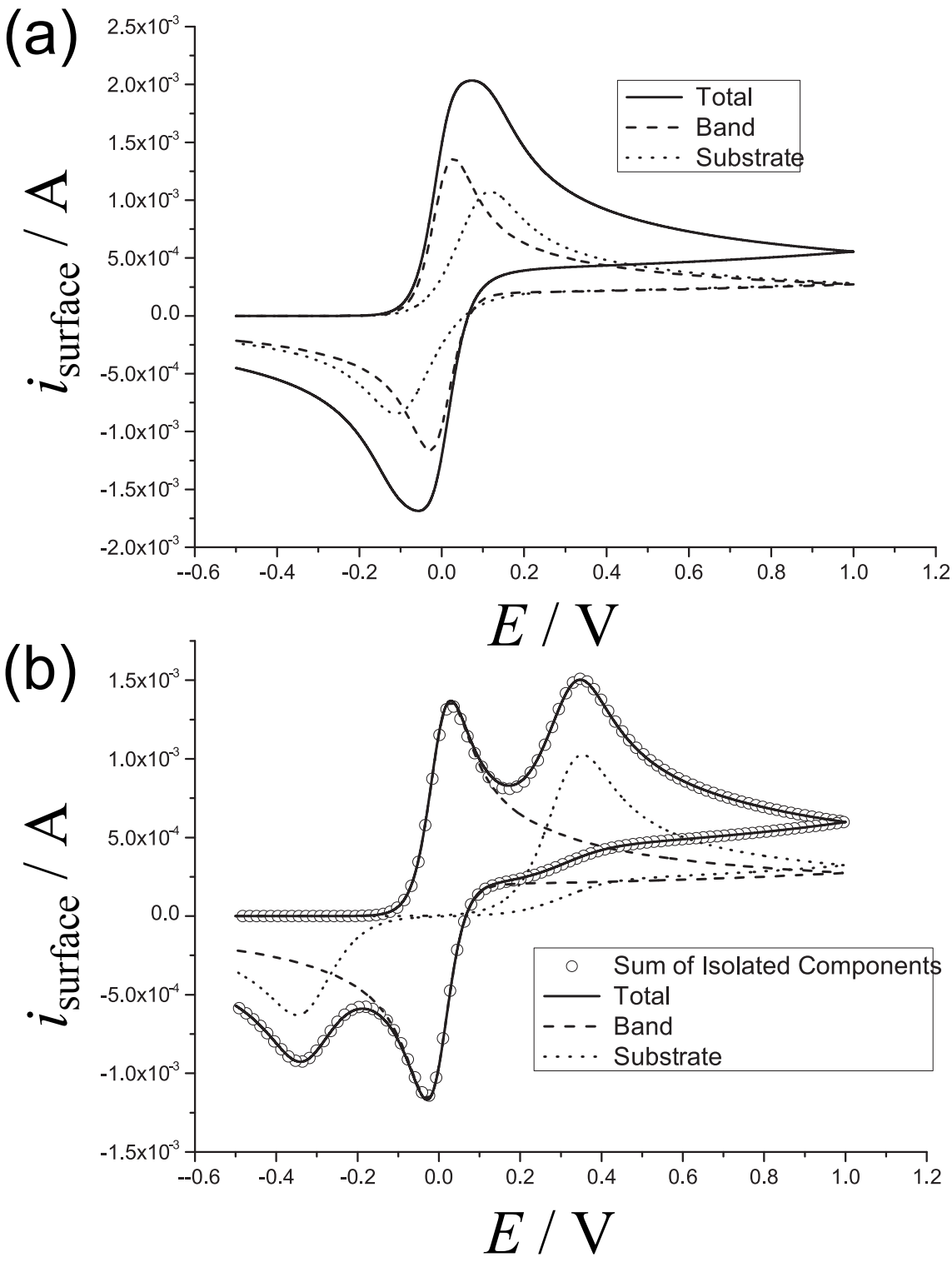

Figure 4.11: *Total and component cyclic voltammetry for a systems with* $\Theta = 0.5$, $r_{band} = 10^{-3}$ *m, scan rate = 0.1 V* s^{-1}, $k_{isd} = 10$ *cm* s^{-1} *and (a)* $k_{sub} = 10^{-5}$ *m* s^{-1} *(b)* $k_{sub} = 10^{-7}$ *m* s^{-1}. *(b) also shows the summation of voltammetry of individual components of equivalent area.*

contribution. Consequently, the two contributions are of similar magnitude in this region and so are more easily resolvable, even at a relative high value of k_{sub}. This explains why this apex extends above the plateau in k_{sub}. At lower surface coverage, the plateau is at a lower value of k_{sub} and hence the apex is more pronounced.

4.3.3 Carbon Electrodes

Next the band array model is used to simulate the electrochemistry of the HOPG surface (as justified below in Section 4.3.4). In high quality HOPG samples, highly redox active edge plane defects are typically seen in narrow bands 1-20 layers (3.35 - 67 Å) wide, with a surface coverage that can be as low as about 0.5%.[20] The oxidation of an exemplar electro-analyte, ferrocyanide, has been shown to proceed with a rate constant of 0.022 cm s^{-1} at edge plane HOPG.[18] No direct measurement has been made of the rate constant of the basal plane, as even the highest quality HOPG contains edge plane defects, but an effective rate constant for a BPPG electrode on the order of 10^{-9} cm s^{-1} has been reported.[18] The actual value of the rate constant of the basal plane itself may be even smaller than this since the edge plane defects contribute to, and therefore increase, the observed value.

It is thought that under most experimental conditions, electron transfer at the basal plane is so much slower than at the edge plane that it can effectively be *considered* inert. This has been demonstrated experimentally by selectively covering the basal plane in an inert blocking material, which resulted in no significant change to the voltammetry.[20] However as was demonstrated in Figure 4.10, it is still possible for a significant amount of current to be passed at the basal plane without any influence on the overall voltammetry, so this experimental evidence merely provides an upper limit of the activity of the basal plane.

One method of demonstrating that the basal plane does indeed contribute to HOPG voltammetry would be to show that it is possible to produce split peak voltammetry as discussed in Section 4.3.2. Figure 4.12 shows simulated cyclic voltammetry of the oxidation of ferrocyanide ($D = 6.1 \times 10^{-6}$ cm^2 s^{-1} with an initial concentration of 10 mM) at HOPG modelled as a microband array for a range of edge plane surface coverages and scan rates using experimentally derived

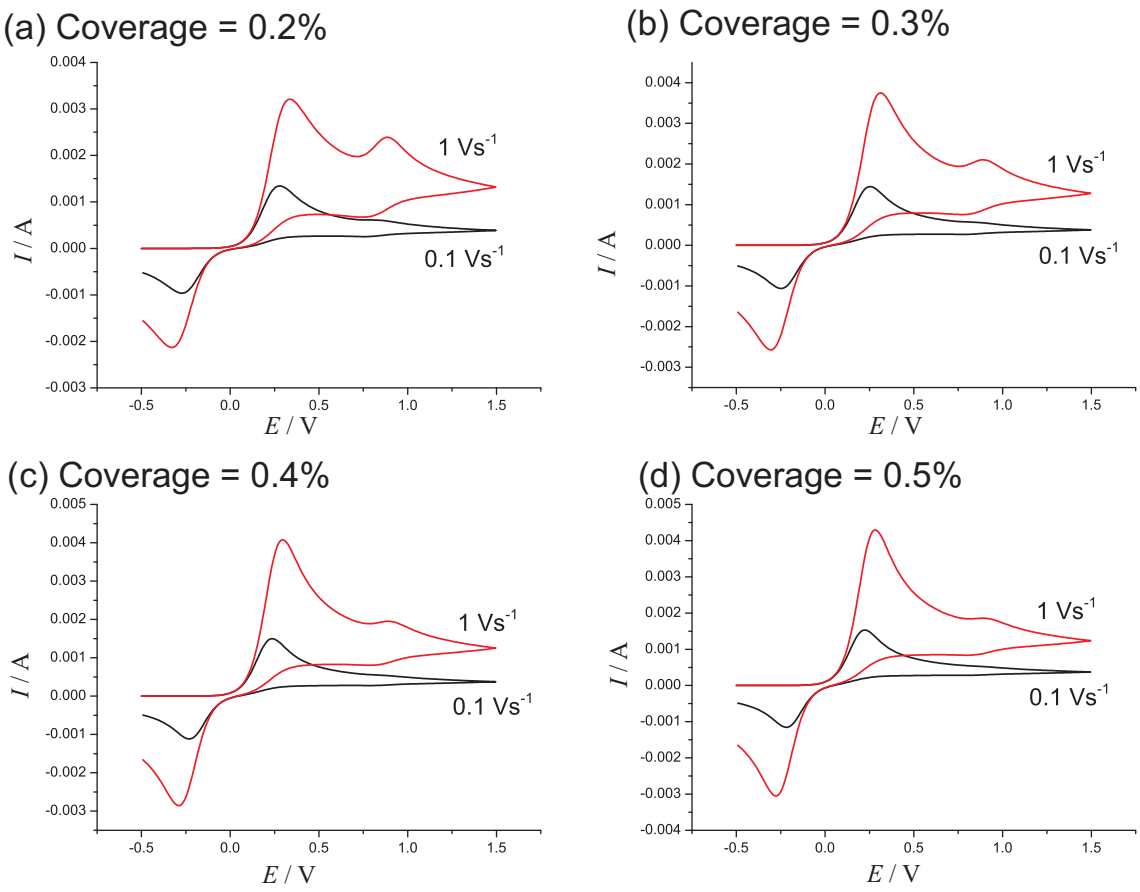

Figure 4.12: *Cyclic voltammetry of ferrocyanide (initial concentration = 10 mM; $D = 6.1 \times 10^{-6}$ cm^2 s^{-1}) oxidation at HOPG modelled as an array of microbands for scan rates of 0.1 and 1 V s^{-1}. The width of the edge plane bands, $r_{\text{band}} = 6.7$ nm (= 20 layers), the rate constant of reaction at edge plane, $k^0_{\text{edge}} = 0.022$ cm s^{-1}, and basal plane, $k^0_{\text{basal}} = 10^{-9}$ cm s^{-1}.*

parameters: $r_{\text{band}} = 6.7$ nm (= 20 layers); $k^0_{\text{edge}} = 0.022$ cm s^{-1}; $k^0_{\text{basal}} = 10^{-9}$ cm s^{-1}. It can be seen that for coverages of 0.5% and below, two peaks are indeed resolvable at 1 V s^{-1}. Such a low coverage (0.5%) is physically realisable and is commercially available[25] but probably represents the upper limit in terms of HOPG quality. At somewhat higher coverages no such splitting is observed. The band width of 6.7 nm used in these simulations is equivalent to 20 layers of edge plane and represents the upper limit of the size of an edge plane defect.[20] In a real HOPG sample the average defect size is likely smaller than this. Consequently, the contribution of the basal plane to the voltammogram in a real sample should be greater than indicated in these simulations, all other factors being equal, making split peak voltammetry easier to observe. A faster scan rate yields a more defined second peak but would

likely be impractical experimentally because of significant electrode capacitance. If the basal plane is active but with a lower rate constant than 10^{-9} cm s^{-1}, the second peak would be shifted to more positive potentials which would probably push it outside the electrochemical window (at least in aqueous solution). If an analyte with a substantially slower diffusion coefficient were used, the second peak would appear more defined. These theoretical results could therefore be tested experimentally by performing CVs of a slowly diffusing analyte on ultra-high quality HOPG in a solvent with a wide potential window.

4.3.4 Comparison of Electrode Geometries

The geometry of an electrode can have a significant impact on the rates of electron transfer that are seen. As demonstrated, there is a significant difference in diffusional mode between small, 'micro-scale' electrodes, and larger 'macro-scale' ones; smaller electrodes generally exhibit a greater current density because of convergent diffusion. For micro-scale electrodes, the shape of the electrode can also have a significant impact on the electron transfer and thus the voltammetry. In the simple case of single microelectrodes, it is evident that a long, thin band electrode will generally show a different current response to a disc electrode of the same area, since the centre region of the disc will not be as accessible to diffusing material as the centre of the band. For arrays of microelectrodes, the situation is additionally complicated by the timescale-dependent diffusional modes highlighted in Section 1.3. Obviously if the electrodes are of 'macro-scale', the voltammetric response will be determined exclusively by the geometric area of the electrode materials and the shape will be irrelevant.

Herein, the variation of voltammetric response with electrode geometry is investigated for large (i.e., composed of many unit cells) island/substrate arrays as above. Primarily 'HOPG-like systems' are considered, which for the purpose of this study are defined as those with a low surface coverage, small island width (specifically, $r_{\mathrm{isd}} = 6.7$ nm in the case of band, step and ring, corresponding to 20 layers of edge plane), and with islands possessing a rate constant very much greater than the substrate. Unless otherwise stated, the analyte species is ferrocyanide with an initial

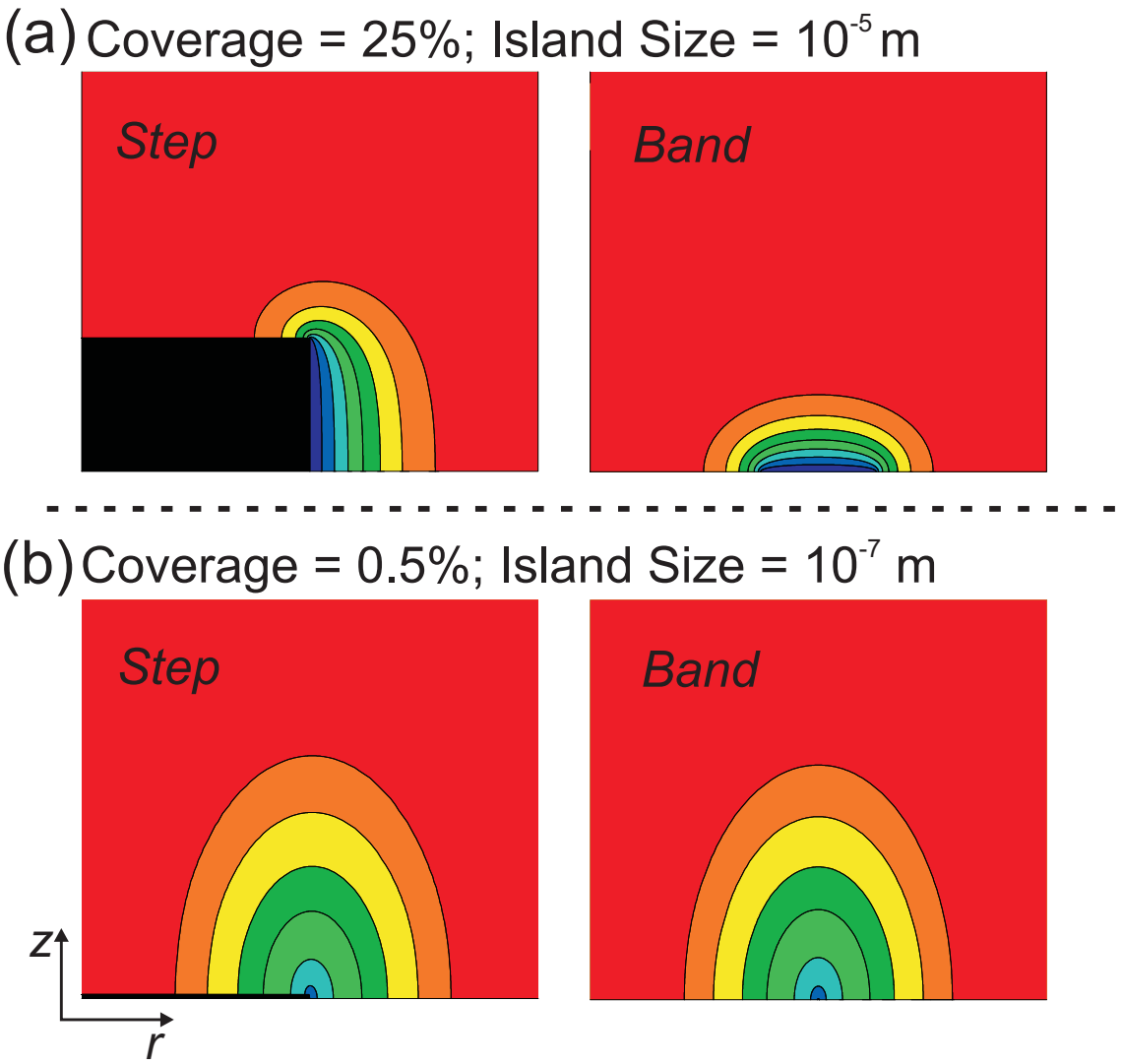

Figure 4.13: *Representative concentration profiles of species 'A' for the process 'A ⇌ B + e⁻' of band and step electrodes during cyclic voltammetry. The diffusion coefficient of both species is 10^{-9} cm^2 s^{-1}, the scan rate is 0.1 V s^{-1} and the rate constant of the step and band islands is 1 cm s^{-1} (the substrate is inert). For the step electrode, the black area indicates the interior of the electrode and only the vertical face is electroactive.*

concentration of 10 mM, which has electron transfer rate constants of $k^0_{\text{isd}} = 0.022$ cm s^{-1}; $k^0_{\text{sub}} = 10^{-9}$ cm s^{-1} on the islands and substrate respectively. Four different geometries are considered: the band, the step, the disc, and the blocking-disc, as depicted in Figure 4.2. The step geometry models the geometry of ordered graphitic surfaces such as those depicted in Figure 4.1 in which the plane of the electroactive island is perpendicular to the plane of the substrate in Cartesian coordinates. This model has recently been used by Edwards et al.[21] to attempt simulation of an HOPG surface using the commercial general engineering finite element package 'Comsol Multiphysics'.

Figure 4.14 displays zone diagrams showing the values of electrode size and substrate rate constant that result in split peak voltammetry for the ring and disc model for fixed scan rate of 0.1 V s^{-1}, diffusion coefficient of 10^{-5} cm s^{-1}, and island rate constant of 1 cm s^{-1}. The general features of the diagrams are the same as those seen for bands in Figure 4.9.

Band and Step

In comparing the step and band geometry, a range of simulations were run keeping the band-width/step-height at 6.7 nm and varying the scan rate, ν from 0.01 to 10 Vs^{-1}, and the surface coverage, Θ from 0.01 to 10%, with the rate constants as specified in Section 4.3.4. Two voltammograms may be compared quantitatively by considering the mean-scaled absolute deviation (MSAD), defined by:

$$\%\text{MSAD} = 100 \times \frac{1}{n} \sum_{n} \left| \frac{i_{\text{band}} - i_{\text{step}}}{i_{\text{band}}} \right| \tag{4.26}$$

where n is the number of E-i data points in the voltammogram, and i is the measured current at each data point.

Figure 4.15 shows representative voltammetry at a scan rate of 100 mV s^{-1} and a variety of surface coverages. Very good agreement is seen at lower surface coverages ($\leq$ 1%) but some significant deviations are obvious at 10% coverage. Similar behaviour was seen over the whole range of scan rates studied and for the case where the substrate surface is inactive ($k_{\text{sub}} = 0$). This is easily explained by considering Figure 4.13 which shows concentration profiles of a step and a band (each of sizes 10^{-5} m and 10^{-7} m) taken during CVs, at the same point in the forward

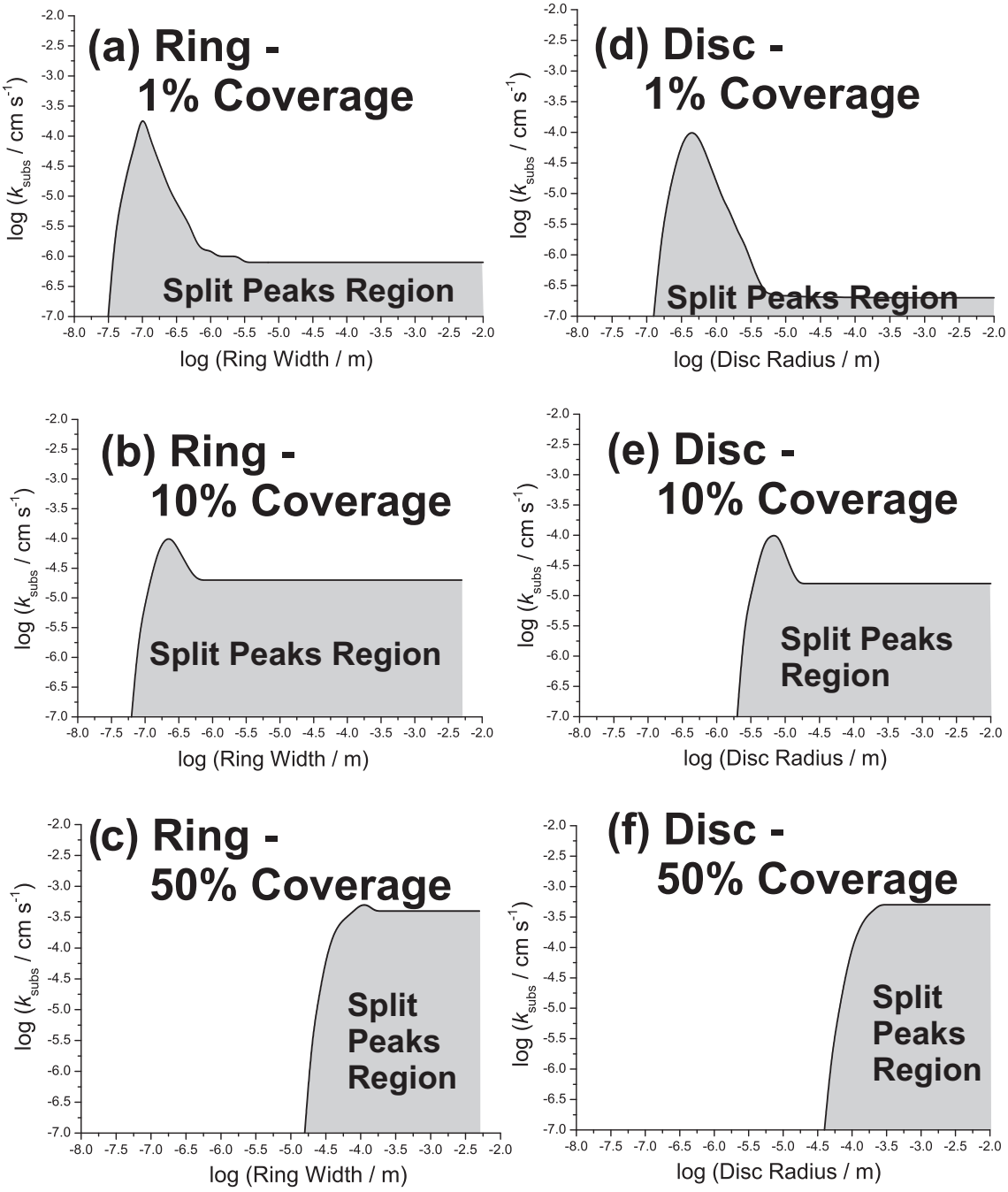

Figure 4.14: *Schematics showing the region of the 'Electrode size'-'Substrate rate constant' space for which there are two peaks in the forward sweep of a cyclic voltammogram for ring and disc surface coverages of (a) 1%, (b) 50%, and (c) 10%. Scan rate* $= 0.1\ V\ s^{-1}$*; diffusion coefficient* $= 10^{-5}\ cm^2\ s^{-1}$*; island rate constant* $k_{\mathrm{isd}} = 10\ cm\ s^{-1}$*.*

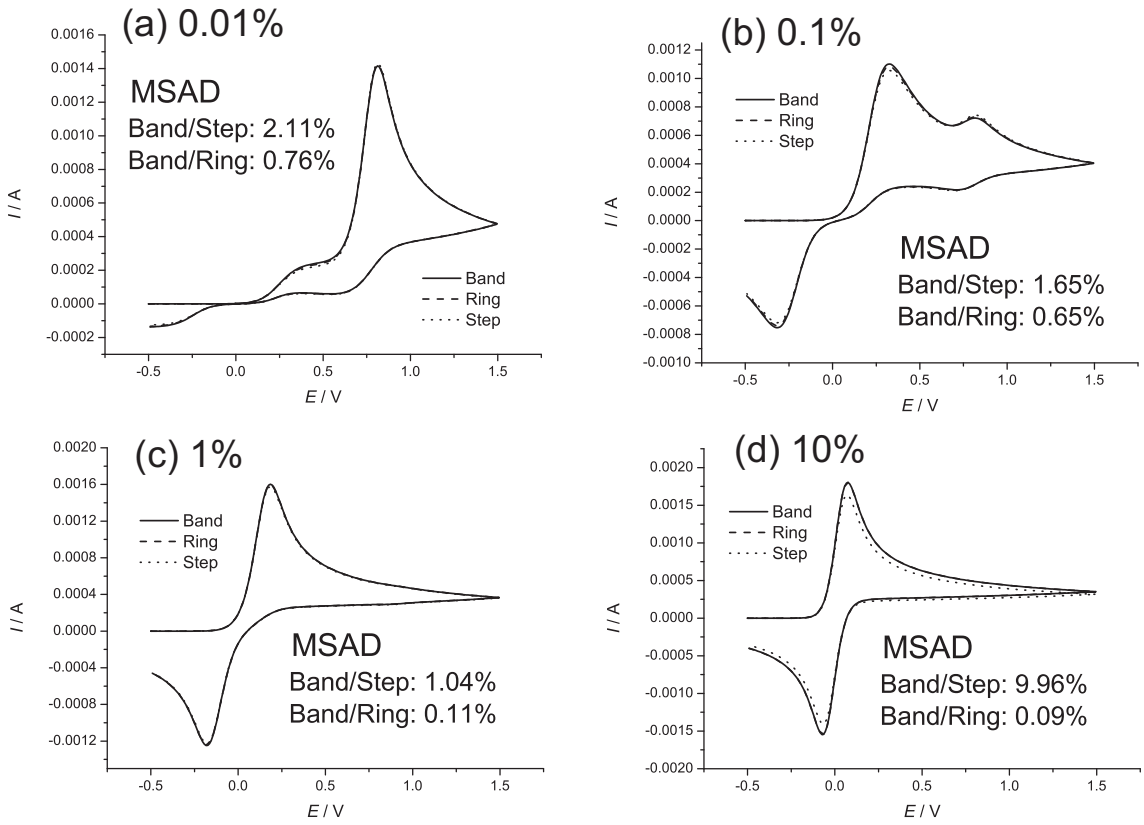

Figure 4.15: *Cyclic Voltammetry of HOPG-type band, step and ring models at a scan rate of 100 mV s^{-1} and a variety of surface coverages. For all 3 models the analyte is aqueous ferrocyanide with an initial concentration of 10 mM, $D = 6.1 \times 10^{-6}$ cm^2 s^{-1}, and $k^0_{\mathrm{isd}} = 0.022$ cm s^{-1}, $k^0_{\mathrm{sub}} = 10^{-9}$ cm s^{-1}. The width of the island in all cases is 6.7 nm. Mean scaled absolute deviations between the models are also given.*

sweep. It can be seen that if the electrode size is comparable to the domain width, the appearance of the band and step concentration profiles are quite dissimilar (Figure 4.13 (a)), therefore markedly different voltammetry is to be expected. However, if the domain width is very much greater than the electrode size, the band/step is more 'point-like' and the concentration profiles are very similar as shown in Figure 4.13 (b). Therefore it can be concluded that for small electrodes, the two models will show good agreement if the domain width is much greater than the size of the band/step. Consequently, the 'band' array may be considered as good a model of an HOPG surface as the 'step' model, and should generally be used in preference to it as it is simpler to implement and is somewhat less computationally demanding.

Band and Ring

Next, the band is compared to the blocked-disc or 'ring' geometry. Again the width of the band is maintained at 6.7 nm with the ring width being half that (such that the smallest width of 'island material' between two neighbouring substrate discs is 6.7 nm), the analyte is aqueous ferrocyanide (with the same rate constants and diffusion coefficient as before), and the same range of scan rates and surface coverages are investigated. Surprisingly, given the differences in the two models, excellent agreement is seen between them over the entire range of simulations as demonstrated in Figure 4.15. This section of the study was then extended to determine over what range of island sizes this equivalence holds; using the same parameters except island width, arrays of bands with widths of 10^{-7}, 10^{-6}, 10^{-5}, and 10^{-4} m and their ring equivalents were simulated. Representative voltammetry at 100 mV s^{-1} is shown in Figure 4.16. Again excellent agreement was seen between the two models over the entire simulation set with no MSAD higher than about 2%, and most lower than 1%; typically, better fits were seen at lower surface coverages.

If the rate constant of the substrate is reduced to zero, agreement between the two resulting models, a microband array and a partially blocked electrode, is nowhere near as good, as demonstrated in Figure 4.17.

Therefore it may be concluded that although the band model and partially blocked electrode model do not in general produce identical voltammetry, for the purposes of modelling 'HOPG-like systems' (as defined in Section 4.3.4), either model may reasonably be used despite the fact that the latter model is less physically realistic.

Band and Disc

Although they are all very different geometries, the band, step, and ring models all share a common attribute: the size of the smaller dimension of the electroactive island (band width/step height/ring width), which allows them to be easily compared. For the disc electrode, there is no equivalent dimension, making a meaningful comparison of the band and disc models more difficult. Instead the band model (band width = 6.7 nm) is compared with a family of disc models, which vary only in their

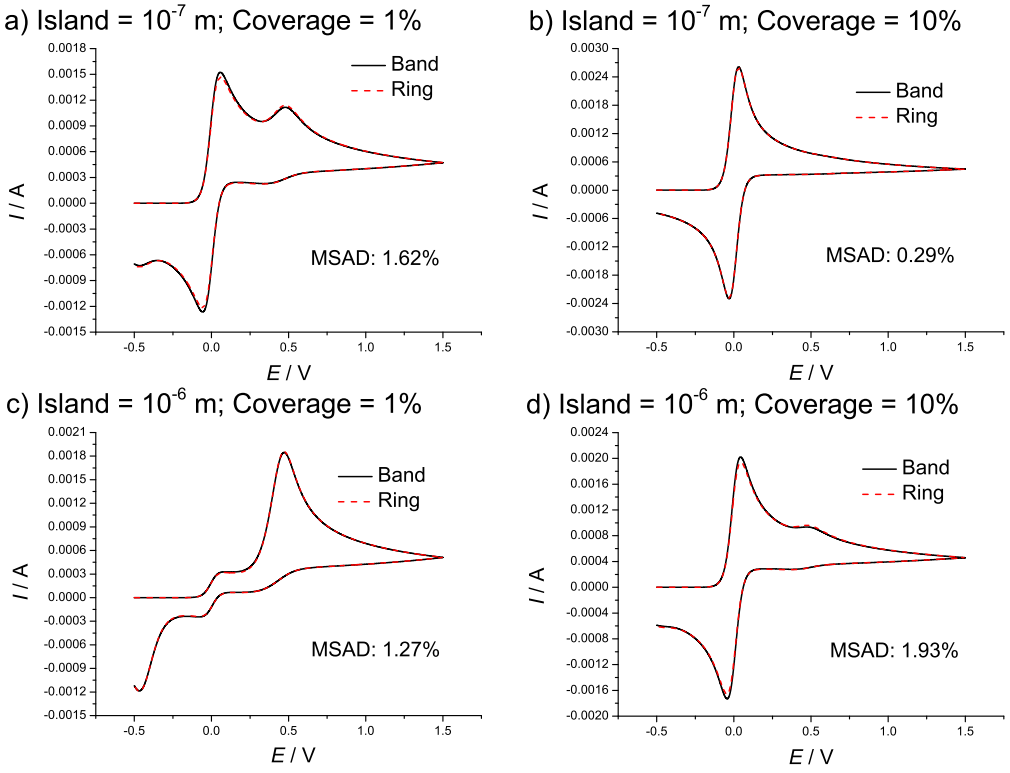

Figure 4.16: *Cyclic Voltammetry of band and ring models at a scan rate of 100 $mV\ s^{-1}$. The analyte is aqueous ferrocyanide with an initial concentration of 10 mM, $D = 6.1 \times 10^{-6}\ cm^2\ s^{-1}$, and $k^0_{\mathrm{isd}} = 0.022\ cm\ s^{-1}$, $k^0_{\mathrm{sub}} = 10^{-9}\ cm\ s^{-1}$. Island width and surface coverage are specified.*

disc radius. In doing so, an attempt is made to find a particular disc model (i.e. a particular radius) which will produce voltammetry equivalent to the band model over a wide range of scan rates and surface coverages.

Initially, disc radii of 3.35×10^{-9}–3.35×10^{-6} m were investigated. Analyte parameters and rate constant were the same as in the preceding sections. Figure 4.18 shows voltammetry from discs of radii 3.35×10^{-9} and 3.35×10^{-8} m at 1 V s^{-1}; it can be seen that the band model voltammetry appears to lie somewhere between the two disc models, an observation that was mirrored at other scan rates. For a given surface coverage, it was possible to find a disc radius that provided a good fit over a large range of scan rates, however no single radius was found to fit over a range of surface coverages. Two specific examples of such fits are shown in Figure 4.19: a radius of 2×10^{-8} m at a coverage of 0.1%, and a radius of 2.4×10^{-8} m at a coverage of 0.01%.

For systems with HOPG-like dimensions (band width and surface coverage) the

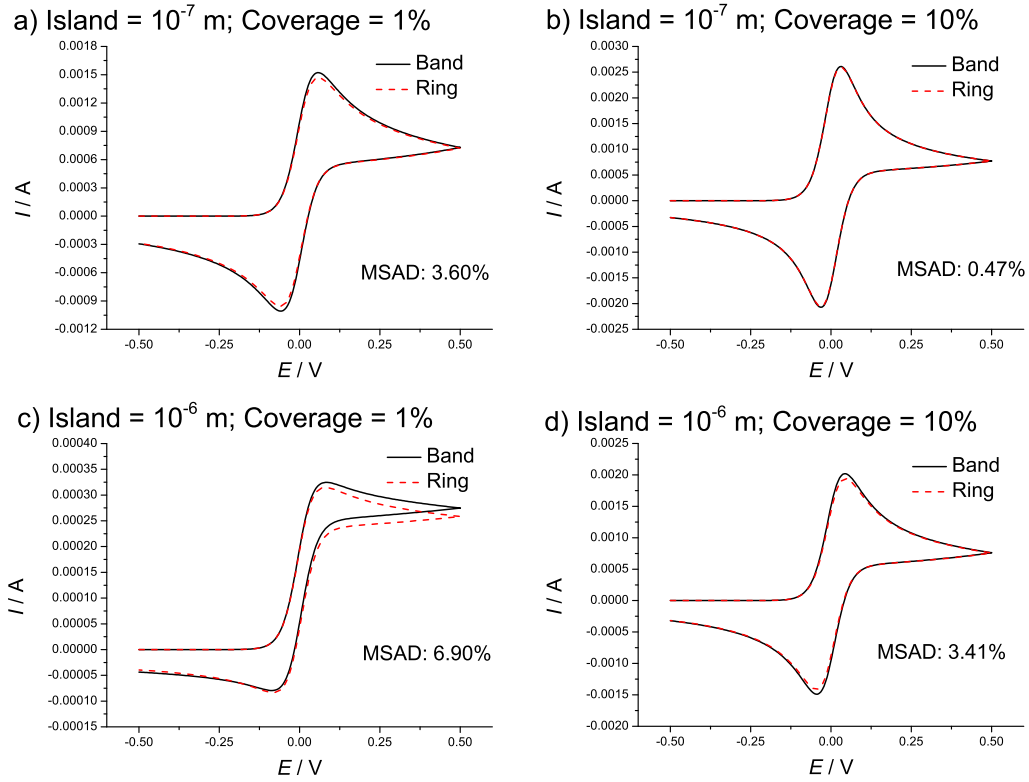

Figure 4.17: *Cyclic Voltammetry of band and ring models at a scan rate of 100 $mV\ s^{-1}$ with an inactive substrate. The analyte is aqueous ferrocyanide with an initial concentration of 10 mM, $D = 6.1 \times 10^{-6}\ cm^2\ s^{-1}$, and $k^0_{\mathrm{isd}} = 0.022\ cm\ s^{-1}$, $k^0_{\mathrm{sub}} = 0$. Island width and surface coverage are specified.*

band and step models may be used interchangeably but as the surface coverage increases, the correlation between the two models breaks down. On the other hand, the band and ring systems show excellent agreement over a much wider range of surface coverages and island widths. This relationship holds as long as the rate of electron transfer is very much slower at the substrate than at the island, but not when it is zero at the substrate. Finally, while it is possible to find agreement between the voltammetry of discs and bands of specific sizes, it is not generally the case that the two models will show agreement over any significant range of scan rates/surface coverages.

4.4 Conclusions

The voltammetry of electrochemically heterogeneous electrode surfaces has been explored and the conditions under which split peak voltammetry may be observed have

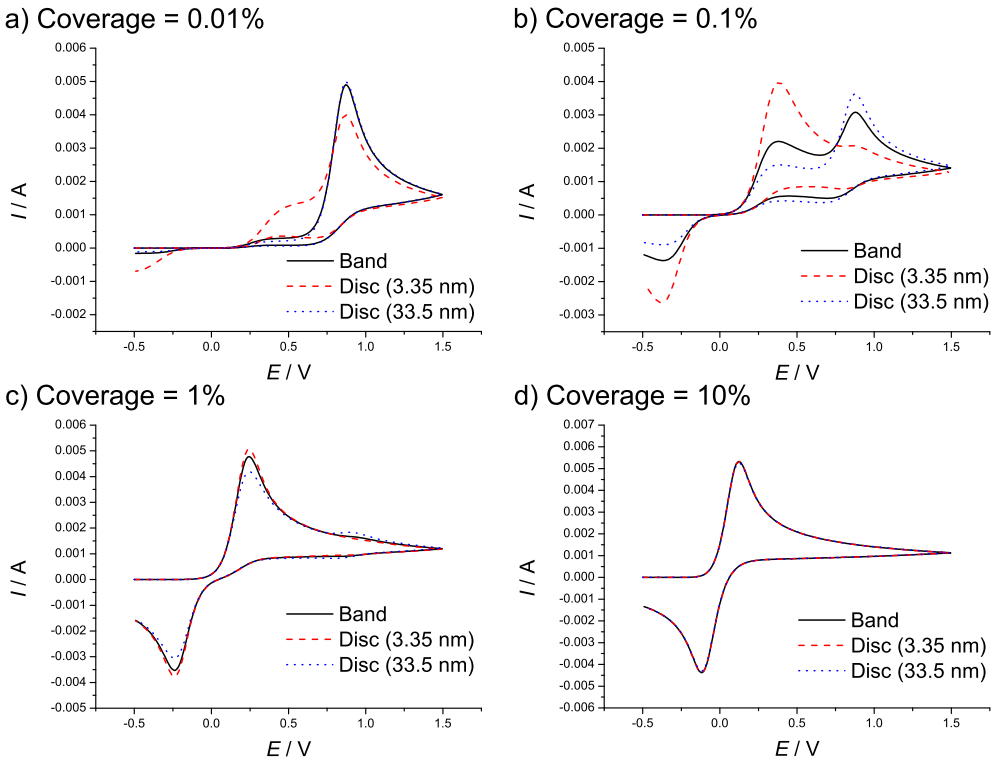

Figure 4.18: *Cyclic Voltammetry of band and 2 disc models at a scan rate of 1 V* s^{-1}*. The analyte is aqueous ferrocyanide with an initial concentration of 10 mM,* $D = 6.1 \times 10^{-6}$ cm^2 s^{-1}*, and* $k^0_{\mathrm{isd}} = 0.022$ cm s^{-1}*,* $k^0_{\mathrm{sub}} = 10^{-9}$ cm s^{-1}*. Band width is 6.7 nm and surface coverage and disc radii are specified.*

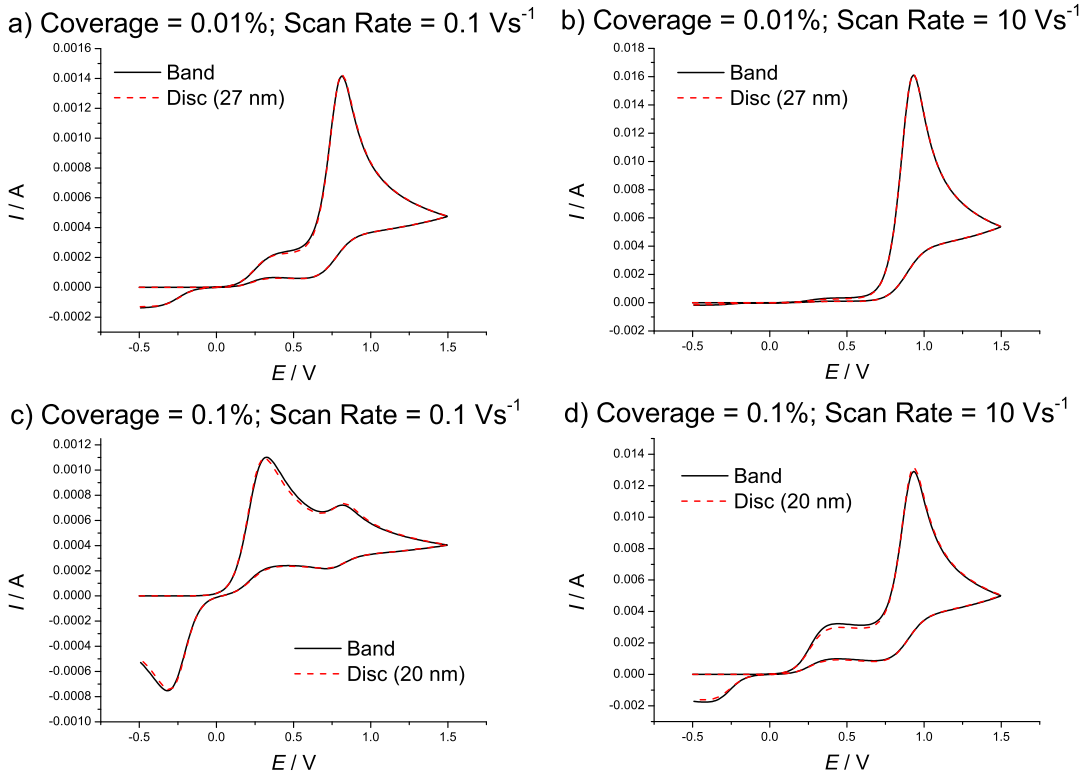

Figure 4.19: *Cyclic Voltammetry of band and best disc model fits. The analyte is aqueous ferrocyanide with an initial concentration of 10 mM, $D = 6.1 \times 10^{-6}$ cm^2 s^{-1}, and $k^0_{\text{isd}} = 0.022$ cm s^{-1}, $k^0_{\text{sub}} = 10^{-9}$ cm s^{-1}. Band width is 6.7 nm and surface coverage, disc radii, and scan rates are specified.*

been elucidated. It is possible for the slower substrate surface to have no influence on voltammetry (in comparison to an inert substrate), even if significant current is passed at the substrate surface. It has been demonstrated that it is possible to design an experiment to challenge the hypothesis that the basal plane plays no part in the voltammetry of HOPG by searching for split peak voltammetry. Finally a number of geometric models of a heterogeneous surface have been compared. It was shown that for the purposes of modelling ferrocyanide oxidation at HOPG and similar surfaces (i.e., those with a low surface coverage of small, highly active islands on a significantly less active substrate), the step, band and ring models may be used interchangeably as the voltammetry resulting from these models is equivalent.

Bibliography

[1] K. R. Ward, N. S. Lawrence, R. S. Hartshorne and R. G. Compton, *Phys. Chem. Chem. Phys.*, 2012, **14**, 7264–7275.

[2] R. J. Forster, *Chem. Soc. Rev.*, 1994, **23**, 289–97.

[3] H. Reller, E. Kirowa-Eisner and E. Gileadi, *J. Electroanal. Chem.*, 1982, **138**, 65–77.

[4] R. M. Pemberton, F. J. Rawson, J. Xu, R. Pittson, G. A. Drago, J. Griffiths, S. K. Jackson and J. P. Hart, *Microchim. Acta*, 2010, **170**, 321–330.

[5] K. C. Honeychurch, S. Al-Berezanchi and J. P. Hart, *Talanta*, 2011, **84**, 717–723.

[6] T. J. Davies, S. Ward-Jones, C. E. Banks, J. Del. Campo, R. Mas, F. X. Munoz and R. G. Compton, *J. Electroanal. Chem.*, 2005, **585**, 51–62.

[7] T. J. Davies and R. G. Compton, *J. Electroanal. Chem.*, 2005, **585**, 63–82.

[8] I. Streeter, N. Fietkau, J. Del. Campo, R. Mas, F. X. Munoz and R. G. Compton, *J. Phys. Chem. C*, 2007, **111**, 12058–12066.

[9] I. Streeter and R. G. Compton, *J. Phys. Chem. C*, 2007, **111**, 15053–15058.

[10] B. A. Brookes, T. J. Davies, A. C. Fisher, R. G. Evans, S. J. Wilkins, K. Yunus, J. D. Wadhawan and R. G. Compton, *J. Phys. Chem. B*, 2003, **107**, 1616–1627.

[11] T. J. Davies, B. A. Brookes, A. C. Fisher, K. Yunus, S. J. Wilkins, P. R. Greene, J. D. Wadhawan and R. G. Compton, *J. Phys. Chem. B*, 2003, **107**, 6431–6444.

[12] C. Amatore, J. M. Savéant and D. Tessier, *J. Electroanal. Chem.*, 1983, **147**, 39–51.

[13] H. Chang and A. J. Bard, *Langmuir*, 1991, **7**, 1143–53.

[14] R. L. McCreery, *Chem. Rev.*, 2008, **108**, 2646–2687.

[15] C. E. Banks, R. R. Moore, T. J. Davies and R. G. Compton, *Chem. Commun.*, 2004, **16**, 1804–1805.

[16] R. R. Moore, C. E. Banks and R. G. Compton, *Anal. Chem.*, 2004, **76**, 2677–2682.

[17] C. C. M. Neumann, C. Batchelor-McAuley, C. Downing and R. G. Compton, *Chem.–Eur. J.*, 2011, **17**, 7320 7326.

[18] C. E. Banks and R. G. Compton, *Anal. Sci.*, 2005, **21**, 1263–1268.

[19] K. K. Cline, M. T. McDermott and R. L. McCreery, *J. Phys. Chem.*, 1994, **98**, 5314–19.

[20] T. J. Davies, M. E. Hyde and R. G. Compton, *Angew. Chem., Int. Ed.*, 2005, **44**, 5121–5126.

[21] M. A. Edwards, P. Bertoncello and P. R. Unwin, *J. Phys. Chem. C*, 2009, **113**, 9218–9223.

[22] T. J. Davies, R. R. Moore, C. E. Banks and R. G. Compton, *J. Electroanal. Chem.*, 2004, **574**, 123–152.

[23] R. G. Compton and C. E. Banks, *Understanding Voltammetry*, ICP, London, 2nd edn., 2010.

[24] A. Einstein, *Ann. Phys.*, 1905, **17**, 549–560.

[25] *http://www.2spi.com/catalog/new/hopgsub.php*.

Chapter 5

Voltammetry at a Spherical Particle on a Surface

In this chapter, the steady-state voltammetry of a one-electron reduction is studied numerically for a conductive spherical particle resting on a supporting surface. The process is assumed to occur exclusively on the surface of the sphere and not at all on the support. For electrode kinetics in the fully irreversible limit, a simple relationship between the half-wave potential and the kinetic parameters, α (the transfer coefficient) and k^0 (the rate constant of the reaction), the radius of the sphere, and the diffusion coefficient of the species in solution is established. Further, an expression that completely describes the voltammetric waveform in the same limit is developed. Additionally a simple transformation that maps the irreversible steady-state voltammetry for an isolated spherical electrode, such as may be obtained from any commercially available electrochemical simulation package, onto the voltammetry of a sphere on a surface is described. The sphere on a supporting plane model has recently been used to explain the current-time behaviour seen for nanoparticle impacted electrode surfaces such that electrode processes occur on the sphere surface only while it is in contact with the plane;[1] accordingly, the theory presented here is of potential significant application in this area.

The work constituting this chapter has been published in the *Journal of Electroanalytical Chemistry*.[2]

5.1 Introduction

Recent work has begun to explore aspects of the voltammetric behaviour of spherical particles supported on a surface of different material such that electrode processes occur exclusively on the sphere and not at the plane support. The latter acts simply to provide electrical contact to the sphere. It is known that the limiting steady-state current for a spherical particle on a surface is:[3]

$$I_{\text{lim}} = 4\pi \ln(2) F D c^* r_{\text{e}} \tag{5.1}$$

Streeter et al. explored the limiting current to spheroids and hemispheroids of various distorted shapes.[4] Further work has explored the voltammetric behaviour of randomly distributed assemblies of spherical nanoparticles on a surface in both theory and experiment,[5] and an equation that fully describes the current-time chronoamperometric transient for such systems has been presented.[6] More recently, it has been realised[1] that this type of model can be applied to experiments in which nanoparticles in solution under Brownian motion impact an electrode for a period of time before diffusing away, such that electrode processes can occur on the particle surface during the period of impact. A number of other studies have also been carried out in the area of single nanoparticle detection[7–10] and a recent paper has looked at the effects of monolayers of single nanoparticle electrocatalysis.[11] Further, the use of nanoparticles in electroanalysis has been recently reviewed.[12] The same model can also be applied to the case of the dropping mercury electrode used in polarography.[13]

5.2 Theory

5.2.1 Theoretical Model

Throughout this study, a one electron reduction,

$$\text{A} + \text{e}^- \rightleftharpoons \text{B} \tag{5.2}$$

is considered. It is assumed that at the start of each experiment, the concentration

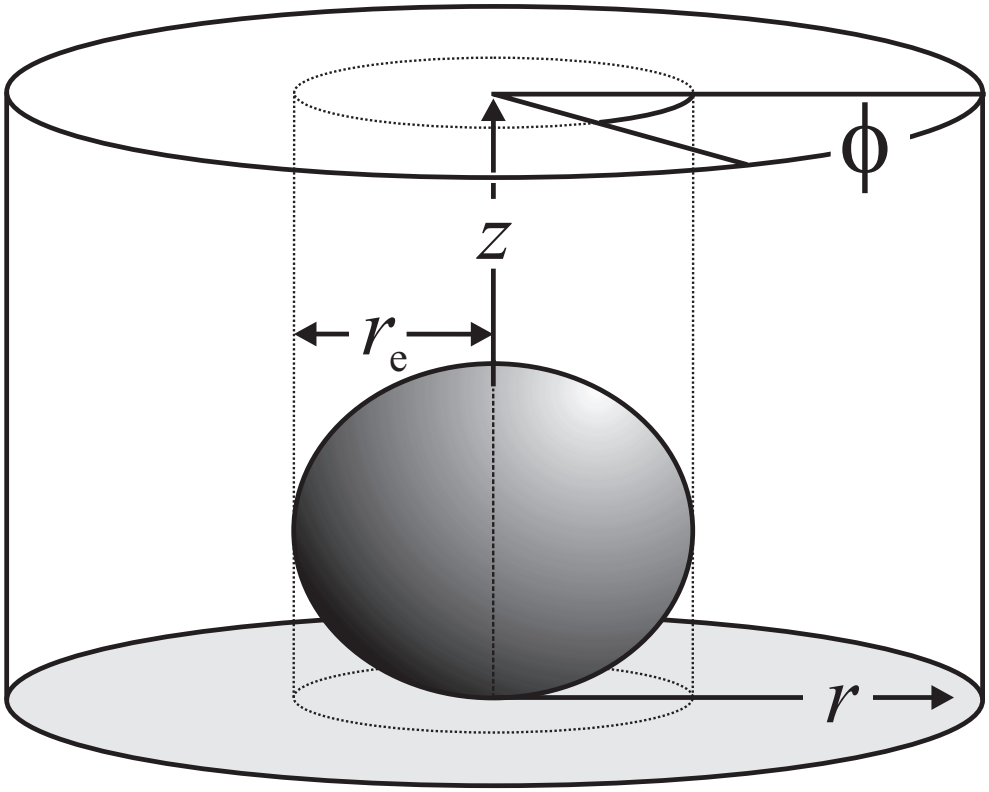

Figure 5.1: *The (r, z, ϕ) cylindrical polar coordinate system used to represent a spherical nanoparticle, with radius r_e on an insulating surface.*

of reduced species A is uniform and equal to some bulk value, c^*, and there is no oxidised species B present in the system. Additionally it is assumed that the diffusion coefficients of the two chemical species are equal such that at every point in space, the concentrations of species A and B sum to c^* (See Section 2.3.1). Consequently, only the behaviour of species A need be considered as the concentration profile of species B can be inferred from that of A.

The electrode system consists of a conductive spherical particle, radius r_e, on a supporting surface that is infinite in extent. Such a system can be described in a cylindrical polar coordinate system (r, z, ϕ), as depicted in Figure 5.1, with the origin at the point of contact between the sphere and the surface. Like the microdisc electrode model, this system is axisymmetric, so that there can be no gradient of concentration with respect to angle ϕ. Consequently, only a 2 dimensional (r, z) 'slice' of the sphere, as shown in Figure 5.2, needs to be considered when modelling it. Note that the system may alternatively be described in spherical polar coordinates.[6]

This is the same coordinate system used for the microdisc model and the form

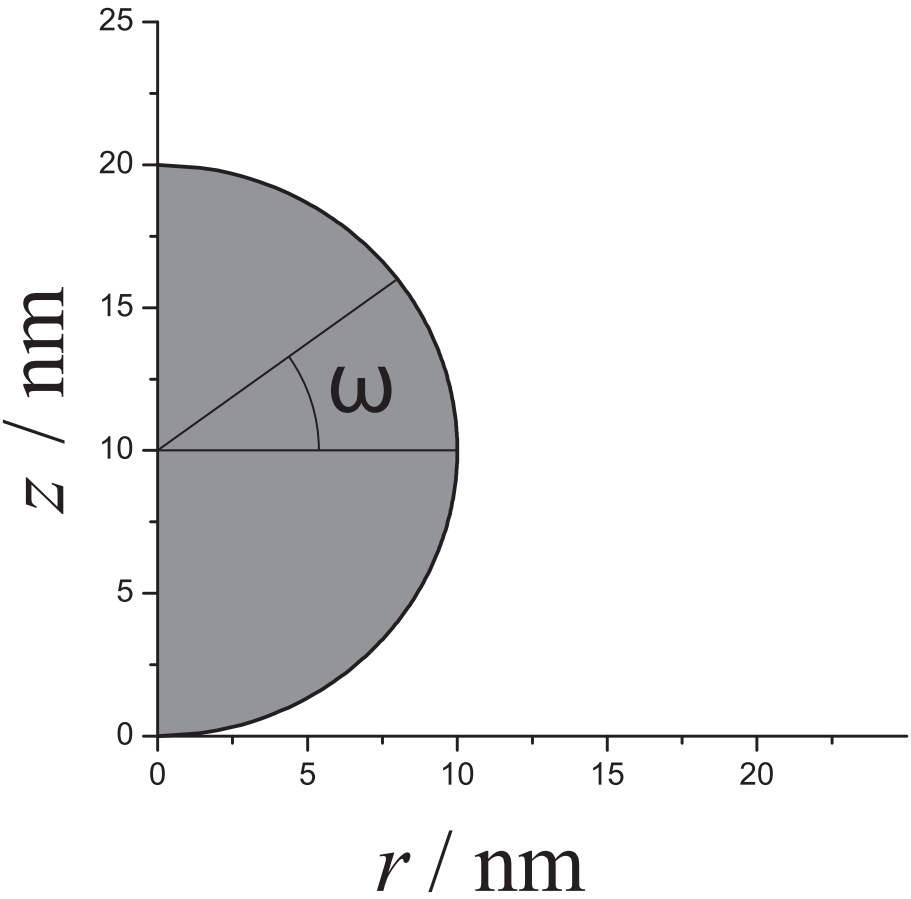

Figure 5.2: *The reduced 2D (r, z) coordinate system used to model a spherical nanoparticle in simulations. Though not one of the coordinates, angle ω is useful for current calculations and for specifying the discretized spatial grid.*

of Fick's second law is therefore:

$$\frac{\partial c}{\partial t} = D\left(\frac{\partial^2 c}{\partial r^2} + \frac{\partial^2 c}{\partial z^2} + \frac{1}{r}\frac{\partial c}{\partial r}\right) \tag{5.3}$$

In each simulated experiment, linear sweep voltammetry (LSV) is used. The potential is swept from some relatively positive potential at which species A is stable to some more negative potential at which it is reduced, at a constant rate ν. The electrode surface is defined by the set of r, z points that satisfy the equation

$$r^2 + (z-1)^2 = r_e^2 \tag{5.4}$$

The flux, j_0, of species A perpendicular to the electrode surface at each point on the surface is given by the Butler-Volmer equation:

$$j_0 = D\frac{\partial c}{\partial n} = k^0 \left[\exp\left(\frac{-\alpha F(E - E_f^0)}{RT}\right) c_0 - \exp\left(\frac{(1-\alpha)F(E - E_f^0)}{RT}\right)(1 - c_0) \right] \tag{5.5}$$

where c_0 is the concentration of species A at the electrode surface and n is some coordinate normal to the electrode surface. In terms of the cylindrical polar coordinate system:

$$\frac{\partial c}{\partial n} = \frac{\partial c}{\partial z}\sin\omega + \frac{\partial c}{\partial r}\cos\omega \tag{5.6}$$

where ω is the angle shown in Figure 5.2 and may be calculated from

$$\omega = \tan^{-1}\left(\frac{z - r_e}{r}\right) \tag{5.7}$$

The space is assumed to extend infinitely in both the r and z directions. The outer boundaries which are sufficiently removed from the electrode surface such that no changes in concentration away from the bulk value can occur on the experimental timescale[14] are at a minimum distance of $6\sqrt{Dt_{\max}}$ from the electrode, i.e.,

$$r_{\max} = r_e + 6\sqrt{Dt_{\max}} \tag{5.8}$$

$$z_{\max} = 2r_e + 6\sqrt{Dt_{\max}} \tag{5.9}$$

The central axis is a symmetry boundary and therefore permits no particle flux, so

$$\left.\frac{\partial c}{\partial r}\right|_{r=0} = 0 \tag{5.10}$$

5.2.2 Normalization

The simulation model is normalized according to the same set of dimensionless parameters that were used for the microdisc model:

$$C = \frac{c}{c^*} \tag{5.11}$$

$$d = \frac{D}{D_\mathrm{A}} = 1 \tag{5.12}$$

$$R = \frac{r}{r_\mathrm{e}} \tag{5.13}$$

$$Z = \frac{z}{z_\mathrm{e}} \tag{5.14}$$

$$T = \frac{D_\mathrm{A} t}{r_\mathrm{e}^2} \tag{5.15}$$

Under this system, Fick's second law is given by:

$$\frac{\partial C}{\partial T} = \frac{\partial^2 C}{\partial R^2} + \frac{\partial^2 C}{\partial Z^2} + \frac{1}{R}\frac{\partial C}{\partial R} \tag{5.16}$$

and the Butler-Volmer equation is given by:

$$\frac{\partial C}{\partial Z}\sin\omega + \frac{\partial C}{\partial R}\cos\omega = K^0\left(C_0 e^{-\alpha\theta} - (1-C_0)e^{\theta-\alpha\theta}\right) \tag{5.17}$$

The implementation of this boundary condition under the ADI method is fully detailed in Section 5.2.4, below.

At the beginning of the simulation ($T = 0$), $C = 1$ across the whole simulation space. The radius of the particle is 1 in the normalized coordinate system, and so the outer spatial boundaries are positioned at:

$$R_\mathrm{max} = 1 + 6\sqrt{T_\mathrm{max}} \tag{5.18}$$

$$Z_\mathrm{max} = 2 + 6\sqrt{T_\mathrm{max}} \tag{5.19}$$

where T_max is the maximum dimensionless time that the simulated experiment will run for. The concentration is set to its bulk value, $C = 1$, at this boundary. The simulation space and its attendant boundary conditions are illustrated in Figure 5.3.

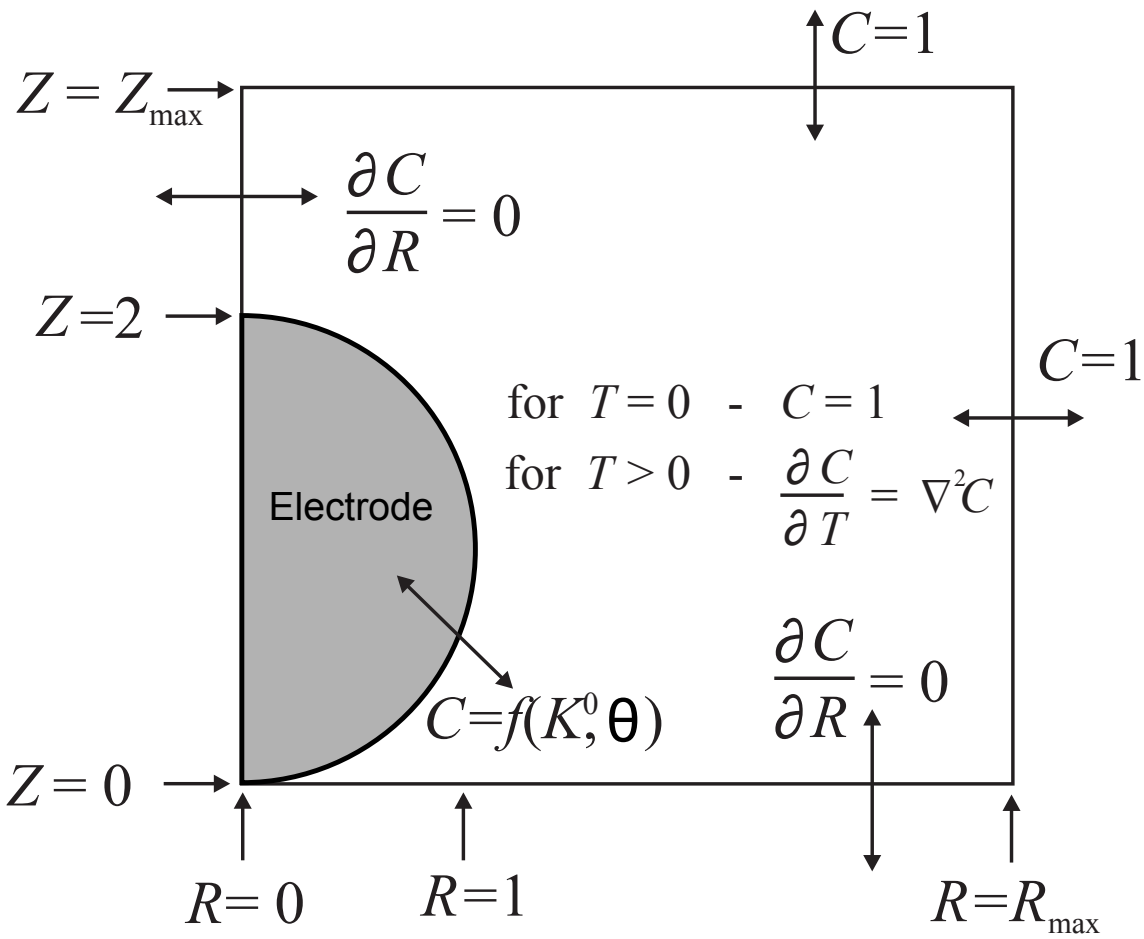

Figure 5.3: *The simulation space for a spherical particle in normalized units.*

5.2.3 Simulation Procedure

This 2-dimensional continuous space is discretized by dividing it up into a finite grid of spatial points as shown in Figure 5.4. In the normalized (R, Z) coordinate system, the surface of the spherical particle is described by:

$$R^2 + (Z-1)^2 = 1 \tag{5.20}$$

The distribution of spatial points in the region of the nanoparticle is specified such that the points exactly fit to the particle surface, making Butler-Volmer and current calculations much simpler than they might otherwise be. This is achieved by dividing the sphere into a series of angular increments, each of size $\Delta\omega$, and then calculating the values of R and Z at each successive value of ω, where ω is the

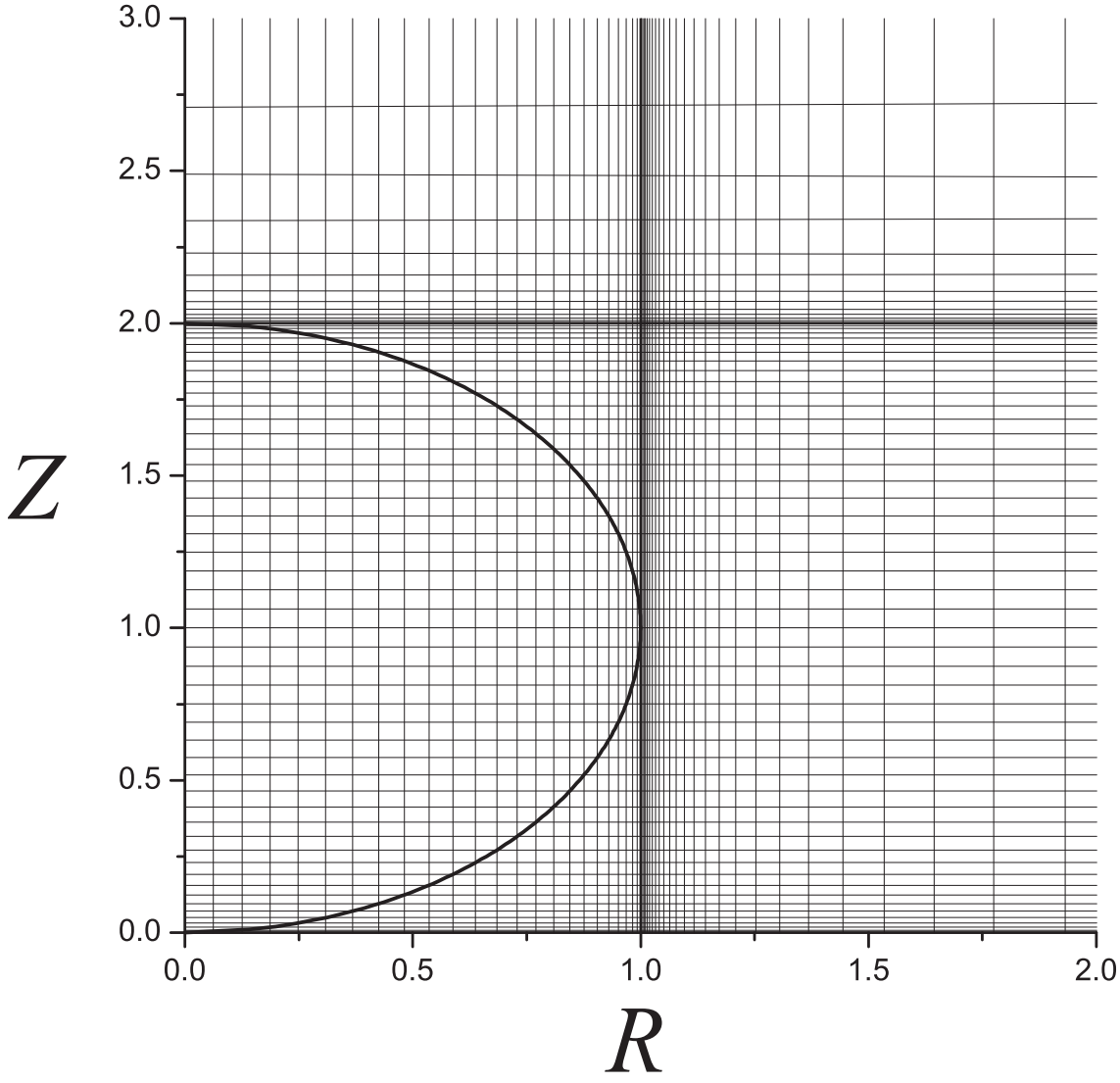

Figure 5.4: *The spatial grid used for simulation. Some points have been omitted for clarity.*

angle shown in Figure 5.2. To generate the R grid, ω was taken from $-\pi/2$ to 0 in increments of $\Delta\omega$, from which:

$$R = \cos\omega \tag{5.21}$$

To generate the Z grid, ω was taken from $-\pi/2$ to $\pi/2$ in increments of $\Delta\omega$, from which:

$$Z = 1 + \sin\omega \tag{5.22}$$

This procedure generates a grid of points that covers $0 \leq R \leq 1$ and $0 \leq Z \leq 2$. A similar method has been used to simulate conical electrodes[15] and hemispherical electrodes.[16] The grid spacing expands exponentially from the surface of the nanoparticle in both directions to the bulk solution boundaries as for the microdisc model.

Simulations are performed alternating direction implicit (ADI) discretisation[17,18] and solved using the tridiagonal Thomas algorithm.

5.2.4 Butler-Volmer Kinetics on a Curved Surface

For all of the other electrode systems encountered thus far, the electroactive surface has been parallel to one of the coordinates. Consequently, when applying the ADI discretisation method, the boundary condition at the points on the electrode surface (Butler-Volmer equation) need only be considered in the implicit direction of a sweep. However, for a curved surface in a rectangular coordinate system, the flux at each point on the electrode surface must necessarily be determined from the sum of the components in each of the orthogonal coordinates. In normalized coordinates, the flux to the surface of a sphere at a point at angle ω is:

$$J_\omega = \frac{\partial C}{\partial Z}\sin\omega + \frac{\partial C}{\partial R}\cos\omega \tag{5.23}$$

Consequently for each sweep in the ADI method, a term in one coordinate (the sweep direction) must be considered implicitly whilst that in the other coordinate must be considered explicitly. For the Z implicit sweep at timestep $k-\frac{1}{2}$:

$$\frac{\partial C^{k-\frac{1}{2}}}{\partial Z}\sin\phi = K^0\left[\exp(-\alpha\theta)C_{0,0}^{k-\frac{1}{2}} - \exp(\theta-\alpha\theta)(1-C_{0,0}^{k-\frac{1}{2}})\right] - \frac{\partial C^{k-1}}{\partial R}\cos\phi \tag{5.24}$$

where $C_{0,0}$ is the concentration at the given point on the spherical surface. In a discrete form, this is written as:

$$\begin{aligned}\left(C_{0,Z_1}^{k-\frac{1}{2}} - C_{0,0}^{k-\frac{1}{2}}\right)\sin\phi =& \Delta Z K^0\left[\exp(-\alpha\theta)C_{0,0}^{k-\frac{1}{2}} - \exp(\theta-\alpha\theta)(1-C_{0,0}^{k-\frac{1}{2}})\right] \\ &- \frac{\Delta Z}{\Delta R}\cos\phi\left(C_{0,R_1}^{k-1} - C_{0,0}^{k-1}\right)\end{aligned} \tag{5.25}$$

where C_{0,Z_1} is the concentration at the point adjacent to the surface point in the

Z direction (the implicit direction in this case) and $C_{R_1,0}$ is the point adjacent to the surface point in the R direction (the explicit direction). The value of ΔZ is the spacing between the two adjacent grid points (0, 0) and (0, Z_1) which, from Equation 5.22 is

$$\Delta Z = \sin(\omega + \Delta\omega) - \sin\omega \tag{5.26}$$

for a given value of ω. Likewise, the value of ΔR is the spacing between the two adjacent grid points (0, 0) and (R_1, 0) which, from Equation 5.21 is

$$\Delta R = \cos(\omega + \Delta\omega) - \cos\omega \qquad \text{for } \omega < 0 \tag{5.27}$$

$$\Delta R = \cos\omega - \cos(\omega - \Delta\omega) \qquad \text{for } \omega > 0 \tag{5.28}$$

Equation 5.25 may be rearranged into a more useful form:

$$\begin{aligned}\left[\frac{\sin\omega}{\Delta Z} + K^0\exp(-\alpha\theta) + K^0\exp(\theta-\alpha\theta)\right] C_{0,0}^{k-\frac{1}{2}} - \left[\frac{\sin\omega}{\Delta Z}\right] C_{0,Z_1}^{k-\frac{1}{2}} \\ - \left[K^0\exp(\theta-\alpha\theta) + \frac{C_{0,R_1}^{k-1} - C_{0,0}^{k-1}}{\Delta R}\cos\omega\right] = 0\end{aligned} \tag{5.29}$$

where the first two terms are implicit and the third is explicit. For the R implicit sweep, the equation is:

$$\begin{aligned}\left[\frac{\cos\omega}{\Delta R} + K^0\exp(-\alpha\theta) + K^0\exp(\theta-\alpha\theta)\right] C_{0,0}^{k} - \left[\frac{\cos\omega}{\Delta R}\right] C_{R_1,0}^{k} \\ - \left[K^0\exp(\theta-\alpha\theta) + \frac{C_{Z_1,0}^{k-\frac{1}{2}} - C_{0,0}^{k-\frac{1}{2}}}{\Delta Z}\sin\omega\right] = 0\end{aligned} \tag{5.30}$$

where again the first two terms are implicit and the third is explicit.

5.2.5 Current Calculations

For a free spherical particle that is not resting on a surface, the current measured at the electrode in amps, I, is

$$I = FAj \tag{5.31}$$

where F is the Faraday constant, A is the surface area of the electrode, and j is the flux of electroactive material through the electrode at a point on its surface, which is proportional to the concentration gradient of the material normal to the surface by Fick's first law. A spherical particle *on a surface* differs in behaviour from a free sphere since it is not uniformly accessible, therefore the material flux is not uniform across the surface. Consequently, the total flux must be determined by calculating the flux at each point on the surface and integrating over the surface.

As the simulation grid is rectangular, the dimensionless flux at each point on the particle surface, J_ω, is found by summing its components in the R and Z directions, according to Equation 5.23. At the end of each half-timestep (sweep), the component of the flux in the implicit direction is recorded (i.e., $\sin\omega \times \partial C/\partial Z$ is recorded after the Z sweep and $\cos\omega \times \partial C/\partial R$ is recorded after the R sweep) and J_ω is calculated at the end of each full timestep by summing the two components.

The total dimensionless current of the whole sphere, J, is then found by integrating J_ω over the particle surface:

$$J = \int_{-\pi/2}^{\pi/2} J_\omega \cos\omega \, d\omega \tag{5.32}$$

The relationship between J and the real current, I, is

$$I = \frac{2\pi F D c^*}{r_\mathrm{e}} J \tag{5.33}$$

where the factor 2π comes from integrating about angle ϕ.

5.2.6 Computation

A convergence study was run to determine optimum parameters for spatial and temporal grid densities which gave a good compromise between runtime and simulation accuracy. The simulations were converged to an accuracy of 0.2% relative to the analytical expression for steady state current (Equation 5.1). Typical simulation runtime was about 20 mins. In the present study the focus is on steady state voltammetry, and so it would be possible to perform the simulations in a non-time dependent manner. This was achieved by setting $\partial C/\partial T = 0$ in Equation 5.16 and

solving simultaneously over the whole space for a series of values of potential. While this approach is much less computationally demanding since time convergence is not an issue, a dynamic, slow scan rate linear voltammetric sweep was used for this study as this technology is more easily easily extended to non-steady state conditions for use in other work.

5.2.7 Isolated Spherical Particles

The behaviour of an isolated spherical microelectrode, i.e., one not heavily shielded a surface, which can be manufactured from gold for example,[19] has been extensively studied and is well understood.[20] An isolated sphere is theoretically equivalent to a hemispherical electrode on a surface except that the latter has exactly half the current response of the former. When linear sweep voltammetry (LSV) is performed at a sufficiently slow scan rate on a microelectrode, a sigmoidal, steady-state response is seen. Examples of simulated steady-state voltammetry for an isolated spherical electrode in the reversible and irreversible limits are shown in Figure 5.5. For an isolated spherical electrode, the limiting steady-state reduction current, I_{lim}, is given by:

$$I_{\mathrm{lim}} = 4\pi F D c_{\mathrm{A}}^{*} r_{\mathrm{e}} \tag{5.34}$$

Additionally, in the limit of fully irreversible electrode kinetics, the waveshape may be deduced from the equation:[20]

$$E = E_{\mathrm{f}}^{0} + \frac{RT}{\alpha F} \ln\left(\frac{r_{\mathrm{e}} k^{0}}{D}\right) + \frac{RT}{\alpha F} \ln\left(\frac{I_{\mathrm{lim}} - I}{I}\right) \tag{5.35}$$

It is convenient to present this and many of the equations in the following work in a normalised form. Though these transformations are largely the same as those used to normalise the numerical model for simulation purposes, their use here is presentational and unrelated to the numerical implementation. The normalised current, potential, and rate constant are defined respectively as:

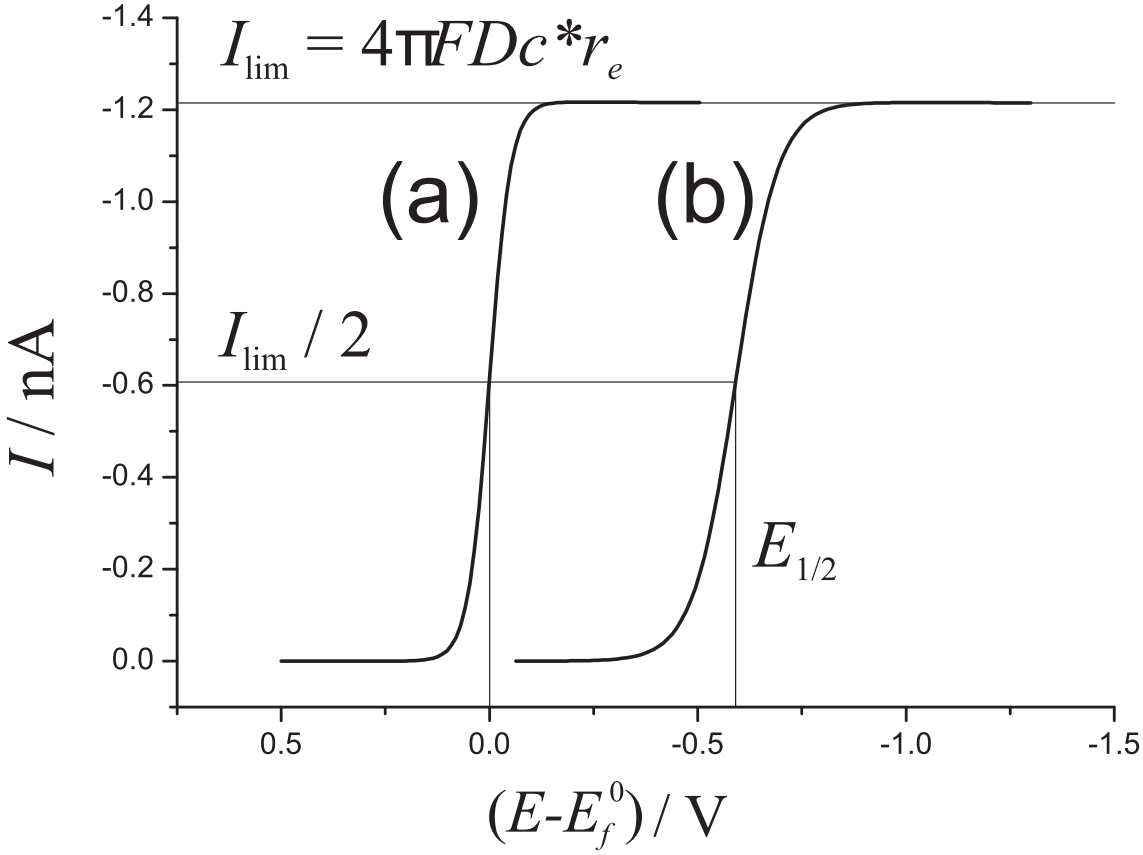

Figure 5.5: *Simulated LSVs of an isolated spherical particle with* $r_e = 100$ *nm,* $c_A = 10$ *mM,* $D_A = D_B = 10^{-5}$ cm^2 s^{-1} *and* $\alpha = 0.5$*. (a) Fully reversible system with* $k^0 = 10$ *cm* s^{-1} *(Notice that* $E_{1/2} = 0$*); (b) Fully irreversible system with* $k^0 = 10^{-5}$ *cm* s^{-1}*.*

$$J = \frac{I}{I_{lim}} \tag{5.36}$$

$$\theta = \frac{F}{RT}(E - E_f^0) \tag{5.37}$$

$$K^0 = \frac{k^0 r_e}{D} \tag{5.38}$$

Note that the limiting dimensionless current is therefore necessarily $J_{lim} = 1$. From Equation 5.35 the normalised current-potential relationship is:

$$J = \frac{K^0}{K^0 + e^{\alpha\theta}} \tag{5.39}$$

The half-wave potential, $E_{1/2}$, of a steady-state voltammogram is the potential at which a current equal to half the limiting current (as defined in Equation 5.34) is passed. By setting $I = I_{lim}/2$ in Equation 5.35, it is seen that:

$$E_{1/2} = E_f^0 + \frac{RT}{\alpha F} \ln\left(\frac{r_e k^0}{D_A}\right) \tag{5.40}$$

or equivalently,

$$\theta_{1/2} = \frac{\ln K^0}{\alpha} \tag{5.41}$$

where $\theta_{1/2} = (F/RT)(E_{1/2} - E_f^0)$. From Equation 5.39, it is clear that the waveshape is dependent only on the parameters K^0 and α. Since $K^0 = k^0 r_e/D$, increasing k^0 by a constant factor has exactly the same effect on $E_{1/2}$ as either increasing the radius, r_e, or decreasing the diffusion coefficient, D, by the same factor.

5.3 Results and Discussion

The limiting steady-state current for a spherical particle on a surface is:[3]

$$I_{lim} = 4\pi \ln(2) F D c^* r_e \tag{5.42}$$

A large number of simulations were performed by varying the parameters α, in the range 0.3–0.7, and K^0, in the range 10^{-12}–1. Examples of the simulated voltammetry are shown in Figure 5.6. For fixed values of α, the variation of the dimensionless half-wave potential, $\theta_{1/2}$, with the dimensionless rate constant, K^0, was studied. By plotting $\theta_{1/2}$ against $\log K^0$ and fitting the data as shown in Figure 5.7, it was found that in the irreversible limit:

$$\theta_{1/2} = \frac{\ln K^0}{\alpha} + \lambda \tag{5.43}$$

where λ is observed to be some function of α but is independent of K^0. By plotting λ against α and fitting this curve, it was determined that to a good approximation:

$$\lambda = -\frac{\ln(\ln(2))}{\alpha} \tag{5.44}$$

as shown in Figure 5.8, therefore,

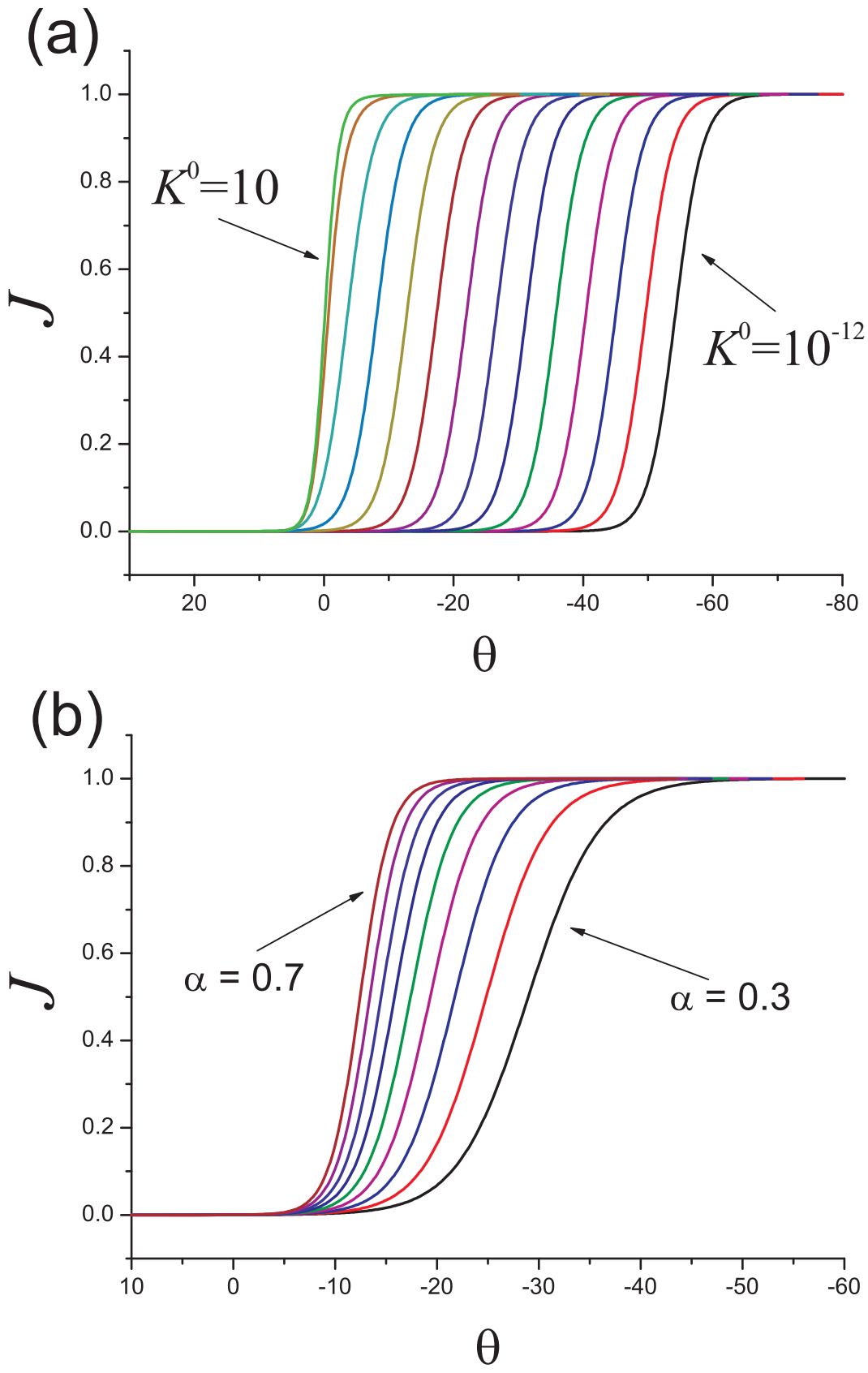

Figure 5.6: *Steady-state LSVs of a spherical particle on a surface. (a) Variation with dimensionless rate constant K^0 for $\alpha = 0.5$; (b) variation with α for $K^0 = 10^{-4}$.*

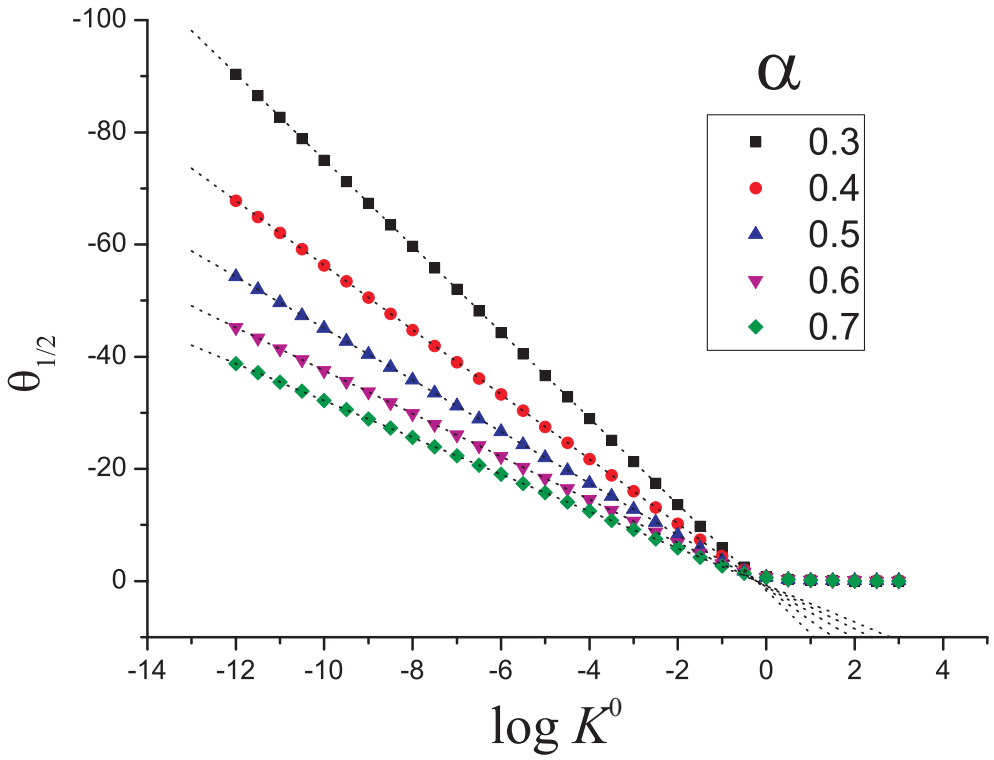

Figure 5.7: *Variation of half-wave potential, $\theta_{1/2}$, with K^0 for a range of values of α. Symbols indicate the simulated results, and dotted lines correspond to Equation 5.45*

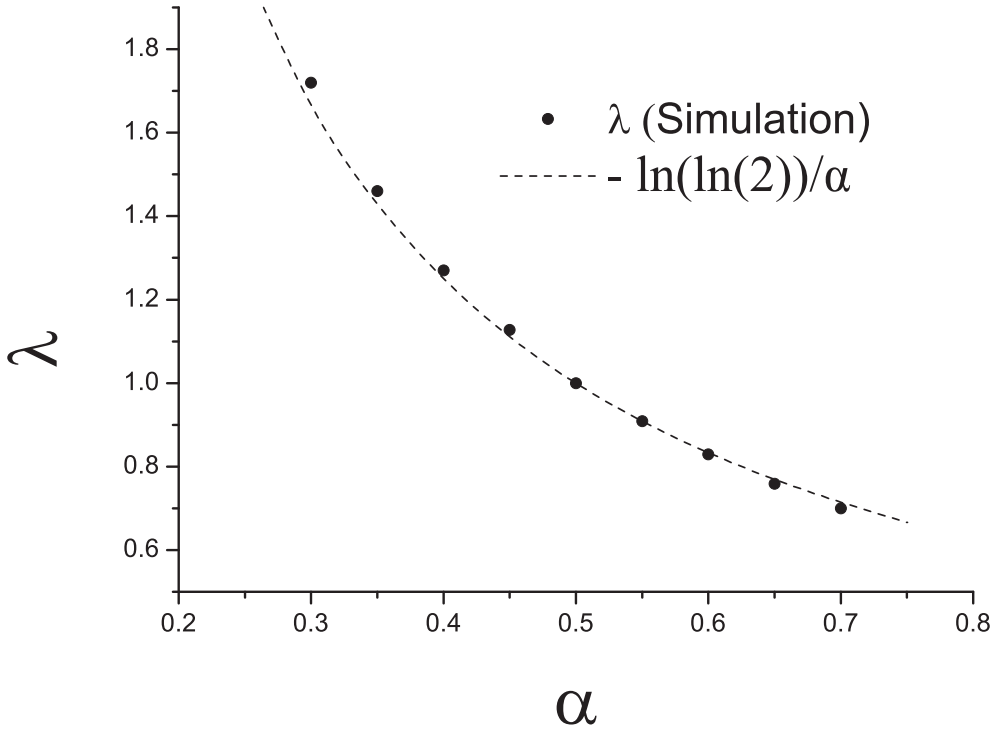

Figure 5.8: *Variation of the λ term in Equation 5.43 with α.*

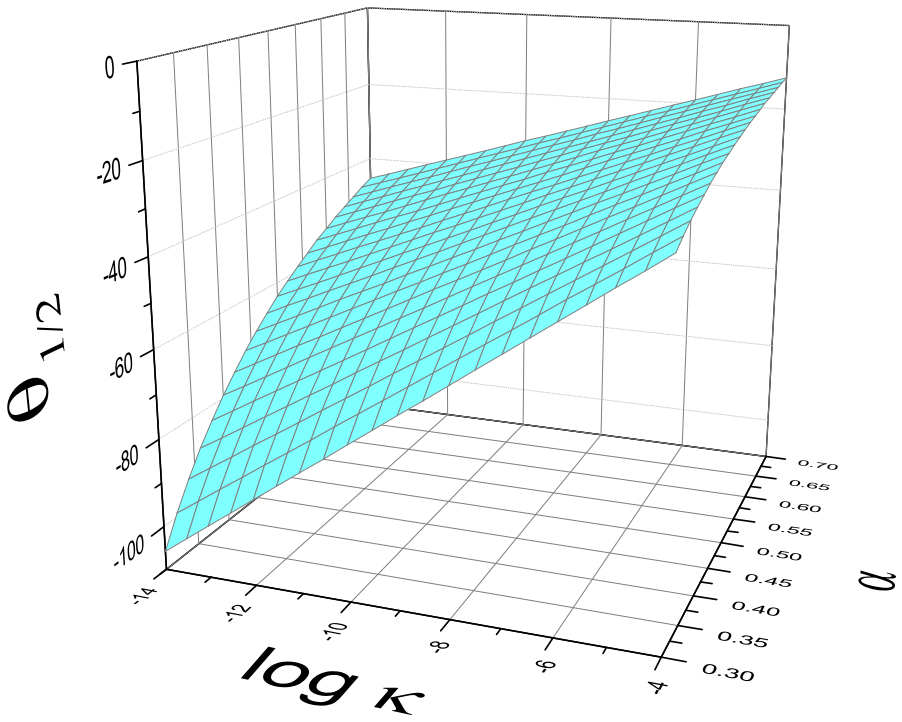

Figure 5.9: *Variation of half-wave potential, $\theta_{1/2}$, with α and K^0, according to Equation 5.45*

$$\theta_{1/2} = \frac{\ln K^0}{\alpha} - \frac{\ln(\ln 2)}{\alpha} = \frac{1}{\alpha} \ln\left(\frac{K^0}{\ln(2)}\right) \tag{5.45}$$

Figure 5.9 shows a graphical representation of this relation. Figure 5.10 displays the percentage error of this equation as a function of α and K^0 in the irreversible region. The error tends to be greater for larger K^0 and smaller α, but is never greater than 0.25% in the whole region, well within typical experimental accuracy. The real half-wave potential, $E_{1/2}$, is therefore:

$$E_{1/2} = E_f^0 + \frac{RT}{\alpha F} \ln\left(\frac{r_e k^0}{D_A}\right) - \frac{RT}{\alpha F} \ln(\ln(2)) \tag{5.46}$$

From this, and the discussion of isolated spherical particles in Section 5.2.7, it can be inferred that in the limit of irreversible kinetics, the waveshape is described by:

$$E = E_f^0 + \frac{RT}{\alpha F} \ln\left(\frac{r_e k^0}{D}\right) + \frac{RT}{\alpha F} \ln\left(\frac{I_{\lim} - I}{I}\right) - \frac{RT}{\alpha F} \ln(\ln(2)) \tag{5.47}$$

By rearranging, the dimensionless current is given directly by:

$$J = \frac{K^0}{K^0 + \exp(\alpha\theta)\ln(2)} \tag{5.48}$$

Figure 5.11 shows the results of several simulations with varying values of α and k^0 compared with the waveshape predicted by this equation. It can be seen that there is extremely good agreement between simulation and expression, observed in all cases. The dimensioned current is therefore described by:

$$I = \frac{4\pi\ln(2)FDc_{\mathrm{A}}r_{\mathrm{e}}^2k^0}{k^0r_{\mathrm{e}} + D\exp\left((\alpha F/RT)(E - E_f^0)\right)\ln(2)} \tag{5.49}$$

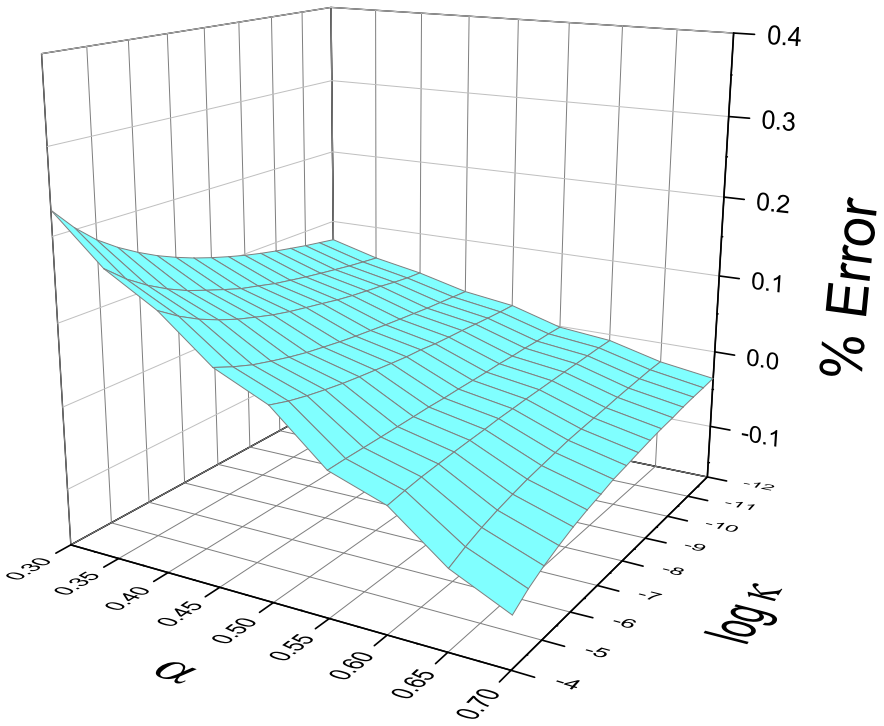

Figure 5.10: *Percentage error of Equation 5.45 defined as* 100%×*(Expression-Simulated Result)/Simulated Result*

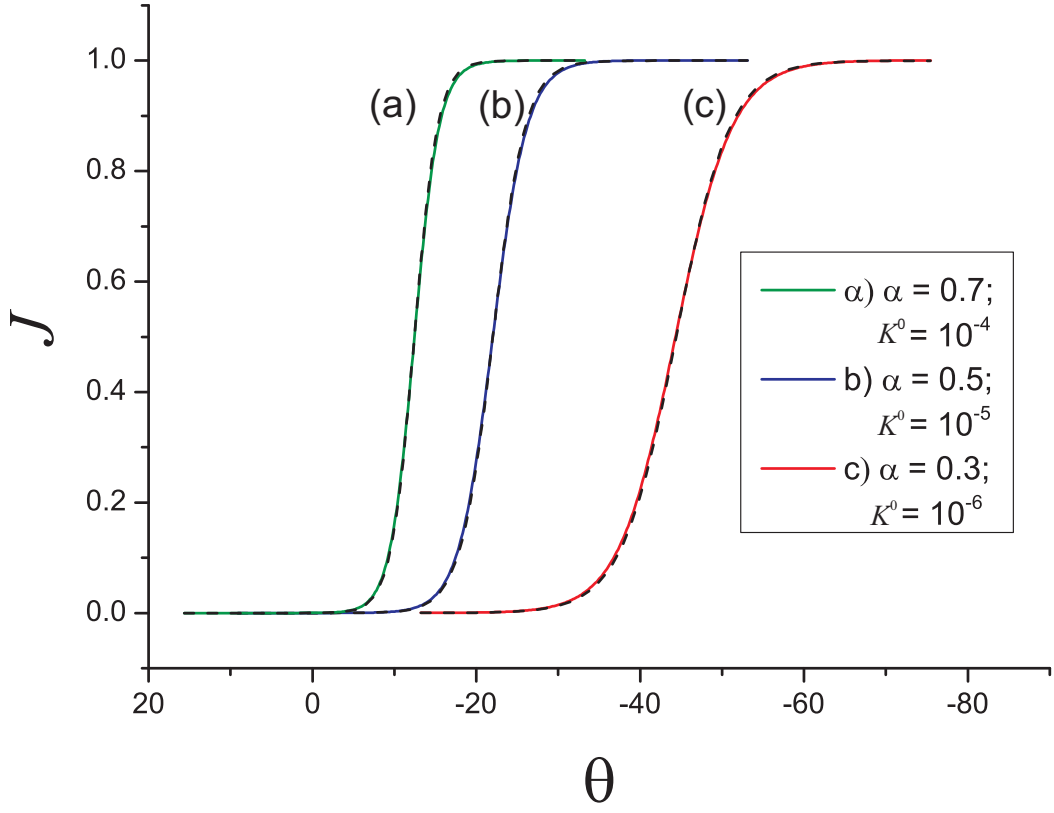

Figure 5.11: *LSVs of spherical particles on a surface: agreement between the results of simulation (coloured lines) and the predictions of Equation 5.48 (dashed lines).*

5.3.1 Mapping of 'Isolated Particle' to 'Particle on a Surface'

Since the only difference between Equations 5.35 and 5.47, is the constant term $-\ln(\ln(2))(RT/\alpha F)$, there exists a simple procedure to transform the observed steady-state voltammetry of an isolated spherical particle into the voltammetry that is observed if the same particle is placed on a supporting surface. First, the voltammogram is scaled in the I direction according to the ratio of the limiting currents of the two electrodes:

$$\frac{I_{\text{lim, surface}}}{I_{\text{lim, iso}}} = \frac{4\pi \ln(2) nFDc^{*}r_{\text{e}}}{4\pi nFDc^{*}r_{\text{e}}} = \ln 2 = 0.69315 \tag{5.50}$$

Second, the whole voltammogram is translated by $9.41/\alpha$ mV ($= 18.82$ mV if $\alpha = 0.5$ and $T = 298$ K) in the positive direction on the E axis.

As the electrode kinetics are in the irreversible limit, this translation may be

achieved either by increasing E_f^0 by $\ln(\ln(2))(RT/\alpha F)$ mV *or* by increasing the rate constant, K^0, by a constant factor. The value of this constant factor can be determined by equating the equations for the dimensionless half wave potential, Equations 5.41 and 5.45, setting different (dimensionless) rate constants, K_i^0 and K_s^0 for the isolated and surface-bound particles respectively:

$$\frac{\ln K_s^0}{\alpha} - \frac{\ln(\ln(2))}{\alpha} = \frac{\ln K_i^0}{\alpha} \tag{5.51}$$

hence,

$$K_i^0 = \frac{K_s^0}{\ln(2)} \tag{5.52}$$

Consequently, for the purposes of steady state voltammetry, a spherical particle on a surface may be easily and conveniently modelled by simulating an isolated spherical particle with 0.693× the normal reactant concentration and by either increasing E_f^0 by $\ln(\ln(2))(RT/\alpha F)$ (= 18.82 mV if $\alpha = 0.5$ $T = 298$ K) or by increasing the rate constant, k^0, by a factor of $1/\ln(2) = 1.443$. Such modelling may be performed on any commercially available simulation package, such as Digisim.

5.4 Conclusions

An expression that completely describes the steady-state current response of an electroactive spherical particle on a surface in the irreversible limit has been presented along with an expression for the half-wave potential under the same conditions. Further, a mapping between the voltammetry of an isolated spherical particle and that of a particle on a surface has been established. It is hoped that this work will make possible the extraction of kinetic parameters from voltammetry of single nanoparticles on a surface, which is particularly important in the search for nano-electrocatalytic effects.

Bibliography

[1] J. M. Kahk, N. V. Rees, J. Pillay, R. Tshikhudo, S. Vilakazi and R. G. Compton, *Nano Today*, 2012, **7**, 174–179.

[2] K. R. Ward, N. S. Lawrence, R. S. Hartshorne and R. G. Compton, *J. Electroanal. Chem.*, 2012, **683**, 37–42.

[3] P. A. Bobbert, M. M. Wind and J. Vlieger, *Phys. A (Amsterdam, Neth.)*, 1987, **146A**, 69–88.

[4] I. Streeter and R. G. Compton, *J. Phys. Chem. C*, 2007, **111**, 18049–18054.

[5] I. Streeter, R. Baron and R. G. Compton, *J. Phys. Chem. C*, 2007, **111**, 17008–17014.

[6] S. R. Belding and R. G. Compton, *J. Phys. Chem. C*, 2010, **114**, 8309–8319.

[7] X. Xiao and A. J. Bard, *J. Am. Chem. Soc.*, 2007, **129**, 9610–9612.

[8] X. Xiao, F.-R. F. Fan, J. Zhou and A. J. Bard, *J. Am. Chem. Soc.*, 2008, **130**, 16669–16677.

[9] S. J. Kwon, F.-R. F. Fan and A. J. Bard, *J. Am. Chem. Soc.*, 2010, **132**, 13165–13167.

[10] E. J. E. Stuart, N. V. Rees and R. G. Compton, *Chem. Phys. Lett.*, 2012, **531**, 94–97.

[11] X. Xiao, S. Pan, J. S. Jang, F.-R. F. Fan and A. J. Bard, *J. Phys. Chem. C*, 2009, **113**, 14978–14982.

[12] F. W. Campbell and R. G. Compton, *Anal. Bioanal. Chem.*, 2010, **396**, 241–259.

[13] S. G. Mairanovsky and M. B. Neiman, *Russ. Chem. Bull.*, 1955, **4**, 373–376.

[14] A. Einstein, *Ann. Phys.*, 1905, **17**, 549–560.

[15] E. J. F. Dickinson, I. Streeter and R. G. Compton, *J. Phys. Chem. C*, 2008, **112**, 11637–11644.

[16] K. R. Ward, N. S. Lawrence, R. S. Hartshorne and R. G. Compton, *J. Phys. Chem. C*, 2011, **115**, 11204–11215.

[17] D. Britz, *Digital Simulation in Electrochemistry, Third Edition.*, Springer, Heidelberg, Germany, 2005.

[18] W. H. Press, S. A. Teukolsky, W. T. Vetterling and B. P. Flannery, *Numerical Recipes*, Cambridge University Press, Cambridge, 3rd edn., 2007.

[19] C. Demaille, M. Brust, M. Tsionsky and A. J. Bard, *Anal. Chem.*, 1997, **69**, 2323–2328.

[20] A. J. Bard and L. R. Faulkner, *Electrochemical Methods: Fundamentals and Applications.*, John Wiley & Sons, New York, 2nd edn., 2001.

Chapter 6

The EC′ Mechanism at Hemispherical Electrodes

In this chapter, the EC′ (catalytic) mechanism,

$$\mathrm{A} \rightleftharpoons \mathrm{B} + \mathrm{e}^- \tag{6.1}$$

$$\mathrm{B} + \mathrm{X} \xrightarrow{k_2} \mathrm{A} + \mathrm{P} \tag{6.2}$$

is studied at a regularly distributed array of hemispherical particles on a planar surface using cyclic voltammetry. It is assumed that the supporting surface itself is not electroactive and therefore that the heterogeneous electron transfer in occurs exclusively on the surface of the particles. Simulations have been performed for a range of scan rates, particle surface coverages, and heterogeneous reaction rate constants. Additionally, for the case of an isolated particle, the effect of the concentration of reactant species 'X' has also been examined. Particular attention is paid to the 'split-wave' phenomenon, where two peaks are observed in the forward scan of a cyclic voltammogram, which tends to occur when the initial concentrations of A and X are similar and the homogeneous rate constant is relatively high. The conditions under which two peaks are resolvable are elucidated and expressions are presented for the first peak current and potential for the case of an isolated particle.

The work constituting this chapter has been published in the *Journal of Physical Chemistry C*.[1]

6.1 Introduction

6.1.1 The EC′ Mechanism

The EC′ (catalytic) mechanism is a two-step electron transfer process illustrated schematically in Figure 6.1. The net result of the process is the transformation of reactant species X to product species P, catalysed by species A which is itself regenerated. This form of 'catalysis' is distinct from the usage of the word in its usual electrochemical sense wherein the electrode catalyses the electron transfer such as in Process 6.1; rather in this case, the A/B redox couple catalyses the transformation of X to P. The second step, Process 6.2, is a bimolecular homogeneous reaction and as such has a second order rate constant, k_2 that is typically expressed in units of $\mathrm{dm^3\ mol^{-1}\ s^{-1}}$.

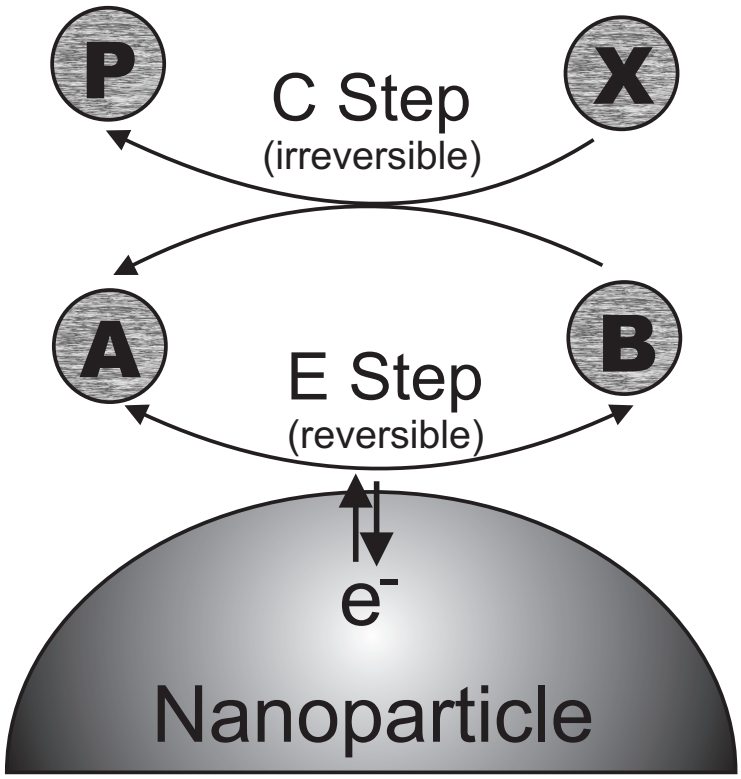

Figure 6.1: *Schematic of the EC′ catalytic reaction mechanism.*

An exemplar EC′ reaction is the oxidation of cysteine to cystine:[2]

$$\mathrm{Fe(CN)_6^{4-}} \rightleftharpoons \mathrm{Fe(CN)_6^{3-}} + e^- \tag{6.3}$$

$$\mathrm{Fe(CN)_6^{3-}} + \text{cysteine} \xrightarrow{k_2} \mathrm{Fe(CN)_6^{4-}} + \text{cystine} \tag{6.4}$$

The same redox couple also has potential applications in gas sensing, for example of H_2S.[3]

It is known that under certain conditions, a cyclic voltammogram of an EC′ system will show two distinct peaks in the forward sweep.[2] This typically occurs when the initial concentrations of species A and species X are similar and when the second order rate constant, k_2, is above a certain value. Figures 6.2 and 6.3 (a) show the progression of cyclic voltammograms that result when the initial concentrations of A and X are the same and and k_2 is increased, keeping all other parameters constant. For low k_2, the voltammetry is similar to that observed for a simple one-electron reduction (the E mechanism), as expected, however as the the rate constant increases, so too does peak current response. The explanation is as follows: a faster rate constant means a more rapid regeneration of A within the diffusion layer and hence greater current. As k_2 is increased further, the waveform begins to split into two distinct peaks, with greater k_2 resulting in a more obvious separation. For a fast scan rate this also leads to a decrease in peak height with increasing peak-to-peak separation (Figure 6.2), although the peak currents tend to limiting values as k_2 increases and the peaks become more distinct. From Figure 6.3, it can be seen that even though the heights of both forward peaks decrease slightly with increasing k_2, the integrated current in the forward sweep still increases.

In the past, some attention has been given to the problem of simulating the EC′ mechanism, though often using the simplifying assumption that the chemical step is pseudo-first order, i.e., that species X is present in large excess, and a few studies have examined the split-wave phenomenon. Simple one-dimensional systems such as planar macroelectrodes or isolated spherical electrodes, have been considered[4,5] and such simulations may easily be performed on commercially available software packages such as Digisim.[6] Some characterisation of the reaction at more complex electrode geometries such as the microdisc[7] has also been reported.

A series of papers by Savéant et al.[8–13] examining the 'Homogeneous Catalysis of Electrochemical Reactions', explored systems similar to the EC′ mechanism described herein and noted the appearance of split polarographic waves resulting from a high second order rate constant in experiment.[11] Following this, Fischer

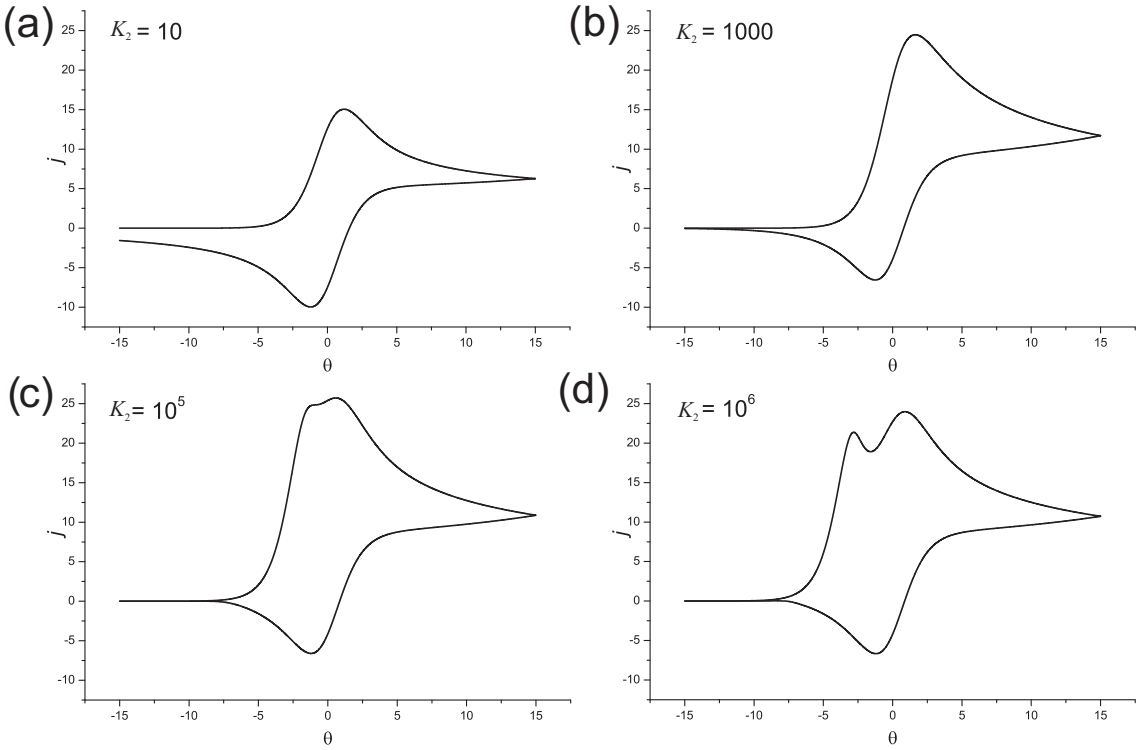

Figure 6.2: *Cyclic voltammograms for an isolated system with* $\sigma = 1000$*;* $C_X = 1$*; and a variety of rate constants,* K_2 *(see Section 6.3.1 for definitions).*

et al. studied the EC′ mechanism theoretically and experimentally at the channel electrode[14,15] and at the rotating-disc electrode.[16–18] Additionally, Dimarco et al.[4] studied the second order EC′ reaction on a planar surface in some detail, providing insight into the appearance of split-wave voltammetry.

The purpose of this chapter is to examine the EC′ mechanism in detail both at isolated hemispherical particles and arrays of such particles, and to explore the split-wave phenomenon by characterising the observed cyclic voltammetric behaviour for a range of rate constants and particle surface coverages.

6.1.2 Arrays of Micro- and Nano-Particles

Throughout this study, it is assumed that the supporting surface itself is not electroactive for the range of potentials studied and therefore that heterogeneous electron transfer occurs exclusively on the surface of the particles. The arrays are modelled using the well established diffusion domain approximation[19,20] (see 2.8.1).

Electrodes modified with particles with radii in the micrometer range can dis-

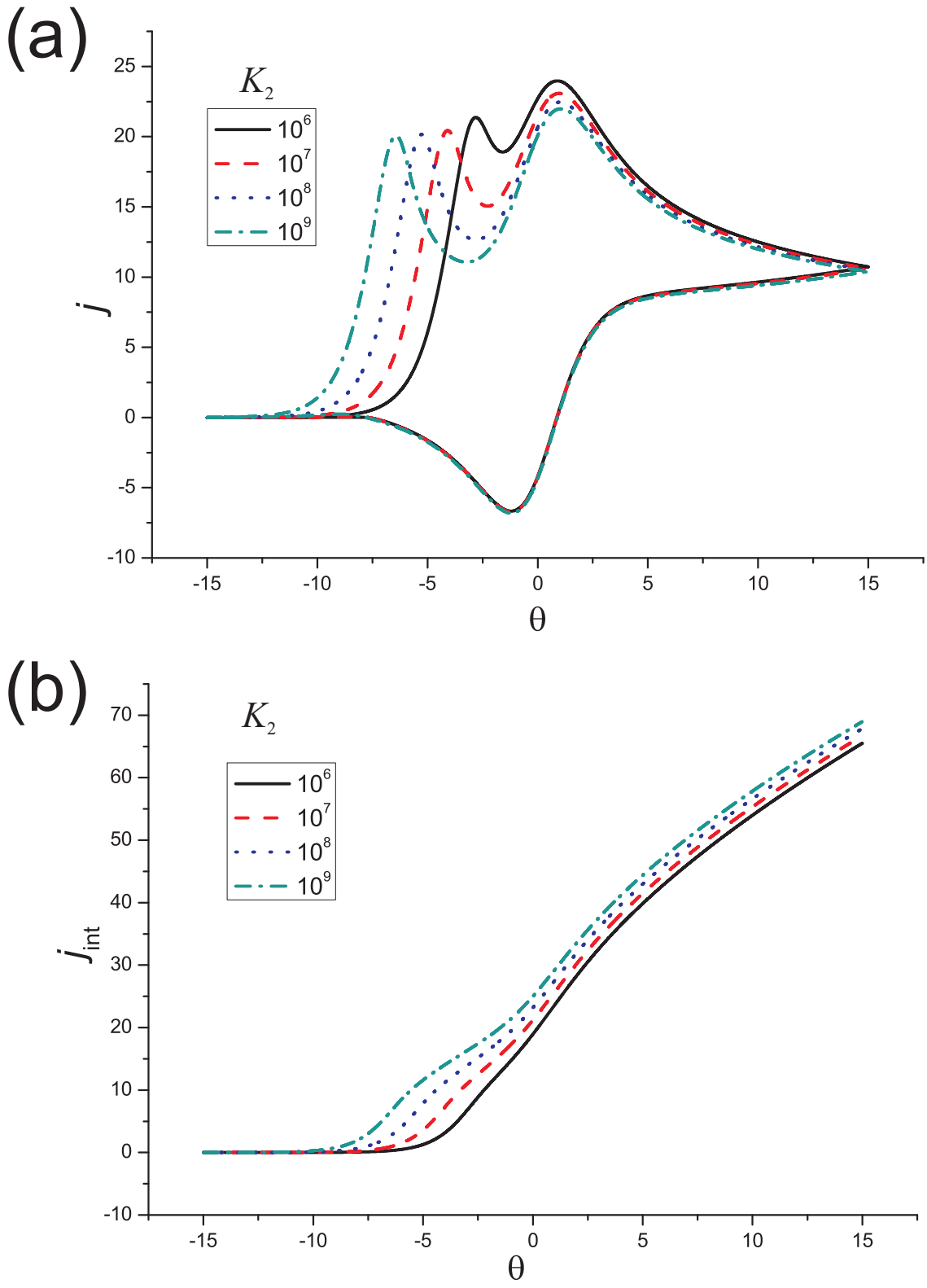

Figure 6.3: *a) Cyclic voltammograms for an isolated system with* $\sigma = 1000$*;* $C_X = 1$*; and a variety of rate constants,* K_2*; b) integrated current response for the same (see Section 6.3.1 for definitions).*

play a number of well documented[21,22] experimentally useful properties that are not observed in the bulk material, including enhanced signal-to-noise ratio, suppression of charging current, and enhanced mass transport effects arising from the convergent nature of diffusion to microparticles.[21,22] These benefits can be expected to be achieved to an even greater extent with particles in the nanometer range.[23] A detailed review of the properties and uses of nanoparticles in relation to electroanalysis was given by Welch[24] and has been updated by Campbell.[25] In addition, Compton et al. have presented an overview[26] of the design, fabrication, characterisation and applications of *arrays* of nanoelectrodes.

Because of the high rate of mass transport to the individual particles, well separated micro- and nano-particles can display a high sensitivity[25] and electrodes modified with sparse distributions of nanoparticles are often used for this reason. Conversely, for arrays of micro- and nano-particles that are somewhat denser, the current response approximates that observed for a macro electrode of the same total geometric area[27,28] despite only partial coverage by electroactive material. This allows expensive catalytic materials (gold, platinum, etc.) to be used more sparingly while still achieving the same experimental results, thus lowering the electrode cost.[24]

Recently, with regards to simulation of such systems, Davies et al. have examined the voltammetry of regular[29] and random[30] distributions of microdisc electrodes; Streeter has investigated the diffusion limited current to isolated nanoparticles of a variety of geometries;[31] and Belding has explored the problem of randomly distributed arrays of disc[32] and spherical nanoparticles.[27] This chapter aims to extend the existing knowledge in this field through a detailed examination of a more complicated electrochemical reaction, namely the electrocatalytic reaction.

6.2 Theoretical Model

6.2.1 Mathematical Model

The development of a mathematical model for simulation of an array of hemispherical particles draws on elements of the model developed for an array of microdisc

electrodes (described in Chapters 2 and 3 and utilised in Chapter 4), and of that for a spherical particle (described and utilised in Chapter 5) and also requires the introduction of some new techniques and concepts. As with the microdisc and the sphere, the hemisphere array is most appropriately described in a cylindrical polar coordinate system, (r, z, ϕ), as shown in Figure 6.4. It is cylindrically symmetrical, allowing its representation to be reduced to two spatial dimensions, r, and z since:

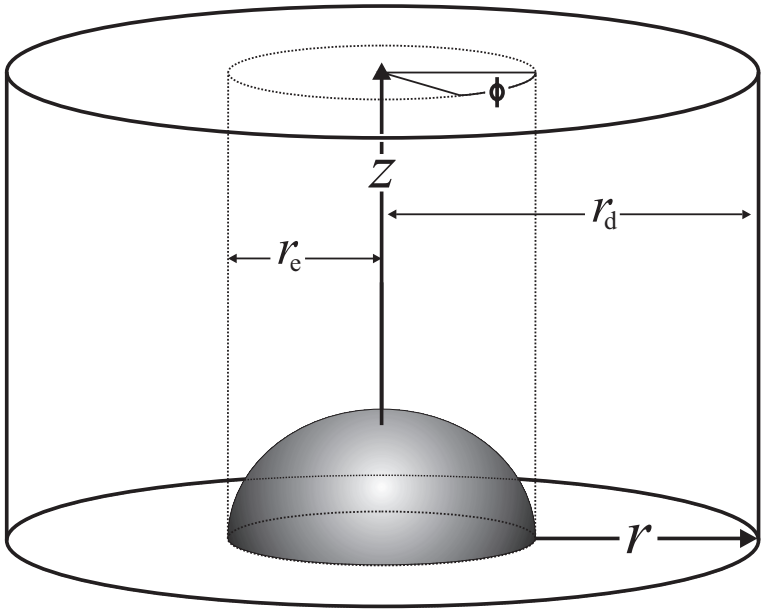

Figure 6.4: *Unit cell for an array of hemispherical electrodes with particle radius,* r_e*, and domain radius,* r_d*.*

$$\frac{\partial c}{\partial \phi} = \frac{\partial^2 c}{\partial \phi^2} = 0 \tag{6.5}$$

In this study, both isolated hemispheres and arrays of hemispheres are studied. An isolated hemisphere can be modelled in a one-dimensional spherical polar coordinate system, with a single coordinate, r, which is the distance normal to the surface. However, the mathematical model for an array of hemispheres may also be used (although somewhat less efficiently) to model an isolated hemisphere and so it is the array model that is focused on here.

In the case of an array, as illustrated in Figure 6.5, it is assumed that there are many hemispheres each with radius r_e, regularly distributed over the supporting surface such that the centre-to-centre separation between neighbouring hemispheres, d, is constant. As a result, each hemisphere is assumed to sit in an identical envi-

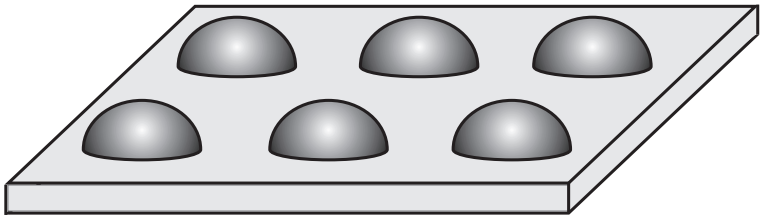

Figure 6.5: *Regularly distributed hemispherical particles on a planar supporting surface*

ronment, and therefore the diffusion domain approximation may be used (Section 2.8.1), allowing the reduction to two spatial dimensions even in the case of an array.

Mass transport of species s is governed by the diffusion equation in two-dimensional cylindrical polar coordinates:

$$\frac{\partial c_s}{\partial t} = D\left(\frac{\partial^2 c_s}{\partial r^2} + \frac{1}{r}\frac{\partial c_s}{\partial r} + \frac{\partial^2 c_s}{\partial z^2}\right) \tag{6.6}$$

assuming a large excess of inert supporting electrolyte such that migratory contributions to mass transport are negligible. It is assumed that the diffusion coefficient D, is the same for all chemical species. There are four chemical species present in the system, A, B, X, and P, each of which participates in the homogeneous reaction step (Process 6.2). This requires the modification of Equation 6.6 to account for changes in concentration caused by the reaction. The reaction proceeds at a rate equal to $k_2 c_\mathrm{B} c_\mathrm{X}$, therefore the complete mass transport equations for each species are as follows:

$$\frac{\partial c_\mathrm{A}}{\partial t} = D\left(\frac{\partial^2 c_\mathrm{A}}{\partial r^2} + \frac{1}{r}\frac{\partial c_\mathrm{A}}{\partial r} + \frac{\partial^2 c_\mathrm{A}}{\partial z^2}\right) + k_2 c_\mathrm{B} c_\mathrm{X} \tag{6.7}$$

$$\frac{\partial c_\mathrm{B}}{\partial t} = D\left(\frac{\partial^2 c_\mathrm{B}}{\partial r^2} + \frac{1}{r}\frac{\partial c_\mathrm{B}}{\partial r} + \frac{\partial^2 c_\mathrm{B}}{\partial z^2}\right) - k_2 c_\mathrm{B} c_\mathrm{X} \tag{6.8}$$

$$\frac{\partial c_\mathrm{X}}{\partial t} = D\left(\frac{\partial^2 c_\mathrm{X}}{\partial r^2} + \frac{1}{r}\frac{\partial c_\mathrm{X}}{\partial r} + \frac{\partial^2 c_\mathrm{X}}{\partial z^2}\right) - k_2 c_\mathrm{B} c_\mathrm{X} \tag{6.9}$$

$$\frac{\partial c_\mathrm{P}}{\partial t} = D\left(\frac{\partial^2 c_\mathrm{P}}{\partial r^2} + \frac{1}{r}\frac{\partial c_\mathrm{P}}{\partial r} + \frac{\partial^2 c_\mathrm{P}}{\partial z^2}\right) + k_2 c_\mathrm{B} c_\mathrm{X} \tag{6.10}$$

The simulation space for a hemisphere including all of its boundary conditions is illustrated in Figure 6.6. At the start of each experiment, it is assumed that the concentration of each chemical species, s, is uniform across the whole space and

equal to its bulk value, c_{s}^{*}. Note that while c_{A}^{*} and c_{X}^{*} may have arbitrary, non-zero values, it is always the case that $c_{\mathrm{B}}^{*} = c_{\mathrm{P}}^{*} = 0$.

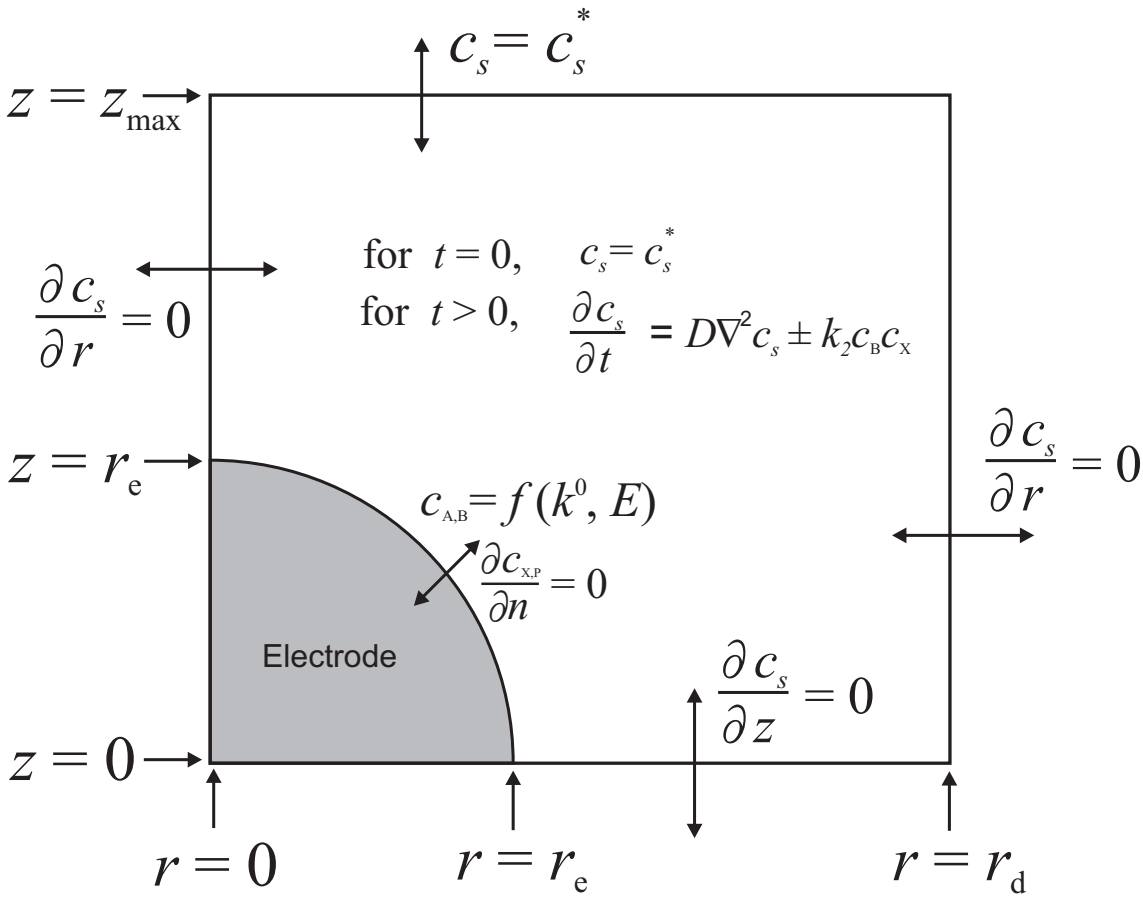

Figure 6.6: *Simulation space for an array of hemispherical electrodes with the EC′ mechanism.*

It is supposed that the solution extends infinitely in the z direction, and so the space continues up to a distance where no reaction at the electrode can have any effect on the concentration on the experimental timescale. This distance is called $z_{\max}$ and is equal to:

$$z_{\max} = r_{\mathrm{e}} + 6\sqrt{Dt} \tag{6.11}$$

For every chemical species, there are conditions of no flux at the domain boundary ($r = r_{\mathrm{d}}$), the axial boundary ($r = 0$) and at the inactive solid surface ($z = 0$):

$$\left.\frac{\partial c_s}{\partial r}\right|_{r=r_\mathrm{d}} = 0 \tag{6.12}$$

$$\left.\frac{\partial c_s}{\partial r}\right|_{r=0} = 0 \tag{6.13}$$

$$\left.\frac{\partial c_s}{\partial z}\right|_{z=0} = 0 \tag{6.14}$$

The electrode surface is defined by thee set of r, z points that satisfy the equation:

$$r^2 + z^2 = r_\mathrm{e}^2 \tag{6.15}$$

where r, $z \geq 0$. The flux, j_0, of species A perpendicular to the electrode surface at each point on the surface is given by the Butler-Volmer equation:

$$j_0 = D\frac{\partial c_\mathrm{A}}{\partial n} = k^0\left[\exp\left(\frac{-\alpha F(E-E_f^0)}{RT}\right)c_{\mathrm{A},0} - \exp\left(\frac{(1-\alpha)F(E-E_f^0)}{RT}\right)c_{\mathrm{B},0}\right] \tag{6.16}$$

where $c_{\mathrm{A},0}$ and $c_{\mathrm{B},0}$ are the concentrations of species A and B at the electrode surface and n is some coordinate normal to the electrode surface. In all cases, it is assumed that the heterogeneous electron transfer is fully reversible, such that k^0 is large. In terms of the cylindrical polar coordinate system:

$$\frac{\partial c}{\partial n} = \frac{\partial c}{\partial z}\sin\omega + \frac{\partial c}{\partial r}\cos\omega \tag{6.17}$$

Species X and P are not electroactive under the potential range studied in the experiment and so experience a condition of no flux at the electrode surface:

$$\frac{\partial c}{\partial n} = 0 \tag{6.18}$$

6.2.2 Simulation Procedure

The mathematical model is normalized according to the same set of dimensionless transformations that were used for the sphere model in Section 5.2.2. There is one additional parameter in this model: the second order rate constant, k_2. The dimensionless second order rate constant, K_2, is defined as

$$K_2 = \frac{c_{\mathrm{A}}^* r_{\mathrm{e}}^2}{D} \tag{6.19}$$

The mass transport equation for species s in normalized units is therefore:

$$\frac{\partial C_s}{\partial T} = D\left(\frac{\partial^2 C_s}{\partial R^2} + \frac{1}{R}\frac{\partial C_s}{\partial R} + \frac{\partial^2 C_s}{\partial Z^2}\right) \pm K_2 C_{\mathrm{B}} C_{\mathrm{X}} \tag{6.20}$$

where,

$$C_s = \frac{c_s}{c_{\mathrm{A}}^*} \tag{6.21}$$

The Butler–Volmer boundary conditions are implemented in exactly the same manner as described for spherical particles in Section 5.2.4.

The procedure for generating a discrete spatial grid for use with a hemispherical particle (as shown in Figure 6.7) is similar to that employed in Chapter 5 for a spherical one. In the normalized (R, Z) coordinate system, the surface of the particle is described by:

$$R^2 + Z^2 = 1 \tag{6.22}$$

the distribution of spatial points in the region of the particle's surface is specified such that the points exactly fit to the particle surface. The quarter-circle profile of the hemisphere is divided into a series of angular increments, $\Delta\omega$, and then the values of R and Z are calculated at successive values of ω, where ω is the angle formed between a line that intersects the origin, and the R axis. For a given point on the particle's surface:

$$R = \sin\omega \tag{6.23}$$

$$Z = \cos\omega \tag{6.24}$$

The result is that the spacing between neighbouring points decreases when moving from $R = 0$ to $R = 1$, as demonstrated in Figure 6.8, and likewise for Z.

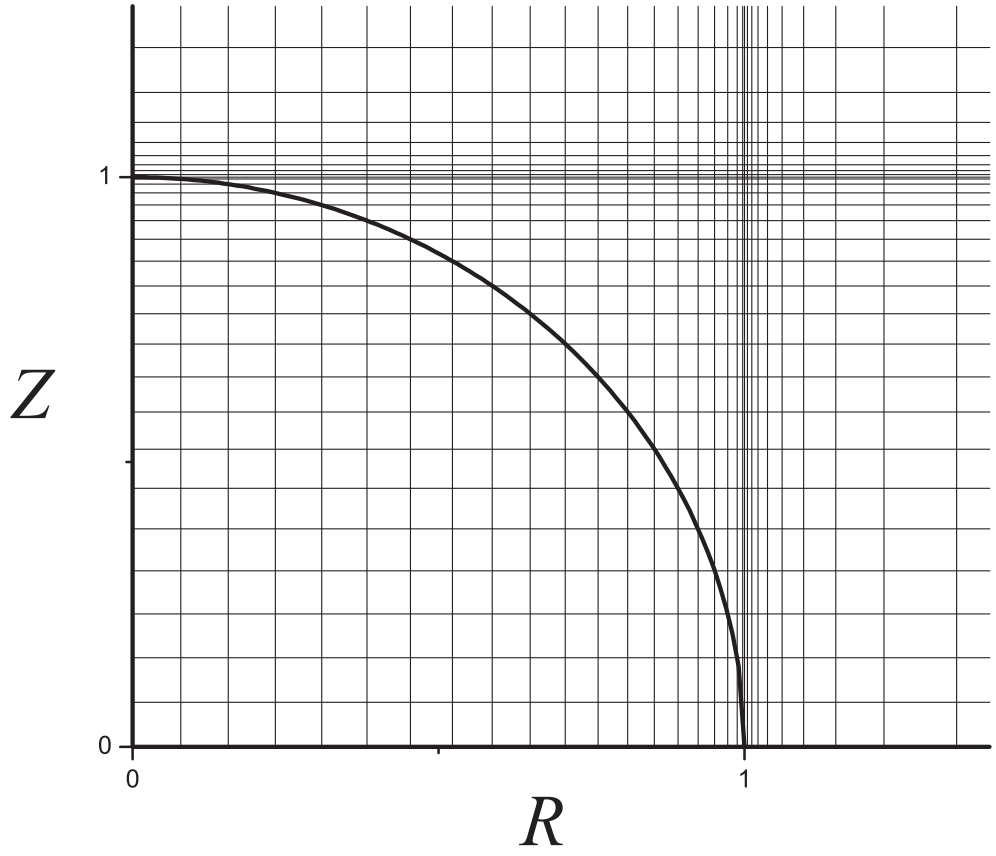

Figure 6.7: *Discrete spatial grid for a hemispherical electrode in two dimensions. Calculations are carried out at the nodes (intersections of the grid lines).*

6.2.3 Current Calculation

For an isolated hemispherical particle on an infinite planar surface, the measured current, I, is

$$I = FAj_{\mathrm{A}} \tag{6.25}$$

where A is the surface area and j_{A} is the flux of species A at some point on the hemispheres surface. As such an electrode is uniformly accessible, the flux itself is uniform across the surface. For the case of an array of hemispheres however, this is not the case. The imposition of the domain boundary between adjacent particles means that diffusion to a particle is no longer isotropic; there will be a greater influx of fresh material from above (perpendicular to the z axis) than there will from the sides (perpendicular to the r axis). Consequently, the flux of A across the surface is not uniform and so the total flux must be determined by calculating the flux at

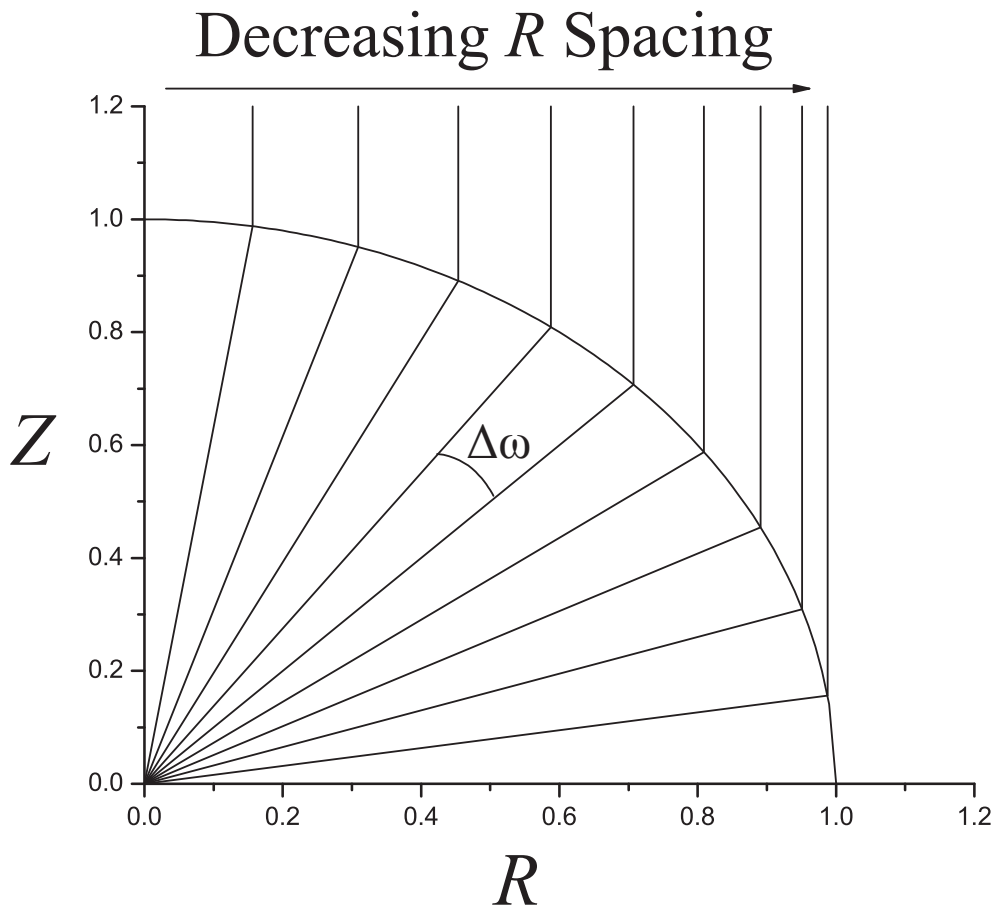

Figure 6.8: *Regular $\Delta\omega$ increments used to create a contracting R grid across the electrode.*

each point on the surface and then integrating over the surface.

As the simulation grid is rectangular, the dimensionless flux, J_ω, at a given point on the surface is found by summing the components in the R and Z directions:

$$J_\omega = \frac{\partial C_\mathrm{A}}{\partial R}\cos\omega + \frac{\partial C_\mathrm{A}}{\partial Z}\sin\omega \tag{6.26}$$

The total dimensionless current of the whole electrode is then found by integrating J_ω over the surface:

$$J = \int_0^{\pi/2} J_\omega cos\omega \, d\omega \tag{6.27}$$

The real current is then

$$I = \frac{2\pi N F D c_{\mathrm{A}}^{*}}{r_{\mathrm{e}}} J \tag{6.28}$$

where N is the total number of hemispheres in the array.

6.2.4 Numerical Solution

In contrast to previous chapters, simulation of the EC′ mechanism requires the storage and calculation of the concentration profiles of more than one species. At least three species, A, B, and X need to be stored to properly simulate the voltammetry, and it may also be desirable to store the profile for species P if one is interested in the quantity of product formed.

The electrode surface boundary conditions and the homogeneous reaction terms in the mass transport equations couple the concentrations of the species so it is not possible to solve the transport equation for a given species in isolation; the transport equations for all species need to be solved simultaneously. This requires the solution of a matrix equation in which the matrix has more than three non-zero diagonals. Consequently, an extended multi-diagonal version of the Thomas algorithm must be used for the solution. An additional complication occurs due to the fact that the homogeneous reaction terms in the mass transport equations are non-linear; they contain a product of two concentration terms: $c_{\mathrm{B}} c_{\mathrm{X}}$. Because of this, the simultaneous equations cannot be solved for directly in a single step. Instead, the iterative Newton–Raphson algorithm, described in detail in Section 3.2.2, is employed, which converges on the correct solution.

6.3 Results and Discussion

6.3.1 Presentation of Results

The results in this chapter are all represented in terms of a set of normalized units (which are largely the same as those used internally by the simulations). The following transformations are used:

$$C_s = \frac{c_s}{c_{\mathrm{A}}^*} \tag{6.29}$$

$$R = \frac{r}{r_{\mathrm{e}}} \tag{6.30}$$

$$\sigma = \frac{F}{RT}\frac{r_{\mathrm{e}}^2}{D}\nu \tag{6.31}$$

$$\theta = \frac{F}{RT}(E - E_f^0) \tag{6.32}$$

$$K_2 = \frac{c_{\mathrm{A}}^* r_{\mathrm{e}}^2}{D} k_2 \tag{6.33}$$

$$J = \frac{I}{2\pi N F D c_{\mathrm{A}}^* r_{\mathrm{e}}} \tag{6.34}$$

where N is the number of unit cells in the array. Note that $D = D_{\mathrm{A}} = D_{\mathrm{B}} = D_{\mathrm{X}}$. Throughout, a given system is defined in terms of three parameters: the ratio of the initial concentrations of species X and species A, C_{X}^*; the normalized scan rate, σ; and the normalized second order rate constant, K_2. A fourth parameter, the surface coverage, Θ (not to be confused with normalized potential, θ), is also need in the case of a particle array, defined as:

$$\Theta = \frac{r_{\mathrm{e}}^2}{r_{\mathrm{d}}^2} \tag{6.35}$$

Note that the surface coverage is related to the normalized unit cell radius by:

$$R_{\mathrm{d}} = \frac{1}{\sqrt{\Theta}} \tag{6.36}$$

Use of this set of normalized units considerably simplifies the exploration of the parameter space and the presentation of results. The use of real units would require the independent investigation of at least eight parameters: c_{A}^*, c_{X}^*, ν, r_{e}, r_{d}, D, E_{f}^0, and k_2. Each set of normalized parameters therefore corresponds to a family of real systems.

6.3.2 Isolated Particle

As noted, for the case of an isolated hemispherical particle on a surface, the system is angularly isotropic and so simulations may be reduced to one spatial coordinate: the radial coordinate r. One-dimensional (1D) simulations compute relatively rapidly,

with run-times on the order of seconds rather than hours which 2 dimensional simulations require. Approximately 5000 1D simulations were performed by varying the dimensionless scan rate, σ, in the range 10^{-3} - 10^{4}; the second order rate constant, K_2, in the range 1 - 10^{10}; and the initial concentration of species X, C^*_{X}, in the range 1 - 10.

6.3.3 The Effect of K_2: The Split Wave

As described in Section 6.1, a high second order rate constant can lead to voltammetry with a split wave. Figure 6.9 shows the evolution of the concentrations of species A and X at the particle surface overlaid with the forward sweep of the cyclic voltammogram. It can be seen that the first peak corresponds to the transition from kinetic to diffusion control of species X whereas the second corresponds to the same transition for species A. In the same manner as the case of a planar surface,[18] it may be seen that the shape of the voltammogram is determined by the superposition of these two transitions: if they occur on a similar timescale, then only one peak is observed whereas when the X transition is made more rapid (by increasing K_2), two distinct peaks may be observed. As an intermediate case, the X peak may appear as a shoulder to the A peak; it may be described qualitatively but there is no quantifiable peak current that can be measured. This behaviour is that which is observed in the case of a planar electrode.[4]

6.3.4 The Effect of C^*_{X}

It can be seen in Figure 6.10 that for a given rate constant, increasing the concentration of X leads to a substantial increase in the height of both peaks but also that the first increases far more than the second, totally obscuring the latter at higher concentrations of X for the reasons justified in Section 6.3.3. Such a large current response is possible even though the potential is significantly below the formal potential of the A/B couple ($\theta = 0$) since the continual depletion of B and production of A in the chemical step drives the equilibrium at the electrode surface more in favour of B by Le Châtelier's principle (assuming the A/B redox couple is electrochemically reversible). This feedback means that as soon as the potential reaches a

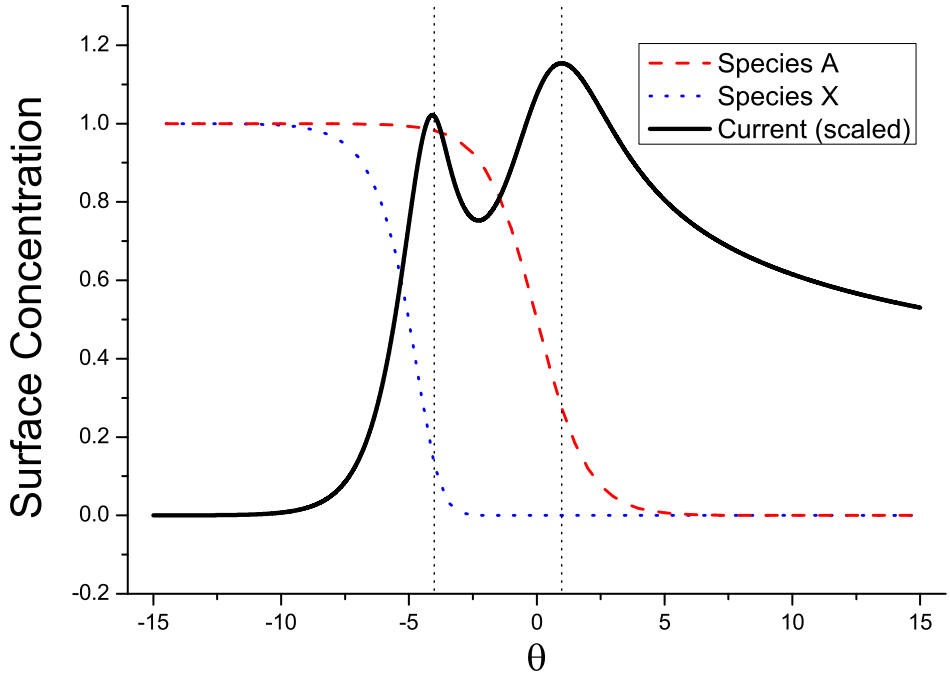

Figure 6.9: *Evolution of surface concentrations of species A and X with overlaid linear sweep voltammetry for an isolated system with* $\sigma = 1000$*;* $K_2 = 10^7$*;* $C_{\mathrm{X}}^* = 1$*. Note that LSV is scaled in the vertical axis for clarity.*

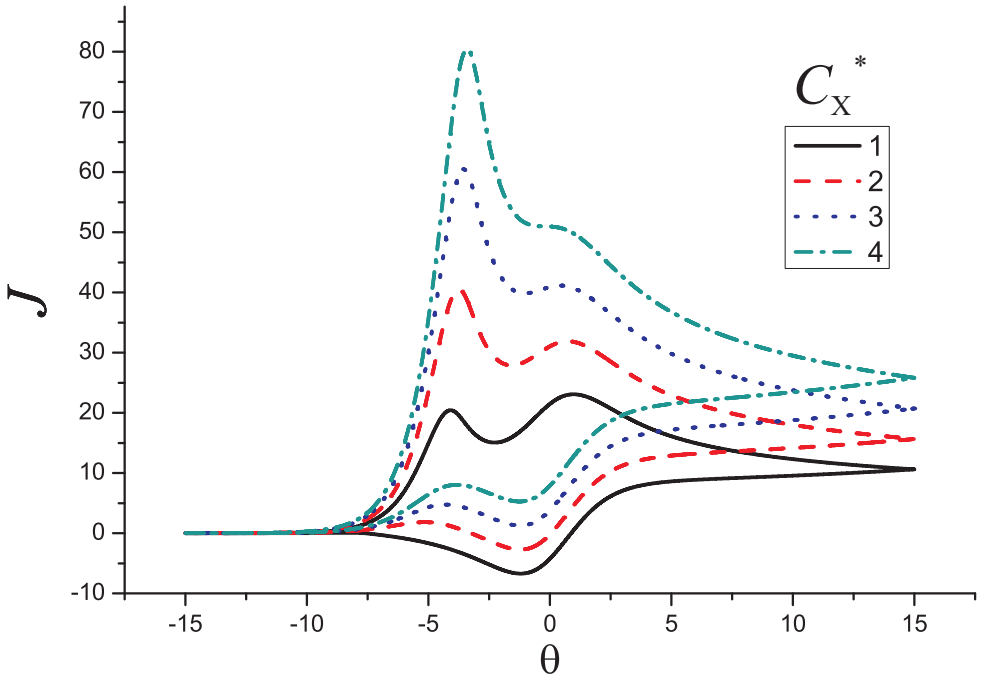

Figure 6.10: *Cyclic voltammograms for a system with* $\sigma = 1000$*;* $k_2 = 10^7$*; and a range of concentrations,* C_{X}^**.*

level where the electrochemical reduction of A to B is kinetically viable, species X will be consumed in the vicinity of the electrode and a sharp current peak will be observed.

6.3.5 The Effect of σ and Steady-State Voltammetry

For a simple E process at a hemispherical particle, a very low scan rate ($\sigma \leq 10^{-3}$) typically gives steady-state cyclic voltammetry since diffusion to the particle is convergent. Similar behaviour is also observed under the EC′ mechanism, however instead of the characteristic sigmoid normally associated with steady-state voltammetry, a 'double-sigmoid' is observed (for high K_2) with the first plateau being associated with the depletion of species X and the second with that of species A as per Section 6.3.3. Figure 6.11 depicts a series of steady-state voltammograms for increasing concentrations of X. As the limiting current is related to the diffusion of both A and X, the value measured is equivalent to that in an E system with one electroactive species with initial concentration $C^* = C^*_{\mathrm{A}} + C^*_{\mathrm{X}}$ (assuming equal diffusion coefficients). Note that in the dimensionless unit system used in this investigation, this limiting current is simply equal to the sum of the concentrations of A and X as demonstrated in Figure 6.11.

Figure 6.12 shows cyclic voltammetry from a system with $K_2 = 5 \times 10^4$, $C^*_{\mathrm{X}} = C^*_{\mathrm{A}}$ and a range of scan rates, σ. It is clear that for a split wave system, as the scan rate is increased, the peak-to-peak separation (of the forward scan peaks) tends to decrease, as is observed in a planar system.[4] This is because (i) the first peak moves toward a more negative potential with decreasing scan rate since the scan takes a longer time and X is therefore depleted at a lower potential; and (ii) the second peak moves to a more positive potential with decreasing scan rate as expected for a hemispherical electrode.[33] An interesting consequence of this peak movement is that for a certain range of rate constants, k_2, the voltammogram will transition from a single peak to a split wave as the scan rate is decreased, as demonstrated for the example of $K_2 = 5 \times 10^4$ in Figure 6.12. Of course as the system moves to very low scan rates ($\sigma \leq 0.001$), the cyclic voltammograms tend towards a more sigmoidal shape and thus no peaks are observed at all. For the range of isolated particle

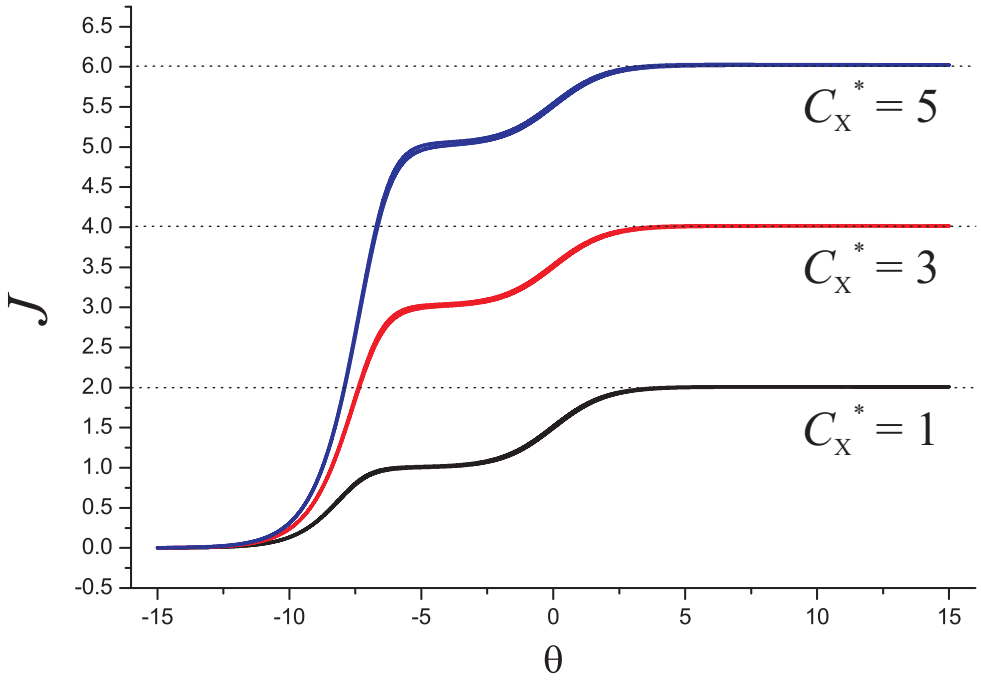

Figure 6.11: *Steady-state voltammograms for a system with* $\sigma = 0.001$*;* $K_2 = 10^7$*; and a range of initial concentrations,* C_X^**.*

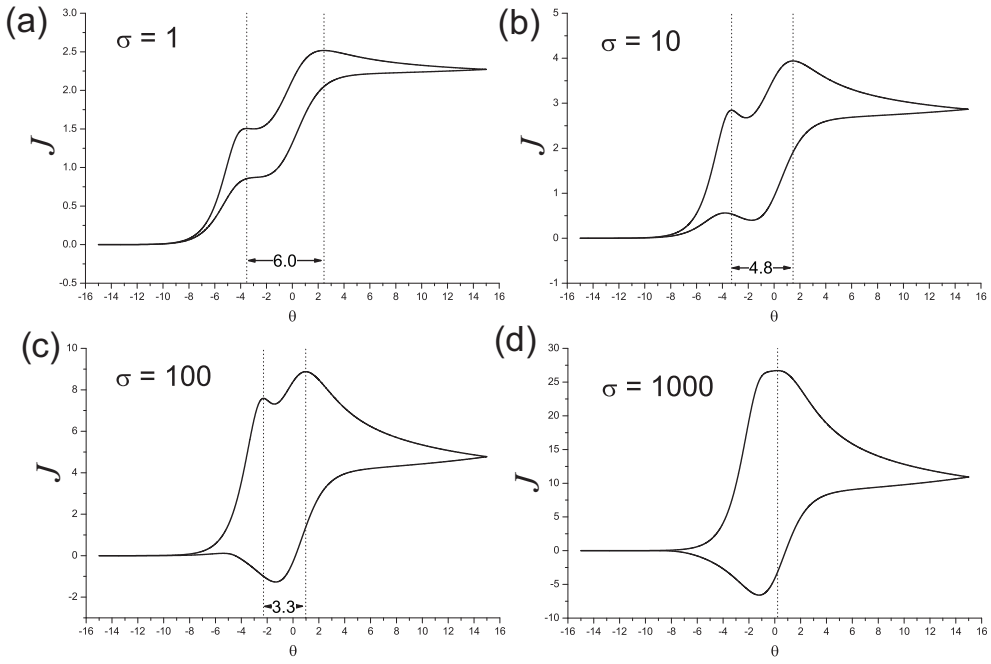

Figure 6.12: *Cyclic voltammograms of isolated systems with* $k_2 = 5 \times 10^4$*,* $C_X = 1$*, and a variety of scan rates,* σ*. Peak to peak separation* $\Delta\theta_{pp}$ *is shown in each case.*

systems studied, it was not generally possible to resolve the two peaks at any value of $K_2 < 3 \times 10^4$ for any scan rate. For high scan rates ($\sigma \geq 100$), resolution was generally only possible for $K_2 > 10^6$.

6.3.6 Expressions for Peak Potentials and Currents

Figure 6.13 displays the variation of the first (or 'only' for cases where the peaks cannot be resolved) peak current and potential for range of values of C_{X}^* and K_2 at a fixed scan rate ($\sigma = 1000$). For cases where $K_2 < 10^6$, the two peaks are generally not resolvable so the peak characteristics (Figures 6.13 (a) and (c)) are determined by their superposition and are thus difficult to predict. However, as can be seen in Figures 6.13 (b) and (d), when $K_2 > 10^6$ (i.e. when peak resolution is possible), relatively simple relationships exists between K_2, C_{X}^*, and peak current and potential.

From careful analysis of the simulated data, the relationship for the peak potential, θ_{p} is deduced to be of the form:

$$\theta_{\mathrm{p}} = (\alpha_1 \log K_2 + \alpha_2) \log C_{\mathrm{X}}^* - \alpha_3 \log K_2 + \alpha_4 \tag{6.37}$$

where the coefficients, α_1, α_2, α_3 and α_4 depend on the scan rate. For a scan rate of $\sigma = 1000$, this relationship is found to be:

$$\theta_{\mathrm{p}} = (0.02 \log K_2 + 1.01) \log C_{\mathrm{X}}^* - 1.18 \log K_2 + 4.20 \tag{6.38}$$

For all simulated cases (for $\sigma = 1000$; $K_2 > 10^6$; $1 \leq C_{\mathrm{X}}^* \leq 10$) this expression was accurate to within 1%.

Where the peaks are sufficiently separated ($k_2 > 5 \times 10^6$), the first peak current, J_{p}, is approximately independent of the value of K_2 and is simply,

$$J_{\mathrm{p}} = \beta C_{\mathrm{X}}^* \tag{6.39}$$

where β depends on the scan rate as shown in Figure 6.14. In the limit of fast scan rate,

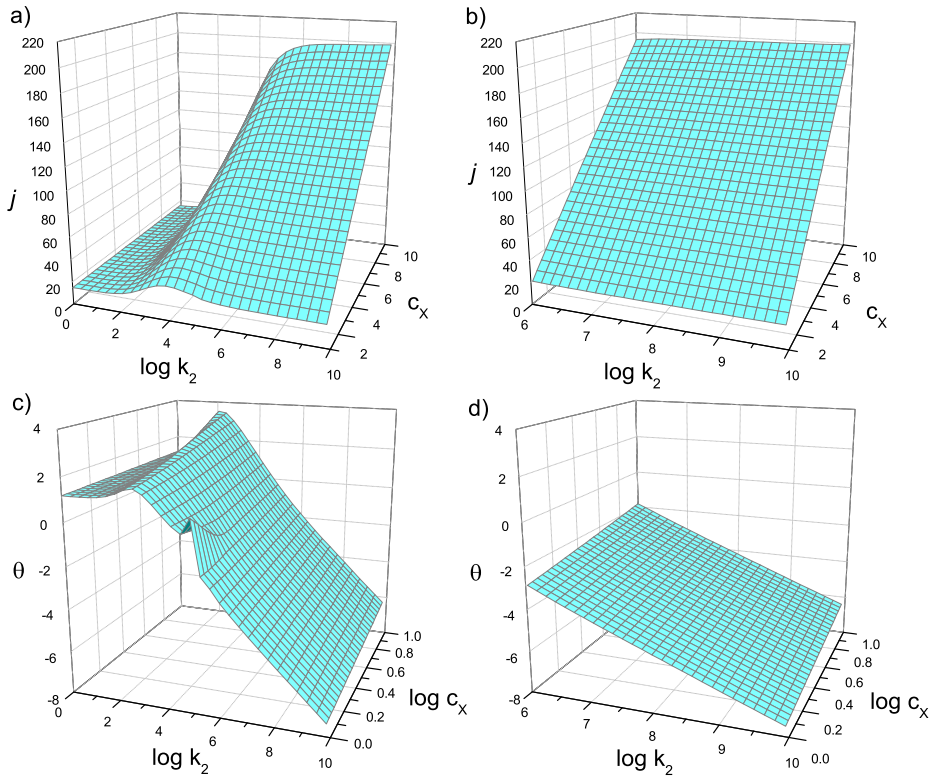

Figure 6.13: *Variation of first peak current [a) and b)] and potential [c) and d)] with c_X and k_2 for an isolated system with $\sigma = 1000$.*

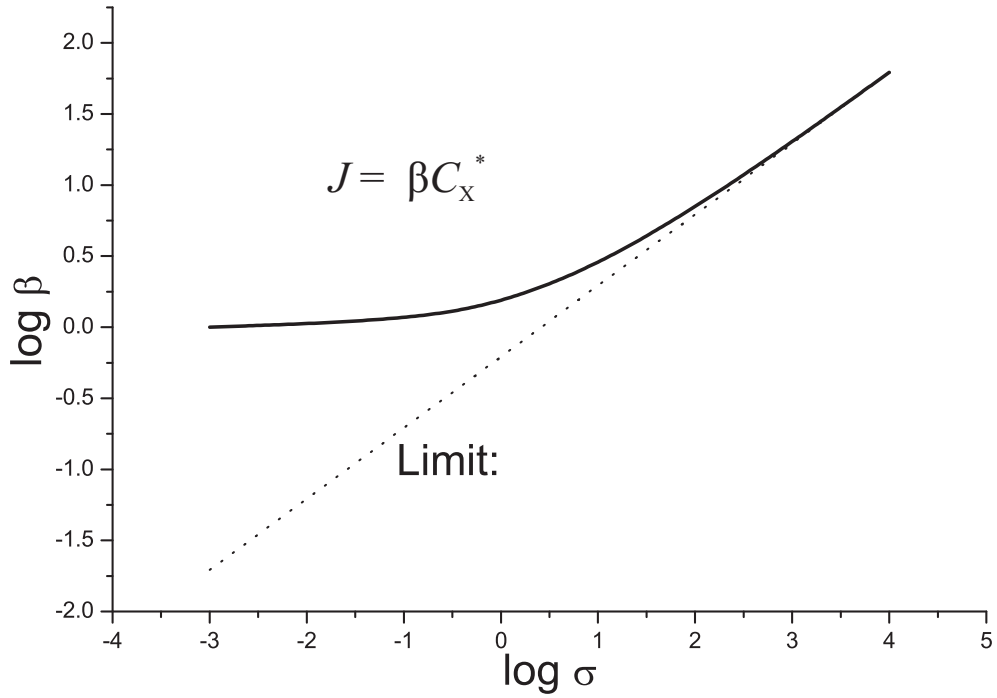

Figure 6.14: *Variation of first peak current with σ. Dotted line indicates the apparent high scan rate limit.*

$$J_{\mathrm{p}} = 0.62 C_{\mathrm{X}}^{*} \sqrt{\sigma} \tag{6.40}$$

in the same manner as the well known Randles-Ševčik equation[34,35] for fully reversible electrode kinetics.

6.3.7 Particle Arrays

When particles have sufficiently small inter-particle separation, they are no longer diffusionally independent on the experimental timescale. Consequently, the simulation space is no longer spherically symmetric and a simple one dimensional simulation is no longer appropriate. Using the two-dimensional simulation approach detailed in Section 6.2, a range of simulations were performed, varying the scan rate, σ, from 0.1 to 1000; the surface coverage, Θ, from 0.1 to 0.9; and the second order rate constant, K_2, from 1 to 10^6. The surface coverage is defined as:

$$\Theta = \frac{r_{\mathrm{e}}^2}{r_{\mathrm{d}}^2} \tag{6.41}$$

Note that in all cases, the current is that recorded at a single particle in the array, not that recorded from the entire array. The array current is equal to the current from a single particle multiplied by N, the number of particles in the array.

In a manner consistent with previous studies on particle arrays,[32] as the distance between adjacent particles decreases, the peak current of all peaks decreases as adjacent diffusion fields overlap and material within each particle's diffusion domain is depleted as evidenced in Figure 6.15. Figure 6.16 shows concentration profiles of species 'A' for several systems. It can be seen that decreasing the scan rate and increasing the surface coverage leads to a change in diffusional behaviour, as the diffusional mode transitions, from Case 2 (see Section 1.3), in which diffusion is convergent to each particle, to Case 4, in which diffusion is linear to the surface.

6.3.8 Surface Coverage

As Θ is increased (and thus particle separation is decreased), the amount of time for which radial diffusion dominates is reduced; as a CV scan progresses, the mode

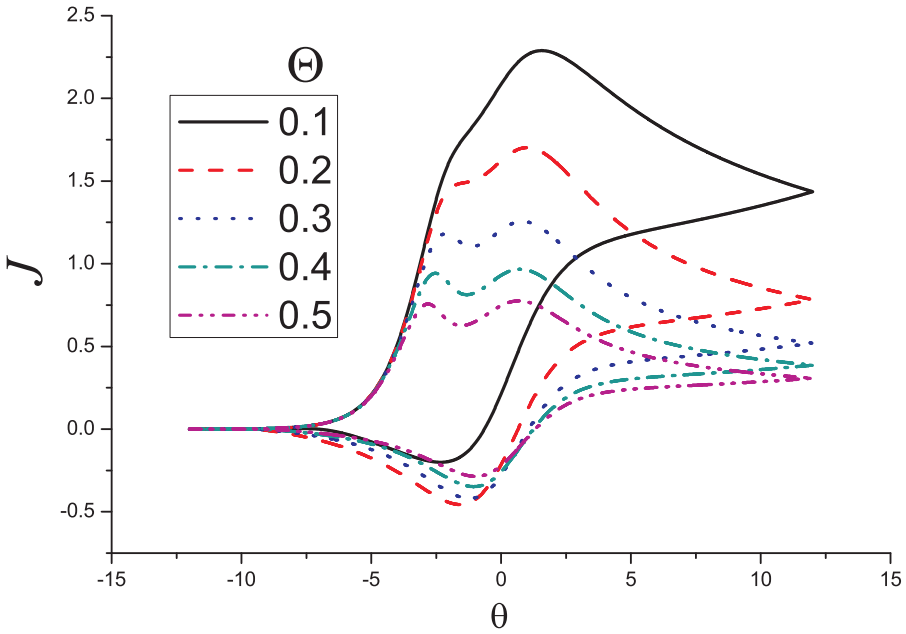

Figure 6.15: *Cyclic Voltammograms of systems with $\sigma = 1$, $k_2 = 1000$ and a variety of surface coverages, Θ. Peak heights decrease with increasing surface coverage and split wave behaviour becomes resolvable.*

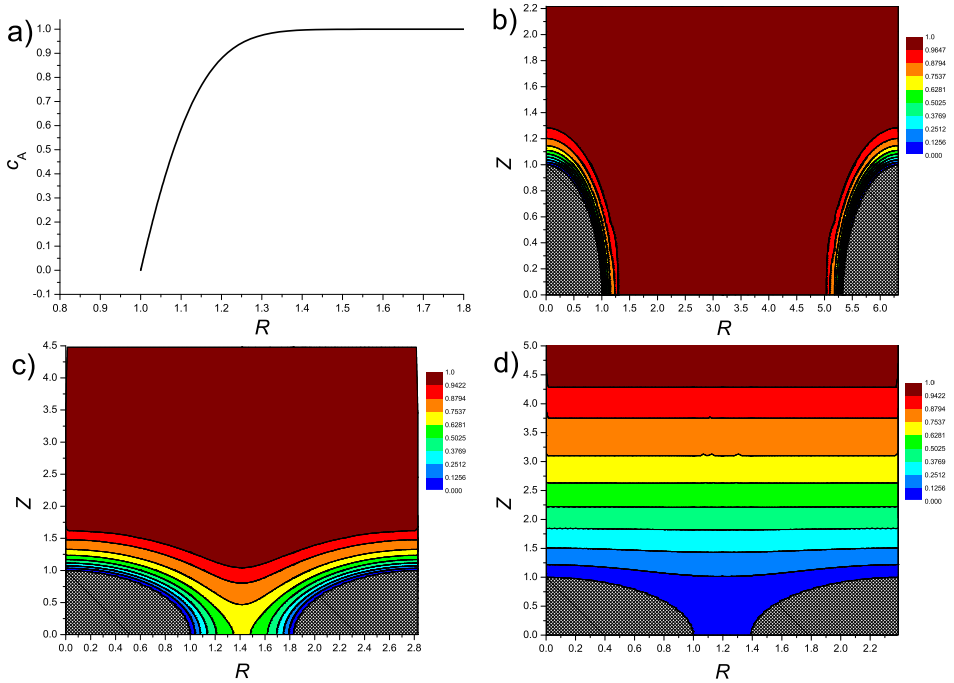

Figure 6.16: *Concentration Profiles of species 'A' taken at the end ($\theta = 10$) of the forward potential sweep of a CV for systems with $k_2 = 10$; a) and b) $\sigma = 1000$, $\Theta = 0.1$; c) $\sigma = 100$, $\Theta = 0.5$; d) $\sigma = 1$, $\Theta = 0.7$. Figures a) and b) show the same profile for a diffusionally isolated (Case 2) particle in 1 (radial) and 2 (R,Z) dimensions respectively. Figures c) and d) show Case 3 and Case 4 behaviour respectively. Hashed areas represent the electrode. Colours indicate value of C_X.*

of diffusion transitions from Case 2 to Case 3, and then possibly to Case 4. This transition will occur sooner for a smaller diffusion domain and so the amounts of A and X available to the electrode through radial diffusion are reduced. Consequently, both peaks move to a more negative potential since material is depleted more rapidly.

In section 6.3.5, it was seen that for an isolated particle, decreasing the scan rate while keeping all other parameters fixed, could lead to a transition from single peak to split peak behaviour. Figure 6.15, which shows cyclic voltammetry for a system with a low scan rate ($\sigma = 1$) and a range of surface coverages, demonstrates that increasing Θ can also lead to a similar transition. In this example, this splitting is attributable to 2 separate factors. The first is the tendency for $\Delta\theta_{\mathrm{pp}}$ (the peak-to-peak separation of the peaks of the forward sweep) to increase with increasing surface coverage. As previously stated, increasing Θ results in a shift of both peaks to more negative potential, however as shown in Figure 6.17, for a low scan rate, $\Delta\theta$ increases with increasing Θ since the X peak tends to shift more than the A peak. It should be noted that at higher scan rates this may not necessarily be the case. The second factor is the change in relative heights of the two peaks. In the example of Figure 6.15, it is obvious that as the surface coverage is increased, the height of the second peak, $J_{\mathrm{p,A}}$, decreases relative to that of the first, $J_{\mathrm{p,X}}$.

From Figure 6.18, it can be seen that for a given scan rate and rate constant, the ratio of the peak heights, $J_{\mathrm{p,A}}/J_{\mathrm{p,X}}$, tends to increase with increasing particle separation (decreasing surface coverage), and tends toward some limiting value as $R_{\mathrm{d}} \to \infty$ (i.e. as the particle becomes isolated). If $J_{\mathrm{p,A}}$ is sufficiently large, it will obscure $J_{\mathrm{p,X}}$ and no split-wave behaviour will be observed. A similar variation in $J_{\mathrm{p,A}}/J_{\mathrm{p,X}}$ with σ can be seen in Figure 6.19.

As a consequence of these two factors, split-wave behaviour in an array of particles may be seen to occur for substantially lower rate constants, K_2, than are possible in the isolated particle case.

6.3.9 Scan Rate

For arrays of particles, a change in scan rate has an effect similar to that seen in the isolated case. As shown in Figure 6.20, peak separation becomes more apparent

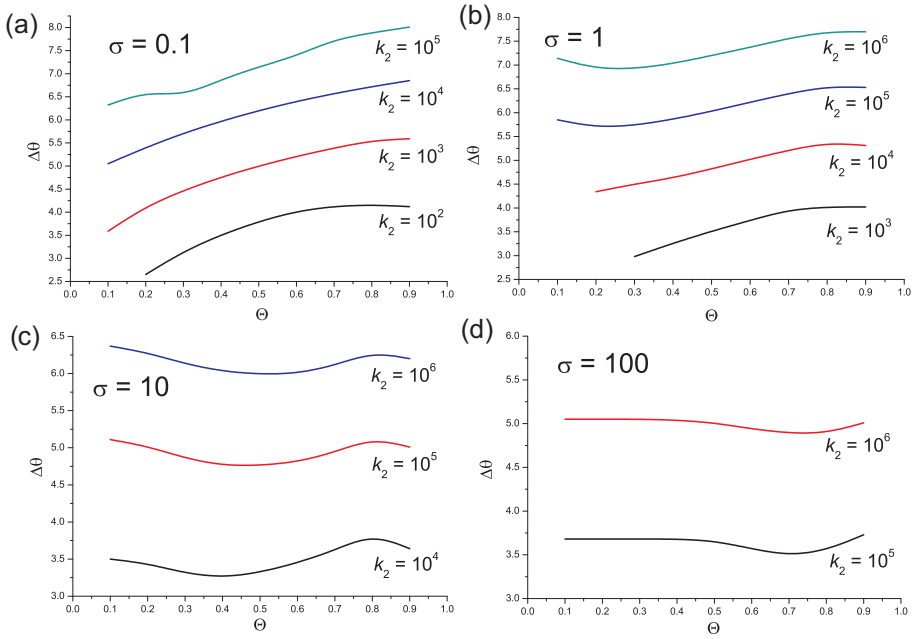

Figure 6.17: *Forward sweep peak-to-peak separation for systems with a range of surface coverages, rate constants and (a)* $\sigma = 0.1$*, (b)* $\sigma = 1$*, (c)* $\sigma = 10$*, and (d)* $\sigma = 100$*.*

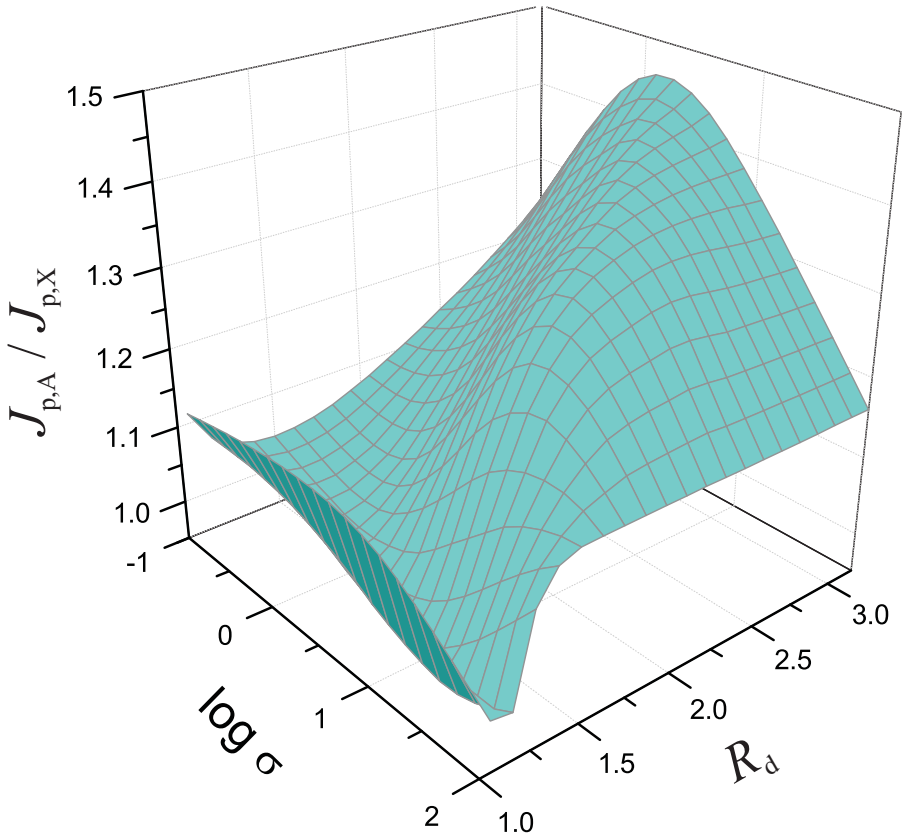

Figure 6.18: *Variation of the ratio of forward sweep peak heights,* $J_{p,A}/J_{p,X}$ *with scan rate and diffusion domain radius* R_d $(= \sqrt{1/\Theta})$*. for systems with* $K_2 = 10^5$*.*

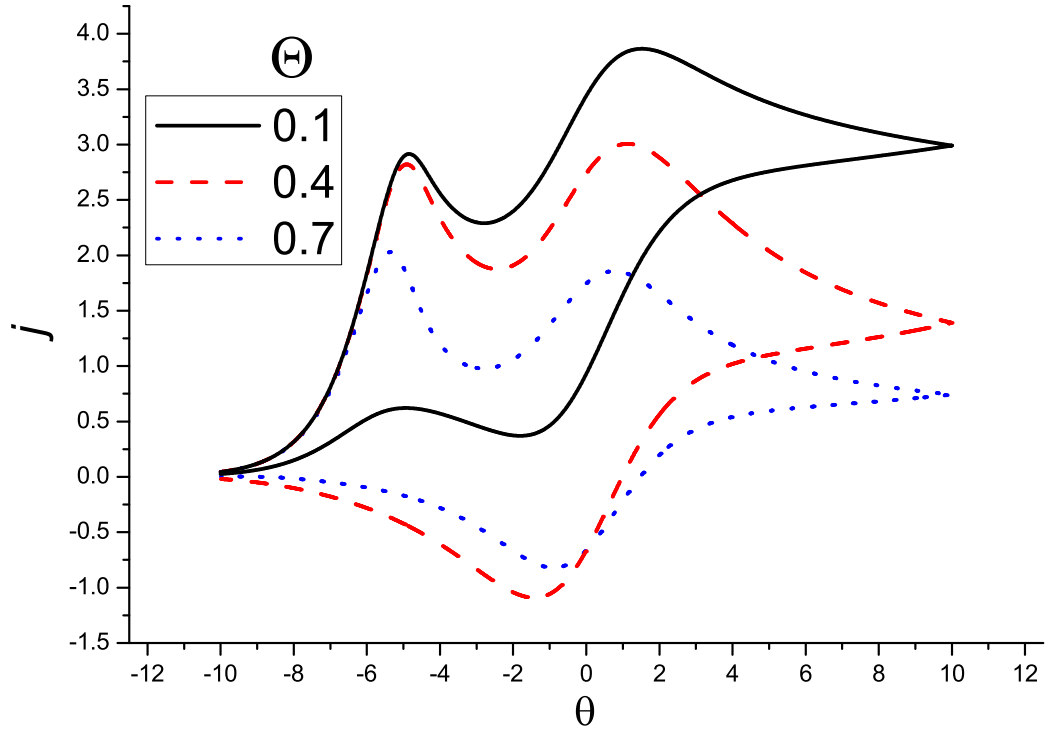

Figure 6.19: *Cyclic voltammograms for systems with* $\sigma = 10$*;* $K_2 = 10^6$ *and a range of surface coverages,* Θ*.*

as the scan rate is decreased and there may be a transition from a single peak to a split wave. The main difference between the isolated and array cases is that as the scan rate is decreased, there is no tendency towards steady state behaviour (i.e., sigmoidal cyclic voltammograms) for the case of an array. This difference can be seen by comparing Figure 6.20 with Figure 6.12. As the scan rate is decreased, the scan takes more time and thus case 4 diffusional behaviour is seen. As discussed in Section 6.3.8, this means that radial diffusion to the particles can only continue for a finite time; when the diffusion fields overlap, the diffusion becomes planar and no steady-state voltammetry can be observed.

6.4 Conclusions

The effect of a number of parameters, namely scan rate, σ; rate constant, K_2; surface coverage, Θ; and initial concentration of species X, C_X^*, on the cyclic voltammetry of the EC′ mechanism on particle modified electrodes has been investigated. The occurrence of resolvable split wave behaviour is dependent upon a number of com-

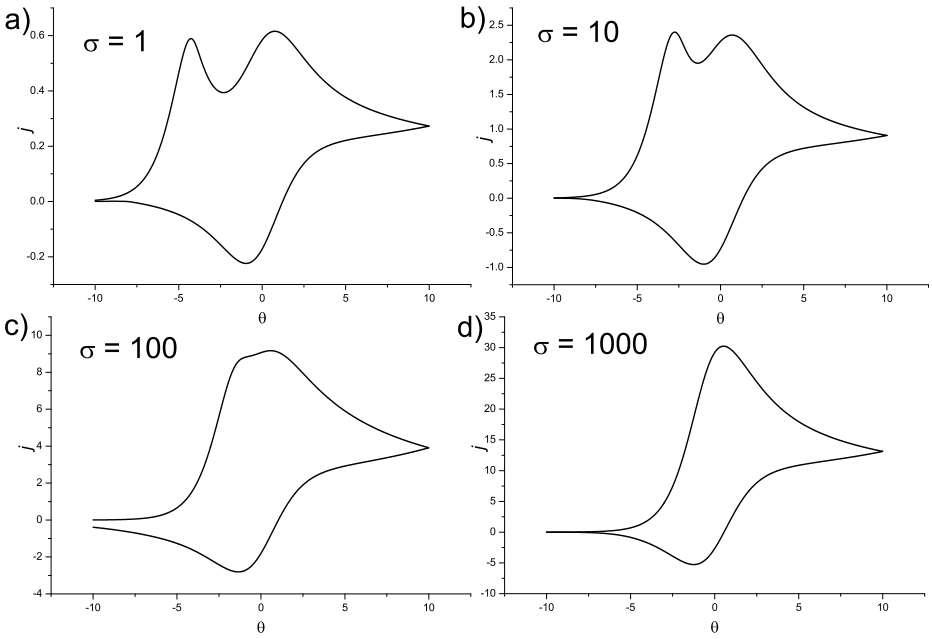

Figure 6.20: *Cyclic voltammograms for systems with* $K_2 = 10^4$, $\Theta = 0.6$ *and a variety of scan rates,* σ. *Similar behaviour is seen for higher surface coverages.*

peting factors. First, a high rate constant, K_2, ensures that the presence of species X makes a substantial contribution to the voltammogram (i.e., a large current response), as well as ensuring that the peaks are well separated.

A low scan rate causes the separation between the two forward peaks, $\Delta\theta_{\mathrm{pp}}$ to increase making resolution easier, though for the isolated case, a very low scan rate leads to steady-state behaviour where no peaks are observed. Additionally, the concentration of X must be similar to that of A; too low and little current response is seen, too high and $J_{\mathrm{p,X}}$ will completely obscure $J_{\mathrm{p,A}}$. Finally, a high surface coverage generally leads to better peak resolution as $J_{\mathrm{p,A}}/J_{\mathrm{p,X}}$ becomes closer to unity and $\Delta\theta_{\mathrm{pp}}$ increases. It is hoped that the insights offered by this work will aid in the analysis and deconvolution of experimentally obtained cyclic voltammetry of the EC′ mechanism.

Bibliography

[1] K. R. Ward, N. S. Lawrence, R. S. Hartshorne and R. G. Compton, *J. Phys. Chem. C*, 2011, **115**, 11204–11215.

[2] R. G. Compton and C. E. Banks, *Understanding Voltammetry*, ICP, London, 2nd edn., 2010.

[3] P. Jeroschewski, K. Haase, A. Trommer and P. Gruendler, *Electroanal.*, 1994, **6**, 769–72.

[4] D. M. Dimarco, P. A. Forshey and T. Kuwana, *ACS Symposium Series*, 1982, **192**, 71–97.

[5] D. Britz, *Int. J. Electrochem. Sci.*, 2006, **1**, 1–11.

[6] S. W. Feldberg and J. F. Campbell, *Anal. Chem.*, 2009, **81**, 8797–8800.

[7] K. Harriman, D. J. Gavaghan and E. Suli, *J. Electroanal. Chem.*, 2004, **569**, 35–46.

[8] C. P. Andrieux, J. M. Dumas-Bouchiat and J. M. Savéant, *J. Electroanal. Chem. Interfacial Electrochem.*, 1978, **88**, 43–8.

[9] C. P. Andrieux, J. M. Dumas-Bouchiat and J. M. Savéant, *J. Electroanal. Chem. Interfacial Electrochem.*, 1978, **87**, 55–65.

[10] C. P. Andrieux, J. M. Dumas-Bouchiat and J. M. Savéant, *J. Electroanal. Chem. Interfacial Electrochem.*, 1978, **87**, 39–53.

[11] C. P. Andrieux, J. M. Dumas-Bouchiat and J. M. Savéant, *J. Electroanal. Chem. Interfacial Electrochem.*, 1980, **113**, 1–18.

[12] C. P. Andrieux, C. Blocman, J. M. Dumas-Bouchiat, F. M'Halla and J. M. Savéant, *J. Electroanal. Chem. Interfacial Electrochem.*, 1980, **113**, 19–40.

[13] J. M. Savéant and K. B. Su, *J. Electroanal. Chem. Interfacial Electrochem.*, 1984, **171**, 341–9.

[14] R. G. Compton, A. C. Fisher and R. A. Spackman, *Electroanal.*, 1992, **4**, 167–82.

[15] A. C. Fisher and R. G. Compton, *Electroanal.*, 1992, **4**, 311–15.

[16] R. G. Compton, M. J. Day, M. E. Laing, R. J. Northing, J. I. Penman and A. M. Waller, *J. Chem.Soc., Faraday Trans. 1: Phys. Chem. Condensed Phases*, 1988, **84**, 2013–25.

[17] R. G. Compton, R. A. Spackman and P. R. Unwin, *J. Electroanal. Chem. Interfacial Electrochem.*, 1989, **264**, 1–25.

[18] R. G. Compton and R. A. Spackman, *J. Electroanal. Chem. Interfacial Electrochem.*, 1990, **285**, 273–9.

[19] H. Reller, E. Kirowa-Eisner and E. Gileadi, *J. Electroanal. Chem.*, 1982, **138**, 65–77.

[20] C. Amatore, J. M. Savéant and D. Tessier, *J. Electroanal. Chem.*, 1983, **147**, 39–51.

[21] K. Stulik, C. Amatore, K. Holub, V. Marecek and W. Kutner, *Pure App. Chem.*, 2000, **72**, 1483–1492.

[22] R. J. Forster, *Chem. Soc. Rev.*, 1994, **23**, 289–97.

[23] D. W. M. Arrigan, *Analyst*, 2004, **129**, 1157–1165.

[24] C. M. Welch and R. G. Compton, *Anal. Bioanal. Chem.*, 2006, **384**, 601–619.

[25] F. W. Campbell and R. G. Compton, *Anal. Bioanal. Chem.*, 2010, **396**, 241–259.

[26] R. G. Compton, G. G. Wildgoose, N. V. Rees, I. Streeter and R. Baron, *Chem. Phys. Lett.*, 2008, **459**, 1–17.

[27] S. R. Belding and R. G. Compton, *J. Phys. Chem. C*, 2010, **114**, 8309–8319.

[28] T. J. Davies, C. E. Banks and R. G. Compton, *J. Solid State Electrochem.*, 2005, **9**, 797–808.

[29] T. J. Davies, S. Ward-Jones, C. E. Banks, J. Del. Campo, R. Mas, F. X. Munoz and R. G. Compton, *J. Electroanal. Chem.*, 2005, **585**, 51–62.

[30] T. J. Davies and R. G. Compton, *J. Electroanal. Chem.*, 2005, **585**, 63–82.

[31] I. Streeter, R. Baron and R. G. Compton, *J. Phys. Chem. C*, 2007, **111**, 17008–17014.

[32] S. R. Belding, E. J. F. Dickinson and R. G. Compton, *J. Phys. Chem. C*, 2009, **113**, 11149–11156.

[33] A. J. Bard and L. R. Faulkner, *Electrochemical Methods: Fundamentals and Applications.*, John Wiley & Sons, New York, 2nd edn., 2001.

[34] J. E. B. Randles, *Trans. Faraday Soc.*, 1948, **44**, 327–38.

[35] A. Ševčík, *Collect. Czech. Chem. Commun.*, 1948, **13**, 349–77.

Chapter 7

The Apparent 'Catalytic' Effect of Nano-Particle Modified Electrodes

In this chapter, The voltammetry of micro- and nano-particle modified electrodes and other electrodes of *partially covered and non-planar* geometry is investigated by simulation. Building on existing theory, it is demonstrated that for a simple one-electron process (assuming that the diffusion fields of neighbouring electroactive regions strongly overlap such that diffusion to the entire surface is linear), the apparent electrochemical rate constant of the reaction, k_{app}, is equal to the product of the true rate constant, k^0, and the ratio, Ψ, of the total electroactive surface area to the geometric surface area of the substrate. It is demonstrated that for a given value of Ψ, the voltammetry is independent of the surface geometry; surfaces covered by, for example, long thin bands of electroactive material, or electroactive hemispherical or spherical particles, show the same voltammetry if they have the same surface area of electroactive material per area of substrate. Distributions of, most importantly, electroactive nanoparticles, with $\Psi > 1$, will display an apparent catalytic effect compared to the bulk material which *can be* solely due to the geometry of the surface and not necessarily related to changes in kinetics at the nanoscale, for example by altered structural or electronic properties. Further, if an electrode surface is modified by a fixed mass of nanocatalyst per unit area, then the response will reflect the size and shape of the modified particles.

The work constituting this chapter has been published in the *Journal of Elec-*

troanalytical Chemistry.[1]

7.1 Introduction

Electrocatalysis lies at the heart of the current intense interest in energy technology such as fuel cells, batteries, and solar energy cells. An area with great potential concerns the use of nano-particles and nano materials to modify electrode surfaces. The electrocatalytic behaviour of such surfaces is usually assessed by means of some form of linear sweep voltammetry either in stationary solution[2–10] or at a rotating electrode,[10–21] and the resulting current-voltage response is used to provide the sought information. The analysis of such data however is not unambiguous. For the case of a flat, uniform surface, the theory of voltammetry is well established as discussed in many textbooks,[22,23] and under these conditions, an electrochemically irreversible wave is shifted to lower overpotentials if the surface is more electrocatalytic to the reaction of interest, as recorded quantitatively by the standard electrochemical rate constant. For the case of *flat*, non-uniform surfaces where part of the electrode is more catalytically active than other parts, the theory is also well understood.[24–26] Commonly encountered situations are arrays of microelectrodes, (for example, microdiscs) distributed over an inactive supporting surface; or a flat electroactive surface partially covered in some flat inert blocking material.

Diffusion of solution-phase material to a flat electrode substrate partially covered in electroactive material may be divided into four limiting categories which depend on the experimental time scale as well as the particle surface coverage[27,28] as discussed in detail in Section 1.3. For the case of an electrode surface modified with nanoparticles, none of this theory is immediately applicable since the surface is not flat. Nevertheless, given the great importance of such measurements, not least, for example, in oxygen reduction catalysts, it is desirable to derive the effective electrochemical rate constant for *non-flat*, non-uniform electrode surfaces. This chapter is concerned with the derivation of this theory by conducting simulations of surfaces modified with spheres, hemispheres, cylinders, bands, etc., before generalising the results. The theory is developed in the context of diffusion only voltammetry but

the effective electrochemical rate constants are expected to be applicable beyond that, notably, for rotating disc measurements where they would correspond to the values inferred by Koutecky-Levich analysis.[29,30] Note that in all cases, the theory developed is exclusively that relevant for 'Case 4' diffusion as described in Section 1.3, i.e., the voltammetry seen where the coverage and catalysis are such that there is linear diffusion to the entire geometric area of the electrode.

7.2 Theory

7.2.1 Simulated Voltammetry

Throughout this chapter the linear sweep voltammetry (LSV) of a one-electron reduction of the form,

$$\mathrm{A} + \mathrm{e}^- \rightleftharpoons \mathrm{B} \tag{7.1}$$

is considered. It is assumed that the concentration of species A is uniform and equal to some bulk value, c_{A}^*, and there is no species B present in the system. Additionally it is assumed that the diffusion coefficients of the two chemical species are equal such that at every point in space, the concentrations of species A and B sum to c_{A}^* (see Section 2.3.1). Consequently, only the behaviour of species A need be considered as the concentration profile of species B can be inferred from that of A.

In a linear sweep voltammetry experiment, the potential at the electrode, E, is swept from some starting potential, E_i, to some final potential, E_v, at a constant rate, ν. The potential at time, t, is given by:

$$E = E_i - \nu t \tag{7.2}$$

A variety of electrode geometries are considered in this study; these are illustrated schematically in Figure 7.1. Simulation methodology for a number of these geometries has been covered in previous chapters and their implementation details will be omitted here, however for novel geometries, necessary details will be given. Geometry (a) is a planar macroelectrode which may be modelled in a 1 dimensional coordinate system and (b) corresponds to an array of microdisc electrodes, each of which is detailed in Chapters 2 and 3. Geometry (c) corresponds to an array of mi-

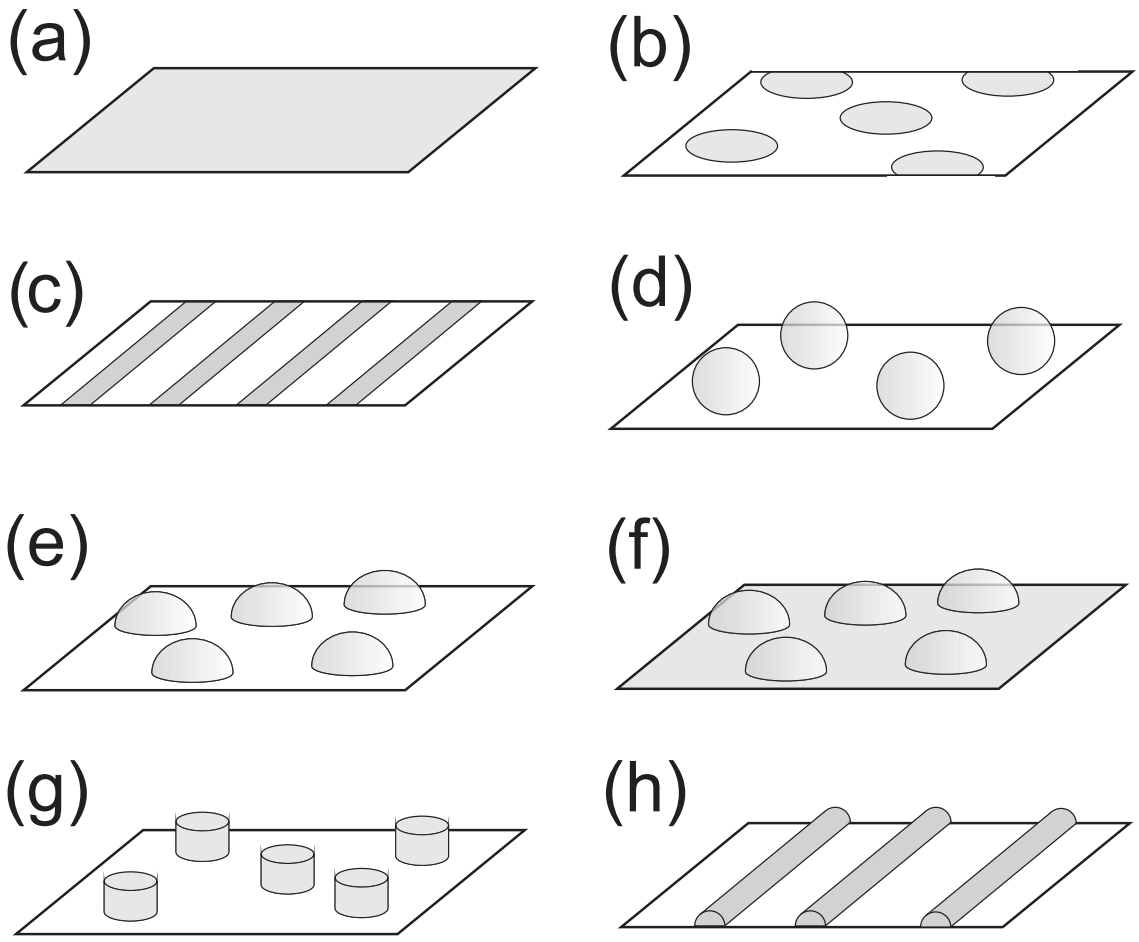

Figure 7.1: *Electrode geometry types used throughout this study. Shaded regions are electroactive, white areas are inactive.*

croband electrodes on an inactive surface which may be modelled in a 2-dimensional Cartesian coordinate system as demonstrated in Chapter 4. Geometries (d) and (e) correspond to arrays of spheres[31–33] and hemispheres which are described in Chapters 5 and 6 respectively. Geometry (f) is an array of hemispheres on an *electroactive* supporting surface. This differs from model (e) only in the change of the boundary condition at the supporting substrate. Geometries (g) and (h) are novel; they are respectively, an array of cylinders,[34] and an array of long hemi-cylindrical 'wires'.

7.2.2 Simulation Model and Boundary Conditions

In each case, a regular array of the relevant particle geometry is assumed. Each particle has the same same size and inter-particle separation. Consequently each is assumed to sit in an identical environment. In the case of particles that are

cylindrically symmetric, the diffusion domain approximation is used to reduce the model from three to two dimensions.

The mass transport of chemical species due to diffusion is described by Fick's second law:

$$\frac{\partial c}{\partial t} = D\nabla^2 c \tag{7.3}$$

where for two-dimensional Cartesian coordinates,

$$\nabla^2 c = \frac{\partial^2 c}{\partial x^2} + \frac{\partial^2 c}{\partial z^2} \tag{7.4}$$

and for two-dimensional cylindrical polar coordinates,

$$\nabla^2 c = \frac{\partial^2 c}{\partial z^2} + \frac{\partial^2 c}{\partial r^2} + \frac{1}{r}\frac{\partial c}{\partial r} \tag{7.5}$$

Note that in all cases it is assumed that an excess of supporting electrolyte is added to the system and that it is not stirred or heated such that the migratory and convectional contributions to mass transport are negligible.

The flux of species 'A' normal to the electrode surface at a given potential is described by the Butler–Volmer equation:

$$D\frac{\partial c}{\partial n} = k^0 \left[c_{\mathrm{A},0} \exp\left(\frac{-\alpha F(E - E_f^0)}{RT}\right) - (1 - c_{\mathrm{A},0}) \exp\left(\frac{(1-\alpha)F(E - E_f^0)}{RT}\right)\right] \tag{7.6}$$

where n is some coordinate normal to the electrode surface. Where a solid surface is not electroactive, a condition of no flux is set:

$$\left.\frac{\partial c}{\partial z}\right|_{z=0} = 0 \tag{7.7}$$

A condition of no flux is likewise applied at the domain boundary (at $r = r_{\mathrm{d}}$ for cylindrical polar coordinates and at $x = x_{\mathrm{d}}$ for Cartesian coordinates), and across the vertical axis ($r = 0$ for cylindrical polar coordinates and $x = 0$ for Cartesian coordinates) which is a line of mirror symmetry. Finally, the solution is assumed to extend infinitely in the z direction, and so a boundary is placed at a distance $z_{\max}$

that exceeds the extent of the diffusion layer, i.e.,

$$z_{\max} = z_{\mathrm{e}} + 6\sqrt{Dt} \tag{7.8}$$

where z_{e} is the size of the electrode in the z direction.

For all of the electrode geometries detailed above, the model system is normalized in the same manner as that used in previous chapters. The normalized diffusion equation is discretised according to the alternating direction implicit method and solved over the discretized space using the Thomas algorithm.

7.2.3 Cylinder and Wire Models

An array of cylindrical 'particles' may be fabricated using standard microfabrication techniques.[35,36] Like a microdisc, a cylindrical electrode is best modelled in cylindrical polar coordinates;[34] the unit cell for a single cylinder is shown in Figure 7.2. The cylinder is defined by its height, z_{e} and radius, r_{e}; the radius of the unit cell, r_{d}, is determined according to the diffusion domain approximation (Section 2.8.1). The simulation space for a cylinder in real units is shown in Figure 7.3. The spatial coordinates are normalized against the cylinder radius, i.e.,

$$R = \frac{r}{r_{\mathrm{e}}} \tag{7.9}$$

$$Z = \frac{z}{r_{\mathrm{e}}} \tag{7.10}$$

As there are two perpendicular electroactive surfaces, the Butler–Volmer equation must be applied separately across each:

$$\text{for } R < 1, \quad \left.\frac{\partial C}{\partial Z}\right|_{Z=Z_{\mathrm{e}}} = K^0(C_{R,Z_{\mathrm{e}}}e^{-\alpha\theta} - (1 - C_{R,Z_{\mathrm{e}}})e^{\theta-\alpha\theta}) \tag{7.11}$$

$$\text{for } Z < Z_{\mathrm{e}}, \quad \left.\frac{\partial C}{\partial R}\right|_{R=1} = K^0(C_{1,Z}e^{-\alpha\theta} - (1 - C_{1,Z})e^{\theta-\alpha\theta}) \tag{7.12}$$

where $Z_{\mathrm{e}} = z_{\mathrm{e}}/r_{\mathrm{e}}$. The current response is calculated from

$$I = 2\pi N F r_{\mathrm{e}} D c^* \left(\int_0^1 \left.\frac{\partial C}{\partial Z}\right|_{Z=Z_{\mathrm{e}}} R\partial R + \int_0^{Z_{\mathrm{e}}} \left.\frac{\partial C}{\partial R}\right|_{R=1} \partial Z \right) \tag{7.13}$$

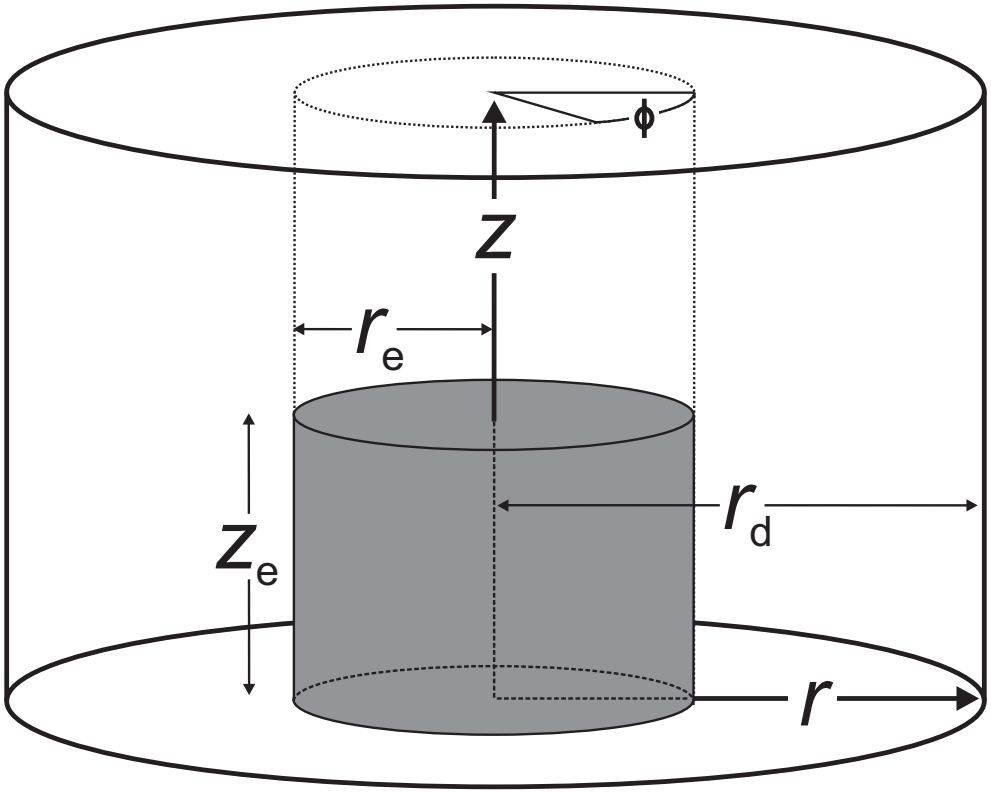

Figure 7.2: *Cylindrical polar coordinate system for a cylindrical electrode, radius r_e, height z_e, and domain radius, r_d.*

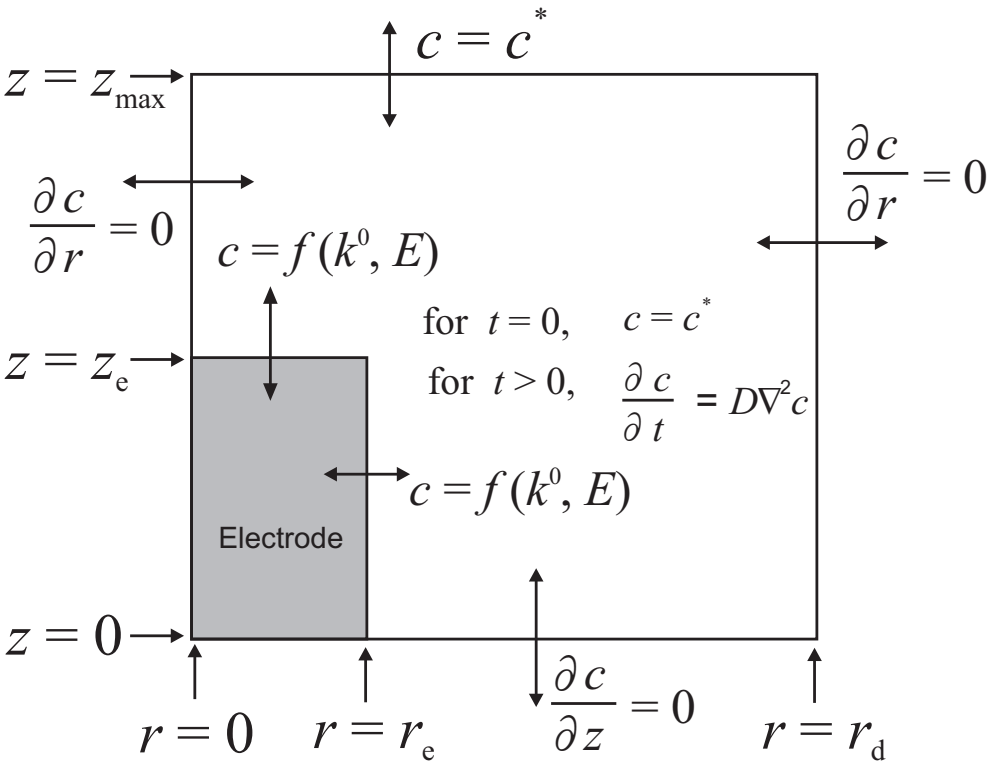

Figure 7.3: *Simulation space for an array of cylindrical electrodes.*

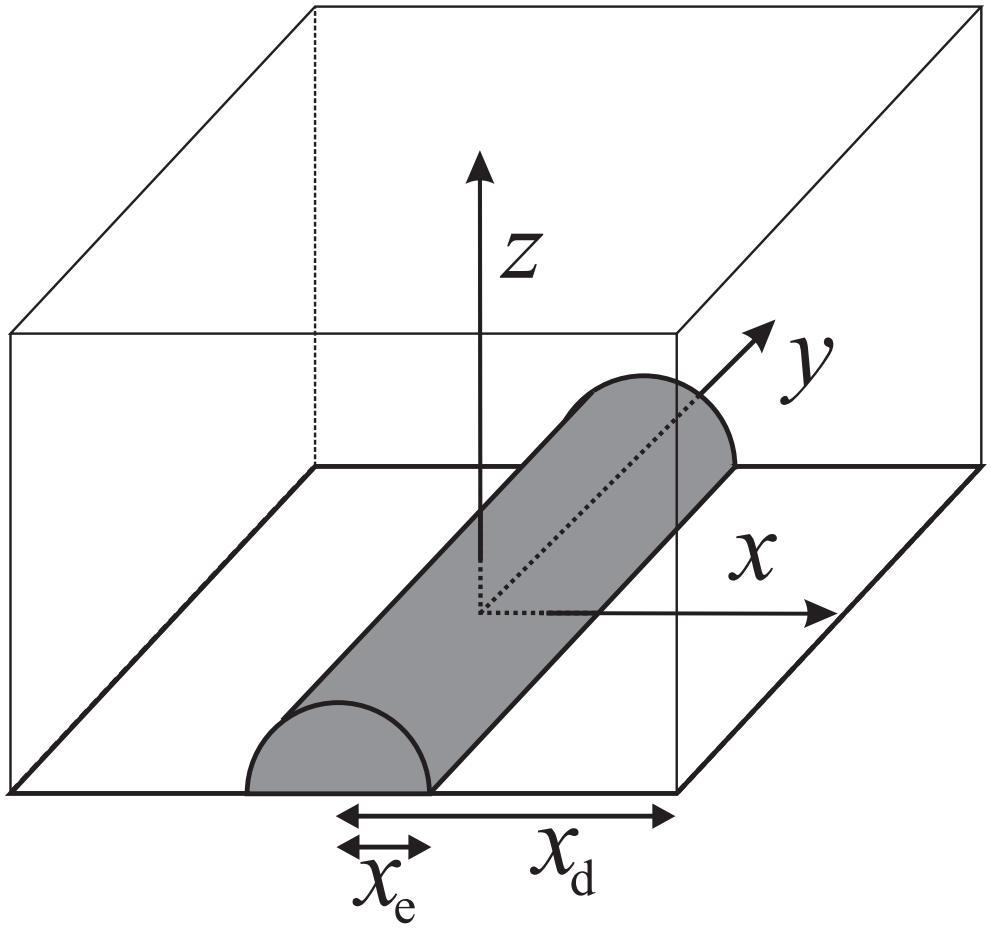

Figure 7.4: *Cartesian coordinate system for a hemicylindrical wire electrode, radius x_e and domain half-width, x_d.*

where N is the number of unit cells in the array.

An array of hemi-cylindrical wire electrodes is best modelled in two-dimensional Cartesian coordinates. Details of simulation in this coordinate system is given for the example of a band electrode in Chapter 4. The unit cell for a wire electrode with radius x_e is shown in Figure 7.4. The simulation space is exactly the same as that described and depicted for a hemispherical electrode in Chapter 6, except that the form of $\nabla^2 c$ is that given by Equation 7.4. Other simulation details including discrete spatial grid generation, proper application of the Butler–Volmer boundary conditions, and current calculations are also identical to those found in that chapter.

7.2.4 Voltammetry of Partially Active Flat Electrodes

The peak current, I_p of the forward sweep of a cyclic voltammogram for a fully reversible one-electron transfer at a planar flat macro-electrode is given by the Randles-Ševčík equation:[37,38]

$$I_{p,\text{rev}} = 0.446FAc^*_{\text{A}}\sqrt{\frac{FD\nu}{RT}} \tag{7.14}$$

where A is the geometric area of the flat surface and ν is the scan rate. For an irreversible process, the relation is:

$$I_{p,\text{irrev}} = 0.496\sqrt{\alpha}FAc^*_{\text{A}}\sqrt{\frac{FD\nu}{RT}} \tag{7.15}$$

Between these two limits, in the quasi-reversible region, the peak current varies[39] as shown in Figure 7.5 (a). The peak position, E_p, of a fully reversible process is always located at $E_p - E^0_f = 28.5$ mV (at 298 K). For an irreversible process, E_p is given by[40,41]

$$E_p = E^0_f - \frac{RT}{\alpha F}\left[0.780 - \ln k^0 + \ln\left(\sqrt{\frac{\alpha FD\nu}{RT}}\right)\right] \tag{7.16}$$

For a flat surface that is partially covered in electroactive material, Equations 7.14 and 7.15 also apply as long as the average distance between neighbouring electroactive sites is small compared to the thickness of the diffusion layer, i.e. if the diffusion is in case 4.[24] Under this condition, I_p is the same regardless of the amount of electroactive surface; I_p depends only on the geometric area of the surface. For such surfaces, the peak position, E_p, in the reversible limit is also the same as that of a macro-electrode ($E_p - E^0_f = 28.5$ mV). Consequently, it is not possible to distinguish between a planar, fully active electrode and a partially active/partially blocked electrode as long as the kinetics of the electron transfer are fast. In the case of an irreversible process however, it can be seen that there is an apparent decrease in the kinetics of the partially active electrode in comparison to the fully active one such that:

$$k^0_{\text{app}} = \Theta k^0 \tag{7.17}$$

where the surface coverage, Θ, is defined as

$$\Theta = \frac{\text{Area covered by electroactive particles}}{\text{Area of substrate}} \tag{7.18}$$

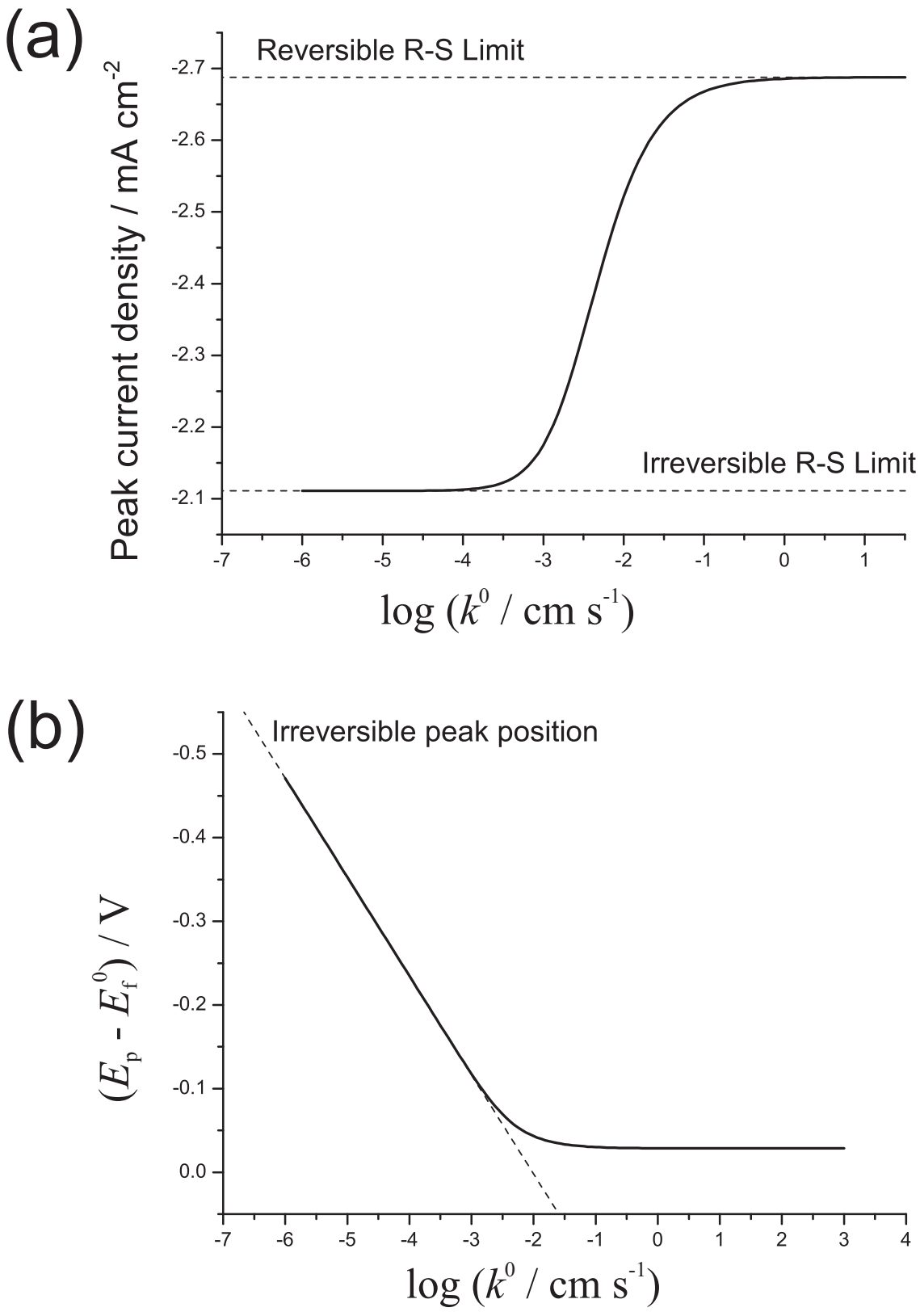

Figure 7.5: *(a) Peak current density and (b) peak potential of linear sweep voltammetry at a planar macroelectrode (with* $c_A^* = 10\ mM$*;* $D = 10^{-5}\ cm^2\ s^{-1}$*;* $\alpha = 0.5$*;* $\nu = 0.1\ V\ s^{-1}$*).*

such that $\Theta = 1$ for a completely active surface and 0 for a completely inactive surface. As a consequence of this apparent change in electrode kinetics, E_p is seen to vary considerably from the value given by Equation 7.16:[24,27]

$$E_p = E_f^0 - \frac{RT}{\alpha F}\left[0.780 - \ln(\Theta k^0) + \ln\left(\sqrt{\frac{\alpha F D \nu}{RT}}\right)\right] \tag{7.19}$$

For a flat surface partially covered in flat electroactive material, the shift in peak potential from that of a fully covered flat surface, ΔE_p, is therefore

$$\Delta E_p = -\frac{RT}{\alpha F}\ln\Theta \tag{7.20}$$

7.3 Results and Discussion

A large number of voltammetric simulations of electrode systems of a variety of non-flat geometries (as detailed in Section 7.2.1) were performed. In all cases, unless otherwise explicitly specified, only simulations under Case 4 diffusion (see Section 1.3) were considered, and it is assumed that the scale of the roughness of the surface is smaller than the scale of the diffusion layer thickness. The effects of the variation of the electrochemical rate constant, k^0, the size of the electroactive particles (typically defined by their radius, r_e), and the surface coverage of those particles, Θ, were investigated. For all figures and examples given herein, the following fixed parameters were used: scan rate, $\nu = 0.1$ V s^{-1}; transfer coefficient, $\alpha = 0.5$; diffusion coefficient, $D = 10^{-5}$ cm^2 s^{-1}; initial concentration of species 'A', $c_A^* = 1$ mM; and temperature, $T = 298$ K; however the effects of their variation were also examined. The modified surfaces were all assumed to be macrodiscs that had a radius of 1.5 mm.

7.3.1 Hemispherical Particles

Figure 7.6 shows how the voltammetry of an array of hemispherical particles varies with the rate constant, k^0, for the specific example of coverage, $\Theta = 0.5$, and hemisphere radius $r_e = 100$ nm, such that diffusion is in case 4. The distance between the centres of two adjacent particles, d, is 283 nm. It can be seen that the peak height transitions from the irreversible to the reversible Randles-Ševčík limit

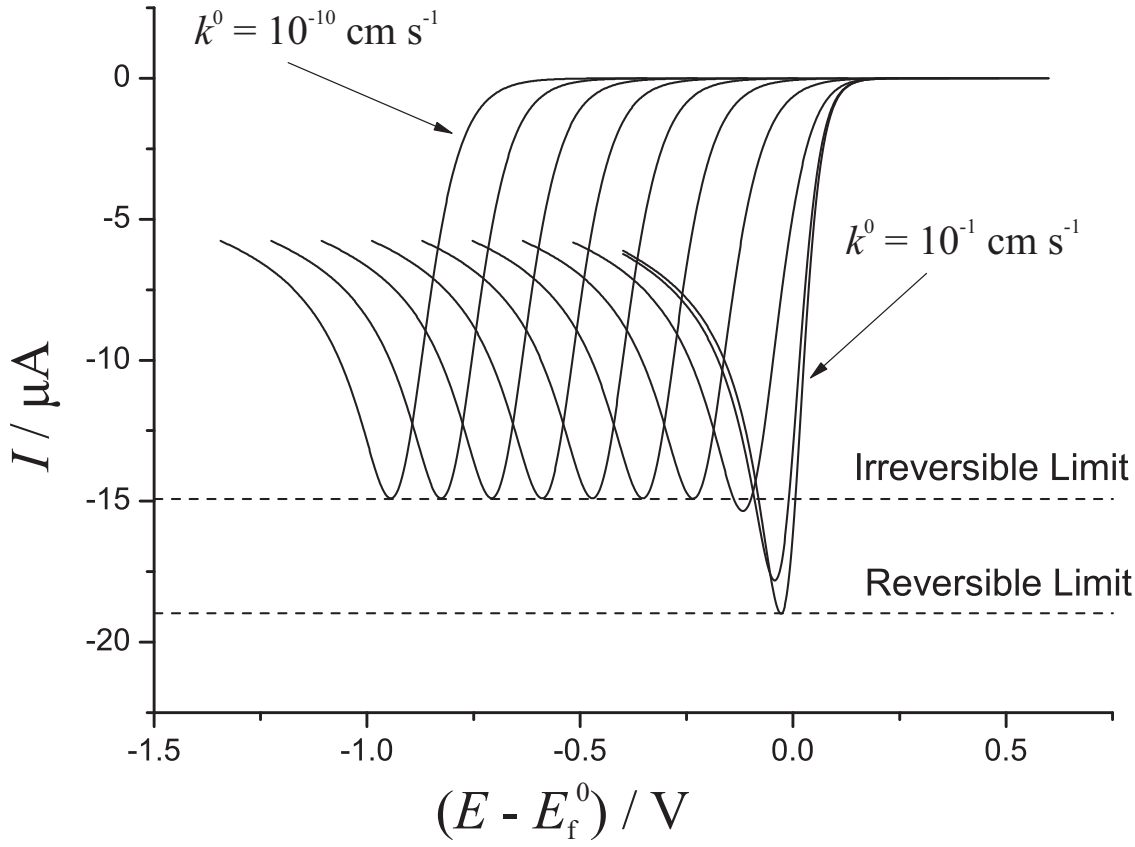

Figure 7.6: *Voltammetry of an array of hemispherical nanoparticles as it varies with rate constant, k^0, in the range 10^{-1}, 10^{-2}, 10^{-3}, ..., 10^{-9}, 10^{-10}, $\Theta = 0.5$, and $r_e = 100$ nm, $d = 282$ nm (with $c_A^* = 1$ mM; $D = 10^{-5}$ cm^2 s^{-1}; $\alpha = 0.5$; $\nu = 0.1$ V s^{-1}).*

as k^0 increases.

7.3.2 Variation of Surface Coverage

Figure 7.7 demonstrates how the peak potential, E_p, of the voltammetry in the irreversible limit ($k^0 = 10^{-7}$ cm^2, $r_e = 100$ nm, $\nu = 0.1$ V s^{-1}) shifts with increasing surface coverage, Θ in the range 0.1-0.7 (corresponding to d in the range 632-239 nm), while still maintaining the same (case 4) peak current, I_p, except at low coverage ($\Theta = 0.1$, $d = 632$ nm), where I_p begins to deviate slightly from the Randles-Ševčík limit.

Also shown is the corresponding peak position for a macroelectrode; notice that this position coincides with the peak potential of the voltammetry for $\Theta = 0.5$ ($d = 282$ nm). Figure 7.8 shows how E_p is affected by Θ (for a range of values of

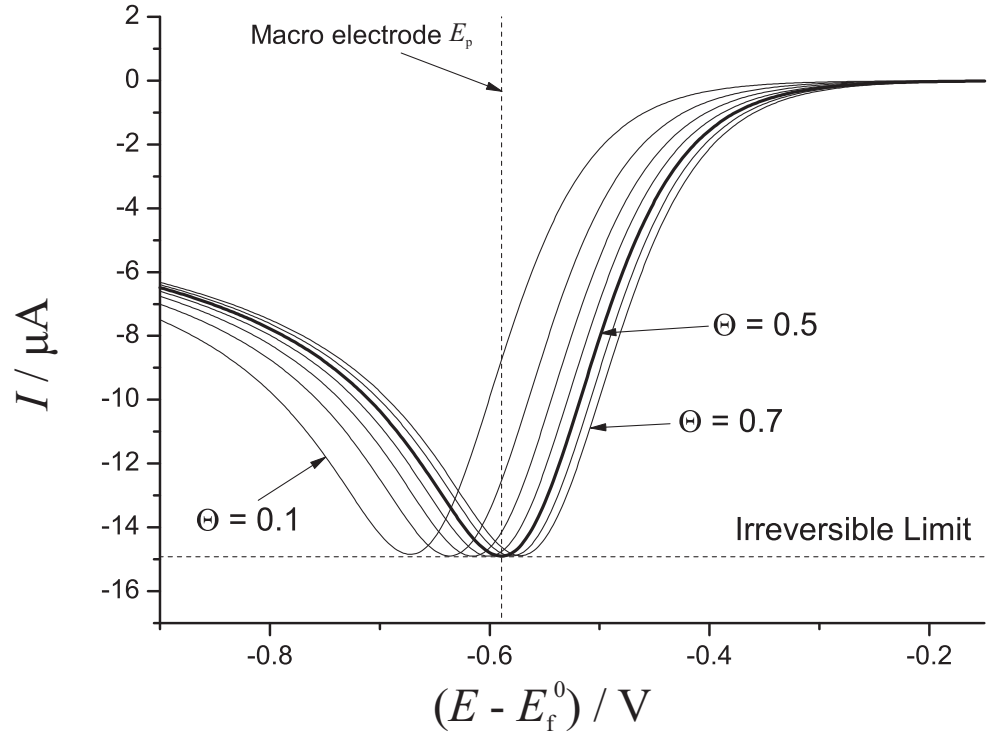

Figure 7.7: *Voltammetry of an array of hemispherical nanoparticles as it varies with surface coverage, Θ, in increments of 0.1.* $k = 10^{-7}$ *cm* s^{-1}, $r_e = 100$ *nm (with* $c_A^* = 1$ *mM;* $D = 10^{-5}$ *cm*^{2} s^{-1}*;* $\alpha = 0.5$*;* $\nu = 0.1$ *V* s^{-1}*).*

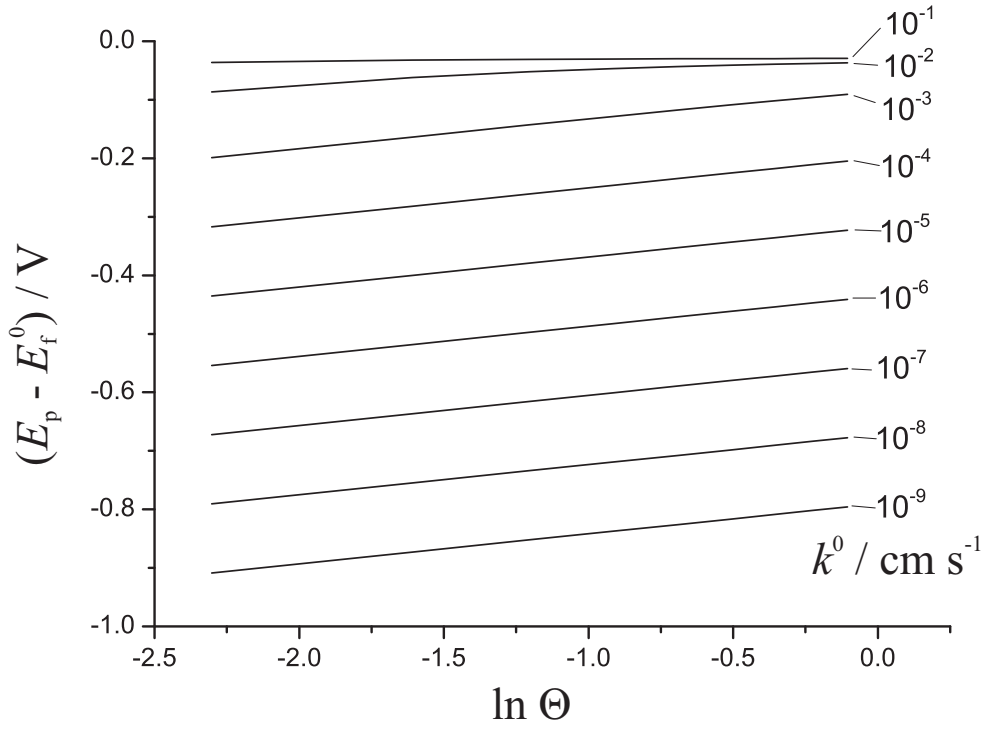

Figure 7.8: *Variation of peak potential,* E_p*, with coverage, Θ, for a range of values of rate constant,* k^0*, for an array of hemispherical particles with* $r_e = 100$ *nm (with* $c_A^* = 1$ *mM;* $D = 10^{-5}$ *cm*^{2} s^{-1}*;* $\alpha = 0.5$*;* $\nu = 0.1$ *V* s^{-1}*).*

k^0). It can be seen that in the limit of irreversible kinetics, E_p varies linearly with $\ln\Theta$ in a similar manner to the arrays of discs discussed in section 7.2.4. Analysis of the peak position data reveals that for irreversible processes at hemispherical particle arrays in the limit of case 4 diffusion:

$$E_p = E_f^0 - \frac{RT}{\alpha F}\left[0.780 - \ln(2\Theta k^0) + \ln\left(\sqrt{\frac{\alpha F D\nu}{RT}}\right)\right] \tag{7.21}$$

The dependence of E_p on α and ν is demonstrated in Section 7.3.3. This equation differs from Equation 7.19 only by the constant factor '2'. This can be related to the fact that the surface area of a hemisphere is twice that of a disc of the same radius. The surface area ratio, Ψ, is defined as

$$\Psi = \frac{\text{Surface area of electroactive particles}}{\text{Geometric area of substrate}} \tag{7.22}$$

Since the electroactive particles are not necessarily flush with the surface, in general Ψ may be greater than 1, which distinguishes it from Θ (though for flat partially active surfaces, $\Psi = \Theta$). The apparent rate constant, k^0_{app} is defined as

$$k^0_{\text{app}} = k^0\Psi \tag{7.23}$$

In the irreversible limit under case 4 diffusion, the peak current is seen to obey the equation:

$$E_p = E_f^0 - \frac{RT}{\alpha F}\left[0.780 - \ln(k^0_{\text{app}}) + \ln\left(\sqrt{\frac{\alpha F D\nu}{RT}}\right)\right] \tag{7.24}$$

where $\Psi = 2\Theta$ for an array of hemispherical particles. This explains the observation from Figure 7.7 that a coverage of $\Theta = 0.5$ ($d = 282$ nm) gives the same peak potential as a planar macroelectrode, all other properties being equal. In the irreversible limit for case 4 transport, the difference in peak potential, ΔE_p, between two electrode surfaces with different electroactive surface areas, Ψ_a and Ψ_b is therefore,

$$\Delta E_p = \frac{RT}{\alpha F}\ln\left(\frac{\Psi_a}{\Psi_b}\right) \tag{7.25}$$

Figure 7.9 shows the peak current, I_p, and potential, E_p, as they vary with $\ln\Psi$, down to the limit of low Ψ for an irreversible process. For this particular family of systems (with $k^0 = 10^{-7}$ cm s^{-1}, $r_e = 100$ nm), the transition between case 3 and case 4 diffusion occurs at approximately $\Psi = 0.4$ ($d = 447$ nm). Below this limit, the particles are sufficiently separated such that the peak current is no

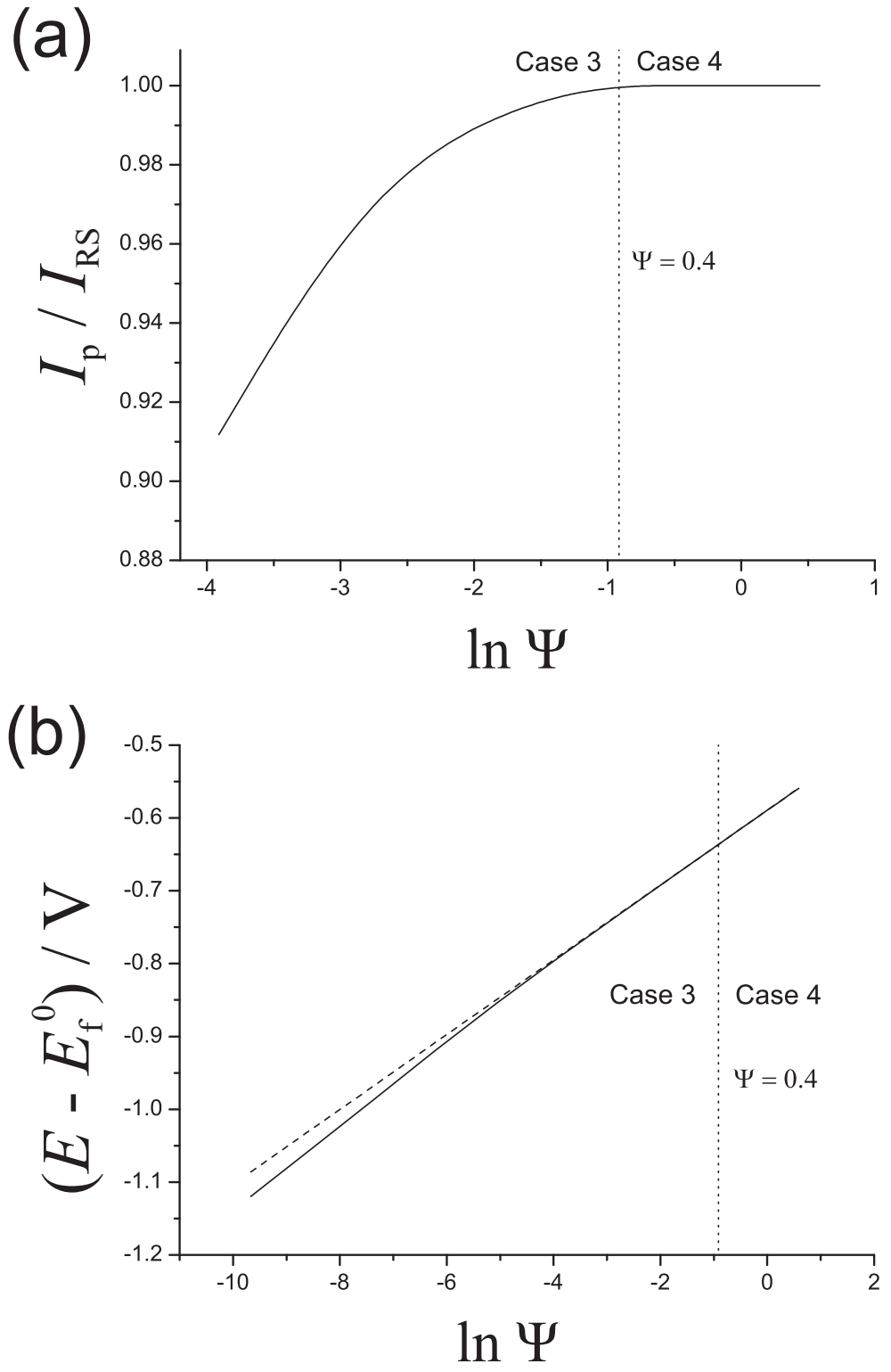

Figure 7.9: *Variation of (a) peak current, I_p, and (b) peak potential, E_p with coverage, Θ, for an array of hemispherical particles with $k^0 = 10^{-7}$ cm s^{-1}, $r_e = 100$ nm (with $c_A^* = 1$ mM; $D = 10^{-5}$ cm^2 s^{-1}; $\alpha = 0.5$; $\nu = 0.1$ V s^{-1}). Dashed line for (b) shows E_p predicted by Equation 7.24.*

longer given by the Randles-Ševčík equation (Equation 7.15). Strictly, Equation 7.24 only applies in the case 4 limit, but as can be seen in Figure 7.9 (b), it provides a good approximation to the real value of E_p even at coverages as low as $\Psi = 0.003$ ($\ln \Psi = -6$, $d = 5.16$ μm), despite the rapid drop off of peak current as the coverage is decreased.

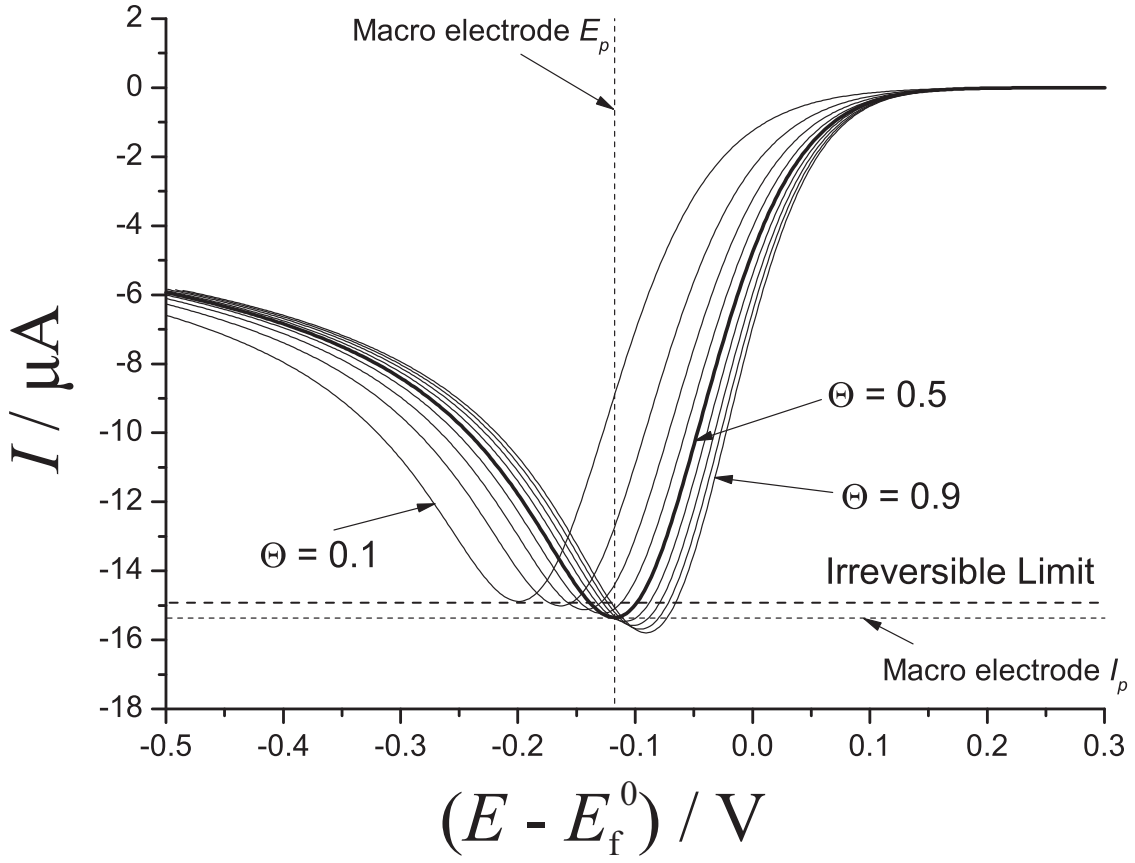

Figure 7.10: *Voltammetry of an array of hemispherical nanoparticles as surface coverage, Θ, is varied in increments of 0.1. $k = 10^{-3}$ cm s^{-1}, $r_e = 100$ nm (with $c_A^* = 1$ mM; $D = 10^{-5}$ cm^2 s^{-1}; $\alpha = 0.5$; $\nu = 0.1$ V s^{-1}).*

Figure 7.10 shows the variation of voltammetry with Θ when $k^0 = 10^{-3}$ cm s^{-1}. For a planar macroelectrode, this rate constant corresponds to the quasi-reversible region. In the figure, although the peak current is at the irreversible limit for low coverage (Θ = 0.1, $d = 632$ nm), as the coverage increases, so too does I_p as k^0_{app} moves into the quasi-reversible region. Once again, the peak potential and current for Θ = 0.5 ($d = 282$ nm) exactly match those of a planar macroelectrode of the same geometric area. This suggests that the relationship $k^0_{app} = k^0\Psi$ applies outside of the purely irreversible limit.

7.3.3 Variation of α and ν

Figure 7.11 (a) demonstrates how variation of the transfer coefficient α (in the range 0.2 – 0.8) affects the voltammetry of an array of hemispherical electrodes with $k^0 = 10^{-7}$ cm s^{-1}, $\Psi = 0.6$ ($\Theta = 0.3$), and $r_e = 100$ nm ($d = 365$ nm). The peak positions of these voltammograms in terms of E_p and I_p show excellent agreement with the values given by Equations 7.24 and 7.15 respectively. By rearrangement of Equation 7.24,

$$\alpha(E_p - E_f^0) = -\frac{RT}{F}\left(0.78 + \ln\left(\sqrt{\frac{FD\nu}{RT}}\right) - \ln(\Psi k^0)\right) - \frac{RT}{F}\ln\sqrt{\alpha} \qquad (7.26)$$

When holding all other variables constant except the independent variable, α, and the dependent variable, E_p, this is an equation of the form

$$\alpha(E_p - E_f^0) = c + m\ln\sqrt{\alpha} \qquad (7.27)$$

where c and m are constant. This linear relationship is demonstrated in Figure 7.11 (b) which shows $\alpha(E_p - E_f^0)$ plotted against $\ln\sqrt{\alpha}$ for a range of values of α for the same electrode system. Excellent agreement between the simulated results and the relationship predicted by Equation 7.26 is seen.

Figure 7.12 demonstrates how E_p varies with the scan rate, ν, for an array of hemispherical electrodes with $k^0 = 10^{-7}$ cm s^{-1}, $\Psi = 0.6$ ($\Theta = 0.3$) , and $r_e = 100$ nm ($d = 365$ nm). Excellent agreement is seen except at very high scan rates. This is because at high scan rates, the time-scale of the experiment is very short compared with the rate of diffusion and so diffusion is no longer in case 4.

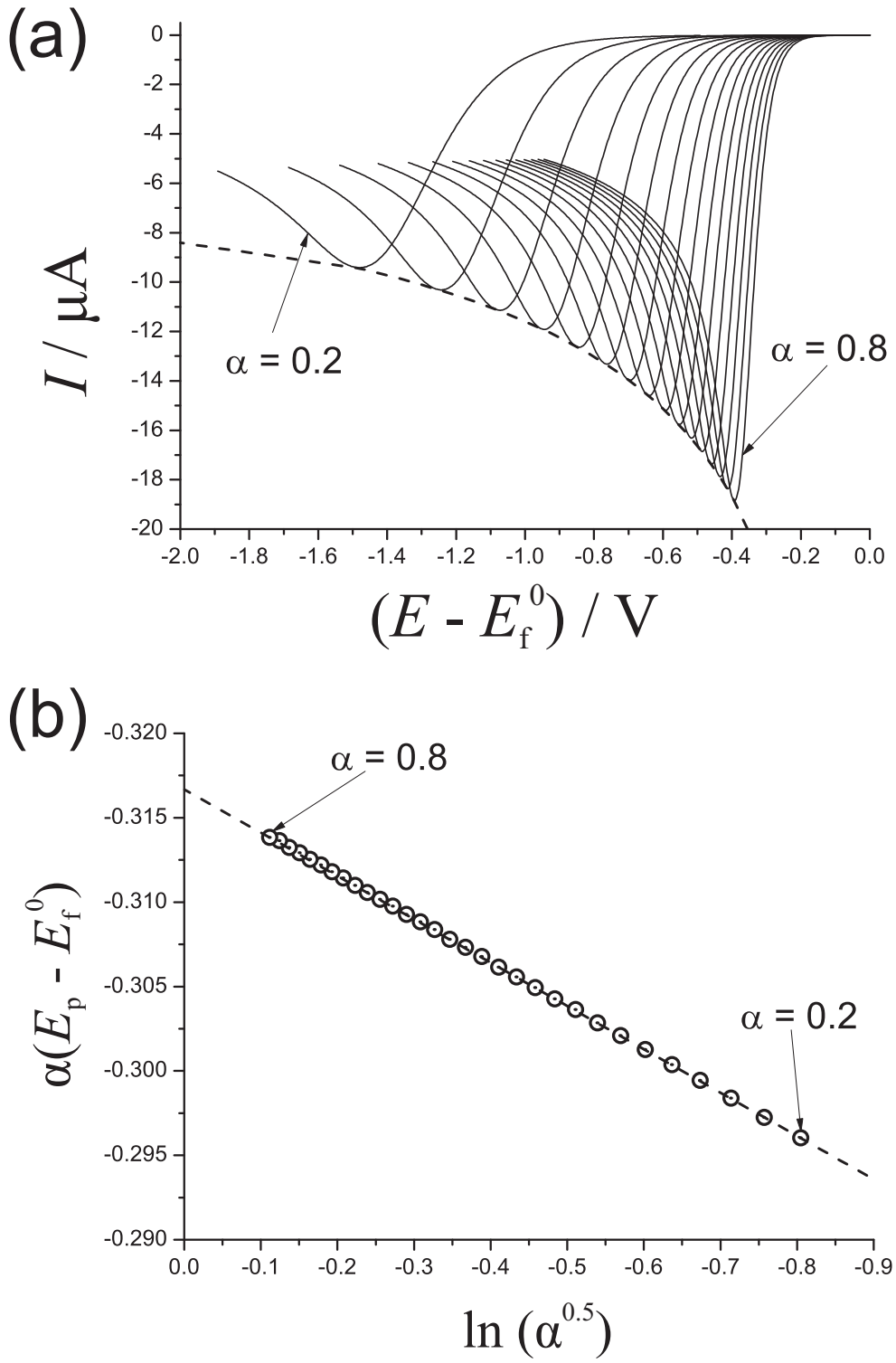

Figure 7.11: *(a) Simulated voltammetry of an array of hemispherical nanoparticles with varying transfer coefficient, α in the range 0.2-0.8 with dashed line showing the peak position for varying α, in terms of E_p and I_p as predicted by Equations 7.24 and 7.15 respectively; (b) the dependence of peak position, E_p of the same with dashed line showing the relationship predicted by Equation 7.26. $\Psi = 0.6$, $k = 10^{-7}$ cm s^{-1}, $r_e = 100$ nm ($c_A^* = 1$ mM; $D = 10^{-5}$ cm^2 s^{-1}; $\alpha = 0.5$; $\nu = 0.1$ V s^{-1}).*

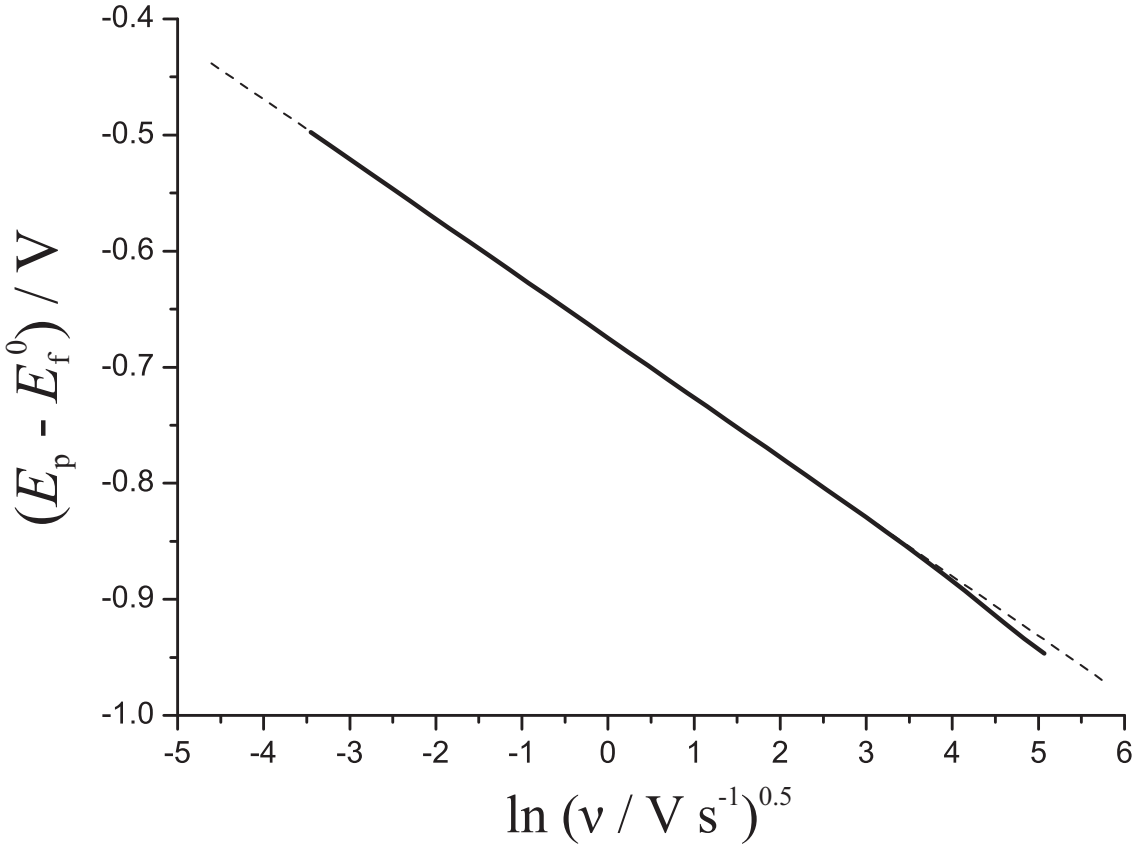

Figure 7.12: *Variation of E_p with scan rate, ν, in the range $10^{-4} - 10^4$ $V\ s^{-1}$, for an array of hemispherical particles with $\Psi = 0.6$, $k = 10^{-7}$ $cm\ s^{-1}$, $r_e = 100$ nm , $d = 365$ nm ($c_A^* = 1$ mM; $D = 10^{-5}$ $cm^2\ s^{-1}$; $\alpha = 0.5$).*

7.3.4 Particle Size

The effect of the size of the electroactive particles on the voltammetry is now considered. As the size of the particles increase (for a fixed Θ), the distance, d, between neighbouring particles increases and so the diffusion transitions from case 4 to case 3 when the size is increased above a certain limit. This size limit is smaller for lower values of Θ since a lower surface coverage results in a greater inter-particle separation. Figure 7.13 demonstrates how E_p and I_p vary with particle radius, r_e, for a range of values of Ψ ($= 2\Theta$) for an irreversible process. It can be seen that for a given value of electroactive surface area, Ψ, in the limit of low particle size (approximately $r_e < 100$ nm for the examples shown), the position of the peak in terms of both potential and current does not depend on r_e. Rather the voltammetric behaviour depends only on the value of Ψ, and not on the size of electroactive material, so long as the diffusion is in case 4.

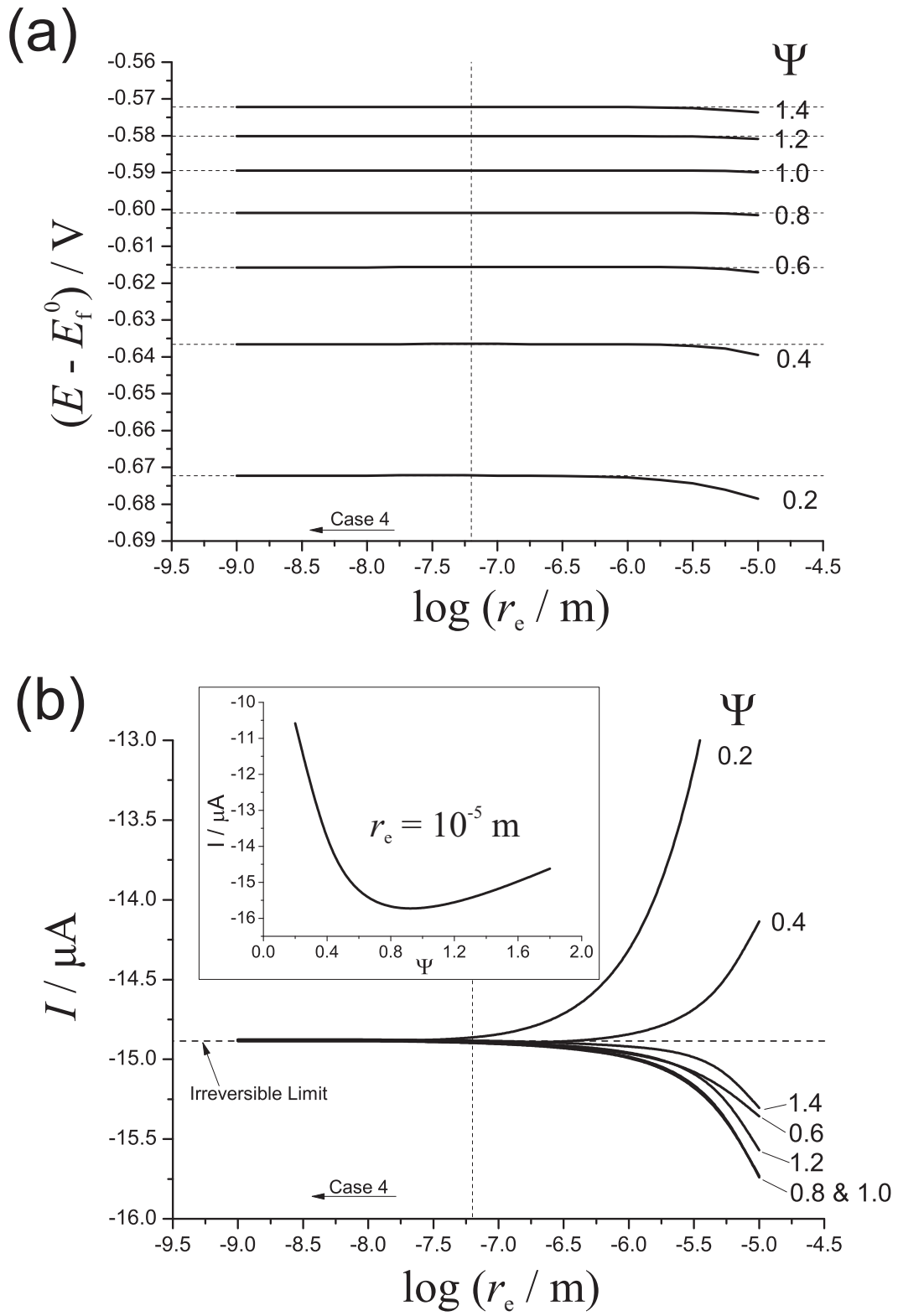

Figure 7.13: *Variation of (a) peak potential, and (b) peak current with particle radius, r_e, for a range of values of Ψ, for an array of hemispherical particles with $k^0 = 10^{-7}$ cm s^{-1}. Dashed horizontal lines in (a) show the value predicted by Equation 7.24. The inset in (b) shows the variation of I_p with Ψ for $r_e = 10^{-5}$ m (with $c_A^* = 1$ mM; $D = 10^{-5}$ cm^2 s^{-1}; $\alpha = 0.5$; $\nu = 0.1$ V s^{-1}).*

The inset in Figure 7.13 (b) demonstrates the apparently anomalous behaviour seen when the particle size is large enough that diffusion is no longer case 4, but where the peak current actually *exceeds* that predicted by the Randles-Ševčík equation for certain coverages. When the individual particles are this large, diffusion has mostly case 1 character on the timescale of the experiment. Consequently, the peak current is determined by the total electroactive surface area of the particles rather than by the geometric surface area of the substrate, and may thus exceed the Randles-Ševčík limit. When the particles are this large, diffusion of fresh analyte material comes both from bulk solution and from the thin layer of solution that exists between the particles in the region of the surface. As the coverage increases, the contribution from this thin layer decreases, leading to a decrease in I_p as shown in the inset in Figure 7.13 (b).

7.3.5 Spheres and Other Particle Shapes

In order to demonstrate that the results derived above (particularly Equation 7.24) are applicable to a variety of electrode geometries, simulations of a number of different geometries were performed. First, an array of electroactive spherical particles on an inactive surface, as depicted in Figure 7.1 (d), is considered. This differs from the hemisphere case in that the surfaces of the particles are not uniformly accessible. This model corresponds to the commonly encountered experimental situation of an ensemble of metal nanoparticles deposited on a surface. A range of simulations were performed for this geometry, again varying k^0, Θ, and r_e. For an array of spheres, the surface area ratio is twice that of an array of hemispheres for the same coverage, i.e.

$$\Psi = \frac{4N\pi r_e^2}{A} = 4\Theta \tag{7.28}$$

such that,

$$k^0_{app} = 4\Theta k^0 \tag{7.29}$$

Figure 7.14 shows how the voltammetry varies with k^0 for a fixed value of $\Theta = 0.2$ ($\Psi = 0.8$), and $r_e = 100$ nm ($d = 447$ nm). As for the voltammetry of a hemispher-

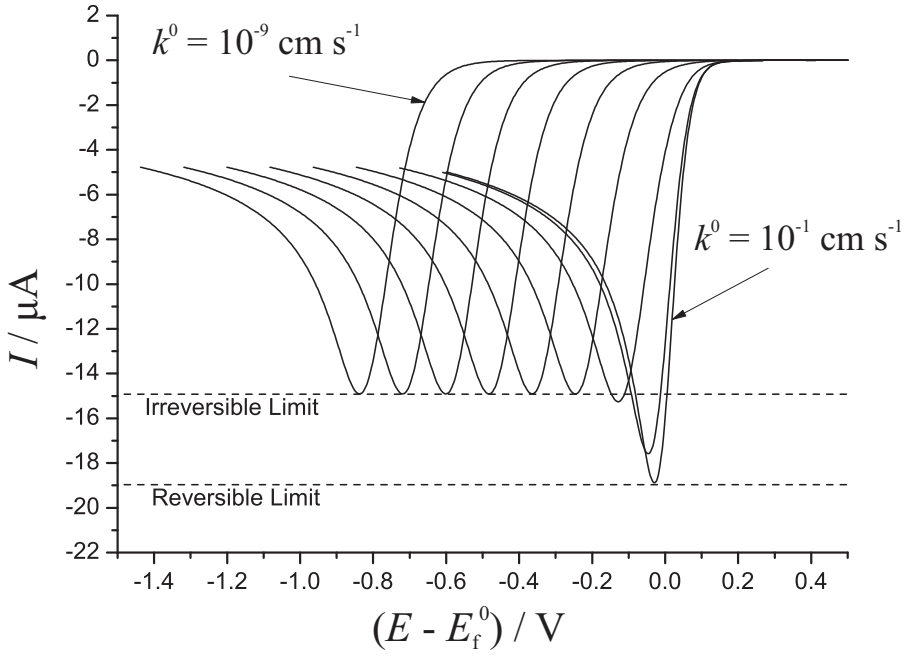

Figure 7.14: *Voltammetry of an array of spherical nanoparticles as it varies with rate constant, k^0, in the range 10^{-1}, 10^{-2}, 10^{-3}, ..., 10^{-9} cm s^{-1}, $\Theta = 0.2$ ($\Psi = 0.8$), and $r_e = 100$ nm, $d = 447$ nm (with $c_A^* = 1$ mM; $D = 10^{-5}$ cm^2 s^{-1}; $\alpha = 0.5$; $\nu = 0.1$ V s^{-1}).*

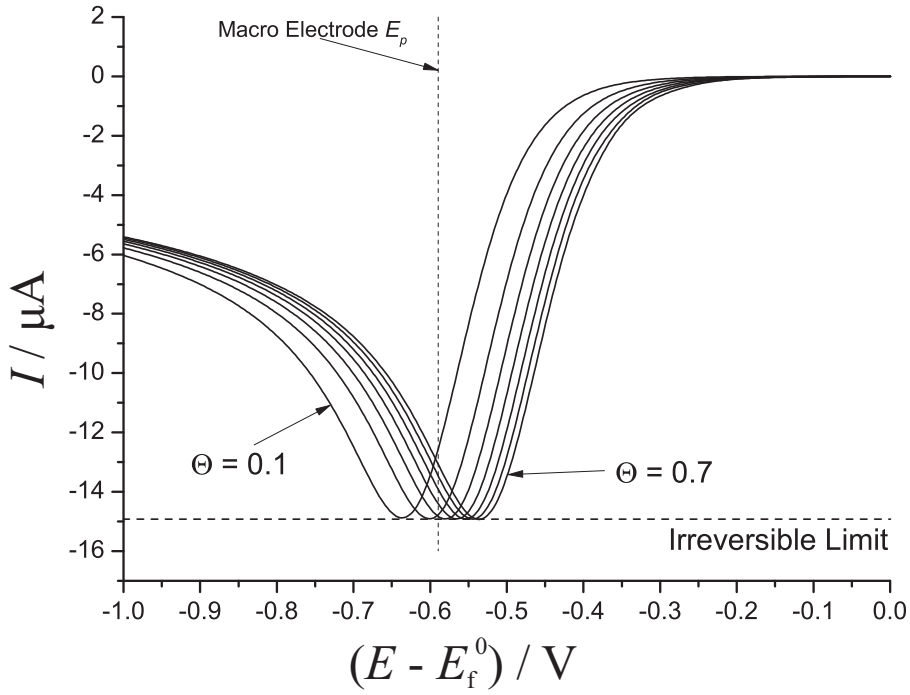

Figure 7.15: *Voltammetry of an array of spherical nanoparticles as it varies with surface coverage, Θ, in increments of 0.1. $k = 10^{-7}$ cm s^{-1}, $r_e = 100$ nm (with $c_A^* = 1$ mM; $D = 10^{-5}$ cm^2 s^{-1}; $\alpha = 0.5$; $\nu = 0.1$ V s^{-1}).*

ical array shown in Figure 7.6, the peak height transitions from the irreversible to the reversible Randles-Ševčík limits as k^0 is increased.

Figure 7.15 demonstrates how the peak potential of the voltammetry in the irreversible limit shifts with Θ in the range $0.1 - 0.7$ ($\Psi = 0.4 - 2.8$) with $r_e = 100$ nm (corresponding to d in the range 632-239 nm) as similarly demonstrated for an array of hemispheres in Figure 7.7. Note the position of E_p for a macro-electrode which corresponds to $\Theta = 0.25$. Figure 7.16 demonstrates how the simulated peak potential is affected by varying Θ for a range of values of k^0 (as shown for hemispheres in Figure 7.8). The dashed lines indicate the values predicted by Equation 7.24, demonstrating excellent agreement with simulated results as long as the kinetics are in the irreversible limit, with deviation from that equation seen only for $k^0 \geq 10^{-3}$ cm s^{-1}.

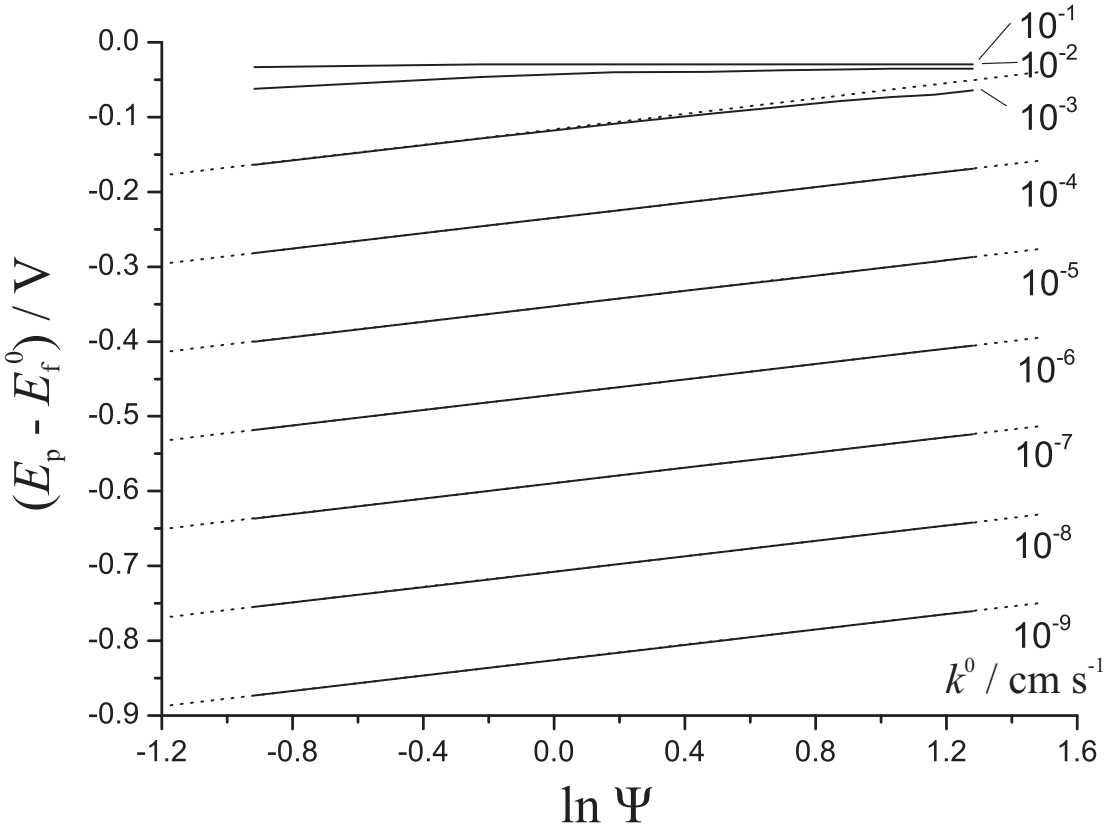

Figure 7.16: *Variation of peak potential, E_p, with coverage, Θ, for a range of values of rate constant, k^0, for an array of spherical particles with $r_e = 100$ nm (with $c_A^* = 1$ mM; $D = 10^{-5}$ cm^2 s^{-1}; $\alpha = 0.5$; $\nu = 0.1$ V s^{-1}). Dotted lines show values predicted by Equation 7.24.*

Three other non-flat electrode geometries were considered: arrays of cylindri-

cal particles on an electro-inactive surface - Figure 7.1 (g); arrays of hemispherical particles on an *active* surface - Figure 7.1 (f); and long hemicylindrical 'wires' on an inactive surface - Figure 7.1 (h). Details of the simulation parameters and figures demonstrating the behaviour of these electrode geometries in terms of the rate constant and surface coverage are given in Appendix A. The peak potential of the voltammetry in all cases obeys Equation 7.24 for kinetics in the irreversible limit as long as the diffusion is in case 4, *cf.* arrays of spheres and hemispheres. For an array of cylindrical particles:

$$\Psi = \frac{N(\pi r_e^2 + 2\pi r_e z_e)}{A} = (2\frac{z_e}{r_e} + 1)\Theta \tag{7.30}$$

where z_e is the height of the cylinder. For long hemicylindrical wires:

$$\Psi = \frac{N\pi r_e l}{A} = \frac{\pi}{2}\Theta \tag{7.31}$$

where l is the length of the wire. Finally for an electroactive surface covered in electroactive hemispheres:

$$\Psi = \frac{(1 - N\pi r_e^2) + 2N\pi r_e^2}{A} = \Theta + 1 \tag{7.32}$$

such that the surface tends toward macro-electrode behaviour as $\Theta \to 0$.

7.3.6 Nanocatalysis

It has been demonstrated above that the peak position of a voltammogram and thus the apparent kinetics is influenced by the surface area of the electroactive material accessible to diffusing species. This has important consequences in the emerging field of nanocatalysis. In recent years, numerous publications have sought to demonstrate that nanoparticulate electrode material can show an apparent catalytic effect when compared to the same material in bulk, typically by the observation of a shift in peak potential towards E_f^0. This is typically attributed to the altered physical and chemical properties of nano-scale materials as compared to their bulk equivalents, perhaps arising from the exposure of different crystal planes or changed electronic structure in nanomaterials.

By consideration of our work above, it is reasonable to conclude that in some, possibly many, cases this effect can be explained (at least partly) with reference to

the geometry of the system. A surface partially covered in electroactive nanoparticles may have a surface area ratio, $\Psi > 1$, and is thus likely to show a shift in peak current relative to a macro-electrode of the same material according to Equation 7.24. This effect is more obvious when comparing two nanoparticle modified surfaces of different coverages: for example, the difference in peak potential, ΔE_p, between electrodes with 10% and 70% coverage of spherical nanoparticles is, according to Equation 7.25, approximately 100 mV.

For a fixed volume (or mass) of electroactive material, the smaller the particles, the greater the total electroactive surface area and therefore the greater the apparent kinetics as $\Psi \propto \frac{1}{r}$ (for spherical and hemispherical particles). Consequently, a mass of material divided into N_a nanoparticles and distributed on a surface will show a greater apparent 'catalytic' effect than the same mass divided into $N_b = N_a/n$ (where $n > 1$) nanoparticles purely because of the geometry of system. Figure 7.17 illustrates this schematically, showing the same volume of material divided into (a) N spherical particles of radius 10^{-7} m and $\Psi = 0.4$ ($d = 632$ nm); and (b) $2N$ particles of radius 7.94×10^{-8} m and $\Psi = 0.504$ ($d = 566$ nm). As the value of Ψ increases when the radius is decreased, the peak potential shifts towards E_f^0. In this case, the difference in peak potential between the two is $\Delta E_p = 11.9$ mV.

From simple geometric arguments it can be shown that in general for two different distributions of particles, 'a' and 'b' such that $N_a/N_b = n$, the ratio of electroactive surface areas is equal to:

$$\frac{\Psi_{\mathrm{a}}}{\Psi_{\mathrm{b}}} = \sqrt[3]{n} \tag{7.33}$$

So from equation 7.25, the difference in peak potentials of the voltammetry of these two distributions is,

$$\Delta E_p = \frac{1}{3}\frac{RT}{\alpha F}\ln n \tag{7.34}$$

7.4 Conclusions

The naive application of semi-infinite diffusion models to electrodes modified with nanoparticles is shown to be significantly in error. In particular, it has been demonstrated that for a one-electron process at partially active, non-planar electrode, the

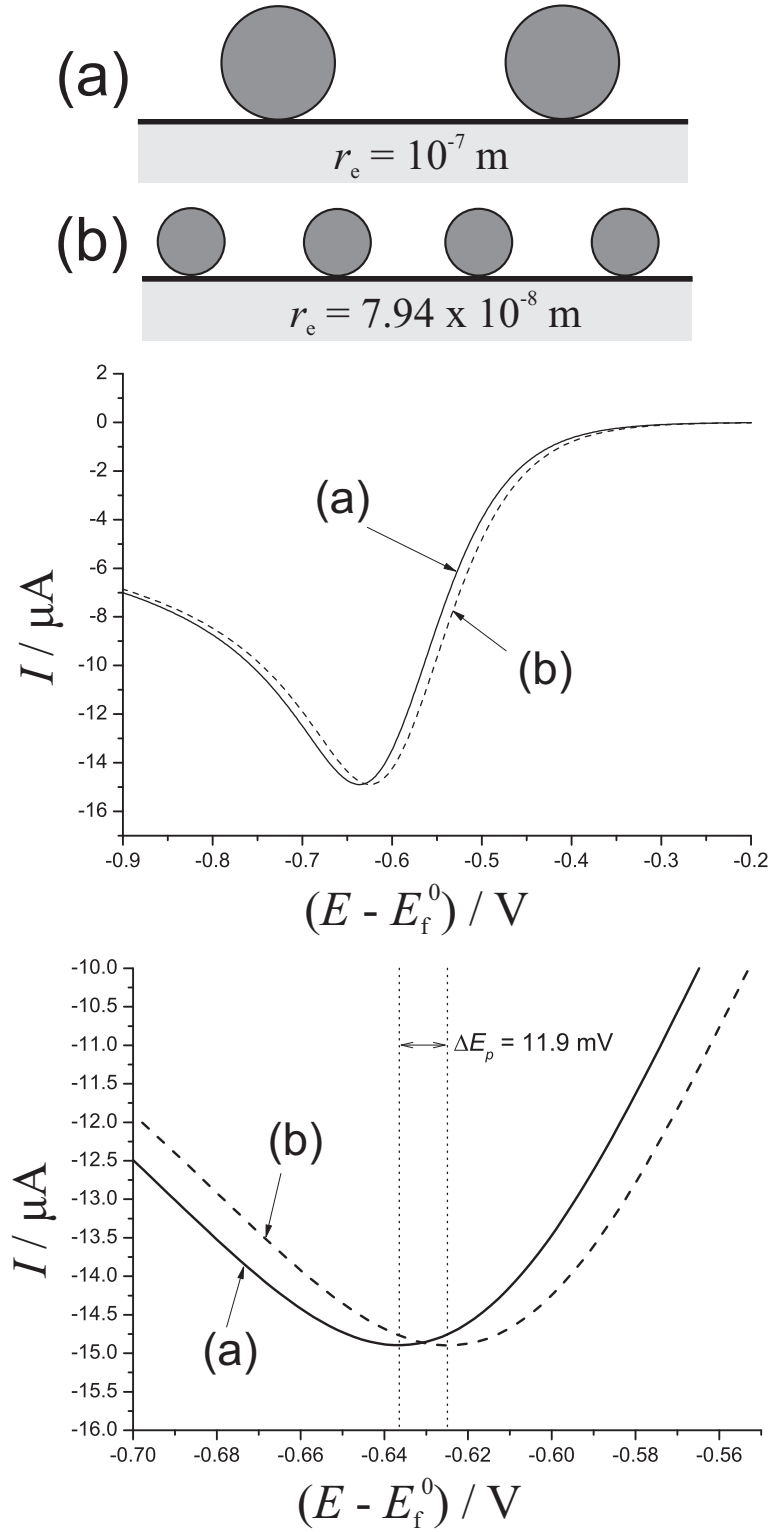

Figure 7.17: *Voltammetry (at two different scales) of two systems with the same mass of electroactive material divided into spherical particles: (a) N particles with $r_e = 100$ nm and $\Psi = 0.4$; (b) $2N$ particles with $r_e = 79.4$ nm and $\Psi = 0.504$. The difference in peak potential between the two is $\Delta E_p = 11.9$ mV. Other parameters: $k^0 = 10^{-7}$ cm s^{-1}, $\nu = 0.1$ V s^{-1}, $c_A^* = 1$ mM, $D = 10^{-5}$ cm^2 s^{-1}, $\alpha = 0.5$.*

apparent rate constant of the reaction, k_{app}, is equal to the product of the true rate constant, k^0, and the ratio, Ψ, of the total electroactive surface area to the geometric surface area of the substrate. This assumes first that the scale of the roughness of the surface is smaller than the scale of the diffusion layer thickness and second that the diffusion can be described as being case 4; that the diffusion fields of neighbouring electroactive regions strongly overlap such that diffusion to the entire surface is linear. An important consequence is that for a given value of Ψ, the voltammetry is independent of the geometry of the surface, at least for the geometries simulated (Figure 7.1). An equation, 7.24, describing the peak potential of the voltammetry in terms of Ψ has been given which allows the determination of the available surface area of electroactive material assuming other system parameters are already known (e.g. if one already knows the peak potential of a macro-electrode made of the same material).

It has further been shown that distributions of electroactive nanoparticles, with $\Psi > 1$, will display an apparent catalytic effect compared to the bulk material which is solely due to the geometry of the surface and unrelated to changes in kinetics at the nanoscale, for example by altered structural or electronic properties. Equally, any distribution of a fixed amount of material will show voltammetric responses reflecting the values of Ψ and hence the surface area of the material. The application to analysis of nanoparticle modified electrode data is evident. In Chapter 9 this concept will be extended to porous layers of significant thickness.

Bibliography

[1] K. R. Ward, M. Gara, N. S. Lawrence, R. S. Hartshorne and R. G. Compton, *J. Electroanal. Chem.*, 2013, **695**, 1–9.

[2] J. Bett and J. Lundquis, *Electrochim. Acta*, 1973, **18**, 343–348.

[3] H. R. Kunz and G. A. Gruver, *J. Electrochem. Soc.*, 1975, **122**, 1279–1287.

[4] W. M. Vogel and J. M. Baris, *Electrochim. Acta*, 1977, **22**, 1259–1263.

[5] L. J. Bregoli, *Electrochim. Acta*, 1978, **23**, 489–492.

[6] M. Peuckert, T. Yoneda, R. A. D. Betta and M. Boudart, *J. Electrochem. Soc.*, 1986, **133**, 944–947.

[7] M. Watanbe, H. Sei and P. Stonehart, *J. Electroanal. Chem.*, 1989, **261**, 375–387.

[8] N. Giordano, P. L. Antonucci, E. Passalacqua, L. Pino, A. S. Arico, V. Antonucci, V. Alderucci and V. Recupero, *Int. J. Hydrogen Energy*, 1994, **19**, 165–168.

[9] O. Antoine, Y. Bultel, R. Durand and P. Ozil, *Electrochim. Acta*, 1998, **43**, Int Soc Electrochem; Electrochem Soc.

[10] K. Yamamoto, T. Imaoka, W.-J. Chun, O. Enoki, H. Katoh, M. Takenaga and A. Sonoi, *Nat. Chem.*, 2009, **1**, 397–402.

[11] O. Antoine, Y. Bultel and R. Durand, *J. Electroanal. Chem.*, 2001, **499**, 85–94.

[12] E. Higuchi, H. Uchida and M. Watanabe, *J. Electroanal. Chem.*, 2005, **583**, 69–76.

[13] K. J. J. Mayrhofer, B. B. Blizanac, M. Arenz, V. R. Stamenkovic, P. N. Ross and N. M. Markovic, *J. Phys. Chem. B*, 2005, **109**, 14433–14440.

[14] H. Ye, J. A. Crooks and R. M. Crooks, *Langmuir*, 2007, **23**, 11901–11906.

[15] S.-J. Lee, S.-I. Pyun, S.-K. Lee and S.-J. L. Kang, *Isr. J. Chem.*, 2008, **48**, 215–228.

[16] K. J. J. Mayrhofer, D. Strmcnik, B. B. Blizanac, V. Stamenkovic, M. Arenz and N. M. Markovic, *Electrochim. Acta*, 2008, **53**, 3181–3188.

[17] J. X. Wang, H. Inada, L. Wu, Y. Zhu, Y. Choi, P. Liu, W.-P. Zhou and R. R. Adzic, *J. Am. Chem. Soc.*, 2009, **131**, 17298–17302.

[18] C. Koenigsmann, W.-p. Zhou, R. R. Adzic, E. Sutter and S. S. Wong, *Nano Lett.*, 2010, **10**, 2806–2811.

[19] M. Shao, A. Peles and K. Shoemaker, *Nano Lett.*, 2011, **11**, 3714–3719.

[20] S. Sun, G. Zhang, D. Geng, Y. Chen, R. Li, M. Cai and X. Sun, *Angew. Chem., Int. Ed.*, 2011, **50**, 422–426.

[21] W. Sheng, S. Chen, E. Vescovo and Y. Shao-Horn, *J. Electrochem. Soc.*, 2012, **159**, 96–103.

[22] A. J. Bard and L. R. Faulkner, *Electrochemical Methods: Fundamentals and Applications.*, John Wiley & Sons, New York, 2nd edn., 2001.

[23] R. G. Compton and C. E. Banks, *Understanding Voltammetry*, ICP, London, 2nd edn., 2010.

[24] C. Amatore, J. M. Savéant and D. Tessier, *J. Electroanal. Chem.*, 1983, **147**, 39–51.

[25] T. J. Davies, B. A. Brookes, A. C. Fisher, K. Yunus, S. J. Wilkins, P. R. Greene, J. D. Wadhawan and R. G. Compton, *J. Phys. Chem. B*, 2003, **107**, 6431–6444.

[26] T. J. Davies and R. G. Compton, *J. Electroanal. Chem.*, 2005, **585**, 63–82.

[27] T. J. Davies, C. E. Banks and R. G. Compton, *J. Solid State Electrochem.*, 2005, **9**, 797–808.

[28] T. J. Davies, S. Ward-Jones, C. E. Banks, J. Del. Campo, R. Mas, F. X. Munoz and R. G. Compton, *J. Electroanal. Chem.*, 2005, **585**, 51–62.

[29] J. Koutecky and V. G. Levich, *Zh. Fiz. Khim.*, 1958, **32**, 1565–75.

[30] S. Treimer, A. Tang and D. C. Johnson, *Electroanal.*, 2002, **14**, 165–171.

[31] I. Streeter and R. G. Compton, *J. Phys. Chem. C*, 2007, **111**, 18049–18054.

[32] S. R. Belding and R. G. Compton, *J. Phys. Chem. C*, 2010, **114**, 8309–8319.

[33] K. R. Ward, N. S. Lawrence, R. S. Hartshorne and R. G. Compton, *J. Electroanal. Chem.*, 2012, **683**, 37–42.

[34] E. J. F. Dickinson, I. Streeter and R. G. Compton, *J. Phys. Chem. C*, 2008, **112**, 11637–11644.

[35] R. Prehn, L. Abad, D. Sanchez-Molas, M. Duch, N. Sabate, F. J. del, Campo, F. X. Munoz and R. G. Compton, *J. Electroanal. Chem.*, 2011, **662**, 361–370.

[36] D. Sanchez-Molas, J. P. Esquivel, N. Sabate, F. X. Munoz and F. J. del, Campo, *J. Phys. Chem. C*, 2012, **116**, 18831–18846.

[37] J. E. B. Randles, *Trans. Faraday Soc.*, 1948, **44**, 327–38.

[38] A. Ševčík, *Collect. Czech. Chem. Commun.*, 1948, **13**, 349–77.

[39] H. Matsuda and Y. Ayabe, *Z. Elektrochem. Angew. Phys. Chem.*, 1955, **59**, 494–503.

[40] P. Delahay, *J. Am. Chem. Soc.*, 1953, **75**, 1190–6.

[41] R. S. Nicholson and I. Shain, *Anal. Chem.*, 1964, **36**, 706–23.

Chapter 8

Nanoconfinement in Infinite Pores

Using simulation, voltammetry within a partially electroactive cylindrical pore is investigated. The system studied consists of an insulating cylindrical tube with a ring electrode within its inner circumference, which is filled with electroactive solution, such that electron transfer occurs on the tube's interior surface. The voltammetry is examined in terms of the dimensions of the electrode ring (radius, r_e, and width, z_e) as well as the voltammetric scan rate and the diffusion coefficient of the electroactive species. Four limiting cases are observed. In the limit $r_e \to \infty$, the voltammetry varies between that expected for a macro-electrode of equivalent area (as $z_e \to \infty$) and that expected for a microband electrode of equivalent area (as $z_e \to 0$). In the limit $r_e \to 0$, the voltammetry demonstrates thin-layer behaviour as $z_e \to \infty$. Finally, in the case where r_e, $z_e \to 0$, the confinement of the solution leads to the unusual case of planar diffusion towards a micro/nano scale electrode with a current response that is equivalent to hypothetical 'macro-electrode' of area twice that of the cross sectional area of the cylinder ($2\pi r_e^2$). The conditions under which these limits operate are defined.

The work constituting this chapter has been published in the *Journal of Electroanalytical Chemistry*.[1]

8.1 Introduction

The transition from semi-infinite diffusion to thin-layer behaviour is at the heart of understanding charge transport behaviour in porous media. Moreover, such issues are presently topical because of the extensive use of porous nanomaterials in a diversity of areas such as hydrogen storage, fuel cells, batteries, etc. Of particular interest in the latter case are claimed effects arising from nano-confinement, that is to say that the diffusional properties of solutes become changed at the nanoscale due to the altered structure of solvents when they are confined to nano-sized pores.[2–10] Such effects can impart beneficial properties to the nano-material.

From an electrochemical perspective, it is important to be able to distinguish enhanced transport effects arising from nano-confinement from simple Fickian diffusion giving rise to thin-layer behaviour. To this end, in this chapter, the voltammetry at an annular electrode located flush with the walls of a cylindrical pore containing electrolyte is considered, and the effect of pore size on the Fickian voltammetry is examined. Four limiting cases resulting from different length scales are identified and equations are given which define the conditions under which they operate. It is hoped that this will provide a partial basis for delineating authentic nano-confinement effects.

8.2 Theory

8.2.1 Model System

Throughout this study a one-electron oxidation of the form,

$$\mathrm{A} \rightleftharpoons \mathrm{B} + \mathrm{e}^- \tag{8.1}$$

is considered, in which only species 'A' is initially present in solution at a uniform concentration, c_{A}^* and the diffusion coefficients of A and B are equal such that at every point in space their concentrations sum to c_{A}^*.

The system under consideration takes the form of a band of conducting electrode material flush with the circumference of an infinitely long cylindrical insulating pore

as illustrated in Figure 8.1. The electrode is defined by two lengths: the radius of the cylinder, r_e, and the height of the band, z_e, as shown in the figure. Electrodes of this type, so called 'annular microbands', have previously been studied theoretically[11] for the case where the annular band is on the external surface of the cylinder. However the treatment here is different: a cylindrical tube (pore) *filled* with electroactive solution is considered, so essentially creating a no-flow tubular electrode.[12–15]

The electrode system may be modelled in a 3-dimensional cylindrical polar coordinate system (r,z,ϕ) as shown in Figure 8.1. As with previously studied systems such as the microdisc electrode (see Chapter 2), this system is axisymmetric such that $\partial c/\partial\phi \equiv 0$. In this coordinate system the mass transport of chemical species due to diffusion is described by Fick's second law:

$$\frac{\partial c}{\partial t} = D\left(\frac{\partial^2 c}{\partial r^2} + \frac{\partial^2 c}{\partial z^2} + \frac{1}{r}\frac{\partial c}{\partial r}\right) \tag{8.2}$$

Note that it is assumed that an excess of supporting electrolyte is added to the system and that it is not stirred or heated such that the migratory and convectional contributions to mass transport are negligible.[16] The system may therefore be modelled as a 2-dimensional (r, z) plane that is parallel to the central axis of the cylinder with the origin at the centre of the band as shown in Figure 8.2. This cross section has mirror symmetry in both the r and z axes so it is only necessary to simulate one quadrant which is marked with hatching in the figure. The space to be simulated is therefore a rectangular region that extends from $r = 0$ (the central axis) to $r = r_e$ (the cylinder radius) in the radial coordinate, r, and from $z = 0$ (the midpoint of the band) to $z = +\infty$ in the axial coordinate, z.

Across the lines of symmetry ($r = 0$ and $z = 0$) there is necessarily no diffusive flux, so at these boundaries there are the conditions:

$$z = 0: \qquad \frac{\partial c}{\partial z} = 0 \tag{8.3}$$

$$r = 0: \qquad \frac{\partial c}{\partial r} = 0 \tag{8.4}$$

Likewise, the insulating outer wall of the cylinder is a solid boundary which also admits no flux:

$$r = r_e,\ z > \frac{z_e}{2}: \qquad \frac{\partial c}{\partial r} = 0 \tag{8.5}$$

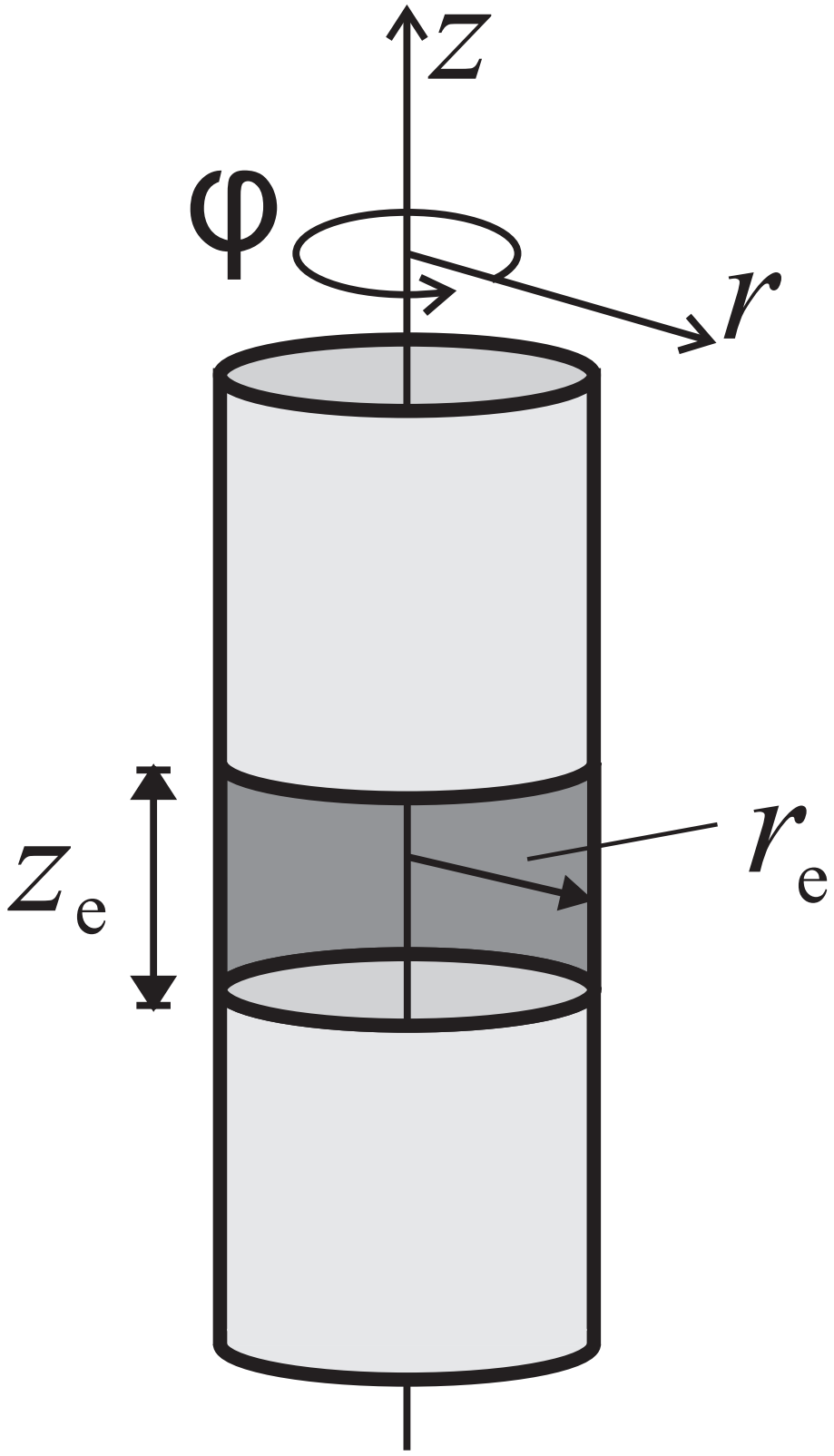

Figure 8.1: *Band of conducting electrode of height z_e, embedded in an infinitely long hollow insulating cylinder of radius r_e and the (r, z, ϕ) cylindrical polar coordinate system. The front section of the conducting band is drawn as transparent.*

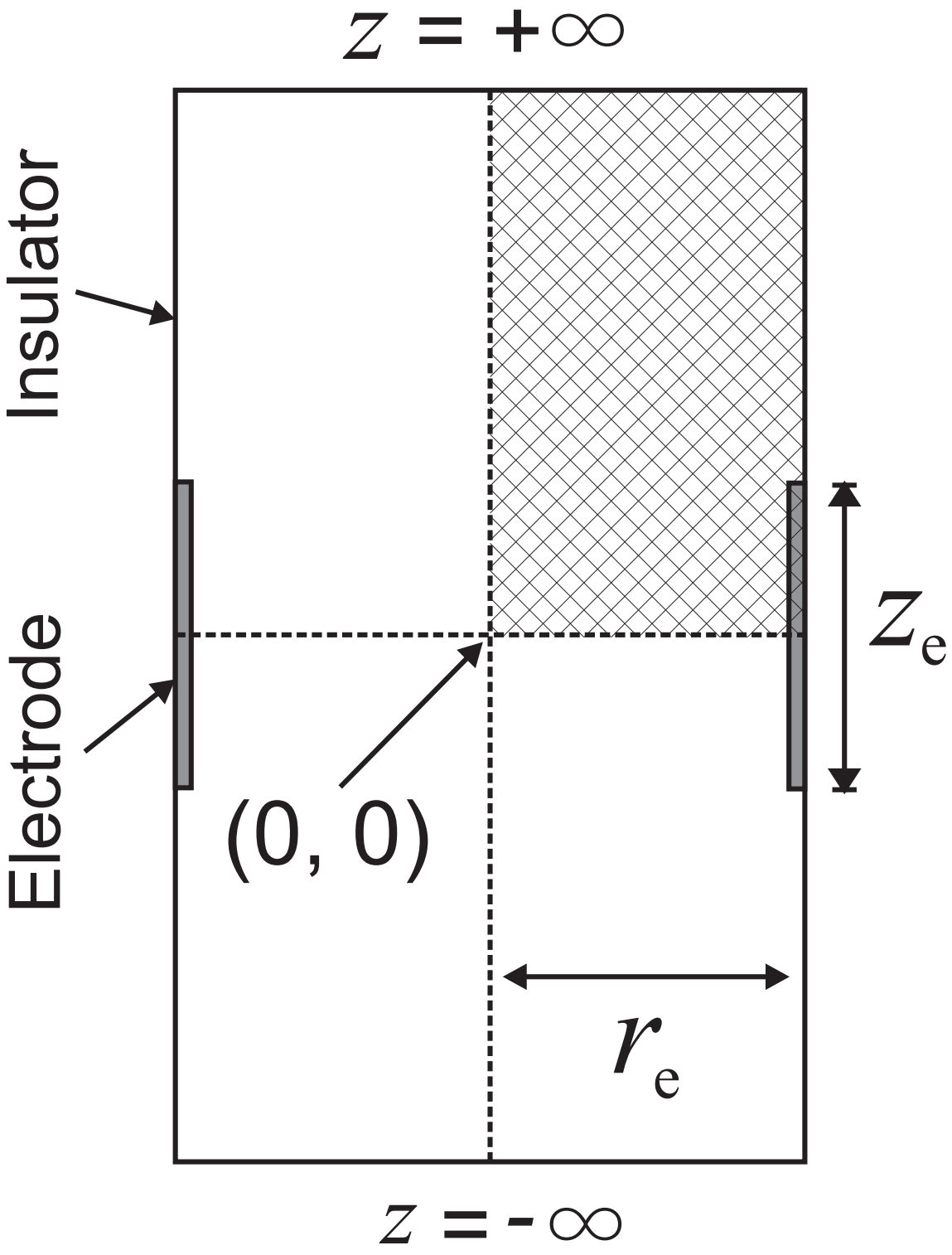

Figure 8.2: *Cross section of the cylindrical electrode system - an (r, z) plane. Marked quadrant is the simulation space.*

At the conducting section of the cylinder wall ($r = r_\mathrm{e}$, $0 < z < z_\mathrm{e}/2$), the Butler–Volmer equation,

$$D \left.\frac{\partial c}{\partial r}\right|_{r=r_\mathrm{e}} = k^0 \left[c_0 \exp\left(\frac{(1-\alpha)F(E-E_f^0)}{\mathcal{RT}}\right) - (1-c_0)\exp\left(\frac{-\alpha F(E-E_f^0)}{\mathcal{RT}}\right)\right] \tag{8.6}$$

is used as a boundary condition. Finally, at the $z = +\infty$ boundary, the concentration may be set to its bulk (initial) value, c_A^*, as the concentration at the boundary cannot possibly be perturbed by the electron transfer processes occurring at the electrode. In practice, the $z = +\infty$ boundary does not need to be infinitely far away from the electrode but just far enough away that no perturbation in the concentration is possible. This distance z_max; is equal to[17]

$$z_\mathrm{max} = z_\mathrm{e} + 6\sqrt{Dt_\mathrm{max}} \tag{8.7}$$

where t_max is the length of the time that the simulated experiment will run for. At this boundary, the concentration is always equal to its bulk value, i.e., $c = c^*$. The 2-dimensional simulation space and all of its boundary conditions are illustrated in Figure 8.3. Note that because of the mirror symmetry in the line $z = 0$, which imposes the boundary condition given in Equation 8.3, the model described herein is equally applicable to a flat-bottomed cylindrical pore with its base at $z = 0$. Such a system would also have a no-flux condition at this solid boundary and would give a current response exactly half that of the infinite cylinder model.

As with other two-dimensional systems already encountered, solution may be achieved through the use of the alternating direction implicit (ADI) method.[18] A schematic of the discretized spatial grid is shown in Figure 8.4. It is generated such the spacing between adjacent points is smallest at the boundaries (except the $z = z_\mathrm{max}$ boundary) and greater further away from them. For the r coordinate, the spacing between two adjacent points, $i+1$ and i, $\Delta r_i = r_{i+1} - r_i$ is given by:

$$r \leq \frac{r_\mathrm{e}}{2}: \qquad \Delta r_i = \Delta r_0 \gamma^i \tag{8.8}$$

$$\frac{r_\mathrm{e}}{2} < r < r_\mathrm{e}: \qquad \Delta r_i = \Delta r_0 \gamma^{(n-1-i)} \tag{8.9}$$

where n is the total number of space points, $\Delta r_0 = r_1 - r_0$ is the spacing between the

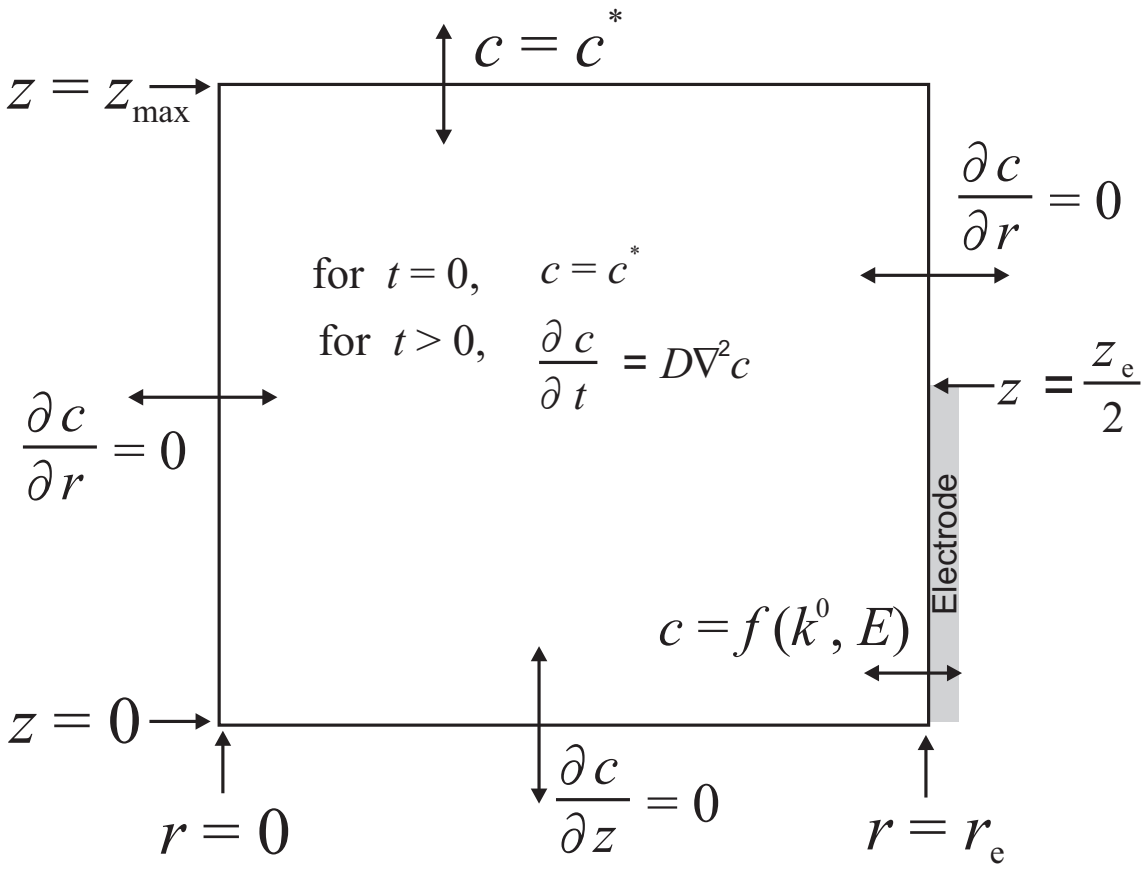

Figure 8.3: *The 2-dimensional simulation space used to simulate cylindrical pores in this study.*

first two points which is explicitly specified, and γ is the space expansion coefficient which is also explicitly specified. In this way the grid spacing expands from the central axis to a point midway along the radius, then contracts again from this point to the cylinder wall. The z grid is similarly defined but additionally expands from the electrode edge ($z = z_e/2$) to the semi-infinite boundary ($z = z_{max}$).

The current is proportional to the total flux at the electrode surface and may be calculated from:

$$I = 4\pi F r_e D \int_0^{z_e/2} \left.\frac{\partial c}{\partial r}\right|_{r=r_e} dz \tag{8.10}$$

8.2.2 Limiting Cases

In terms of spatial extent, there are four limiting cases of the model as depicted in Figure 8.5. Cases (a) and (b) are in the limit $r_e \to 0$, and may be thought of

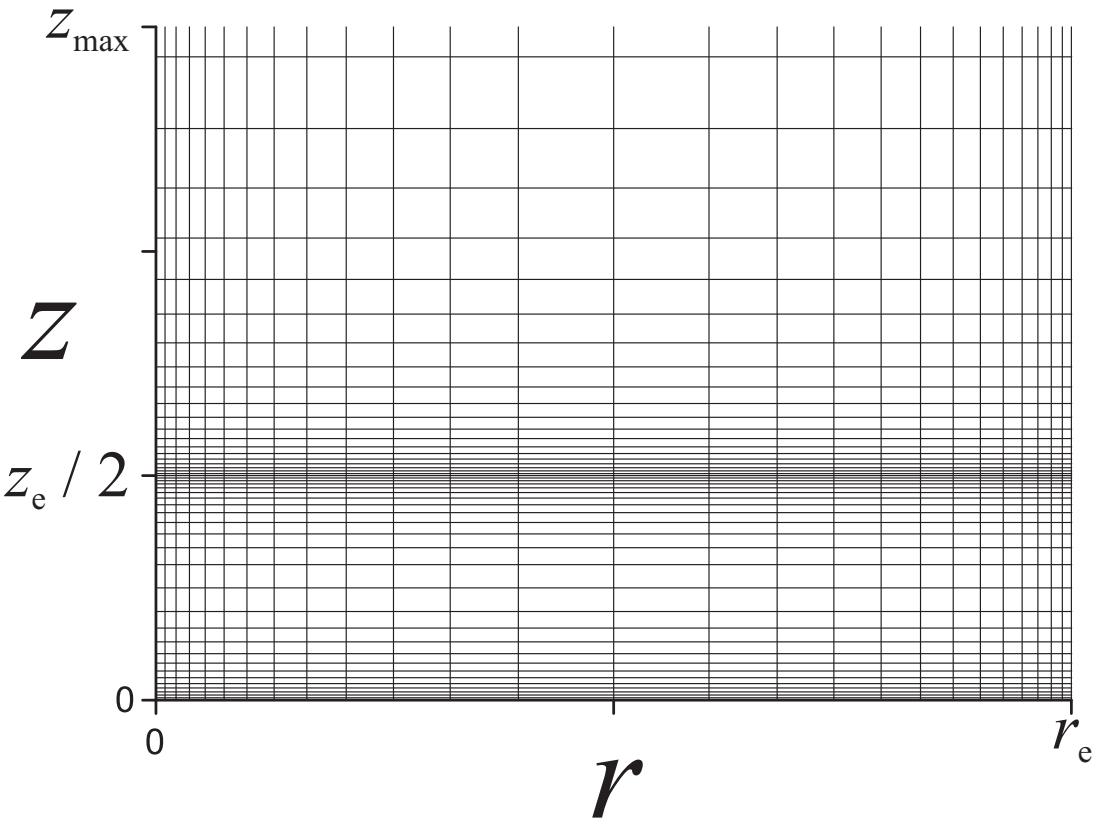

Figure 8.4: *Expanding mesh of spatial points for a 2D simulation space. Some points have been omitted for clarity.*

respectively as a capillary (pore) with a thin electroactive band (as $z_e \to 0$) and a capillary that is entirely electroactive ($z_e \to \infty$). Cases (c) and (d) are in the limit $r_e \to \infty$ and it may be expected that in this limit, simulated results will converge with those of the annular microband model.[11] Under that model, case (c), the $z_e \to 0$ limit, demonstrates behaviour equivalent to a microband of length $l = 2\pi r_e$, and width $w = z_e$. This makes intuitive sense as for large r_e, the curvature of the band is negligible on the scale of the diffusion layer. Further, case (d), the $z_e \to \infty$ limit, demonstrates macro-electrode behaviour.

8.3 Results and Discussion

Rather than considering the system in terms of the cylinder radius, r_e, the scan rate, ν, and the diffusion coefficient, D, it can instead be represented in a normalized form

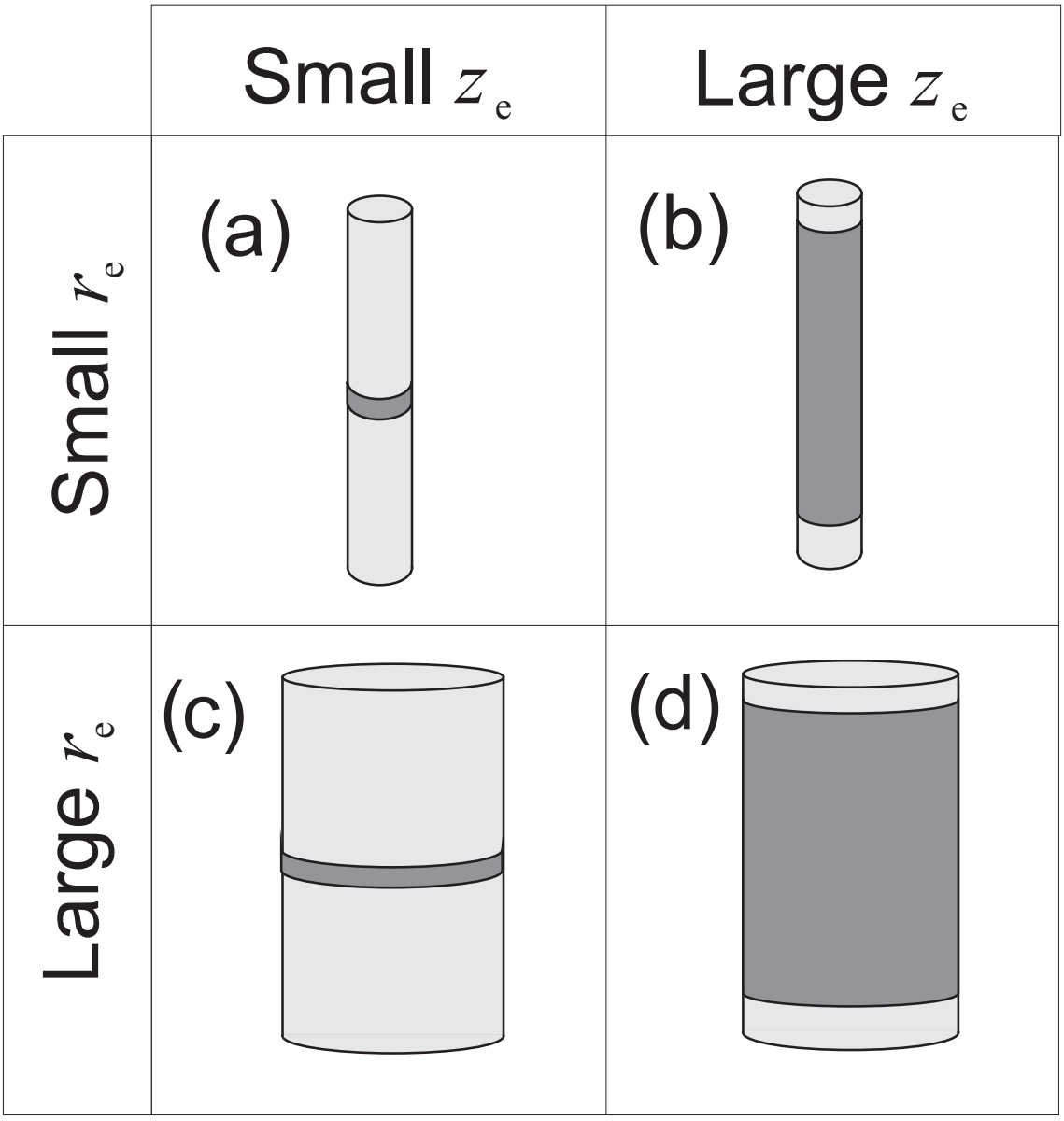

Figure 8.5: *The four limiting cases of the model. Darker areas are conducting while lighter areas are insulating.*

in terms of a dimensionless parameter σ_r, where

$$\sigma_r = \frac{r_e^2}{D}\frac{F}{\mathcal{RT}}\nu \tag{8.11}$$

Accordingly, an increase in the value of σ_r is equivalent to: increasing the cylinder radius, increasing the scan rate, or decreasing the diffusion coefficient; when considering limiting behaviour, it is preferable to consider the limits $\sigma_r \to 0$ and $\sigma_r \to \infty$ rather than $r_e \to 0$ and $r_e \to \infty$. σ_r may be thought of as the 'normalized square of the radius'. A second parameter, the 'normalized square of the height', σ_z, is also necessary and is defined as

$$\sigma_z = \frac{z_e^2}{D}\frac{F}{\mathcal{RT}}\nu \tag{8.12}$$

The voltammetry can be more conveniently represented using dimensionless normalized units. The normalized current, J, is

$$J = J_A = \frac{Ir_e}{FADc_A^*} \tag{8.13}$$

where $A = 2\pi r_e z_e$ is the area of the electrode surface. The dimensionless potential, θ, is defined as:

$$\theta = \frac{F}{\mathcal{RT}}(E - E_f^0) \tag{8.14}$$

where E_f^0 is the formal potential of the electrochemical reaction. For a temperature of 298 K, and a formal potential of 0 V, $\theta = 38.94$. Note that the above is not the only possible normalization scheme but it does simplify the equations and presentation of data for this particular model system. One obvious alternative is to treat σ_r as a dimensionless scan rate and use z_e/r_e as a second parameter, however this scheme makes presentation of data difficult, particularly surface plots, as the region of the σ_r-z_e/r_e space that is explorable is not square.

A large number of simulations were performed by varying σ_r and σ_z both in the range 10^{-8}–10^8, in the limit of fully reversible kinetics.

8.3.1 The Infinite Cylinder - The $\sigma_z \to \infty$ Limit

First, the case of $\sigma_z \to \infty$ is considered. Figure 8.6 shows voltammetry as it varies with σ_r in terms of the normalized parameters, J and θ. Figure 8.7 shows the variation of the dimensionless peak current of the voltammetry, J_p, with the di-

mensionless parameter, σ_r. It can be seen the peak current transitions from one limiting behaviour as $\sigma_r \to 0$ (as illustrated in Figure 8.5 (b)), to a different limiting behaviour, as $\sigma_r \to \infty$ (Figure 8.5 (d)).

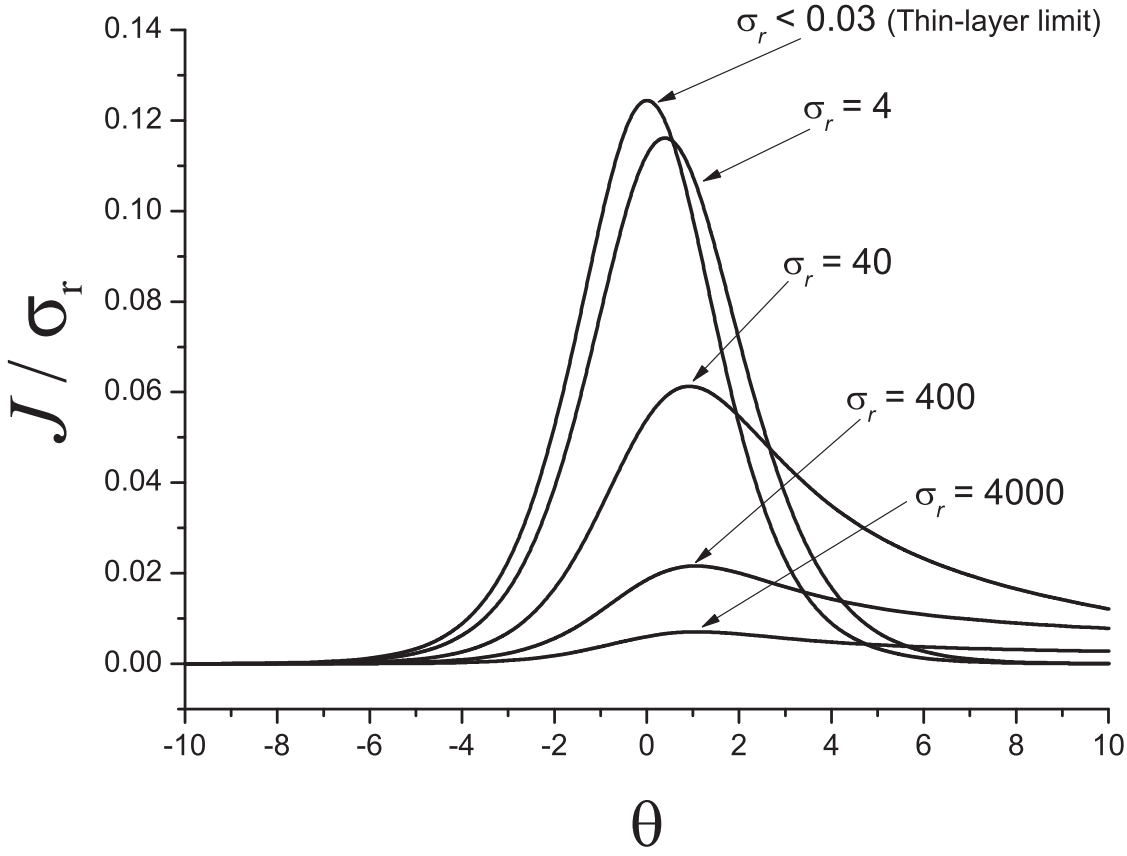

Figure 8.6: *Voltammetry as it varies with σ_r in the $z_e \to \infty$ limit in terms of $J\sigma_r^{-1}$ and normalized potential, θ.*

In the latter case, J_p is seen to obey the Randles-Ševčík equation,[19,20] consistent with the behaviour observed for an 'exterior annular microband'[11] i.e.

$$J_p = 0.446\sqrt{\sigma_r} \tag{8.15}$$

In dimensioned variables this is:

$$I_p = 0.446FAc_{\mathrm{A}}^{*}\sqrt{\frac{FD\nu}{\mathcal{RT}}} \tag{8.16}$$

This behaviour is indicative of a macro-electrode. In the $\sigma_r \to 0$ limit, the dimensionless peak current is seen to obey the relation:

$$J_p = \frac{\sigma_r}{8} \tag{8.17}$$

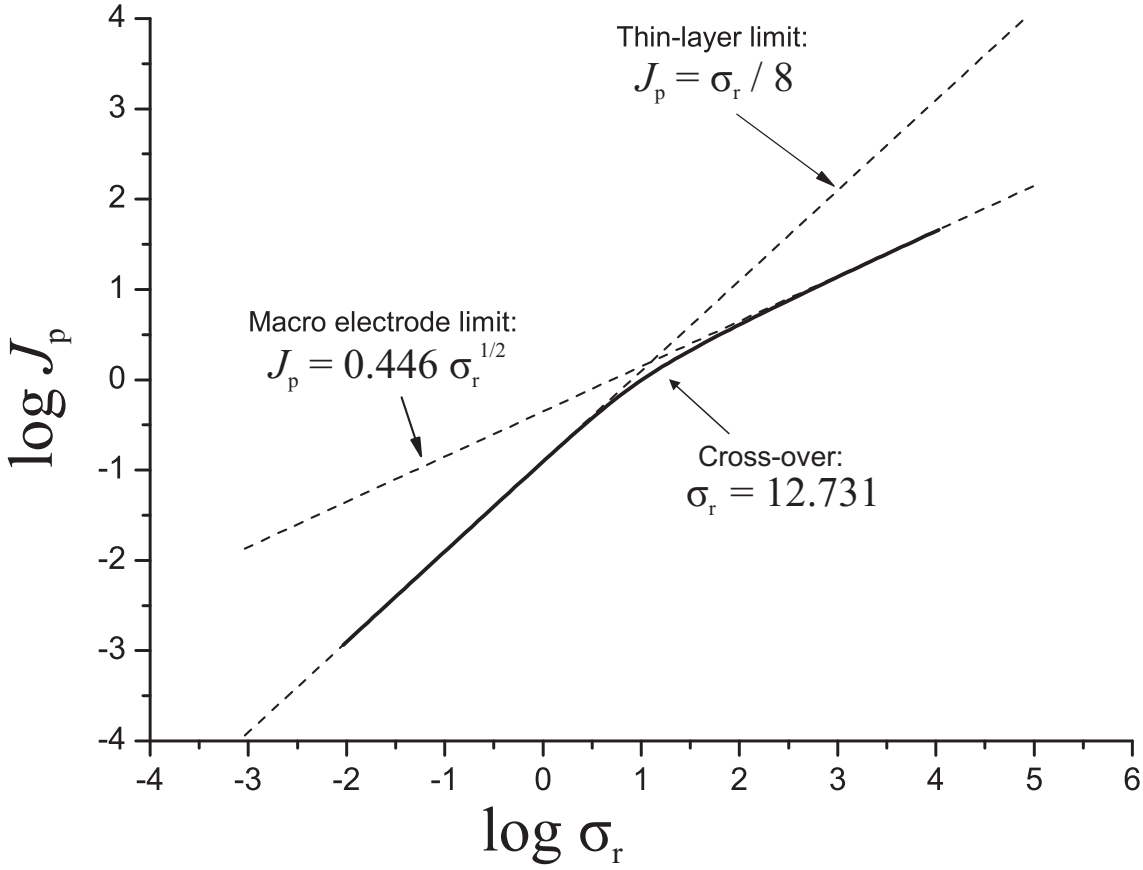

Figure 8.7: *Normalized peak current, J_p of the forward sweep of simulated voltammetry of the interior of an infinite cylinder ($\sigma_z \to \infty$) as it varies with the dimensionless parameter, σ_r.*

In dimensioned variables this is

$$I_p = \frac{F^2 \nu V c_{\mathrm{A}}^*}{4\mathcal{R}\mathcal{T}} \tag{8.18}$$

where

$$V = \pi r_{\mathrm{e}}^2 z_{\mathrm{e}} \tag{8.19}$$

is the volume of the cylinder. This is the behaviour expected to be exhibited by a "thin-layer cell".

Figure 8.8 shows concentration profiles for voltammetry of a system with $\sigma_z = 4 \times 10^7$ and $\sigma_r = 10^2$, which is intermediate between the two limiting cases above. It can be seen the the diffusion field is parallel to the cylinder wall and that the effects diffusion perpendicular to the wall at the outer edges of the electrode (at $z = \pm z_{\mathrm{e}}/2$) are negligible, such that there is effectively no concentration gradient along the z axis. This may be thought of as a 'divergent' diffusion field because the

direction of diffusion is always from the centre of the cylinder to its outer walls. The same behaviour is observed for electrode systems in the thin-layer (small σ_r) limit except that in that case, all the available electroactive solution is rapidly consumed such that the concentration effectively drops to zero after a short time.[21]

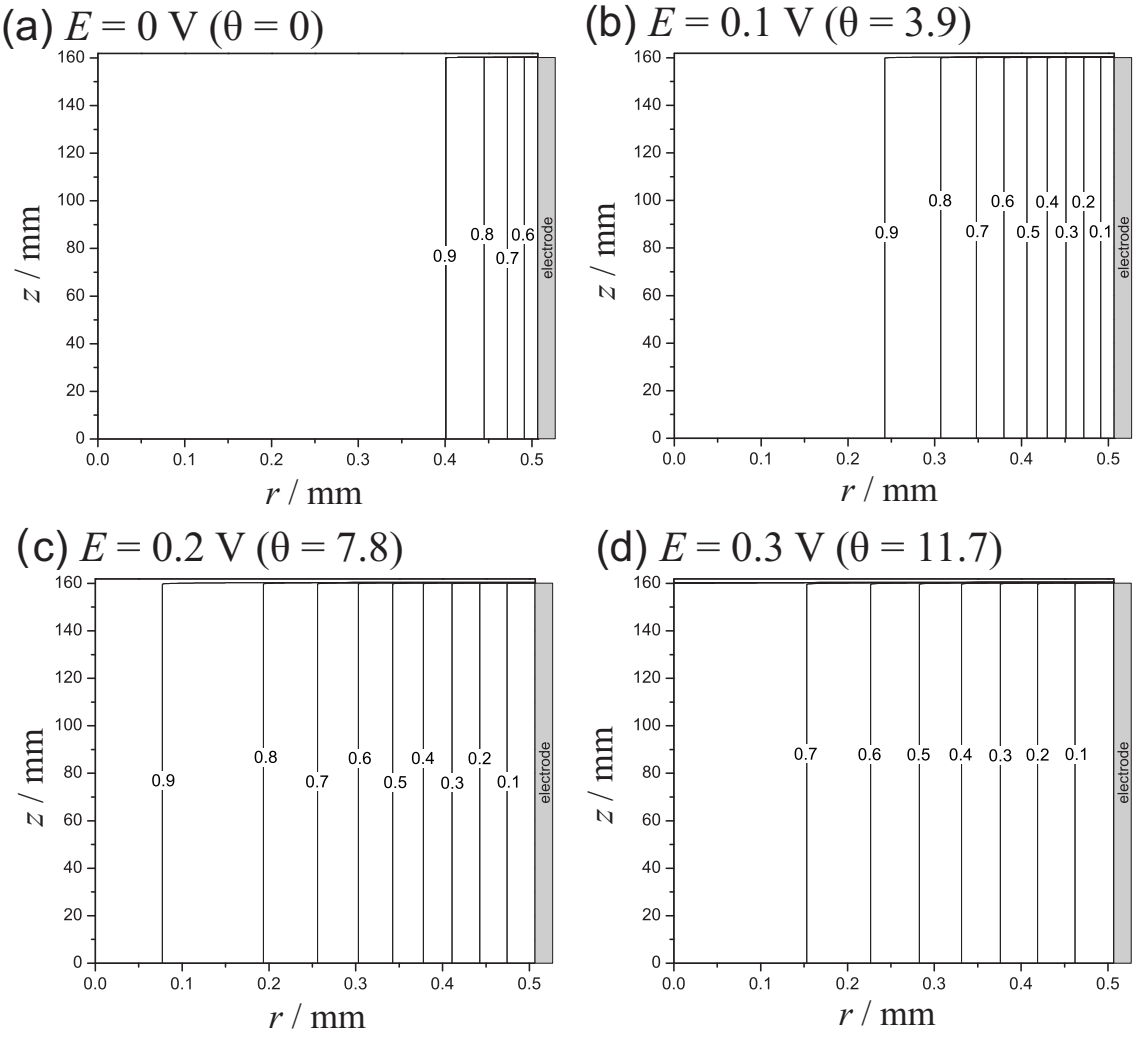

Figure 8.8: *Concentration profiles in terms of c/c^* with lines of isoconcentration (c/c^*) at different points during a voltammetric sweep ($E_f^0 = 0$ V, $T = 298$ K). $r_e = 5 \times 10^{-4}$ m; $z_e = 3.2 \times 10^{-1}$ m; $D = 10^{-9}$ m^2 s^{-1}; $\nu = 0.01$ V s−1 ($\sigma_r = 10^2$, $\sigma_z = 4 \times 10^7$). Only the quadrant indicated in Figure 8.2 is shown.*

By examination of the data presented in Figure 8.7, one can specify the range of σ_r values for which the two limits apply. A reasonable definition of the zone boundaries is that in either limit, the actual peak current differs by less than 1% from the values predicted by the limiting relations (Equations 8.15 and 8.17), i.e. where,

$$\frac{J_{\mathrm{p,predicted}} - J_{\mathrm{p,actual}}}{J_{\mathrm{p,actual}}} < 0.01 \tag{8.20}$$

Under this definition, the thin-layer limiting behaviour is exhibited in the region '$\log \sigma_r < 0.19$', which (at $T = 298$ K) is equivalent to the condition:

$$r_e < 0.2\sqrt{\frac{D}{\nu}} \tag{8.21}$$

or $r_e < 2 \times 10^{-5}$ m for $D = 10^{-5}$ cm^2 s^{-1} and $\nu = 0.1$ V s^{-1}. The macro-electrode limiting behaviour is given by '$\log \sigma_r > 3.6$', which (at $T = 298$ K) is equivalent to the condition:

$$r_e > 10.1\sqrt{\frac{D}{\nu}} \tag{8.22}$$

or $r_e < 10^{-3}$ m for $D = 10^{-5}$ cm^2 s^{-1} and $\nu = 0.1$ V s^{-1}.

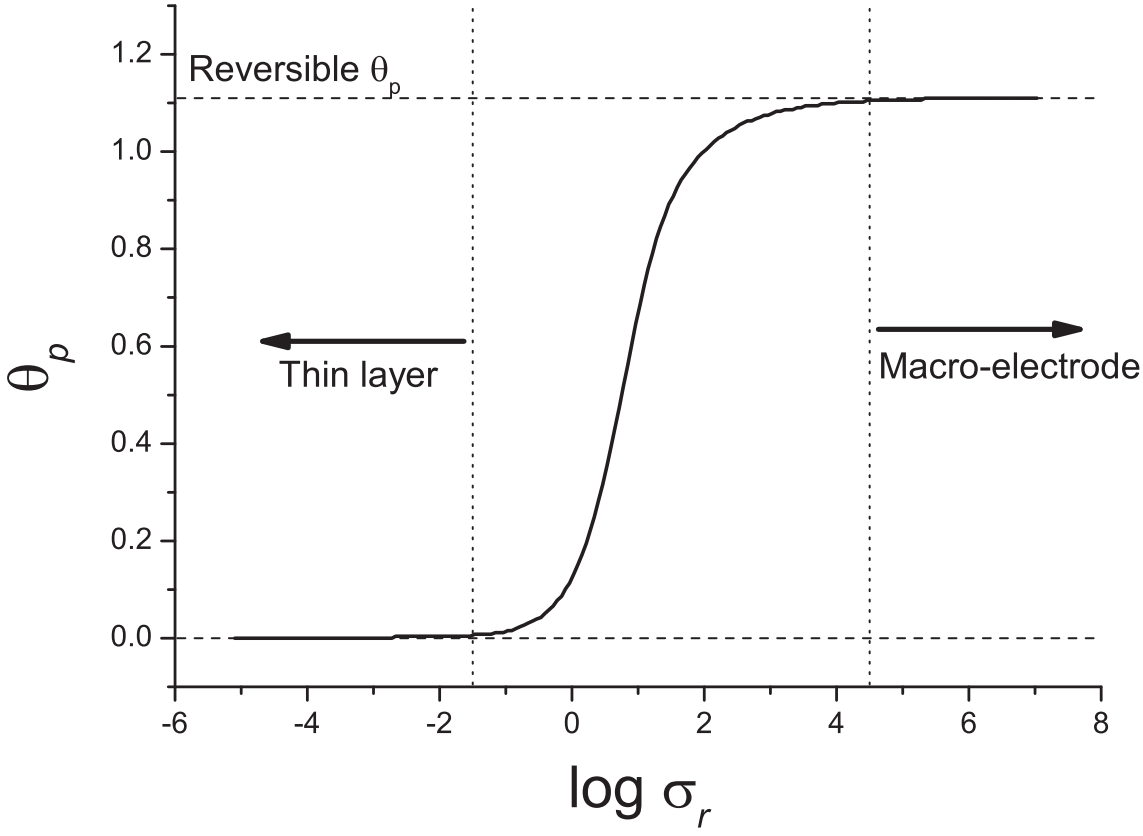

Figure 8.9: *Normalized peak potential, θ_p, of the simulated voltammetry of the interior of an infinite cylinder as it varies with the dimensionless parameter, σ_r.*

Figure 8.9 demonstrates how the peak potential, θ_p, varies with σ_r. In the $\sigma_r \to 0$ limit, $\theta_p = 0$, again as exhibited in thin-layer voltammetry. In the $\sigma_r \to \infty$ limit, the peak potential tends toward that normally observed for a fully reversible electron transfer at a macro electrode, $\theta_p = 1.11$ ($E_p = 28.5$ mV at 298 K). The figure shows the boundaries of these limits according to the definition given in Equation

8.20; these boundaries are further apart than those given by considering J_p. From consideration of θ_p, the thin-layer limit is given by the condition '$\log \sigma_r < -1.5$', and the macro-electrode limit by '$\log \sigma_r > 4.5$'. At $T = 298$ K,

$$r_e \to 0 \qquad r_e < 0.0285\sqrt{\frac{D}{\nu}} \tag{8.23}$$

$$r_e \to \infty \qquad r_e < 28.5\sqrt{\frac{D}{\nu}} \tag{8.24}$$

or $r_e < 2.85 \times 10^{-6}$ m and $r_e < 2.85 \times 10^{-3}$ m respectively (for $D = 10^{-5}$ cm^2 s^{-1} and $\nu = 0.1$ V s^{-1}).

8.3.2 Effect of k^0 and α

Figure 8.10 is a surface plot showing how the peak current varies with both σ_r and the normalized electron transfer rate constant, K^0, defined as:

$$K^0 = \frac{k^0 r_e}{D} \tag{8.25}$$

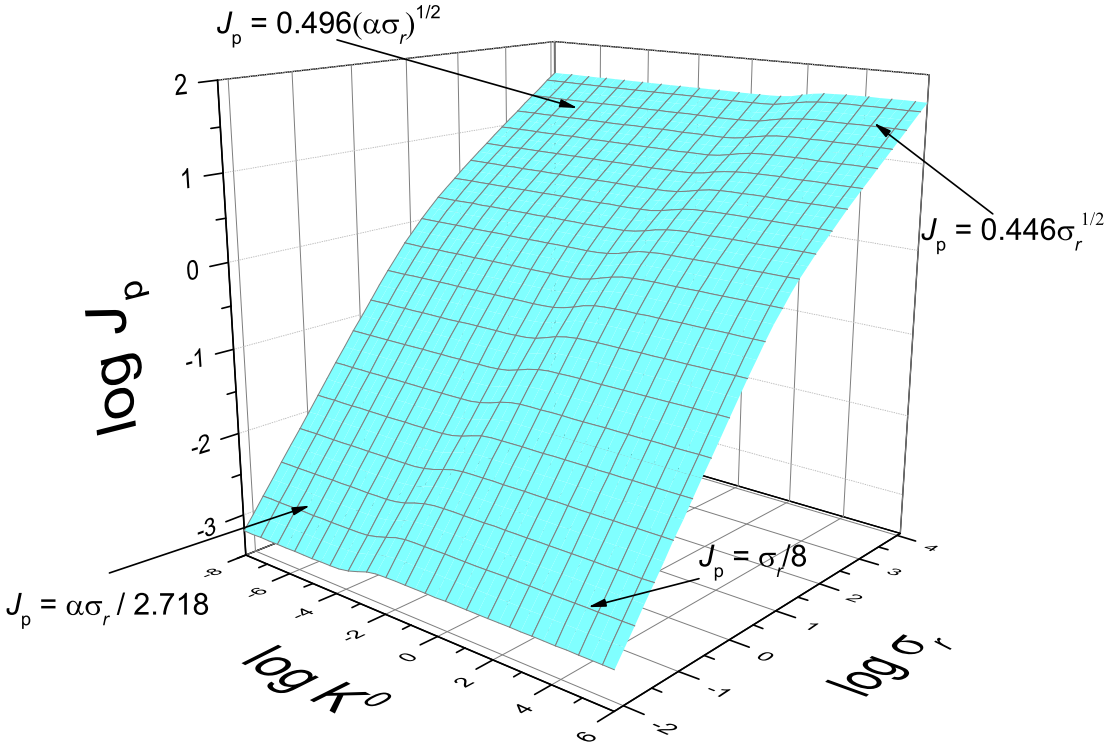

Figure 8.10: *Variation of voltammetric peak current, J_p, with dimensionless scan rate, σ_r, and dimensionless rate constant, K^0. Labels indicate limiting behaviour.*

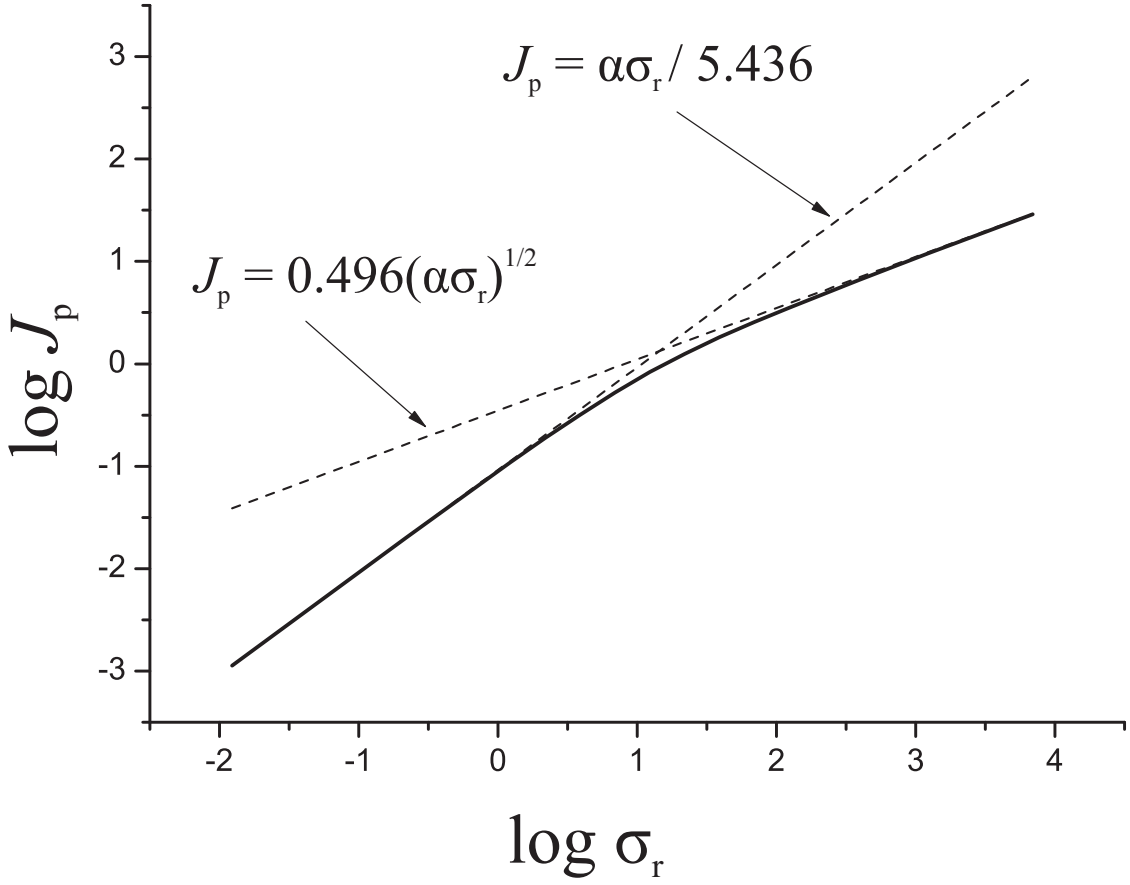

Figure 8.11: *Variation of voltammetric peak current, J_p, with dimensionless scan rate, σ_r, in the electrochemically irreversible limit, $K^0 = 10^{-8}$.*

As can be seen in Figure 8.11, in the electrochemically irreversible limit ($K^0 \rightarrow 0$), for large σ_r, the peak current is seen to obey the irreversible Randles-Ševčík equation[22] :

$$J_p = 0.496\sqrt{\alpha\sigma_r} \tag{8.26}$$

and the peak potential, θ_p, is given by:

$$\theta_p = \frac{1}{\alpha}\left[\ln\left(\frac{K^0}{\sqrt{\alpha\sigma_r}}\right) + 0.78\right] \tag{8.27}$$

both of which are consistent with behaviour normally seen for macro-scale electrodes[23,24] For small σ_r, J_p is observed to obey the relation:

$$J_p = \frac{\alpha\sigma_r}{5.436} \tag{8.28}$$

which in dimensioned variables is:

$$I_p = \frac{\alpha F^2 \nu V c^*}{2.718\mathcal{R}\mathcal{T}} \tag{8.29}$$

and θ_p follows:

$$\theta_p = \frac{1}{\alpha} \ln\left(\frac{2K^0}{\alpha\sigma_r}\right) \tag{8.30}$$

which in dimensioned variables is:

$$E_p = E_0 + \frac{\mathcal{RT}}{\alpha F} \ln\left(\frac{r\mathcal{RT}k^0}{\alpha F r_e \nu}\right) \tag{8.31}$$

Equations 8.29 and 8.29 are consistent with those normally exhibited by thin-layer systems in the irreversible limit.[21,25,26]

8.3.3 Microbands - The $\sigma_r \to \infty$ Limit

Prior work on exterior annular microbands[11] showed that in the $r_e \to \infty$ limit, the curvature of the band is negligible compared to the scale of the diffusion layer and the voltammetric response tends toward that of a flat band electrode of length $l = 2\pi r_e$ and width $w = z_e$ (a microband electrode in the limit of small w). When investigating the $r_e \to \infty$ limit, the voltammetry as it varies with σ_z was considered. An alternative normalized current, J_z, was used which is defined as:

$$J_z = \frac{I z_e}{FADc_A^*} \tag{8.32}$$

with peak current labelled as $J_{z,p}$. This normalization allows direct comparison between the interior annular band and the infinite flat microband models. Figure 8.12 shows $J_{z,p}$ as it varies with σ_z for a range of values of σ_r as well as the equivalent behaviour for an infinite flat microband electrode. As σ_r is increased, the behaviour of the annular system tends toward that of the flat band; when $\sigma_r > 3 \times 10^4$, the behaviours are identical.

8.3.4 Micro-rings - The $\sigma_r, \sigma_z \to 0$ Limit

Next the limit of small σ_r is examined. Figure 8.13 shows the variation of $J_{z,p}$ with σ_z for several small values of σ_r (4×10^{-8}, 4×10^{-6}, 4×10^{-4}) and Figure 8.14 shows voltammetry as it varies with σ_z for $\sigma_r = 4 \times 10^{-6}$.

In both figures, it can be seen that below a certain threshold value of σ_z, the value of the peak current, $J_{z,p}$, does not vary with σ_z. In the limit $\sigma_r, \sigma_z \to 0$, $J_{z,p}$

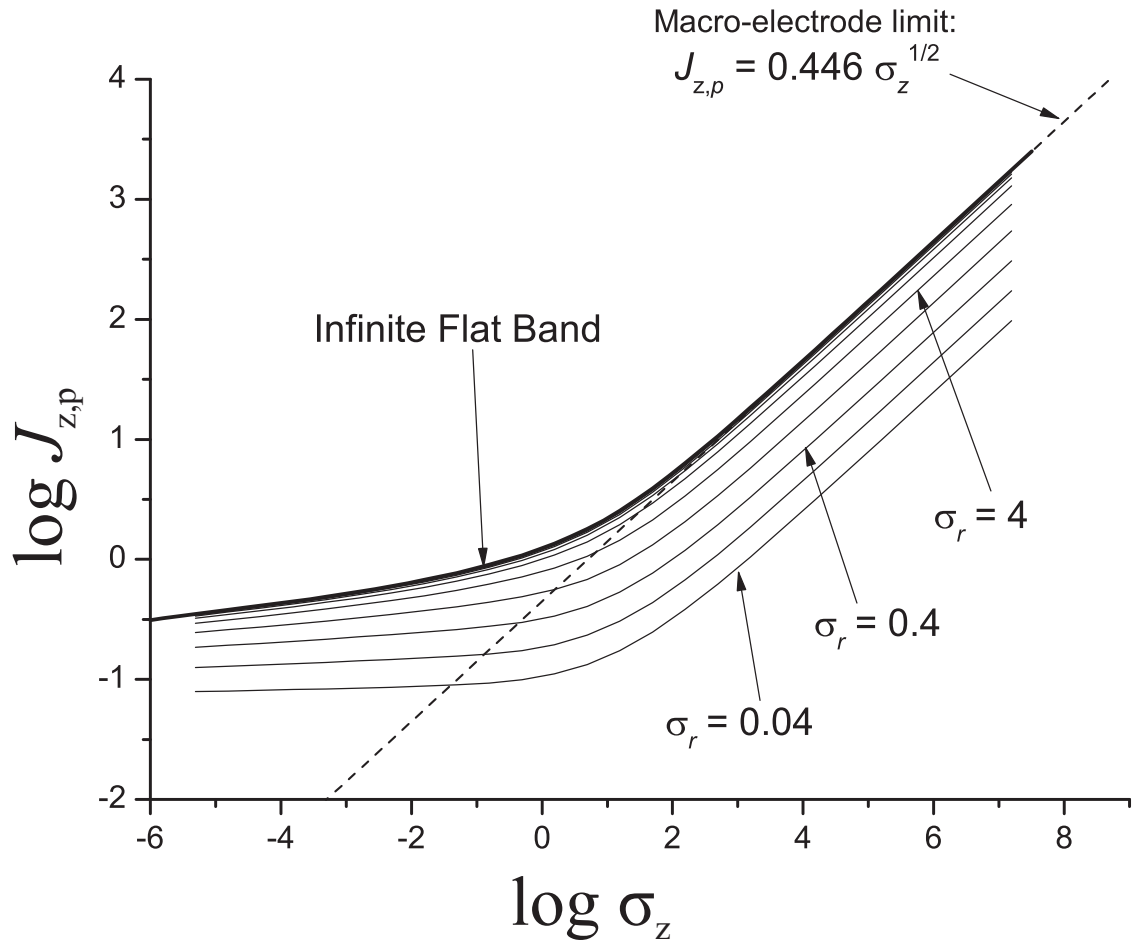

Figure 8.12: *Variation of peak current, $J_{p,z}$ with σ_z for high values of σ_r (from 4×10^{-2} to 4×10^{5} increasing by a factor of $\sqrt{10}$). The thick black line shows $J_{p,z}$ for a flat band electrode of infinite length and the dashed line shows $J_{p,z}$ for a macroelectrode.*

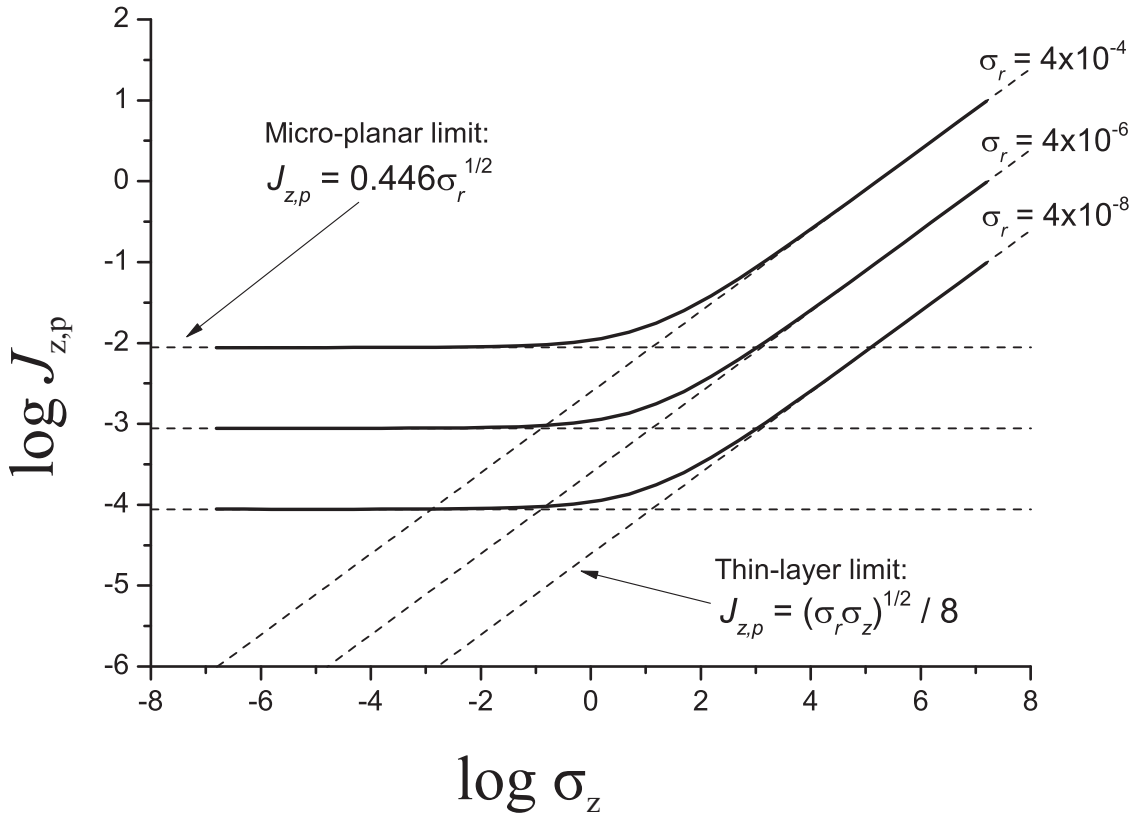

Figure 8.13: *Variation of peak current, $J_{p,z}$ with σ_z for low values of σ_r.*

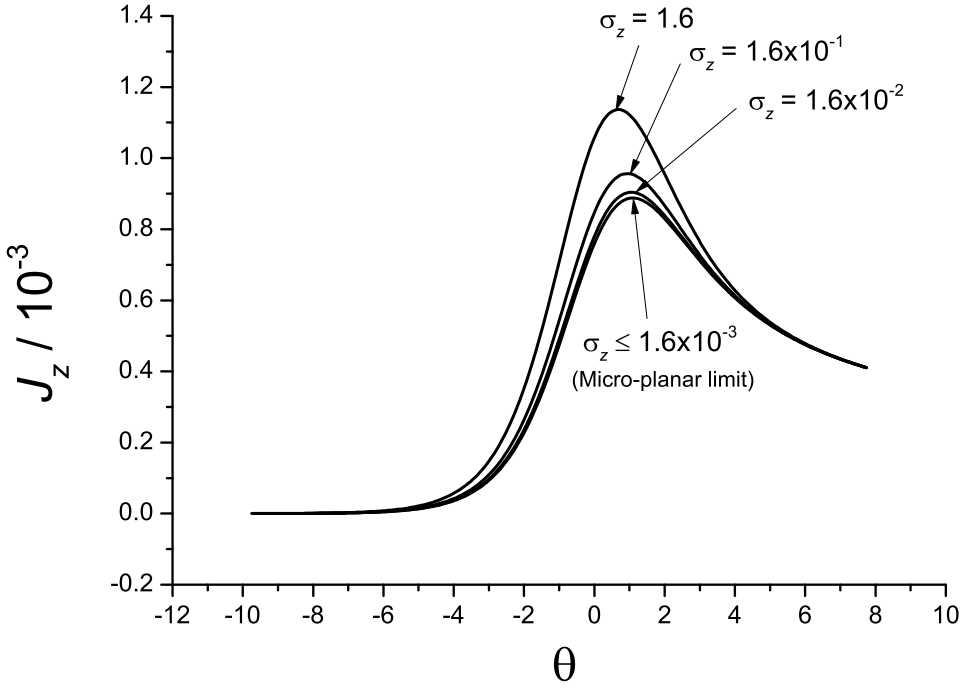

Figure 8.14: *Voltammograms of systems with low σ_z and $\sigma_r = 4 \times 10^{-6}$.*

is observed to obey the relation:

$$J_{z,p} = 0.446\sqrt{\sigma_r} \tag{8.33}$$

which in dimensioned variables is:

$$I_p = 0.446(2\pi r_e^2)Fc^*\sqrt{\frac{FD\nu}{\mathcal{RT}}} \tag{8.34}$$

This is very similar to the Randles-Ševčík equation, Equation 8.16, normally applicable to the peak current of a *macro*-electrode. However, where that equation contains a factor, $A = 2\pi r_e z_e$, which is equal to the total area of the electrode surface, this equation contains a factor, $2\pi r_e^2$. Consequently, the current is independent of the band height, z_e, in this limit. Figure 8.15 shows the variation of peak potential with σ_z. For values of σ_r below about 4×10^{-6}, the curve is invariant, however above this value, variation is observed, particularly at low σ_z.

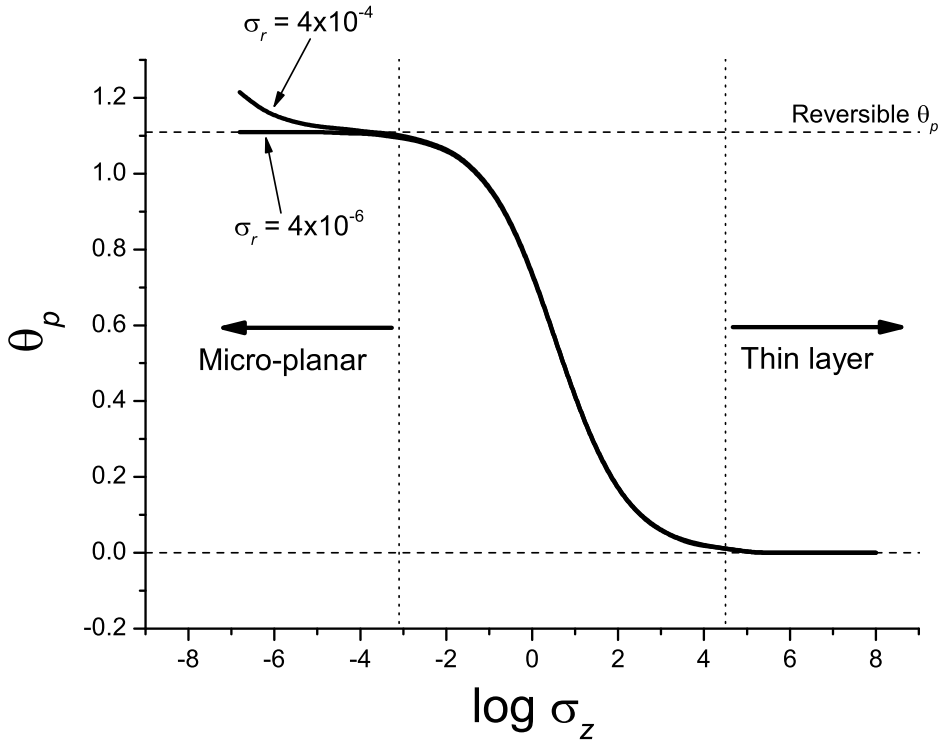

Figure 8.15: *Variation of peak potential, θ_p with σ_z for low values of σ_r. Values of $\sigma_r \leq 4 \times 10^{-6}$ all yield identical curves.*

Figure 8.16 shows a series of concentration profiles for voltammetry of a system with $\sigma_r = 10^{-6}$, $\sigma_z = 4 \times 10^{-4}$, which obeys Equation 8.34. It can be seen that the diffusion layer is linear such that planes of iso-concentration are perpendicular

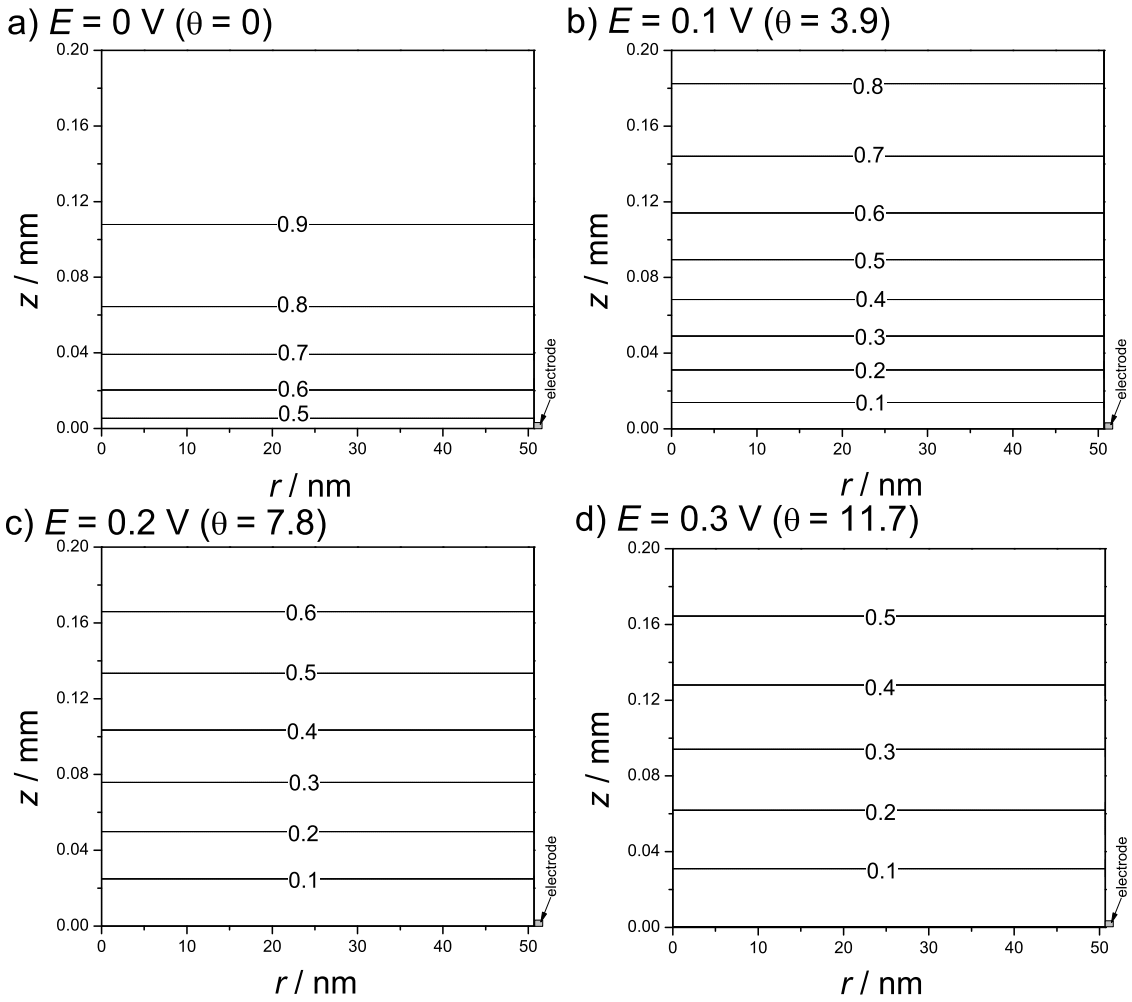

Figure 8.16: *Concentration profiles in terms of c/c^* with lines of isoconcentration (c/c^*) at different points during a voltammetric sweep ($E_f^0 = 0$ V, $T = 298$ K). $r_e = 5 \times 10^{-8}$ m; $z_e = 1 \times 10^{-6}$ m; $D = 10^{-9}$ m^2 s^{-1}; $\nu = 0.01$ V $s{-}1$ ($\sigma_r = 10^{-6}$, $\sigma_z = 4 \times 10^{-4}$). Only the quadrant indicated in Figure 8.2 is shown.*

to the axis of the cylinder. This is in contrast with the profiles for the $\sigma_z \to \infty$ limit shown in Figure 8.8. The behaviour exhibited for low σ_r and low σ_z is an example of 'micro-planar' diffusion and is a consequence of the confinement of the solution. The volume of electroactive solution in the region of the electrode is very small and is rapidly consumed. Therefore, the 'divergent' mode of the diffusion exhibited in the $\sigma_z \to \infty$ limit makes a negligible contribution to the voltammetry. This explains the factor $2\pi r_e^2$ seen in Equation 8.34: the peak current is limited by the rate at which fresh material is transported to the electroactive surface and as the diffusional mode is planar this rate is proportional to the cross-sectional area of the cylinder, πr_e^2. The factor of 2 arises from the fact that diffusion is towards the

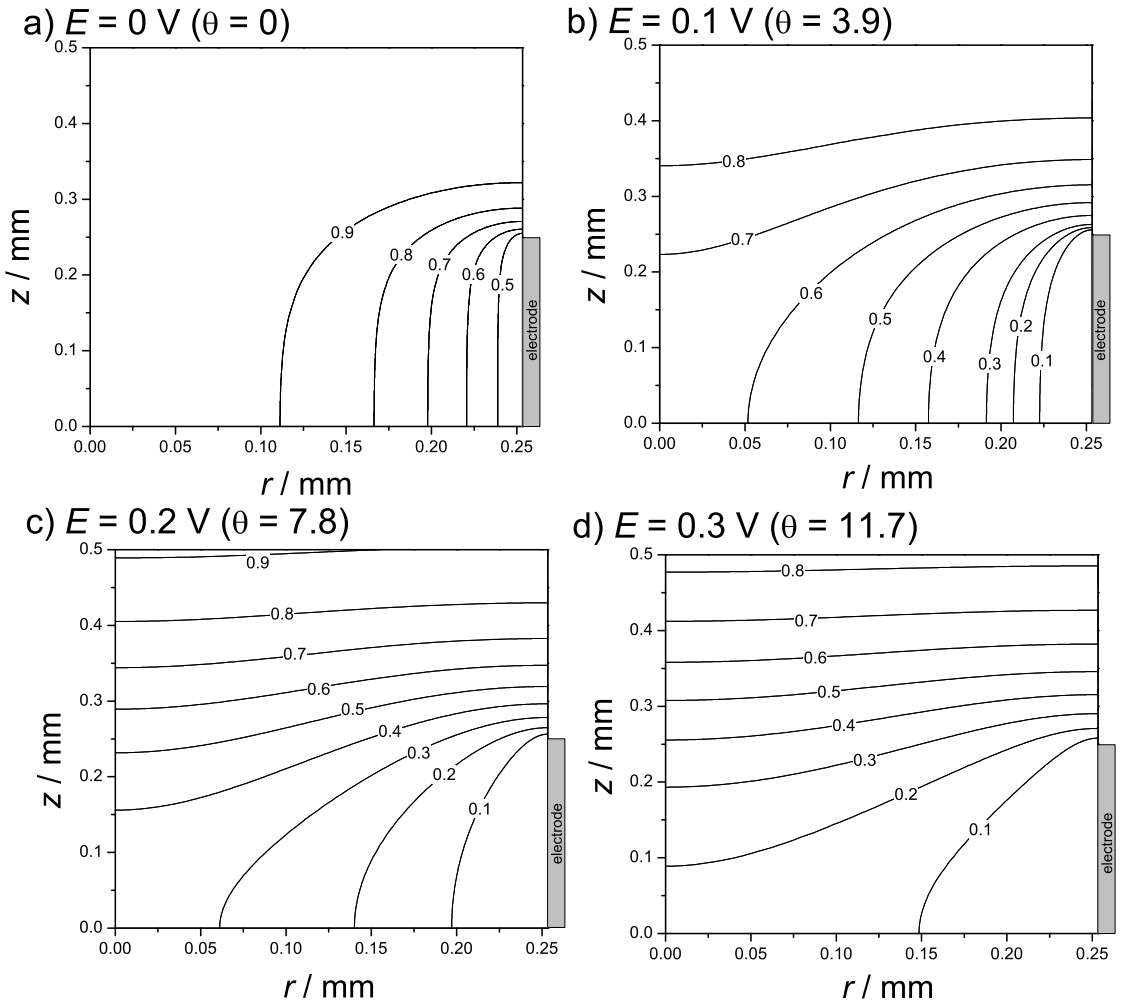

Figure 8.17: *Concentration profiles in terms of c/c^* with lines of isoconcentration at different points during a voltammetric sweep ($E_f^0 = 0$ V, $T = 298$ K). $r_e = 2.5 \times 10^{-4}$ m; $z_e = 5 \times 10^{-4}$ m; $D = 10^{-9}$ m^2 s^{-1}; $\nu = 0.01$ V s−1 ($\sigma_r = 25$, $\sigma_z = 100$). Only the quadrant indicated in Figure 8.2 is shown.*

electroactive ring from opposite directions (positive and negative z). The current response is therefore the same as would be observed if an electroactive disc bisected the inactive cylinder perpendicular to its axis. An example of an intermediate system which demonstrates a combination of the two orthogonal diffusional modes ('divergent' and 'micro-planar') is shown in Figure 8.17 ($\sigma_r = 25$, $\sigma_z = 100$); the diffusion can be described as being convergent towards the electroactive ring in this case.

Figure 8.18 is a surface plot of the peak current J_p as it varies with both σ_r and σ_z, with the limiting behaviours labelled. Figure 8.19 shows the regions of the (σ_r, σ_z) space in which the limiting behaviours are observed according to the tolerance

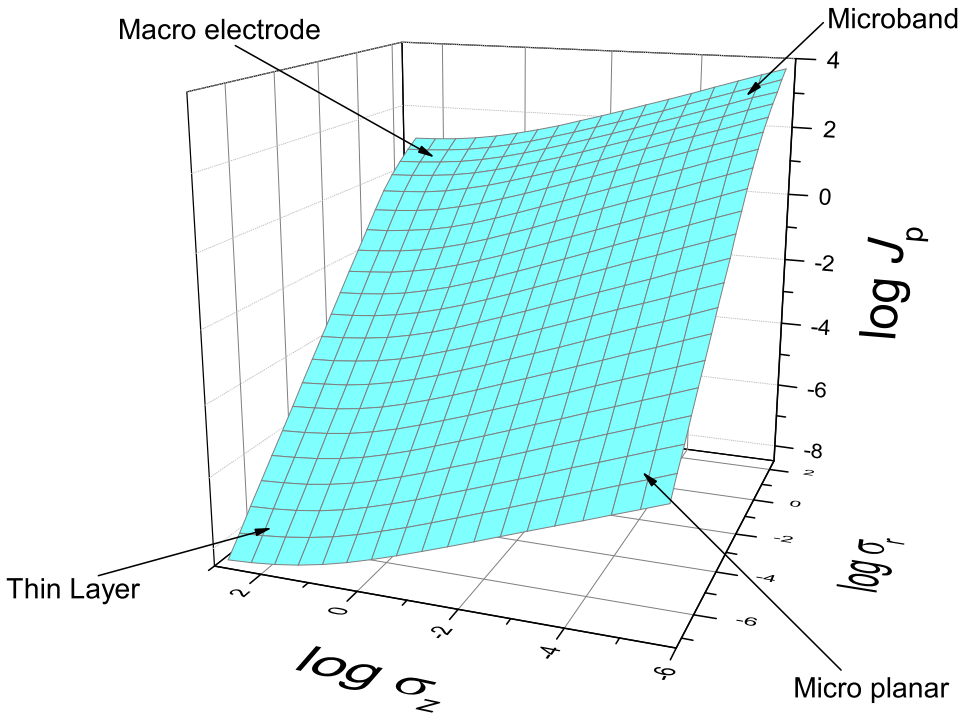

Figure 8.18: *Variation of peak current, J_p with σ_r and σ_z.*

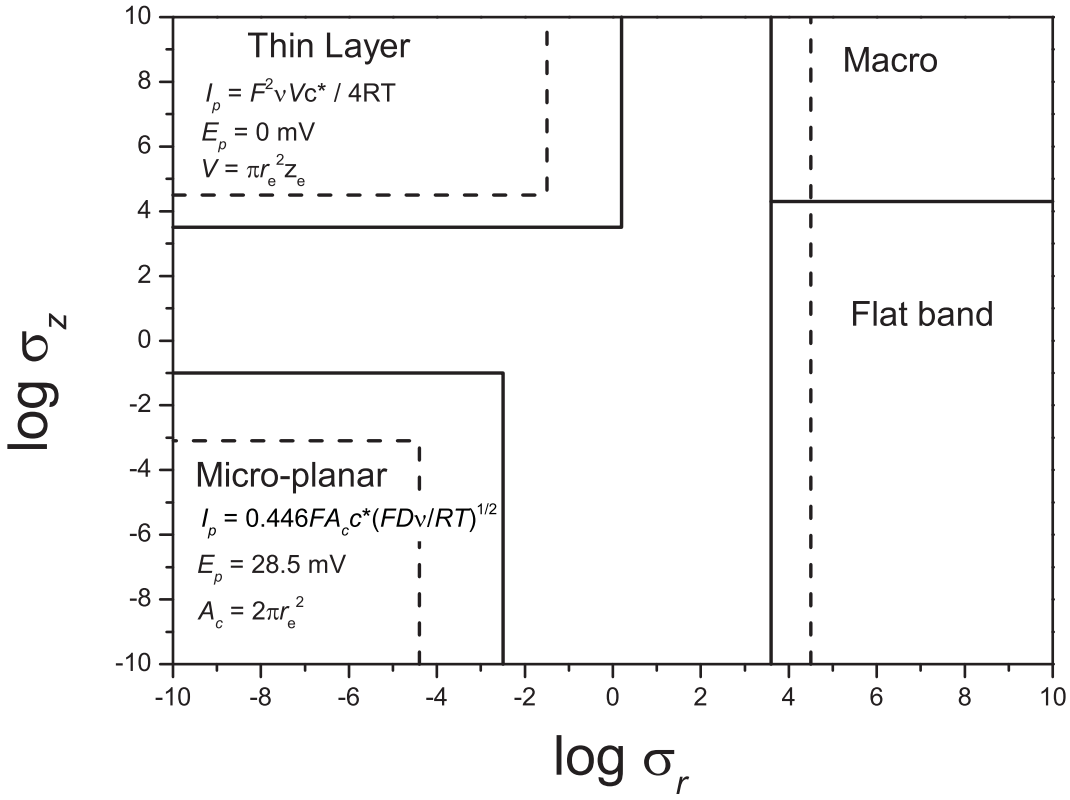

Figure 8.19: *The σ_r, σ_z parameter space showing different zones of limiting behaviour. Dashed lines show limiting behaviour regions as measured from the peak potential; solid lines as measured by the peak current.*

specified in Equation 8.20.

8.4 Conclusions

The voltammetric response of the interior of a cylindrical pore has been explored and characterised. Considering the spatial extent of the system, four limiting behaviours were identified. In the limit of large cylinder radius, behaviour equivalent to a flat band electrode is seen, which is equal to that of a macro electrode for large band-height and a microband electrode for small band height. In the limit of small cylinder radius, thin-layer voltammetry is seen for large band height, and a planar diffusion field is seen for small band-height.

Bibliography

[1] K. R. Ward, L. Xiong, N. S. Lawrence, R. S. Hartshorne and R. G. Compton, *J. Electroanal. Chem.*, 2013, **702**, 15–24.

[2] C. Comanescu, G. Capurso and A. Maddalena, *Nanotechnol.*, 2012, **23**, 385401/1–385401/6.

[3] T. S. Mahadevan, M. Kojic, M. Milosevic, V. Isailovic, N. Filipovic, M. Ferrari and A. Ziemys, Nanotech Conf. Expo 2012, 2012, pp. 412–415.

[4] R. Souda, *J. Phys. Chem. C*, 2012, **116**, 20895–20901.

[5] A. Ziemys, M. Kojic, M. Milosevic and M. Ferrari, *Phys. Rev. Lett.*, 2012, **108**, 236102/1–236102/5.

[6] H. Zhu, A. Ghoufi, A. Szymczyk, B. Balannec and D. Morineau, *Mol. Phys.*, 2012, **110**, 1107–1114.

[7] F. de los Santos and G. Franzese, *Phys. Rev. E*, 2012, **85**, 010602–.

[8] A. R. Klotz, H. B. Brandao and W. W. Reisner, *Macromolecul.*, 2012, **45**, 2122–2127.

[9] J. M. Katzenstein, D. W. Janes, H. E. Hocker, J. K. Chandler and C. J. Ellison, *Macromolecul.*, 2012, **45**, 1544–1552.

[10] C. Iacob, J. R. Sangoro, W. K. Kipnusu, R. Valiullin, J. Kaerger and F. Kremer, *Soft Matter*, 2012, **8**, 289–293.

[11] E. J. F. Dickinson, I. Streeter and R. G. Compton, *J. Electroanal. Chem.*, 2009, **625**, 40–46.

[12] M. Thompson, J. Davis and R. G. Compton, *J. Electroanal. Chem.*, 2006, **587**, 56–59.

[13] R. G. Compton and P. R. Unwin, *J. Electroanal. Chem.*, 1986, **205**, 1–20.

[14] W. J. Blaedel, C. L. Olson and L. R. Sharma, *Anal. Chem.*, 1963, **35**, 2100–3.

[15] W. J. Blaedel and L. N. Klatt, *Anal. Chem.*, 1966, **38**, 879–83.

[16] S. R. Belding, E. J. F. Dickinson and R. G. Compton, *J. Phys. Chem. C*, 2009, **113**, 11149–11156.

[17] I. B. Svir, A. I. Oleinick and R. G. Compton, *Radioelektronika & Inform.*, 2000, **1**, 28–32.

[18] J. W. Peaceman and H. H. Rachford, *J. Soc. Ind. Appl. Math.*, 1955, **3**, 28–41.

[19] J. E. B. Randles, *Trans. Faraday Soc.*, 1948, **44**, 327–38.

[20] A. Ševčík, *Collect. Czech. Chem. Commun.*, 1948, **13**, 349–77.

[21] A. T. Hubbard and F. C. Anson, *Electroanal. Chem.*, 1970, **4**, 129–214.

[22] H. Matsuda and Y. Ayabe, *Z. Elektrochem. Angew. Phys. Chem.*, 1955, **59**, 494–503.

[23] P. Delahay, *J. Am. Chem. Soc.*, 1953, **75**, 1190–6.

[24] R. S. Nicholson and I. Shain, *Anal. Chem.*, 1964, **36**, 706–23.

[25] A. J. Bard and L. R. Faulkner, *Electrochemical Methods: Fundamentals and Applications.*, John Wiley & Sons, New York, 2nd edn., 2001.

[26] A. T. Hubbard, *Crit. Rev. Anal. Chem.*, 1973, **3**, 201–42.

Chapter 9

The Apparent 'Catalytic' Effect of Porous Surfaces

In this chapter, the voltammetry of porous electroactive surfaces is investigated. The surface is modelled as a solid block penetrated by a regularly distributed array of cylindrical pores. This work builds on the single pore model developed in Chapter 8 and the investigation into the apparent catalytic effect exhibited by nanoparticle modified electrodes detailed in Chapter 7. Herein, the effect of the voltage scan rate and the geometry (in terms of pore depth, radius, and inter-pore separation) of the porous surface on the voltammetry is examined for both fully reversible and fully irreversible electrode kinetics. In the latter case, it is demonstrated that when the pores are relatively shallow, a predictable shift in peak potential is observed corresponding to an apparent catalytic effect. For deeper pores, voltammetry corresponding to thin-layer behaviour is observed. The limits under which these behaviours operate are then elucidated.

9.1 Introduction

Electrode systems that can be categorised as porous find a number of uses in the field of electroanalysis. For instance, electrodes modified with a porous film are of interest for use in devices such as batteries, fuel cells and sensors,[1–3] as such electrodes may show mass transport properties that differ significantly from those

observed for a planar macroelectrode. Electrodes modified with porous films such as a layer of carbon nanotubes[4,5] or a polymer film[6,7] can be used for the determination of specific target analytes in the presence of interferent species.

Recently, Chevallier *et al.* used simulation to explore the voltammetry of *insulating* porous films wherein electroactive species can access the electrode surface only by diffusion through the pores,[8] the so-called 'pinhole' model. They concluded that the influence of parameters such as pore size and distribution had a significant qualitative influence on the mass transport properties of the system. Menshykau and Compton compared the behaviours of two theoretical models of porous surfaces: the aforementioned pinhole model, and a second model in which electroactive species dissolves and then diffuses through the layer.[9] They demonstrated that it is possible to distinguish between the two models as the latter transitions between two limiting regions of voltammetric behaviour as the scan rate is increased. Finally, Henstridge *et al.* considered electrodes modified with a *conducting* porous film where the entirety of the film itself is electroactive. They demonstrated that the voltammetry consisted of two components, one resulting from planar diffusion to the top surface of the film and another resulting from thin layer diffusion within the pores.[10] The relative magnitudes of these effects depend on the specific geometry of the system at hand, but they found that for the case of irreversible electrode kinetics, a highly porous surface could lead to voltammetry with two peaks in the forward sweep, with a peak attributed to each diffusional component.

9.2 Theory

Throughout, a one electron oxidation of the form,

$$\mathrm{A} \rightleftharpoons \mathrm{B} + \mathrm{e}^- \tag{9.1}$$

is considered, in which only species A is initially present in solution at a uniform concentration, c_{A}^*, and the diffusion coefficients of A and B are equal such that at every point in space the sum of their concentrations is equal to c_{A}^*.

The electrode system under consideration takes the form of a block of some

porous, electrochemically active material that sits on a surface of supporting substrate that is itself electrochemically inert as shown in Figure 9.1. The exposed upper surface of the block is of geometric area, A, and uniform height, z_e. It is assumed that all other faces of the block are inert or in some way covered such that they are electrochemically inert. The block is supposed to contain a series of cylindrical pores which extend from the upper surface to just above the insulating supporting surface as illustrated in Figure 9.2. The interior surfaces of the pore (bottom and walls) are electroactive and the block is immersed in electroactive solution such that it covers the exposed upper surface and fills the interior of the pores.

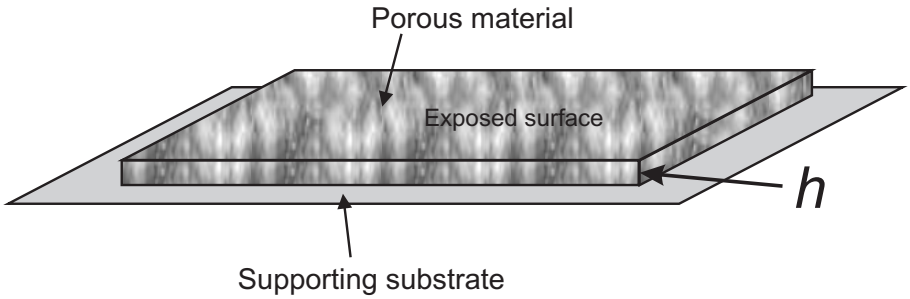

Figure 9.1: *The porous surface.*

It is assumed that the pores are of regular size and shape, with radius r_e, and height z_e, and that they are regularly distributed. Consequently, the surface may be treated as though it is composed of a hexagonal array of identical unit cells, each with a pore at its centre. As with previously studied systems, including the cylindrical electrode (see Chapter 7), the diffusion domain approximation (Section 2.8.1) can be used to approximate the unit cell as being cylindrical in shape, with domain radius r_d, as shown in Figure 9.3. The unit cell is represented in cylindrical polar coordinates but possesses angular isotropy such that:

$$\frac{\partial c}{\partial \phi} = \frac{\partial^2 c}{\partial \phi^2} = 0 \tag{9.2}$$

and so only a two-dimensional (r, z) slice need be modelled. Fick's second law in this coordinate system is:

$$\frac{\partial c}{\partial t} = D\left(\frac{\partial^2 c}{\partial r^2} + \frac{1}{r}\frac{\partial c}{\partial r} + \frac{\partial^2 c}{\partial z^2}\right) \tag{9.3}$$

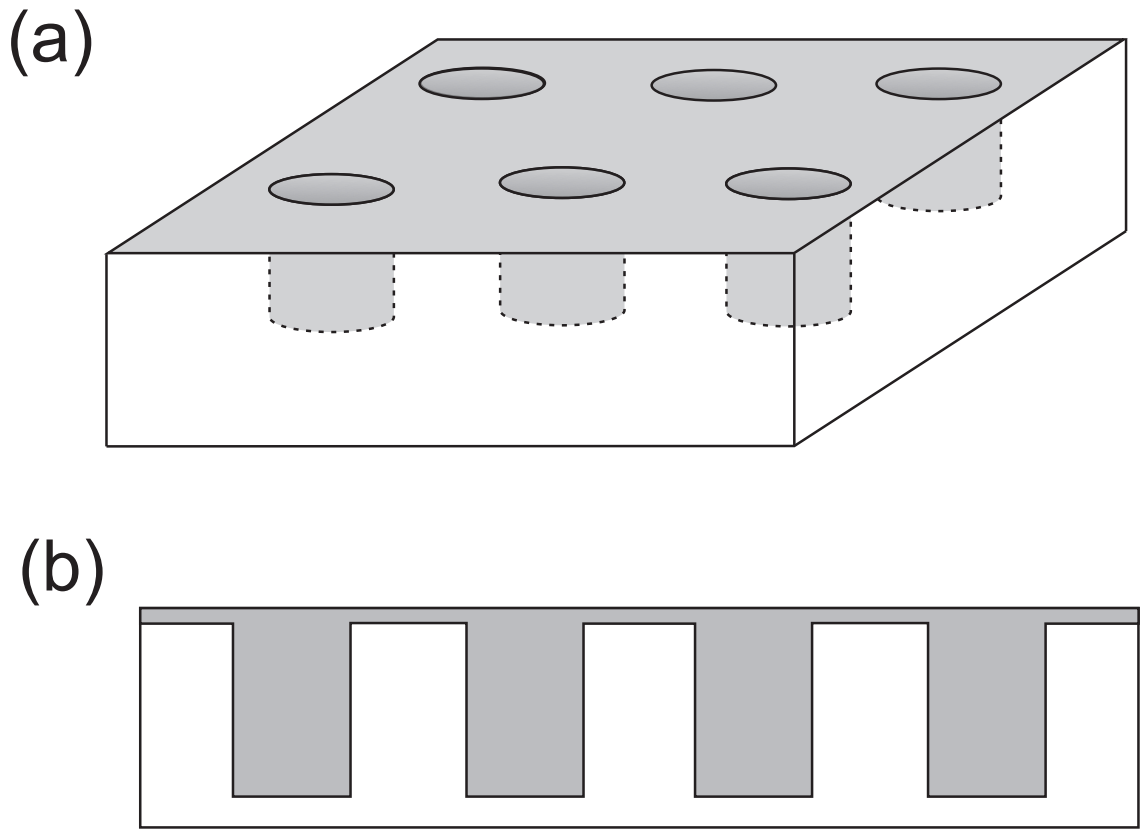

Figure 9.2: *(a) schematic of a porous surface; (b) side on view.*

It is assumed that an excess of supporting electrolyte is added to the system and that it is not heated or stirred such that mass transport is controlled entirely by diffusion (with migration and convection making negligible contributions).

The simulation space including boundary conditions is shown in Figure 9.4. Internally, the simulation makes use of a set of dimensionless units. The spatial coordinates are normalized against the pore radius:

$$R = \frac{r}{r_\mathrm{e}} \tag{9.4}$$

$$Z = \frac{z}{z_\mathrm{e}} \tag{9.5}$$

and the standard normalized parameters, C, T, θ, σ, and K^0 are also used. In normalized units, the pore radius is 1, the height is $Z_\mathrm{e} = z_\mathrm{e}/r_\mathrm{e}$ and the unit cell radius is $R_\mathrm{d} = r_\mathrm{d}/r_\mathrm{e}$.

The electroactive surface area is composed of three segments, and so the potential-dependent boundary condition (the Butler–Volmer equation) must be applied sep-

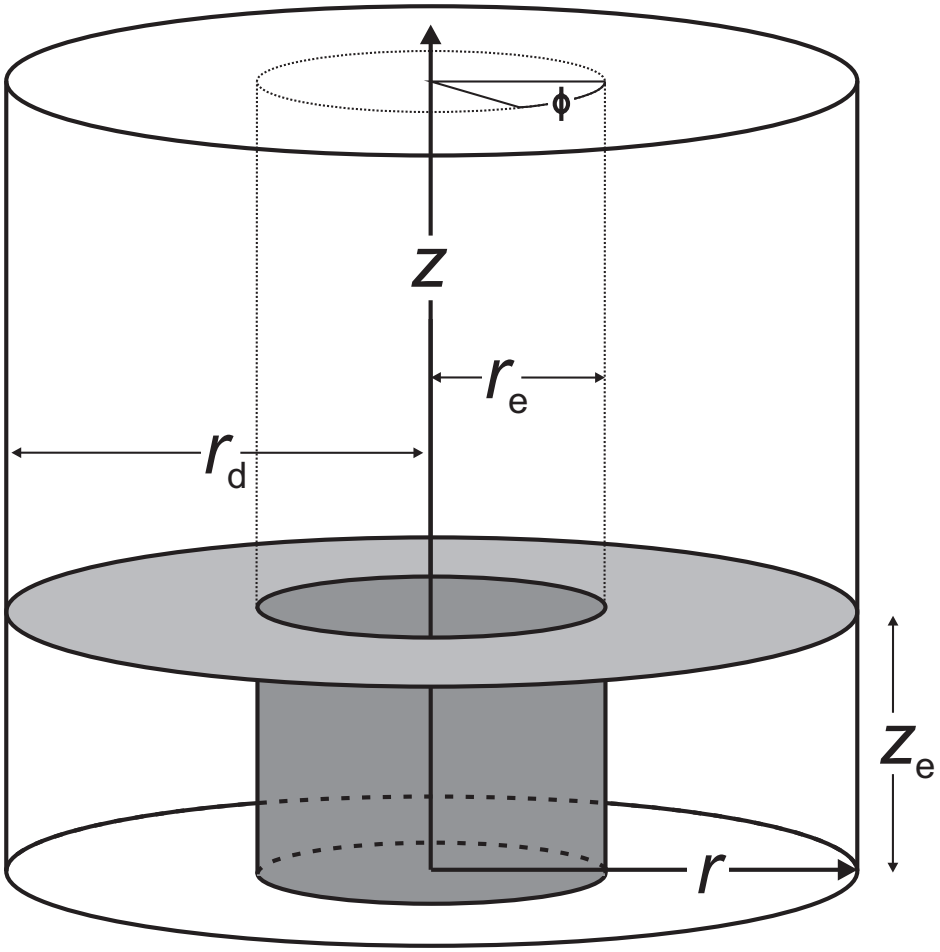

Figure 9.3: *Unit cell and coordinate system for a porous surface.*

arately across each. In normalized units:

$$\text{for } R \leq 1, \quad \left.\frac{\partial C}{\partial Z}\right|_{Z=0} = K^0(C_{R,0}e^{\theta-\alpha\theta} - (1-C_{R,0})e^{-\alpha\theta}) \tag{9.6}$$

$$\text{for } R > 1, \quad \left.\frac{\partial C}{\partial Z}\right|_{Z=Z_\mathrm{e}} = K^0(C_{R,Z_\mathrm{e}}e^{\theta-\alpha\theta} - (1-C_{R,Z_\mathrm{e}})e^{-\alpha\theta}) \tag{9.7}$$

$$\text{for } Z < Z_\mathrm{e}, \quad \left.\frac{\partial C}{\partial R}\right|_{R=1} = K^0(C_{1,Z}e^{\theta-\alpha\theta} - (1-C_{1,Z})e^{-\alpha\theta}) \tag{9.8}$$

Likewise, the current is calculated from the sum of the three separate components:

$$I = 2\pi N F r_\mathrm{e} D c^* \left(\int_0^1 R \left.\frac{\partial C}{\partial Z}\right|_{Z=0} \partial R + \int_1^{R_\mathrm{d}} R \left.\frac{\partial C}{\partial Z}\right|_{Z=Z_\mathrm{e}} \partial R + \int_0^{Z_\mathrm{e}} \left.\frac{\partial C}{\partial R}\right|_{R=1} \partial Z \right) \tag{9.9}$$

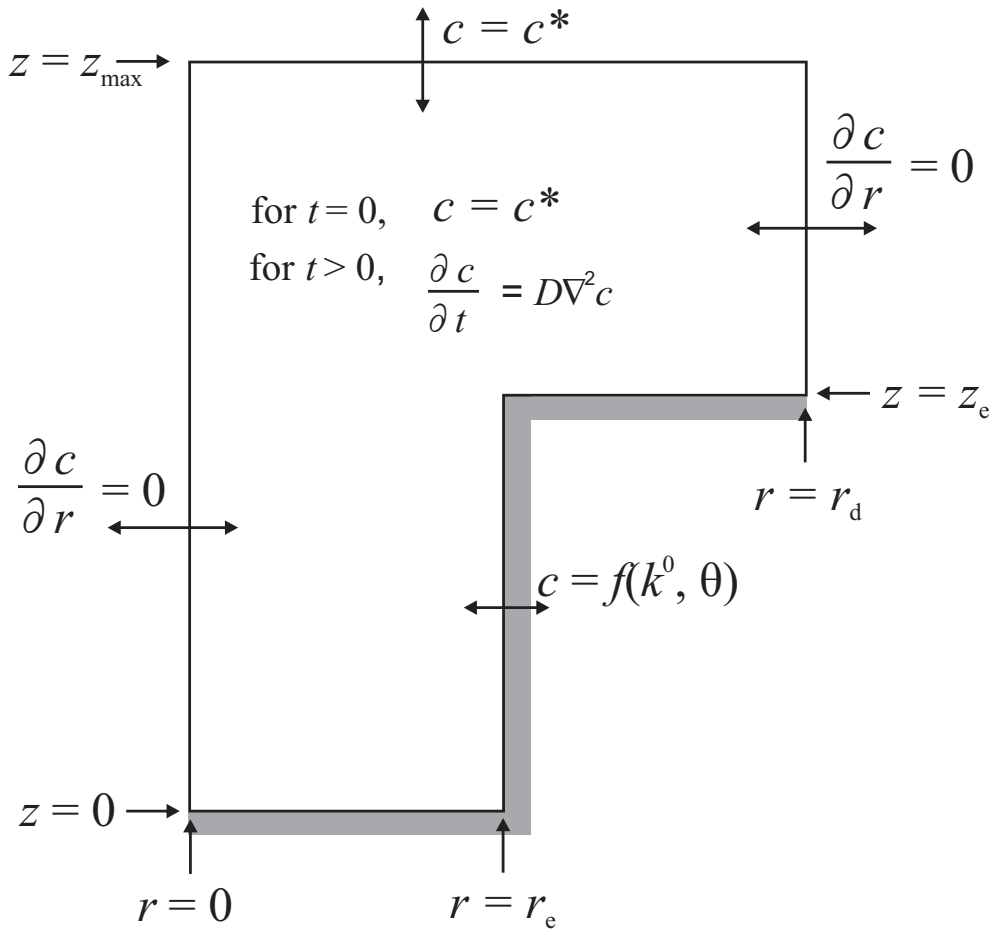

Figure 9.4: *The two-dimensional simulation space for a porous electrode.*

9.3 Results and Discussion

The volume, V, of electroactive solution that permeates the porous material is given by the product of the porosity, Θ, and the block volume:

$$V = \Theta A z_e \tag{9.10}$$

where A is the exposed surface area of the top of the porous material. The porosity is determined from:

$$\Theta = \frac{r_e^2}{r_d^2}; \qquad 0 \leq \Theta \leq 1 \tag{9.11}$$

One approach to analysis of the system is to consider how the voltammetry varies with the pore radius, r_e, pore height, z_e, porosity, Θ, scan rate, ν, and diffusion

coefficient, D. In some cases, analysis and data presentation can be simplified by instead representing the system in terms of *three* independent parameters: Θ, and the normalized parameters, σ_r and σ_z,

$$\sigma_r = \frac{r_e^2}{D}\frac{F}{\mathcal{RT}}\nu \tag{9.12}$$

$$\sigma_z = \frac{z_e^2}{D}\frac{F}{\mathcal{RT}}\nu \tag{9.13}$$

These values can be thought of as the 'normalized square radius' and 'normalized square height' respectively. An increase in the value of σ_r is equivalent to: increasing the cylinder radius, increasing the scan rate, or decreasing the diffusion coefficient. Where appropriate, data are presented in real units for more obvious physical insight and the results are then presented in the more generally applicable set of normalized units.

9.3.1 Fully Reversible Electrode Kinetics

Initially, the investigation considers porous surfaces in which the electrode reaction displays fully reversible kinetics and in which the pores are narrow (low σ_r).

Figure 9.5 shows the scan rate dependence of the peak current, I_p, of voltammetry of a simulated porous surface that has a pore depth $z_e = 10^{-5}$ m, geometric area of 3.14×10^{-6} m^2 and a porosity of 95%. The initial concentration of species A is 10 mM and the diffusion coefficient of both species is 10^{-5} cm^2 s^{-1}. Figure 9.6 shows the same data for a range of values of z_e. It can be seen that the peak current varies between two regions of limiting behaviour. In the limit of low ν, the voltammetry has a typical diffusion limited peak current, I_p, that varies with $\sqrt{\nu}$ as described by the reversible Randles-Ševčík equation:

$$I_p = 0.446FAc_A^*\sqrt{\frac{FD\nu}{RT}} \tag{9.14}$$

Because the scan rate is slow, the peak current is limited by the rate of mass transport of electroactive species from the bulk solution to the porous electroactive surface, and therefore by the geometric area of the block.

In the limit of high scan rate, the voltammetric response is equivalent to that

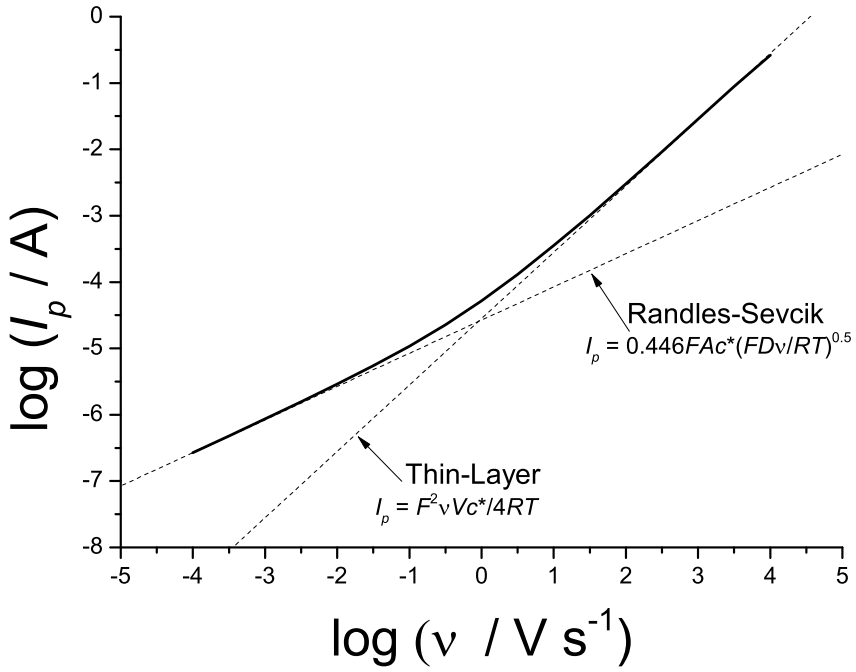

Figure 9.5: *Peak current, I_p, of the voltammetry of a porous surface; $r_e = 10^{-7}$ m, $z_e = 10^{-5}$ m, $\Theta = 0.95$, $A = 3.14 \times 10^{-6}$ m, $c^* = 1$ mM, $D = 10^{-5}$ cm^2, s^{-1}.*

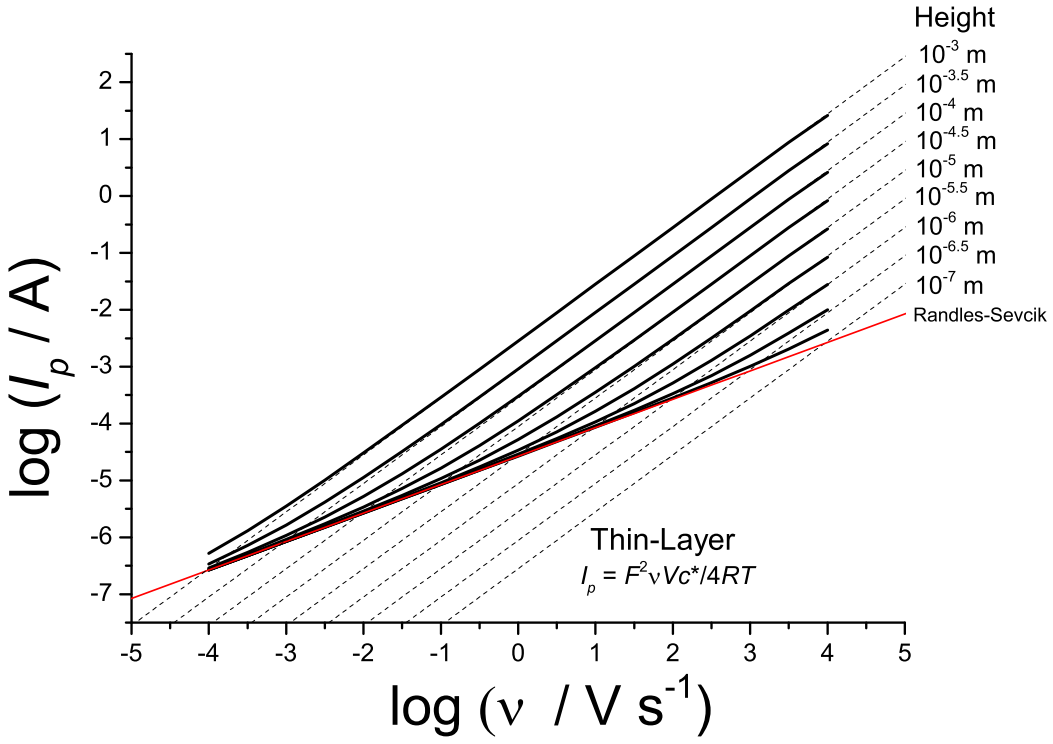

Figure 9.6: *Peak current, I_p, of the voltammetry of a porous surfaces of various pore heights; $r_e = 10^{-7}$ m, $\Theta = 0.95$, $A = 3.14 \times 10^{-6}$ m, $c^* = 1$ mM, $D = 10^{-5}$ cm^2, s^{-1}.*

seen in thin-layer voltammetry with a peak current that is linear in ν as given by the equation:

$$I_p = \frac{F^2 \nu V c_{\mathrm{A}}^*}{4RT} \tag{9.15}$$

Because the scan rate is very fast, there is no time for fresh solution-phase species to diffuse from bulk solution so the peak height is limited by the volume of solution that permeates the porous surface at the start of the scan. The point of cross-over between the two limiting regimes may be found by equating expressions for the peak current, I_p, in the two regimes:

$$\nu = 0.0817 D \frac{A^2}{V^2} \tag{9.16}$$

at 298 K in the limit of fully reversible kinetics. Since $A/V = 1/\Theta z_{\mathrm{e}}$,

$$\nu = 0.0817 \frac{D}{(\Theta z_{\mathrm{e}})^2} \tag{9.17}$$

where ν is in units of V s^{-1}, D is in units of m^2 s^{-1}, and z_{e} is in m. Notice that in Figure 9.6, the shallower the pores are, the higher scan rate must be in order to produce thin layer behaviour and the longer the pores are, the slower the scan rate must be in order to produce a Randles-Ševčík response.

Figure 9.7 shows the variation of normalized peak current, $J_{p,\mathrm{z}}$, where

$$J_{p,\mathrm{z}} = \frac{I z_{\mathrm{e}}}{FADc_{\mathrm{A}}^*} \tag{9.18}$$

with σ_{z} for a range of values of Θ. In the limit of low σ_z, which corresponds to low scan rate, small pore depth, or fast diffusion coefficient, the dimensionless peak current is given by a transformed version of the Randles-Ševčík equation:

$$J_{p,\mathrm{z}} = 0.446\sqrt{\sigma_z} \tag{9.19}$$

In the limit of high σ_z, which corresponds to fast scan rate, large height, or slow diffusion coefficient, the dimensionless peak current is given by a transformed version of the thin-layer equation:

$$J_{p,\mathrm{z}} = \frac{\Theta}{4}\sigma_z \tag{9.20}$$

By equating these two expressions, it can be seen that the cross-over point between the two limiting regions occurs at:

$$\sigma_z = \frac{3.183}{\Theta^2} \tag{9.21}$$

This applies for any set of values of z_e, D, ν, and Θ, in the limit of low r_e.

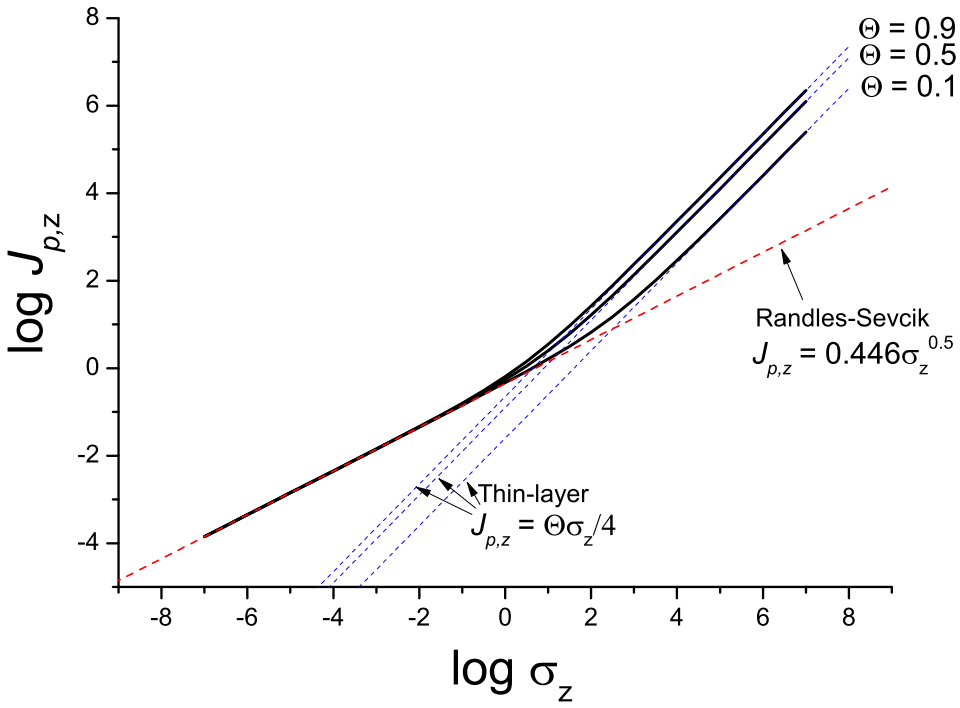

Figure 9.7: *Dimensionless peak current, $J_{p,z}$, of the voltammetry of a porous surfaces as it varies with σ_z for different values of Θ.*

9.3.2 Fully Irreversible Electrode Kinetics

In Chapter 7, it was seen that under the conditions of case 4 diffusion, if an electrode had a greater electroactive surface area than its geometric area, an apparent catalytic effect would be observed. Specifically, the apparent electrochemical rate constant (inferred from the peak potential of the voltammetry) was seen to vary according to:

$$k^0_{\text{app}} = \Psi k^0 \tag{9.22}$$

where k^0 is the true rate constant and Ψ is the ratio of the electroactive surface area to the geometric surface area.

Here, this effect is investigated for the case of a porous surface. For the electrode geometry described in Section 9.2,

$$\Psi = 1 + 2\Theta\frac{z_e}{r_e} \tag{9.23}$$

A large number of simulations were performed, varying both σ_r and σ_z in the range 10^{-8}–10^{-3}, and the porosity, Θ in the range 0.01–0.95. In all cases the electrochemical rate constant, $k^0 = 10^{-9}$ m s^{-1} was used which is in the fully irreversible region.

Figure 9.8 demonstrates how the peak potential varies with Ψ for a small pore depth. This relationship was found to hold for all values of σ_r and Θ, as long as σ_z is less than a certain threshold value. The same relationship for a range of σ_z values is shown in Figure 9.9. As can be seen, for $\sigma_z \leq 0.4$, a porous surface will always produce voltammetry with a peak potential described by Equations 7.23 and 7.24, i.e.,

$$E_p = E_f^0 - \frac{RT}{\alpha F}\left[0.780 - \ln(\Psi k^0) + \ln\sqrt{\frac{\alpha F D\nu}{RT}}\right] \tag{9.24}$$

The condition, $\sigma_z \leq 0.4$, can be alternatively expressed as:

$$z_e \leq 0.1\frac{\sqrt{D}}{\sqrt{\nu}} \tag{9.25}$$

where z_e is in units of m, D is in units of m^2 s^{-1}, and ν is in units of V s^{-1}, and where $T = 298$ K. Therefore, for typical values of $D = 10^{-9}$ m^2 s^{-1} and $\nu = 0.1$ V s^{-1}, a porous surface will show voltammetry with a peak potential predicted by Equation 9.24 if the pore depth is less than about 10 μm. If the pores are deeper and Equation 9.25 is not satisfied, different voltammetric behaviour is seen. In this case, the peak potential varies between two limits. In the limit of high σ_r (as $\Psi \to 1$), the peak potential tends toward that expected for a macro electrode in the limit of irreversible kinetics, regardless of the pore depth as seen in Figure 9.24. In the limit of high σ_z and low σ_r (as $\Psi \to \infty$), the peak potential tends to that predicted for

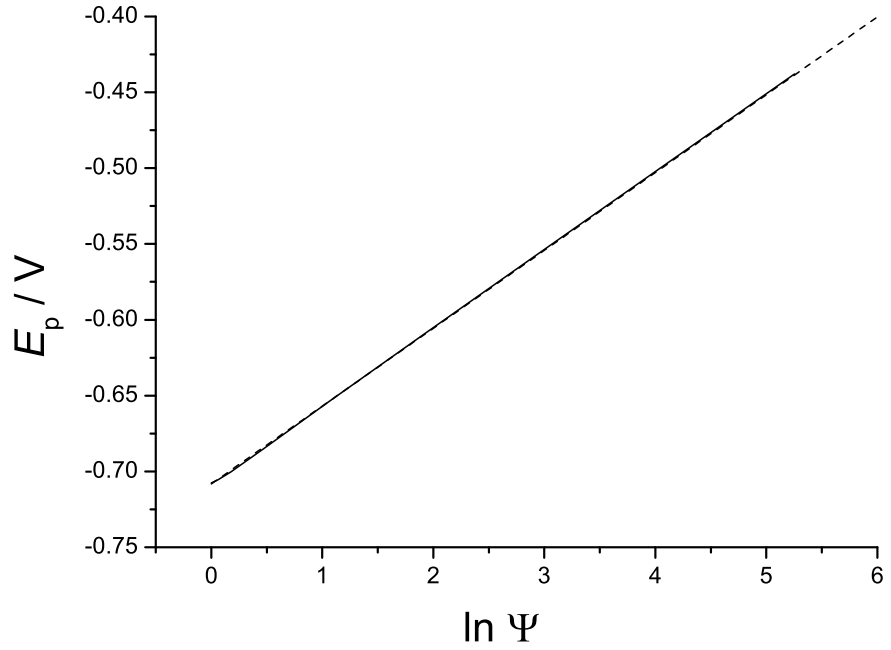

Figure 9.8: *Voltammetric peak current as it varies with surface area ratio, Ψ, with $\sigma_z = 0.04$, $D = 10^{-9}\ m^2\ s^{-1}$, $\nu = 10\ V\ s^{-1}$. Dashed line shows relationship predicted by Equation 9.24.*

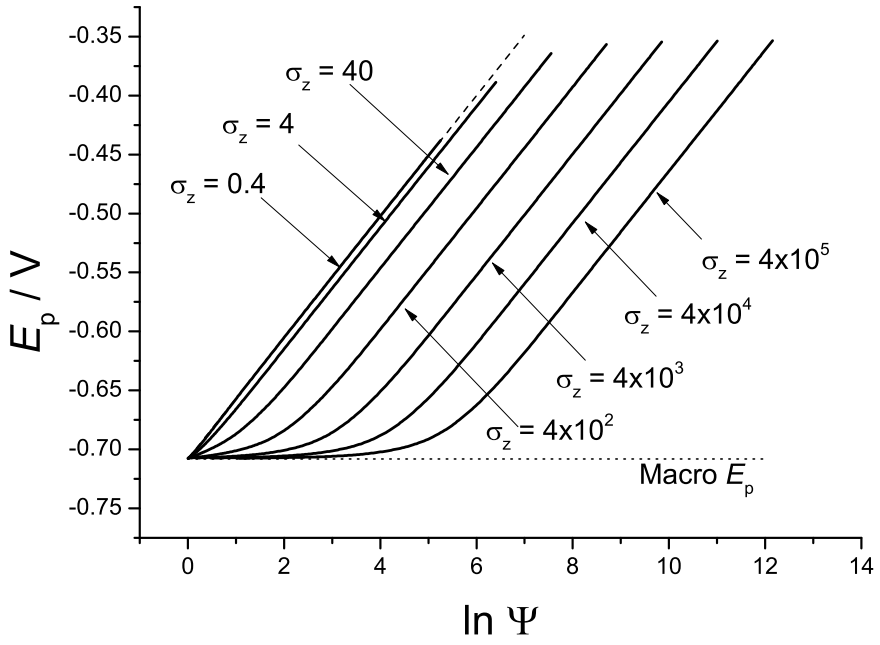

Figure 9.9: *Voltammetric peak current as it varies with surface area ratio, Ψ, for a range of values of σ_z ($D = 10^{-9}\ m^2\ s^{-1}$, $\nu = 10\ V\ s^{-1}$). Dashed line shows relationship predicted by Equation 9.24.*

thin-layer voltammetry:[1]

$$E_p = E_0 + \frac{RT}{\alpha F} \ln\left(\frac{ARTk^0}{\alpha FV\nu}\right) \tag{9.26}$$

The limit given by Equation 9.25 is the maximum scale of surface 'roughness' that will still result in apparent catalytic behaviour. An analogous situation occurs in the case of particle modified electrodes where the peak potential differs from that predicted by Equation 9.24 when the particles become too large.

9.4 Conclusions

The voltammetric behaviour of an electroactive porous surface has been explored under the two different kinetic limits. First, in the case of a surface with fully reversible electrode kinetics and small pore size, it was demonstrated that the peak current varies between two different limiting behaviours as the scan rate is varied. The cross-over point between these two zones was also established. Second, for the case of fully irreversible electrode kinetics, it was established that in the limit of low pore depth, the voltammetry displayed an apparent catalytic effect with the peak potential shifting according to an equation previously developed from observations of nanoparticle covered electrode systems. The limit (in terms of pore depth) under which this effect operates was established.

Bibliography

[1] A. J. Bard and L. R. Faulkner, *Electrochemical Methods: Fundamentals and Applications.*, John Wiley & Sons, New York, 2nd edn., 2001.

[2] M. Winter and R. J. Brodd, *Chem. Rev.*, 2004, **104**, 4245–69.

[3] M. C. Blanco-Lopez, S. Gutierrez-Fernandez, M. J. Lobo-Castanon, A. J. Miranda-Ordieres and P. Tunon-Blanco, *Anal. Bioanal. Chem.*, 2004, **378**, 1922–1928.

[4] M. C. Rodriguez, M. D. Rubianes and G. A. Rivas, *J. Nanosci. Nanotech.*, 2008, **8**, 6003–6009.

[5] Z. Wang, J. Liu, Q. Liang, Y. Wang and G. Luo, *Analyst*, 2002, **127**, 653–658.

[6] B. Fang, H. Liu, G. Wang, Y. Zhou, S. Jiao and X. Gao, *J. App. Polymer Sci.*, 2007, **104**, 3864–3870.

[7] Q. Wan, X. Wang, X. Wang and N. Yang, *Polymer*, 2006, **47**, 7684–7692.

[8] F. G. Chevallier, L. Jiang, T. G. J. Jones and R. G. Compton, *J. Electroanal. Chem.*, 2006, **587**, 254–262.

[9] D. Menshykau and R. G. Compton, *Langmuir*, 2009, **25**, 2519–2529.

[10] M. C. Henstridge, E. J. F. Dickinson and R. G. Compton, *Rus. J. Electrochem.*, 2012, **48**, 629–635.

Conclusions

Numerical techniques have been used to simulate the voltammetric response of a number of different heterogeneous electrode systems. These are systems in which the electrode surface is not flat or in which the electrode kinetics are spatially variant. Specific examples studied were 'highly ordered pyrolytic graphite'-like systems where the electrode is composed of two separate materials each with a different electrochemical rate constant; a conducting spherical particle on an insulating supporting surface; a variety of regularly distributed arrays of conducting particles (discs, bands, hemispheres, spheres, etc.) on an insulating surface; a long insulating cylindrical pore with a conducting band about its inner circumference; and a surface permeated by a regular distribution of cylindrical pores where the entire pore interior was electroactive.

In Chapter 1, the fundamentals of an electrochemical process were outlined. In Chapter 2, a mathematical model for the experimental technique, cyclic voltammetry (CV) was developed for experiments at macroelectrodes, microelectrodes, and arrays of microelectrodes. In Chapter 3, the method of finite differences was applied to the models developed in Chapter 2, and numerical techniques for solving these models were elucidated.

Chapter 4 considered the voltammetry of electrodes composed of two different electroactive materials, each with different kinetic properties. Particular attention was given to the example of systems that are similar to highly ordered pyrolytic graphite (HOPG) in which thin bands of one highly active material are distributed over a surface of some other much less active material. It was demonstrated that under certain circumstances, such a system would be expected to show two peaks in the forward sweep of the voltammetry, one attributed to each surface material.

An experimental design was described that would make it possible to challenge the hypothesis that the slower basal plane of HOPG does not contribute to the voltammetry at all.

In Chapter 5, the steady-state voltammetry of a conducting spherical particle on a planar insulating supporting surface was investigated. An algebraic expression that completely describes the current response in the limit of irreversible kinetics was established. In addition, a mapping of the voltammetry of such a system to that of an isolated spherical particle, which can easily be simulated by any commercially available electrochemical simulation package, was developed.

Chapter 6 looked at the voltammetry of a electrochemical system that undergoes the EC′ (catalytic) mechanism, at an array of hemispherical micro- and nanoparticles. It was demonstrated that under certain conditions, split peak behaviour could be seen in the forward sweep of the voltammetry, which has previously been demonstrated for such systems at a macro-electrode. Additionally it was seen that the separation of the two peaks varied with the surface coverage of the particles such that a higher coverage resulted in greater separation.

Chapter 7 considered a one-electron reduction at a range of systems where an inactive supporting surface was covered with a distribution of electroactive particles of a variety of shapes. Of particular interest were micro- and nano-scale particles that are non-flat, e.g., hemispheres, spheres, etc. Distributions of such particles were demonstrated to show an apparent catalytic effect whereby the electrochemical rate constant (inferred through study of the voltammetric peak potential) appeared to increase with an increasing ratio of electroactive surface area to geometric area. An algebraic expression describing this effect was developed. This has particular relevance to the emerging field of nanoelectrocatalysis.

In Chapter 8, the voltammetry of a conducting band around the interior surface of a long insulating pore was considered. Four limiting voltammetric behaviours were identified corresponding to the large and small limits of the pore radius and band height. Of particular interest was the case where both the radius and band height are small, where the voltammetric response is that expected for a macro-electrode, despite the micro-/nano-scale of the electrode.

Chapter 9 built on the work in Chapters 7 and 8 to simulate the voltammetry of a surface permeated by cylindrical pores. It was demonstrated that in the limit of low pore depth, an apparent catalytic effect is observed, akin to that seen in Chapter 7 and the limit (in terms of depth) under which this effect operates was established

Future work should seek to experimentally confirm the prevalence of the apparent catalytic effect demonstrated in Chapters 7 and 9, and apply the theory to other geometries and experimental conditions. It is commonly held that such an effect (which is often observed experimentally) is due to some altered property at the nanoscale relative to the bulk material, e.g., different exposed crystal planes, altered electronic structure etc. The work in this thesis has demonstrated that such effects *can* be attributed solely to the geometry of the system, however nano-scale effects may also be in operation. In that case, deconvolution may be aided by a thorough investigation into the electronic and crystallographic structure of the nano-particulate electrode systems in question.

Appendix A

Additional Results for Chapter 7

As discussed in Chapter 7, a large number of simulations of electrode systems of a variety of non-flat geometries were performed. The chapter details the results arising from the use of an array of hemispherical particles as well as from an array of spherical particles. Here the results of the other geometrical models are presented to demonstrate that the results derived for an array of hemi/spherical particles are generally applicable.

For all figures and examples given, the following fixed parameters were used: scan rate, $\nu = 0.1$ V s^{-1}; transfer coefficient, $\alpha = 0.5$; diffusion coefficient, $D = 10^{-5}$ cm^2 s^{-1}; initial concentration of species 'A', $c^*_{\mathrm{A}} = 1$ mM; and temperature, $T = 298$ K. The modified surfaces are all assumed to be macrodiscs that have a radius of 1.5 mm.

In the irreversible limit under case 4 diffusion, the peak current is seen to obey the equation:

$$E_p = E^0_f - \frac{RT}{\alpha F}\left[0.780 - \ln(k^0_{\mathrm{app}}) + \ln\left(\sqrt{\frac{\alpha F D \nu}{RT}}\right)\right] \tag{A.1}$$

A.1 Array of Hemicylindrical Wires

For long hemicylindrical wires:

$$\Psi = \frac{N\pi r_{\mathrm{e}} l}{A} = \frac{\pi}{2}\Theta \tag{A.2}$$

where l is the length of the hemicylinder. Figure A.1 shows how the voltammetry of an array of hemispherical particles varies with the rate constant, k^0, for the specific example of coverage, $\Theta = 0.5$, and hemicylinder radius $r_e = 100$ nm, such that diffusion is in case 4. It can be seen that the peak height transitions from the irreversible to the reversible Randles–Ševčík limit as k^0 increases.

Figure A.2 demonstrates how the peak potential, E_p, of the voltammetry in the irreversible limit ($k^0 = 10^{-7}$ cm^2, $r_e = 100$ nm) shifts with increasing surface coverage, Θ in the range 0.1 – 0.7 while still maintaining the same (case 4) peak current, I_p. Also shown is the corresponding peak position for a macroelectrode. Notice that at lower coverage ($\Theta = 0.1$, $d = 632$ nm), I_p begins to deviate somewhat from the Randles-Ševčík limit. All parameters except for the shape of the particles are identical to those used in Figure 5 in the main text. Notice that the deviation from the Randles-Ševčík limit at $\Theta = 0.1$ is greater in the case of the hemicylinder than it is for the hemisphere. This is because the separation between two electroactive regions is greater in the case of the hemicylinder; for the hemispheres ($\Theta = 0.1$, $r_e = 100$ nm), the centre-to-centre separation, d, is 0.63 μm, whereas for the hemicylinders, $d = 2$ μm. Figure A.3 shows how E_p is affected by Θ (for a range of values of k^0). The dashed lines indicate the values predicted by Equation A.1, demonstrating excellent agreement with simulated results as long as the kinetics are in the irreversible limit, with deviation from that equation seen only for $k^0 \geq 10^{-3}$ cm s^{-1}.

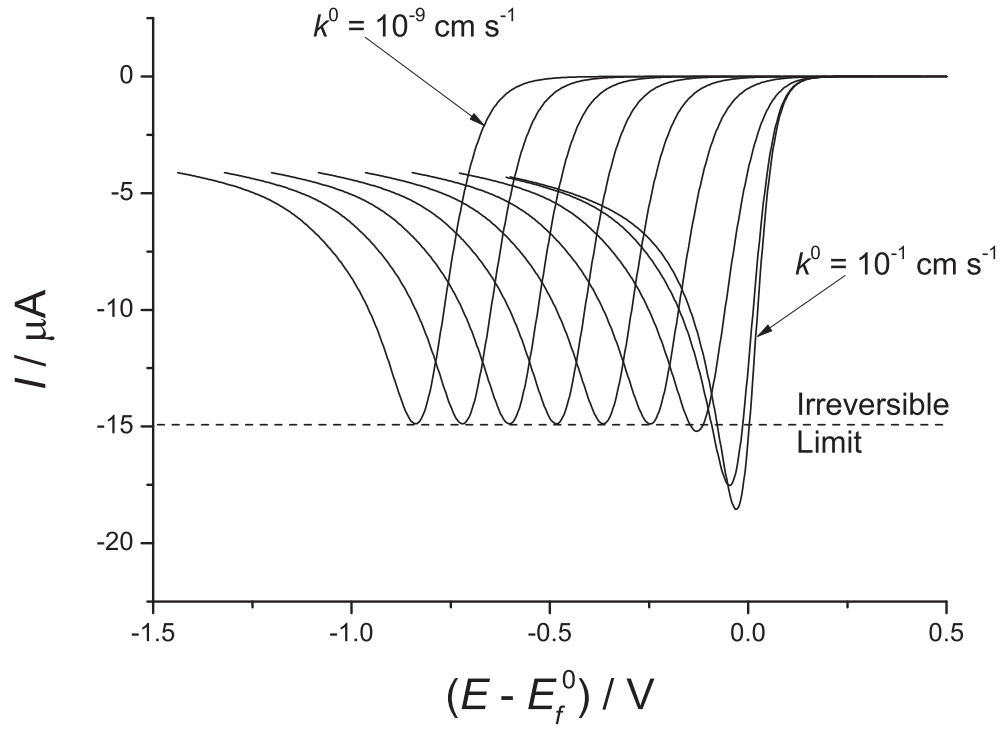

Figure A.1: *Voltammetry of an array of* ***hemicylindrical wires*** *as it varies with rate constant, k^0, in the range 10^{-1}, 10^{-2}, 10^{-3}, ..., 10^{-9}, $\Theta = 0.5$, and $r_e = 100$ nm.*

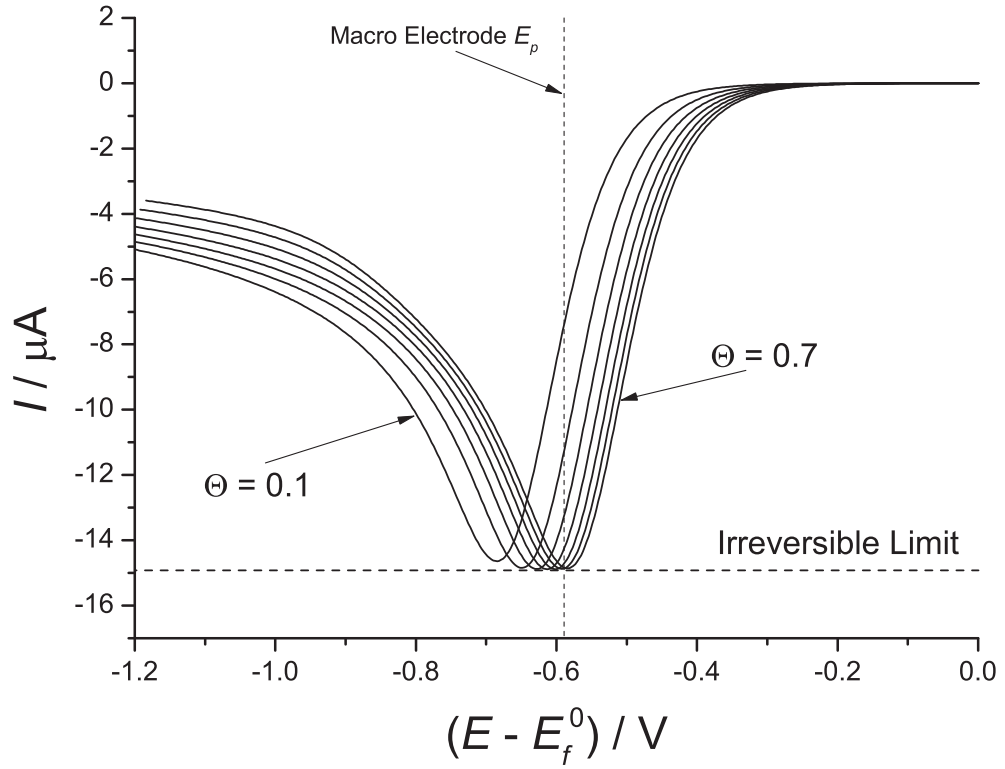

Figure A.2: *Voltammetry of an array of* ***hemicylindrical wires*** *as it varies with surface coverage, Θ, in increments of 0.1. $k = 10^{-7}$ cm s^{-1}, $r_e = 100$ nm.*

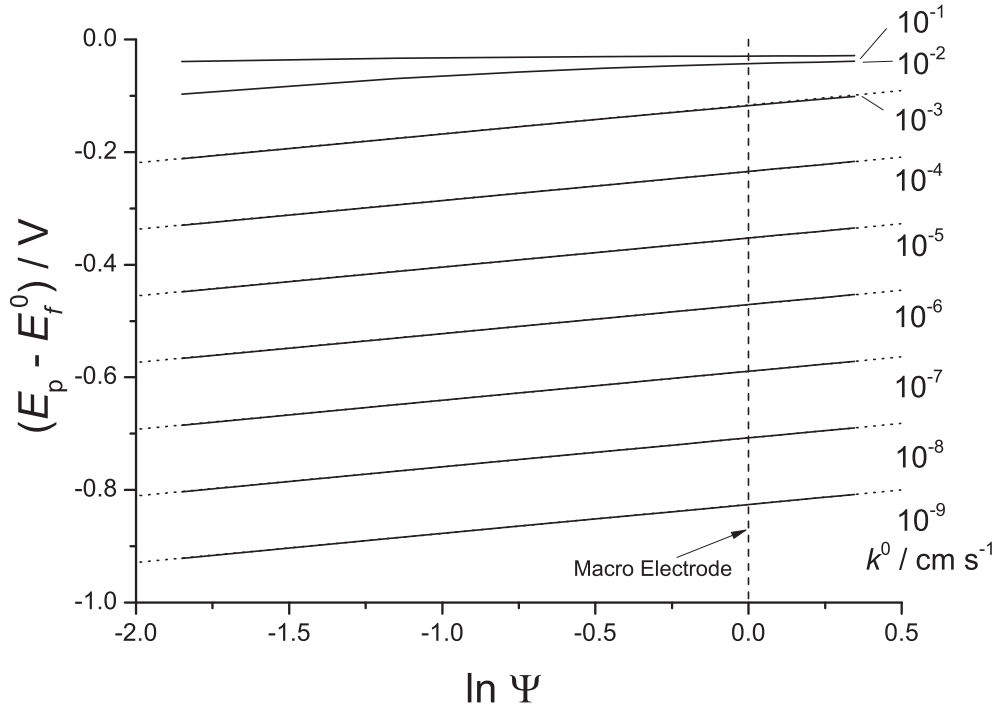

Figure A.3: *Variation of peak potential, E_p, with coverage, Θ, for a range of values of rate constant, k^0, for an array of* ***hemicylindrical wires*** *with $r_e = 100$ nm. Dotted lines show values predicted by Equation A.1.*

A.2 Array of Hemispherical Particles on an Active Surface

For an electroactive surface covered in electroactive hemispheres:

$$\Psi = \frac{(1 - N\pi r_e^2) + 2N\pi r_e^2}{A} = \Theta + 1 \tag{A.3}$$

such that the surface tends toward macro-electrode behaviour as $\Theta \to 0$. This differs from all of the other geometric models that have been investigated in that the peak position does not vary linearly with $\ln \Theta$. Figures A.4, A.5, and A.6 demonstrate the equivalent for a 'hemisphere array on an active surface' of the data that was shown for an array of wires in Figures, A.1, A.2, and A.3 respectively. When the surface is active, the shift in peak potential for increased coverage of hemispheres is much less significant than when the surface is inactive. For this specific example, the difference in peak potential, ΔE_p, between an active surface with $\Theta = 0.1$ and one with $\Theta = 0.7$ is 22 mV, whereas the same comparison for an inactive surface gives $\Delta E_p = 100$ mV.

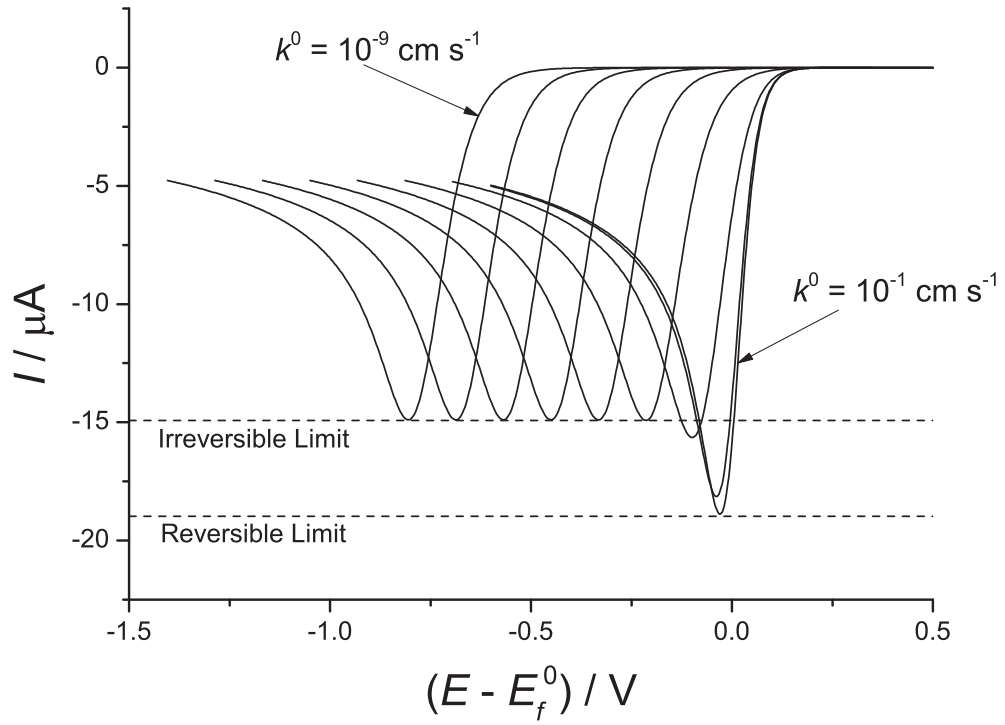

Figure A.4: *Voltammetry of an array of* ***hemispherical particles on an active surface*** *as it varies with rate constant, k^0, in the range 10^{-1}, 10^{-2}, 10^{-3}, ..., 10^{-9}, $\Theta = 0.5$ ($\Psi = 1.5$), and $r_e = 100$ nm, $d = 282$ nm.*

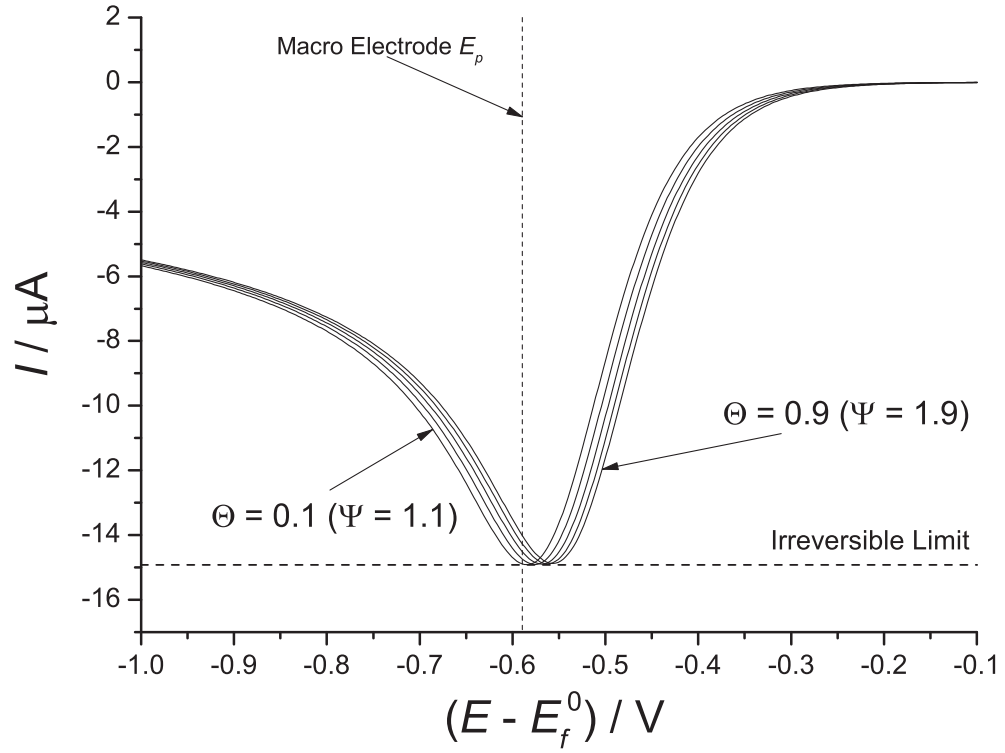

Figure A.5: *Voltammetry of an array of* ***hemispherical particles on an active surface*** *as it varies with surface coverage, Θ, in increments of 0.1. $k = 10^{-7}$ cm s^{-1}, $r_e = 100$ nm.*

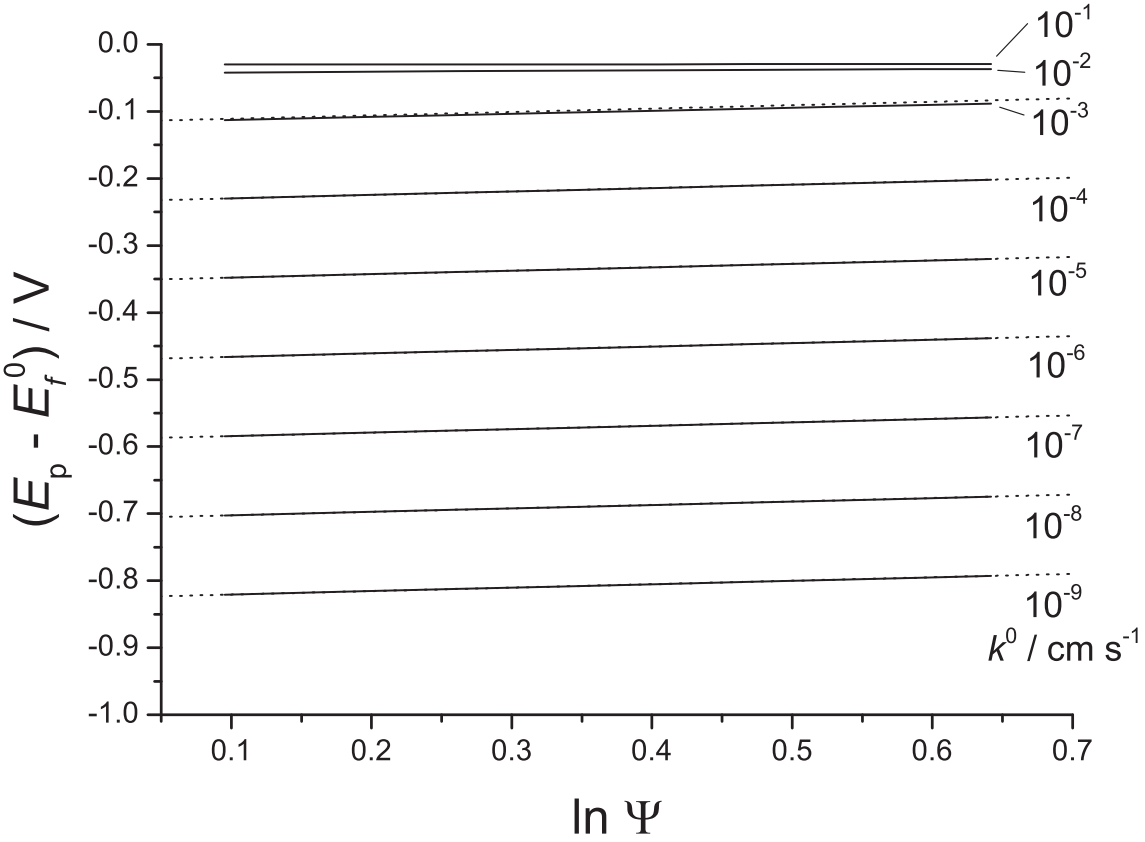

Figure A.6: *Variation of peak potential, E_p, with coverage, Θ, for a range of values of rate constant, k^0, for an array of* ***hemispherical particles on an active surface*** *with $r_e = 100$ nm. Dotted lines show values predicted by Equation A.1.*

A.3 Array of Cylindrical Particles

For an array of cylindrical particles:

$$\Psi = \frac{N(\pi r_e^2 + 2\pi r_e z_e)}{A} = (2\frac{z_e}{r_e} + 1)\Theta \tag{A.4}$$

where z_e is the cylinder height. Figure A.7 shows how the peak potential of the voltammetry varies with surface coverage Θ for the simple case where $r_e = z_e = 100$ nm. Note that in this situation $\Psi = 3\Theta$. Figure A.8 shows how the voltammetry varies with varying cylinder height, z_e, for a fixed cylinder radius, r_e. As can be seen, the a larger z_e leads to a greater value of Ψ and thus a more significant peak shift. Figure A.9 shows how the peak position varies with cylinder height for a range of values of Θ, with dashed lines showing the values predicted by Equation A.1 demonstrating excellent agreement with simulated results.

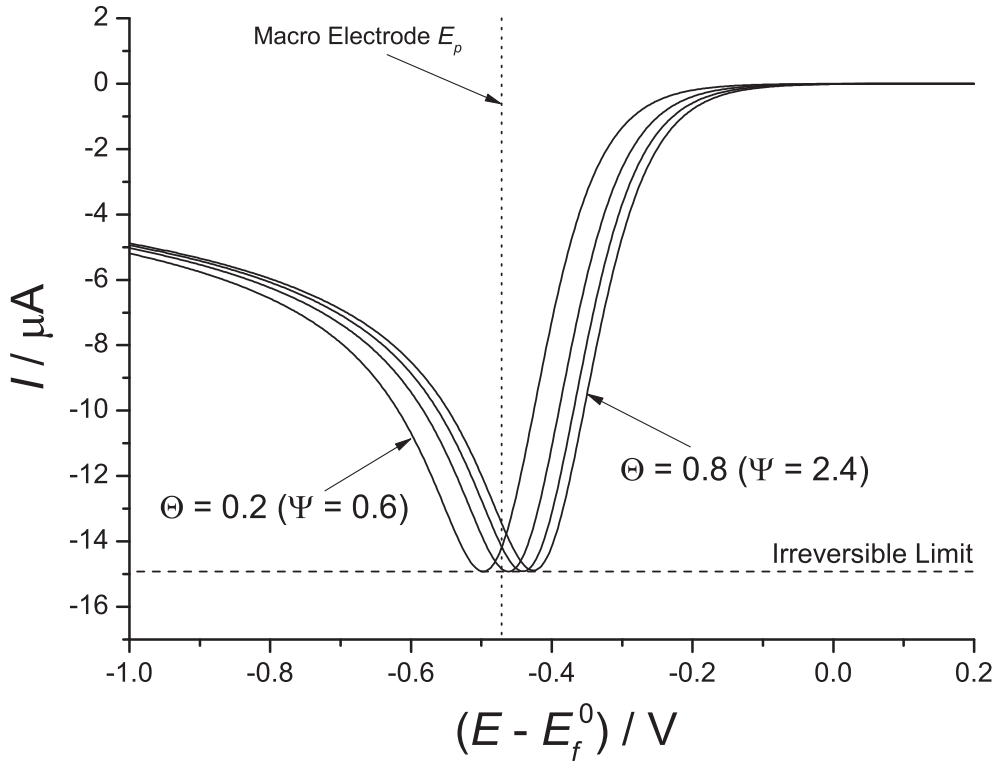

Figure A.7: *Voltammetry of an array of* ***cylindrical particles*** *as it varies with surface coverage, Θ, in increments of 0.2.* $k = 10^{-6}$ *cm* s^{-1}, $r_e = z_e = 100$ *nm.*

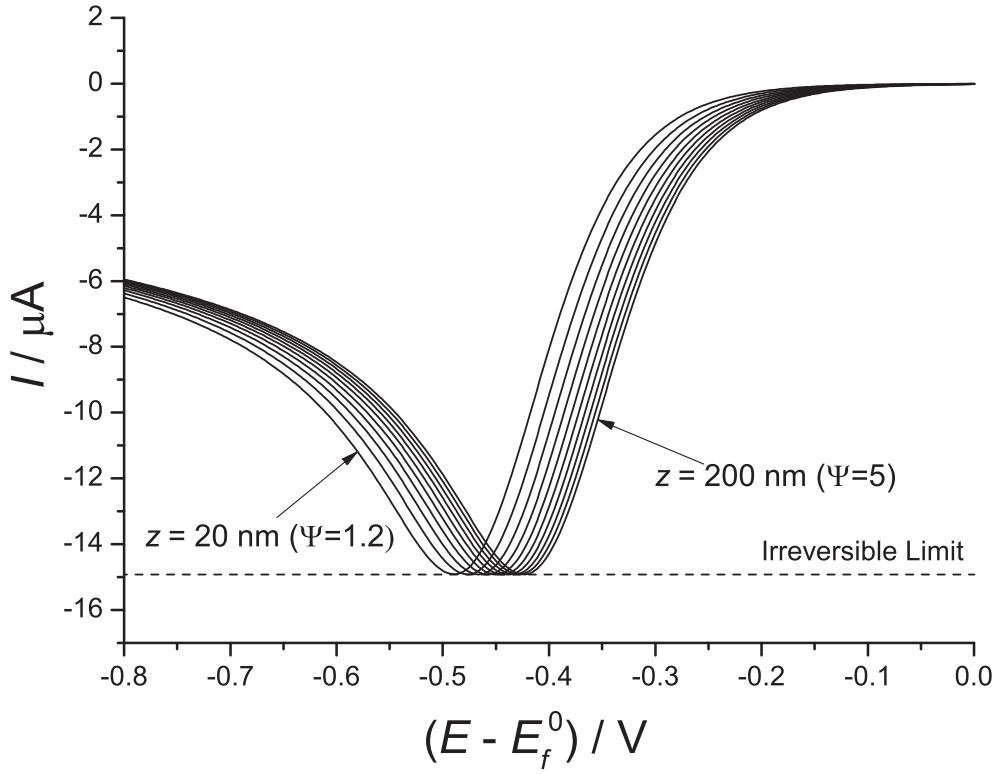

Figure A.8: *Voltammetry of an array of* ***cylindrical particles*** *as it varies with cylinder height,* z_e*, in increments of 20 nm.* $k = 10^{-6}$ *cm* s^{-1}, $\Theta = 0.5$, $r_e = 100$ *nm.*

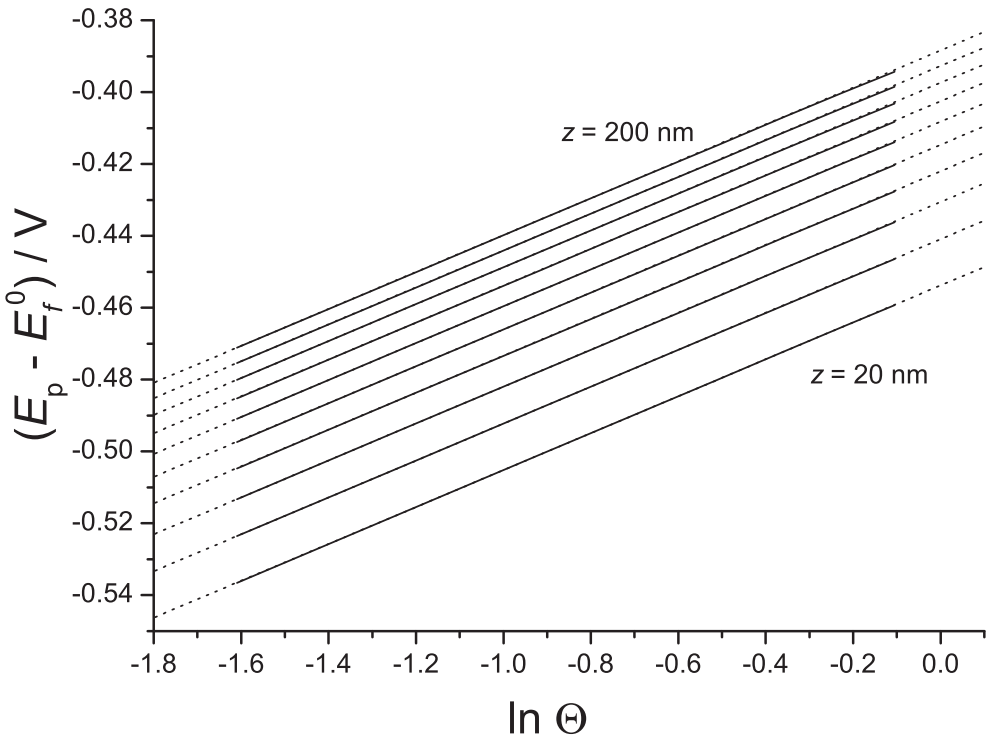

Figure A.9: *Variation of peak potential, E_p, with coverage, Θ, for a range of values of cylinder height, z_e, for an array of* ***cylindrical particles*** *with $r_e = 100$ nm, $k = 10^{-6}$ cm s^{-1}. Dotted lines show values predicted by Equation A.1.*